ULTRA-WIDEBAND CONTACTLESS CURRENT SENSORS FOR POWER ELECTRONICS APPLICATIONS

by

Ali Parsa Sirat

A dissertation submitted to the faculty of
The University of North Carolina at Charlotte
in partial fulfillment of the requirements
for the degree of Doctor of Philosophy in
Electrical Engineering

Charlotte

2023

Approved by:

Dr. Babak Parkhideh

Dr. Tiefu Zhao

Dr. Dipankar Maity

Dr. Maciej Noras

ABSTRACT

ALI PARSA SIRAT. Ultra-Wideband Contactless Current Sensors for Power Electronics Applications. (Under the direction of DR. BABAK PARKHIDEH)

Enhanced power density factors can be achieved in the new generation of power electronics by utilizing wide-bandgap semiconductor switching devices with higher switching speeds and lower losses. These characteristics make high-frequency switching (wide-bandgap-based) power converters superior to silicon-based converters in several respects, including better size, weight, efficiency, and power density than silicon-based converters. This makes wide-bandgap-based power converters ideal for applications where size and weight matter, such as in aerospace or consumer electronics. They are also well suited for applications that require high efficiency or high power density, such as renewable energy systems.

In contrast to traditional converters, WBG power converters have significantly different requirements, making it harder to integrate components and sensors due to their tighter tolerances. Wideband current sensors are also necessary for diagnosing, monitoring, and controlling wide bandgap power converters. Integrated current sensors should also be considered when designing power converter layouts in terms of size and invasiveness, which are properties essential for the next generation of power converters, but cannot be achieved with commercial current sensors currently available. Among these properties are size, speed, noise immunity, accuracy, linearity, capacity, isolation, and non-invasiveness; due to size constraints and cost constraints, these converters are not equipped with current probes as well. Therefore, non-invasive, ultrafast, high-capacity, switch noise-immune sensors are required for wide-bandgap-based power electronics converters. These sensors should also have high accuracy and linearity while providing proper isolation between the power device and the sensing circuitry.

The purpose of this thesis is to present comprehensive analyses of single-scheme and hybrid current sensors, with emphasis on their design and implementation, as well as their integration with power electronics systems for efficient sensing, where the results can be applied to improve accuracy, efficiency, and reliability of current sensing applications. The presented study illustrates that there is no specific method of current sensing that can combine all the required sensing factors at once and the results of multiple feasibility studies have been used to develop guidelines for designing current sensors that provide high-quality output and are readily applicable to the next generation of power converters based on their intended application. Frequency response verification using vector network analyzers and also different types of switching current waveform comparisons will prove the functionality of proposed light-size and low-cost sensing solutions.

TABLE OF CONTENTS

LIST OF TABLES

LIST OF FIGURES

LIST OF ABBREVIATIONS

AMR	Anisotropic Magnetoresistive
BW	Bandwidth
CT	Current Transformer
DPT	Double-Pulse Tester
DUT	Device Under Test
EMI	Electromagnetic Interference
FET	Field-Effect Transistors
FG	Fluxgate
GaN	Gallium Nitride
GMR	Giant Magnetoresistive
HE	Hall Effect
HF	High Frequency
HPF	High Pass Filter
IC	Integrated Circuit
IGBT	Insulated Gate Bipolar Transistor
LF	Low Frequency
LPF	Low Pass Filter
MF	Middle Frequency
MO	Magneto-Optical

MOSFET	Metal Oxide Semiconductor Field Effect Transistor
MR	Magnetoresistive
MS	Multi-Scheme
PCB	Printed Circuit Board
RC	Rogowski Coil
SiC	Silicon Carbide
SNR	Signal-to-Noise Ratio
SS	Single-Scheme
SSCB	Solid-State Circuit Breaker
TI	Texas Instruments
TMR	Tunneling Magnetoresistive
UHF	Ultra-High Frequency
UWB	Ultra-Wideband
VNA	Vector Network Analyzer
WBG	Wide-Bandgap

CHAPTER 1: INTRODUCTION

1.1 Motivation

A variety of applications are served by power converters, including motor drives, renewable energy systems, electric vehicles, aerospace technologies, and data centers. For controlling, protecting, and monitoring, these systems utilize current data at their different electrical nodes and branches [1-2]. For example, in a motor drive, current data is used to compute instantaneous torque and power, adjust the speed and torque, and detect any failure in the system. By using current control loops, power converters can monitor or limit both the instantaneous and average power/current of their inputs, outputs, and internal parts (such as the currents of switches, inductors, legs, or capacitors), thereby controlling the active and reactive powers. Although the requirements for the current sensing signal may differ, for accurate current-mode (peak, valley, average, or sample-and-hold) control, current measurement information is vital [3]. Current control loops provide feedback to the power converter system to ensure stability and optimal operation. This feedback helps the system monitor and adjust its output and input power, as well as its internal parts, to guarantee desired performance. All power system facilities [4] must be equipped with rapid overcurrent and short-circuit protection schemes to prevent components from overheating and malfunctioning. Direct line (or device) current measurement is one of the most efficient methods of providing quick trip information in the event of a fault [5]. For the sake of health monitoring and reliability purposes, accurate current information such as rise or fall times are of immense importance [2]. Knowing current information like rise and fall times can provide insight into the health of power system components, allowing operators to identify potential problems before they become catastrophic. Additionally, having accurate and timely current information can help prevent components from overheating and malfunctioning, which can cause expensive repairs and long outages. For instance, power semiconductor devices have a maximum junction temperature rating after which their performance may start to degrade and ultimately fail, so having accurate current measurement can help prevent such failures [6-7]. All these factors confirm that a precise current measurement (of the different parts) within an optimal power converter is extremely critical, despite the fact that the current measurement requirements for each application may differ. Applications such as motor control, DC-DC and AC-DC power conversion, battery management, and renewable energy all require accurate current measurement [8-9].

1.2 Emerging Wide Bandgap Power Converters

Power converters with outstanding power density factors can be developed with the development of wide-bandgap (WBG) semiconductor switching devices, where size (Figure 1.1), weight, efficiency, and power density are optimized [10-14]. Due to their superior performance over those using Si MOSFETs or IGBTs, WBG converters are especially suitable for applications such as transportation, aerospace, and grid-connected

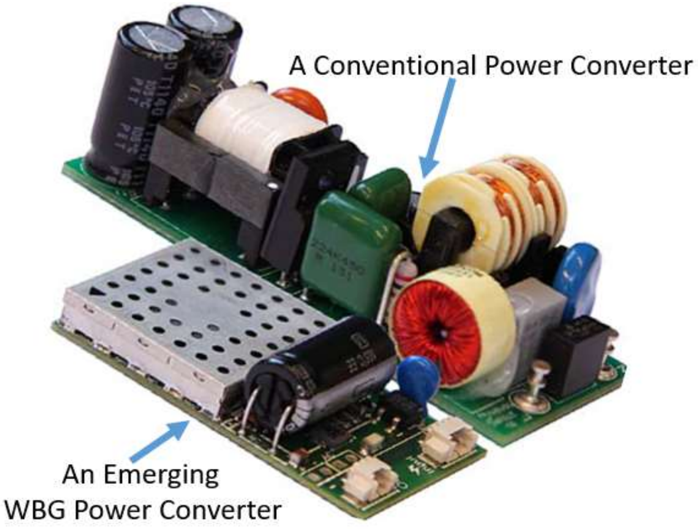

Figure 1.1: Comparison of a conventional Si-based power converter and a WBG-based converter with the same power rating [24].

technologies [13-14]. They are also suitable for renewable energy harvesting and smart grid infrastructure systems, as well as in data centers and industrial processes. As opposed to old-fashioned converters, WBG converters require a greater degree of complexity for design and manufacturing [14-16]. Due to tight requirements, which are primarily concerned with size and bandwidth (BW), it is more difficult to integrate components, such as sensors.

1.2.1 WBG Power Converters Integration Challenges

WBG semiconductor switching devices have facilitated the development of power converters with optimal power/loss (or lower switching/conduction losses) factors (which result in improved efficiency), increased switching/recovery speed, and higher power density. These WBG semiconductor devices offer optimal performance for power conversion applications due to their superior electrical properties [13-15]. By increasing the switching frequency, the size of passive components (such as inductors, transformers, and capacitors) will shrink subsequently, which results in more miniaturized and lighter converters. Additionally, due to their fast-switching speed and low switching losses, these devices have a higher power density, which makes them suitable for high-power applications [17-18]. By reducing the losses, the necessity for heat dissipation will drop as well. This indicates a lighter cooling system can be applied, and accordingly, the overall size, weight, and efficiency will be improved and in generally, a WBG converter has a smaller size/weight and better efficiency/power density than an IGBT or Si Mosfet converter [19]. Power converters with WBG technology have more design and manufacturing issues, making sensor and component integration significantly more challenging. Most of these challenges are related to size, geometry, and bandwidth (BW). For example, tight decoupling layouts in GaN-based converters do not allow parasitic values to be larger than a limit, which means almost nothing can be put on the power trace invasively. Technically, fast switching in WBG converters can highlight the impact of high either *di/d*t or *dv/dt* [16], which can induce destructive voltages and currents on parasitic inductances and capacitances [20-21]. This issue needs to be addressed through converter layout design optimization [22]. For instance, the layout of inductors and capacitors should be optimized to minimize the coupling between them, allowing the system to operate at higher switching frequencies. There is also a requirement for faster sensor technology to be deployed if the operation is to occur more quickly [23]. Specifically, it is necessary to use sensors with greater BW currents and voltages to control and monitor the power converter [24]. As mentioned earlier, a higher amount of *di/dt* and *dv/dt* can be inferred from having an environment with more Electromagnetic Interference (EMI) noises, which can lower the signal-to-noise ratio (SNR) of integrated sensors [16]. Contemplating all these issues, current sensing in WBG HF power electronics is not as easy as in conventional power converters. Due to the effects of EMI on current sensing in WBG HF power electronics, advanced design techniques and fabrication processes may be necessary to maximize the SNR and reduce the effects of EMI on the current sensing [24].

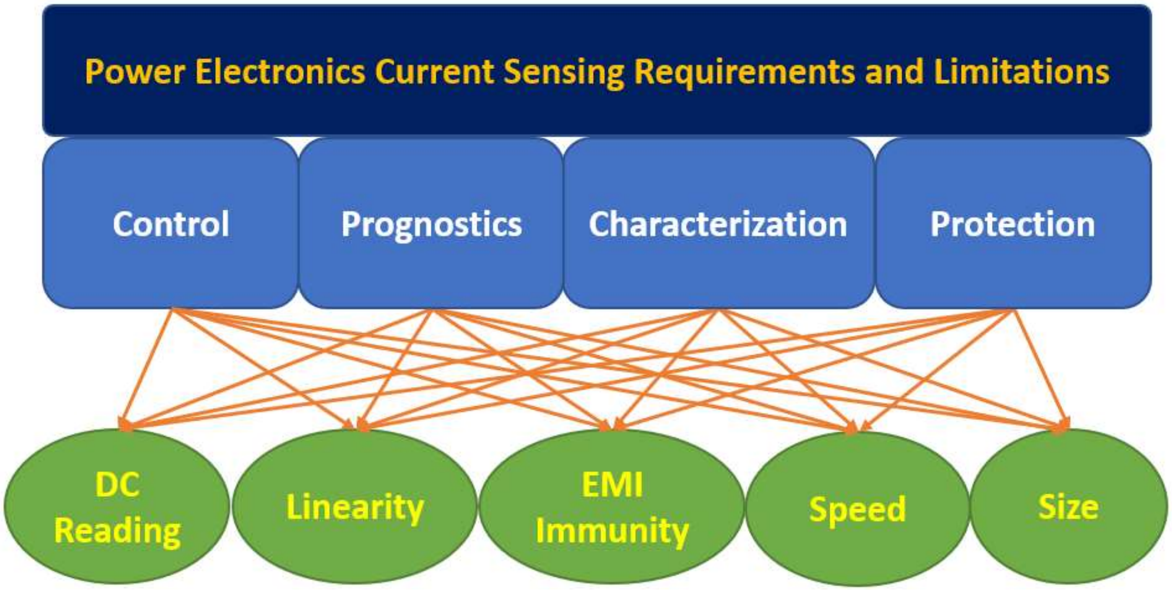

Figure 1.2: The current sensor requirements for high-frequency power converters [24].

1.2.2 Suitable Current Sensor for Optimal Power Converters

Diagnostics, prognostics, and control of WBG power converters require high BW current sensors [24]. Although speed is a major concern, it is not the only concern when it comes to factors such as limited space, bulk, and intrusiveness (from the previous section). Therefore, high precision, miniaturization, and non-intrusive sensors are essential to optimize the performance of WBG power converters [23]. Even though shunt resistors can sense current quickly, they are invasive, consume power, and introduce parasitic values if they are placed in the switch power trace [25-27], which makes them unsuitable for WBG power electronics [23].

To reduce these undesirable effects, inductive current sensors have been proposed as an alternative, as they are more precise and consume less power [24]. A further disadvantage is that most current sensors available in the commercial market lack many of the properties required for emerging converters to utilize for current measurement (concerns like size, BW, noise immunity, accuracy/linearity, high-capacity, isolation/non-invasiveness). As such, there is an urgent need for a new generation of current sensors that can meet these stringent requirements. For instance, in short-circuit protection of SiC Modules, the controller needs to know that the phase (or switch) current reached its threshold in less than1 microsecond. However, in high-power applications, it is not feasible to implement such a current sensor due to lack of a high current capacity (>200A) and high BW (>10MHz) current sensor in the market [28]. WBG power converters require ultrafast (or high BW), high current capacity, precise, high-resolution (or noise-free output), and easy-integration current sensors (or small and non-invasive) sensors. However, it will be demonstrated in Chapter II that all single-scheme current sensors have their own limitations.

1.3 Thesis Contributions

The dissertation provides several new or enhanced concepts and analyses to address the challenges related to design suitable ultra-wideband contactless current sensors for power electronics applications. These contributions are divided into three categories, which have been embedded in body of the four subsequent chapters, enabling each chapter to be read either as a standalone text with a few references to the other chapters or as a whole big-picture narrative. The thesis also summarizes findings and contributions in the conclusion chapter along with future research directions to extend the current research. The following three categories constitute the main contributions:

1) DC Magnetic Current Sensors

Despite the fact that most DC magnetic sensors, including Hall-effect, magnetoresistive, and fluxgate sensors, do not achieve a high current sensing BW, they can still be exploited for certain applications, especially in power converter's current control, if some adjustments and compensations are made to their physical and electrical properties. These adjustments can include the use of external components, such as RC filters and amplifiers, to reduce the noise and to increase the accuracy of the sensing signals. Furthermore, the use of a proper signal conditioning algorithm can also help to improve the overall performance of the sensor. They have been studied specifically in **Chapter 2** for their properties under topics such as invasiveness, bulkiness, EMI-immunity, thermal/offset drift, linear sensing range, power consumption, and cost, where comparison-based discussions provide a better understanding of the nature of these properties. Based on this knowledge, one may select the most suitable ones for applications that are discussed later in that chapter, along with their alternatives in terms of size, cost, and BW. **Chapter 3** discusses their role in optimal hybrid sensors, along with deciding which of them to use for such hybrid implementation, and how to choose an optimal PCB layout. In order to improve noise suppression of the whole sensor output, lowering their cutoff frequency has been proposed and discussed. In **Chapter 5**, experimental results are presented to validate the noise suppression of a hybrid sensor, in which a technical choice between TMR (tunneling magnetoresistive) and micro-fluxgate sensors is presented and conducted. The hybrid sensor was found to have improved noise suppression due to the lower cutoff frequency, where the results of the experiments validated the proposed filtering method. Overall, this thesis is one of the pioneers to introduce commercial on-chip fluxgate sensor applications in power electronics current sensing.

2) High-Frequency Inductive Current Sensors

A significant portion of this thesis is devoted to enhancements and novelties in current transformer and Rogowski coil circuitry, where the Rogowski coil represents the most novelties in terms of signal quality and BW. The Rogowski coil offers better wide-bandwidth, high-dynamic range, and low-noise performance. **Chapter 2** describes their overall advantages and disadvantages over other sensing methods in terms of technical integration concerns (BW, size, cost, etc.). Due to their ultrahigh detection speed as compared to other contactless current sensing methods, the application of these methods in protection, characterization, and reliability is highlighted. A high BW AC current sensing method is developed in **Chapter 2**, which employs compound current transformers in a special all-passive impedance network to generate a fully passive AC current sensor. The proposed sensing network provides a nearly constant bandwidth of sensing signals over a wide frequency range from 10 Hz to 10 MHz without electronics or power supplies. To provide the reader with a powerful understanding of how to select the appropriate hybrid current sensor component based on specific applications,

Chapter 3 identifies the technical similarities and differences between the current transformer and the Rogowski coil. As a result of the comparison of the two inductive methods in **Chapter 3**, electronics Rogowski coils are well suited to several applications involving HF WBG converters, and in **Chapter 4**, all details regarding the design considerations for ultra-wideband PCB-embedded analog Rogowski coils are discussed. Novelties in the design and implementation of integrated Rogowski coils include the following:

a) Different coil design geometries and the relationships between different types of return path (which makes the Rogowski coil to sense differentially) and the *RLC* parasitic elements resulting from the implementation and their effects on the coil's BW and signal response, b) Presenting novel comprehensive mathematical formulas for mutual inductance and stray capacitance of PCB-embedded coils, which have commonly been overlooked in previous research, c) Presenting a comprehensive relationship between the physical properties of PCB-embedded coils (with reference to PCB trace) and the coil's electrical properties, d) An analysis of two novel winding schemes (one involving internally embedded pickup coils, and the other involving helical modular coils) is presented with their analytical advantages discussed, e) Comprehensive frequency-domain formulations and analytics for both inverting and noninverting opamp integrators, f) the difference in the frequency response between inverting integrators and non-inverting integrators and their simple *RC* frequency compensations, g) Passive offset compensation using simple *RC* highpass filters along with their formulations and cutoff frequency selection guidelines, h) Providing four vital characteristics that should be considered when selecting an Opamp part number along with the introduction of two opamps from TI with spectacular performance that can be utilized in switch current sensors, i) Coil termination with small damping resistors

(<10 ohm) and novel formulations and stories for passive *RL* self-integration of the coil, which are essential for both UHF BW sensor extensions as well as reducing coupled noise in the coil and opamp integrators, j) Analytical claims regarding the removal of screen shielding on switch-current Rogowski coils in order to extend the BW, and instead using a small termination, which also results in a need for lower BW opamps for sensor implementation, k) A novel set of formulas for gain-frequency matching of terminated Rogowski coil subcircuits for ultrahigh BW configurations, l) identifying technical problems with the external reset circuitry for switch-current droop compensation, which renders the circuit ineffective for measuring the HF switch current, m) Proposing precision rectifiers based on opamps rather than external reset circuitry for unidirectional HF switch current sensing, n) A proposal for specialized hybrid current sensors that would detect bidirectional HF switch-currents using ultra-wideband Rogowski coils along with DC detectors.

3) Hybrid Contactless DC-UHF Current Sensors

In **Chapter 3**, an all-inclusive literature review is presented on hybrid current sensors in terms of their size, invasiveness, immunity to EMI noises, and BW in which properties that influence those factors are highlighted in order to select components based upon the application requirements. The review concludes with a discussion of the physics, layout designs, and selection of sensing elements for optimal multi-path current sensors, as well as their potential performance in various applications. In **Chapter 5**, the final step is to develop hybrid current sensors capable of detecting bidirectional HF switch currents utilizing ultra-wideband Rogowski coils in conjunction with DC detectors (such as TMR and micro-fluxgate), whereby the reduction in the cut-off frequency of the DC detector is compensated by extending the Rogowski coil so as to reduce noise and nonlinearities within the entire system. As a whole, this thesis is the first published article combining a micro-fluxgate with an embedded Rogowski coil on a PCB for the purpose of detecting power electronics currents with a great degree of accuracy and ultra-high bandwidth.

CHAPTER 2: CURRENT SENSORS INTEGRATION ISSUES

2.1 Introduction

The ability to precisely measure electrical currents is essential for several protection, control, and reliability mechanisms within power converters. Even so, it is likely to be challenging for optimal power electronics converters to develop a single current sensing scheme to measure various types of currents incorporated into WBG devices due to the limited geometry and size of these devices, the required sensing speed, fluctuating ambient temperature, and the high electromagnetic interference (EMI) radiation they cause [29]. This chapter also goes on to explain that there is almost no specific current sensing method that will provide all the necessary size, BW, linearity, isolation, accuracy, and cost to be considered complete, in one place. This is because each of these requirements has different trade-offs for design considerations. As an example of characteristics, accuracy may come at the cost of size, while noise immunity may require increased complexity. This chapter also explains that there is almost no specific current sensing method that will provide all the necessary size, BW, linearity, isolation, accuracy, and cost to be considered complete, in one place. This is because each of these requirements has different trade-offs for design considerations. As an example of characteristics, accuracy may come at the cost of size, while noise immunity may require increased complexity. Hall-effect (HE) sensors are an example of different existing schemes that do not have adequate accuracy and resolution, as well as adequate BW, and along with magnetoresistive (MR) sensors, they need to be compensated for temperature drift. For instance, a Hall-effect device must be compensated for temperature through a closed-loop sensing and complex signal-conditioning circuitry. [25, 30]. Current transformers (CTs) are commonly known for being bulky and becoming magnetically saturated by observing amplitude-significant currents or magnetic fields [31]. Consequently, this saturation can adversely affect the CT's performance and accuracy, making it difficult to rely on the readings from these devices. Even though Rogowski coils have been proven to be a very good option regarding effective volume, cost, and high-frequency sensing, they are not able to detect DC currents (as is the case with CT since DC currents have zero *di/dt*) [32, 33]. Therefore, a second sensor capable of detecting DC currents, such as an HE or MR sensor (or any other applicable magnetometer), is necessary. Shunt resistors can be used to measure the current of a circuit from DC up to MHz (or GHz) frequencies, but they may cause problems regarding their isolation, invasiveness, and temperature-dependent sensitivity, among others. For example, a shunt resistor’s measurement accuracy can be affected by the temperature of the resistor, as the resistance of the resistor increases with the temperature [32]. As well as providing electrical isolation, fluxgate and magneto-optical schemes offer minimal temperature drift, high accuracy, and immunity to EMI noises, and they are particularly advantageous in low-frequency applications, such as measuring DC or low-frequency AC signals. Despite this, implementing these systems is like building a very large, intricate, and expensive circuit by joining together fragile, interlocking components. It is true that they can offer excellent performance, but the cost of implementing them is often too high to make them economically viable [25]. Nevertheless, recent technological advances have made it possible to fabricate on-chip systems that are more efficient and less costly [34]. A study of existing single-scheme current sensors' performance is presented in this section of the thesis to understand the challenges associated with incorporating them into the architecture of emerging power converters. Additionally, the potential of developing novel methods to improve the performance of these single-scheme current sensors is also explored. For instance, the survey evaluated the performance of single-scheme current sensors in terms of their accuracy, linearity, and dynamic range, as well as the influence of high EMI noise on their performance.

2.2 Current Sensing Methods in Power Applications

A current sensor is a device used to measure electric current, either alternating current (AC) or direct current (DC). These devices are used in a variety of applications, including detecting faults, monitoring performance, and detecting changes in system behavior. Basically, power applications employ a variety of current monitoring products to control, characterize, monitor, and protect current flow. Current sensors, for example, are used in power lines to measure the flow of current, which can detect overcurrent or excess currents [35]. Furthermore, current monitoring can be utilized for several purposes, such as fault detection, monitoring performance, and observing changes in system behavior. In this section, single schemes of current sensing methods are categorized into four branches [25] and their working principles are briefly discussed. Afterwards, their integration issues within power electronics are analyzed. The four categories of sensing technologies are: 1) Ohmic current sensors, 2) DC magnetic field detectors, 3) Inductive-based sensing schemes, and 4) Magneto-optic sensing technology.

2.2.1 Ohmic Current Sensors

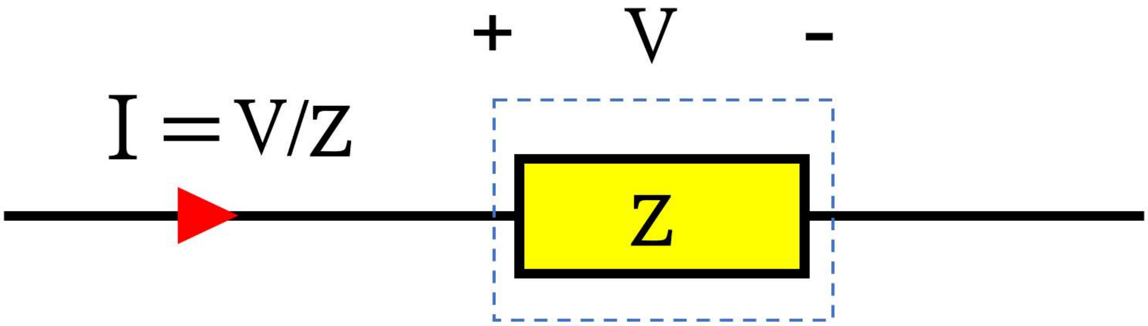

Figure 2.1: Current sensing based on Ohm's Law [24].

By passing the current through a conductor, the voltage drop across the conductor can be measured for current sensing purposes. As shown in Figure 2.1, knowing the impedance of the current sensing element can lead to obtaining the current vector via dividing the measured voltage by the impedance value. This type of current sensing mechanism, which is based on Ohm's law, can be considered as ohmic current sensing principle. All shunt resistors (SMD or coaxial), copper trace method, mosfet sensing (using either sense FETs or on-resistance of the mosfet), and inductor voltage sensing (, in which an integrator is needed to convert the inductor voltage to its current by assuming a constant inductance value) schemes are classified in this category [25, 36].

In resistive methods (such as coaxial shunt), an ultra-high BW can be achieved (even up to a GHz [37, 38]) by lowering parasitic inductance techniques. Their other advantages include simple passive circuitry (except the signal conditioning part), small size, and cheap cost. Still, a significant problem of these schemes is invasiveness (of placing the sensing element in series with the current trace), which also lacks electrical isolation, introducing parasitic elements (such as series inductance) to the power traces, and creates power loss and heat (that can also limit the current sensing capacity of the element) [37-39]. One another big issue of ohmic current sensors is sensitivity change due to temperature variations [25], which is related to temperature-dependency of impedance values. Particularly, metal resistance can vary with any change in its temperature, or inductance value is dependent on temperature as well, especially, in elements that use magnetic cores (, which means inductor voltage sensing method is sensitive to temperature variations too).

2.2.2 DC Magnetometers

Magnetic sensors have evolved from ancient navigation devices to meet requirements for increased sensitivity, smaller sizes, and compatibility with electronics, for a wide range of applications, including current measurement [40]. The intensity of the magnetic field or flux density (B), (as the target of these sensors to detect) can be directly converted to the intensity of electric current (I), based on Ampere's law (2.1), in the context of current sensing:

$$I = \frac{2\pi r}{\mu} \qquad (2.1)$$

In which r is the distance from current carrying conductor, and μ is the magnetic permeability. Furthermore, these sensors can now be easily integrated with other semiconductors, which enhances their versatility and improves their accuracy even further. This is possible due to advances in miniaturization and manufacturing processes, which have allowed for smaller and more efficient components. In addition, the sensors are now able to be connected to digital circuitry, which allows for improved accuracy by providing feedback from the environment and other sources, which enables the sensors to be more accurate, reliable, and responsive [41]. However, there are some drawbacks to magnetic sensors, for example, they can be affected by outside magnetic fields, which can interfere with their accuracy. They also require a power source, which can be a limiting factor in some applications [42]. Three widely used magnetic sensors for current sensing in power applications are: 1) Hall-effect sensors (HE), 2) Magnetoresistive sensors (MR), 3) Fluxgate sensors (FG).

1) HE Sensors are based on the Hall effect phenomenon that occurs across holes or voids in semiconductors or metals when current is injected through contact near the edge or boundary of the gap [43]. Consequently, a voltage is produced on either side of a line connecting the current contacts when a perpendicular magnetic field is applied outside the gap, within the metal or semiconductor material. Accordingly, HE detectors determine magnetic field intensity according to the current sensed through the input interface, which must be subjected to signal conditioning to

produce a valuable output for most applications. Usually, signal conditioning electronics consist of an amplifier stage, temperature compensation, and voltage regulation, necessary for unregulated power sources. Furthermore, the signal conditioner must be optimized for the particular application to ensure the highest accuracy of the output. Hall voltages are low-level signals (that can reach a maximum of a few dozen microvolts when surrounded by one Gauss magnetic field), so an amplifier with low noise, high impedance, and moderate gain is required [44]. This can be achieved by combining transistor-based amplifiers with Hall elements. However, this may not be possible in all cases. Depending on the application, a more sophisticated signal conditioner may be needed. If the signal

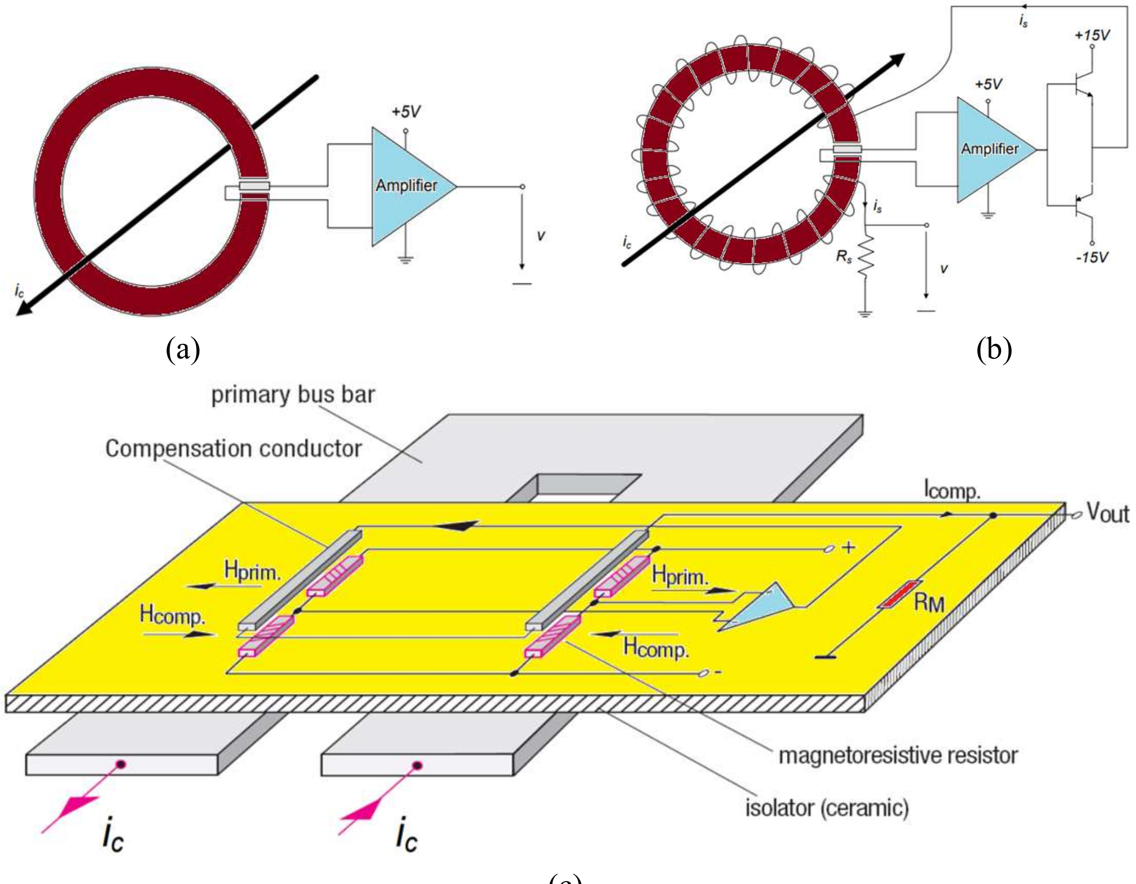

(a) (b)

(c)

Figure 2.2: Different Hall-effect sensors topology: Open-loop with a core (a), Closed-loop with a core (b), closed-loop core-less (or compensated MR) (c) [25].

conditioner is not optimized for the application, it may not provide the highest level of accuracy. Due to interference from external fields, magnetic cores with high permeability can reduce interference effects by maximizing and concentrating magnetic fluxes from the measured current. As shown in Figure 2.2, the HE schemes can be implemented in either an open-loop or a closed-loop system, and depending on the needs of the application, they can be either with a magnetic core or coreless. Closed-loop systems can help reduce nonlinearities by providing feedback to the system and adjusting the parameters accordingly. This allows the system to compensate for any changes in the environment, such as temperature, pressure, or vibration. Furthermore, it is important to note that HE schemes typically have response speeds way lower than 100 kHz, and adding a CT configuration to the system can improve the sensing BW in the closed-loop system [25].

2) MR sensors work by taking advantage of the fact that an external magnetic field affects the electrical resistance in a thin film alloy composed of a ferromagnetic material. The concept for MR sensors was first reported by Hunt in 1971, though magnetoresistance was discovered by Lord Kelvin in 1857 [45]. MR sensors can detect changes in both the strength and direction of the magnetic field by adjusting their resistance, which makes them suitable for a variety of applications such as current sensing. Because of the special material used in making these sensors (usually a mixture of iron and nickel alloys), in addition to being exceptionally

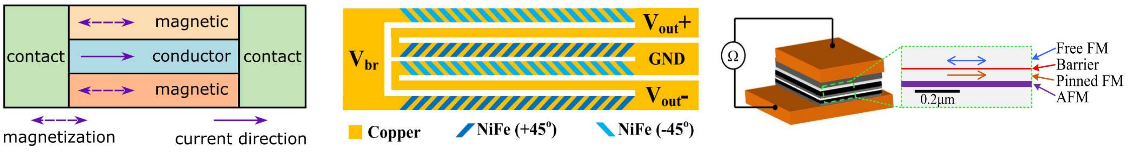

(a) (b) (c)

Figure 2.3: Physical structures of MR sensors: GMR (a), AMR (b), TMR (c) [46].

small and robust, they consume very little energy. The Anisotropic Magnetoresistive (AMR) and Giant Magnetoresistive (GMR) sensors have attracted more attention among the various types of MR, owing to their ease of use and physical characteristics [40]. For instance, AMR sensors are more suitable for low-frequency and low-field applications such as current sensing, while GMR sensors are more suitable for applications that require higher sensitivity and higher resolution. Other types of MR sensors, such as Tunneling Magnetoresistance (TMR) sensors, may be more accurate and precise than AMR and GMR sensors [46]. Moreover, TMR sensors are less susceptible to temperature change and external magnetic fields, so they are more reliable in certain applications. As a result of their small size and outstanding performance, TMR sensors are now becoming more popular for power electronics applications. For example, TMR sensors can detect the presence of a magnetic field with a resolution as low as 1 mT and can detect a signal with a signal-to-noise ratio of over 50 dB. To enhance the linearity of the MR sensor and compensate for any thermal differences, MR sensors are usually installed within a Wheatstone bridge, which enhances the linearity of the sensor [47]. Figure 2.3 depicts the physical structure of three different MR sensors.

3) FG technology sensors take advantage of magnetic core saturation. For instance, by passing a current close to the sensing core and measuring the flux, the core can be saturated and then unsaturated to measure the relative current that causes the magnetic field. A specific magnetic material (usually soft ones) is employed to create the sensing bar/core, which has its own hysteresis curve and becomes saturated after observing a limited amount of current (or magnetic field). In terms of the orientation of the excitation field (generated by the AC current), there are two types of FG sensors. Parallel FG sensors are characterized by parallel

excitation fields, whereas orthogonal FG sensors have excitation fields perpendicular to the sensitivity axis [46]. In figure 2.4, an example of a parallel FG can be seen. A sense coil is coupled with a signal conditioning circuit as well as a compensation coil, so that a closed-loop control can be implemented within the circuit, in which the sensor output is integrated to achieve a high loop gain. From a technical perspective, the integrator is connected to the differential driver that runs an opposing compensation current out of the inner compensation coil. By generating an inverse magnetic field in the compensation coil, the sense coil's initial field returns to zero, which is why this method is also referred to as zero-flux, since it ensures a constant state of differential operation regardless of input signal variations. As a result of the compensation coil constantly generating a magnetic field, nonlinearities in the field caused by the input signals are compensated for. Because of the coil's parasitics and the high magnetization of the core, the excitation signal is typically limited to 10 to 100 kHz, in which the soft material of the core has maximum permeability and eddy currents are minimal. The typical bandwidth of commercial FG detectors is usually about 1 kHz while the maximum reported in the literature (for micro-FG [34]) is less than 100 kHz [46]. With outstanding accuracy, FG elements are continuously propelled in and out of saturation, maintaining zero-hysteresis control, and the shunt resistor senses the

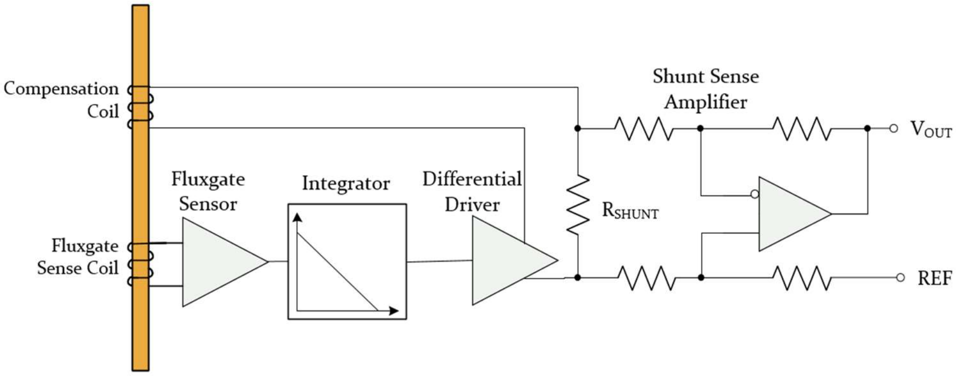

Figure 2.4: The block diagram and circuitry of a parallel fluxgate scheme [24, 47, 61].

current produced by the external current in proportion to that produced by the external field, ensuring steady gain and high linearity. An FG sensor is typically considered to be the most accurate magnetometer among all the different magnetic field detectors available today [25]. For instance, NASA's Juno spacecraft uses a fluxgate magnetometer to measure Jupiter's magnetic field strength with an accuracy of 0.1 nT [24]. However, FG sensors have certain limitations, such as complex control circuitry, which was traditionally a major problem when considering their size and makes the scheme relatively expensive in comparison with other types [25]. As a result of the coming of age of solid-state technology, IC-level FG sensors can solve the problem of size and cost [34].

Several advantages are associated with magnetic field detectors being utilized as current sensors, including DC measurement capability, ease of application, low cost, and good isolation, while the disadvantages of these sensors typically include their low BW, interference with external magnetic fields, their susceptibility to EMI noises (especially when used in conjunction with metal plates that sense), and their limited sensing range, which must always be compromised when integrated into power electronics.

2.2.3 Inductive Current Sensors

Coils, whether they have a magnetic core, can always be subjected to a passive or electronic conditioning circuit to measure alternative current (AC) using Farday's law of induction (2.2):

$$Induced\ Voltage = -M\frac{di}{dt} \qquad (2.2)$$

in which *M* is the mutual inductance between the coil and the conductor. Farday's Law of induction states that the magnitude of the induced voltage in a coil is proportional to the rate of change of the magnetic flux (caused by the target current) passing through the coil. Consequently, induced voltages in higher frequency ranges are larger than those in lower frequency ranges, which means that this type of scheme is more accurate at higher frequencies (although only up to the coil's resonant frequency, parasitics will dampen the induced voltages at frequencies higher than the resonant frequency [32]), and there is no induced voltage when the coil is in a DC or a static magnetic field (*di/dt=0*). By increasing the number of turns in the coil, the induction voltages are also increased, which will again affect the final BW to be decreased [33]. This is because the greater number of turns in the coil will boost the overall inductance of the coil as well, which in turn enhances the amount of energy stored in the coil's magnetic field. This stored energy increases the induced voltages, which increases the circuit self-inductance and lowers the resonant frequency. In power applications, current transformers (CT) (with a magnetic core and all passive circuits) and Rogowski coils (RC) (employing electronics to compensate for the low gain of a core-less coil) are two common sensing schemes of this type [32, 33].

The CT is a type of coil sensing realization that consists of three main parts, namely a coil or winding, a core, and a termination. The coil or winding, core, and termination each serve a specific purpose in the sensing realization, allowing for a wide range of

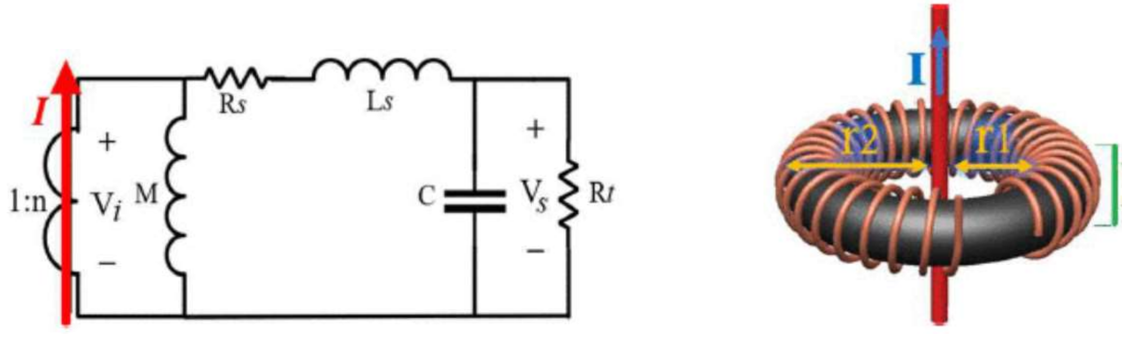

Figure 2.5: Equivalent circuit (Left) and Physical realization (Right) of a toroidal current transformer [24, 32].

sensing capabilities. The number of turns of the coil and the magnetic properties of the core can provide information regarding coil physics and some other electrical properties. The CT sensing realization is versatile, as the number of turns and core properties can be adjusted to better suit various sensing requirements. The equivalent *RLC* of the coil can be calculated using coil and core physics, as shown in Figure 2.5, allowing for the determination of the upper and lower bands of working frequencies. A resistor can be deployed at the termination of each CT for self-integration purposes, allowing it to be modified separately for a specific frequency range. This is like tuning a guitar string - you can adjust the tension, diameter, and length to create the desired sound and make sure it's in tune. Similarly, with the coil and core properties, one can tune the CT sensing to get the results you need within a specific frequency range. For example, the resistor at the termination of the CT can be adjusted to shift the upper frequency limit from 10 kHz to 100 kHz, allowing for a greater range of frequencies to be measured (with lower its sensitivity) [32]. While CTs are ideal for many power applications due to their noise-immunity, low cost, isolation, and passive circuitry, CT integration has several drawbacks, including core saturation (limiting the sensing capacity and accuracy), fluctuations in core permeability at variable temperatures, low permeability at high frequencies, and bulkiness associated with having a magnetic core. However, new advancements in CT technology can mitigate these disadvantages. It is possible, for instance, to reduce the size of CTs while increasing their sensing ability and accuracy by using nanocrystalline cores [49] instead of traditional magnetic cores.

Although RC working principle is very similar to CT, they usually use air-core coils instead of magnetic cores, so they generally require electronic integrator circuitry to compensate for the lower gain provided by an air core (especially at low frequencies). Since air core coils do not experience magnetic saturation, they are often preferred in RC circuits because of their sensing capability, which is not limited as it is with magnetic core

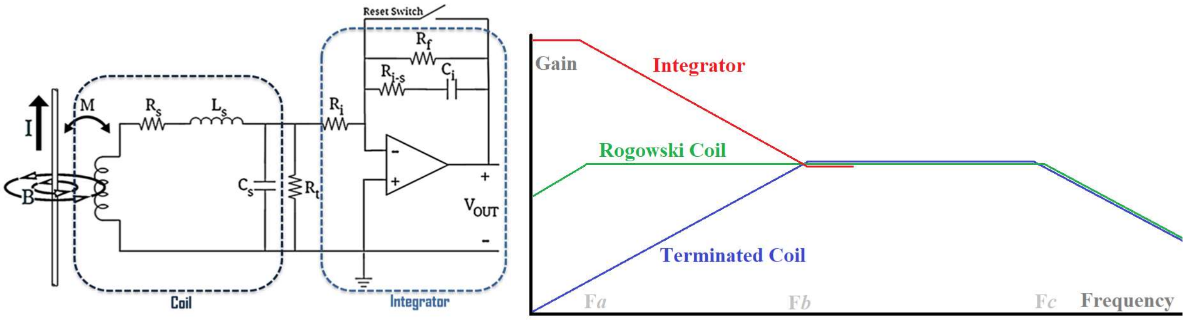

Figure 2.6: Equivalent circuit (Left) and Frequency response (Right) of a Rogowski Coil [24, 48].

coils, and they can also work at higher frequencies. Air core coils' smaller dimensions and volume make them even more appealing for use in RC circuits because of their superior performance. Furthermore, their lightweight design allows them to be easily transported and deployed in a wide variety of applications. In Figure 2.6, there are three major components of an RC current sensor: 1-Coil, 2-termination, and 3- Integrator [24, 33, 48]. Based on the RC's frequency response, it can sense ultra-high frequencies, but like CT, it cannot detect DC or very low frequencies. For example, a specific RC may detect frequencies up to 20 MHz, but not frequencies below 10Hz. RC sensors generally have a higher upper band than CT sensors.

Technically, inductive-based current sensors are good AC transducers and are the only options to non-invasively measure high-frequency currents. In addition, they provide isolation due to their physical characteristics, and their greatest disadvantage may be their incapacity to detect DC.

2.2.4 Magneto-Optical Current Sensing

Magneto-optical (MO) current sensors, which utilize Faraday rotation when polarized light crosses an MO material in a magnetic field, have potential applications in power converters. Fiber optic packaging techniques can make MO current sensors relatively small, and high sensitivity can be achieved using rare-earth ion garnet materials

[50]. In addition, MO current sensors are intrinsically immune to EMI noise and temperature variations. However, there are some potential challenges to implementing MO current sensors. One challenge is that MO materials currently available have limited bandwidth. This means that they may not be able to accurately measure high-frequency currents. The cost-effectiveness of MO current sensors may be limited for some applications, which means it may not be feasible to employ them to measure very low currents, even though MO current sensors are more reliable in a few aspects [25]. An example of a MO current sensor application within a power electronics circuit is shown in Figure 2.7.

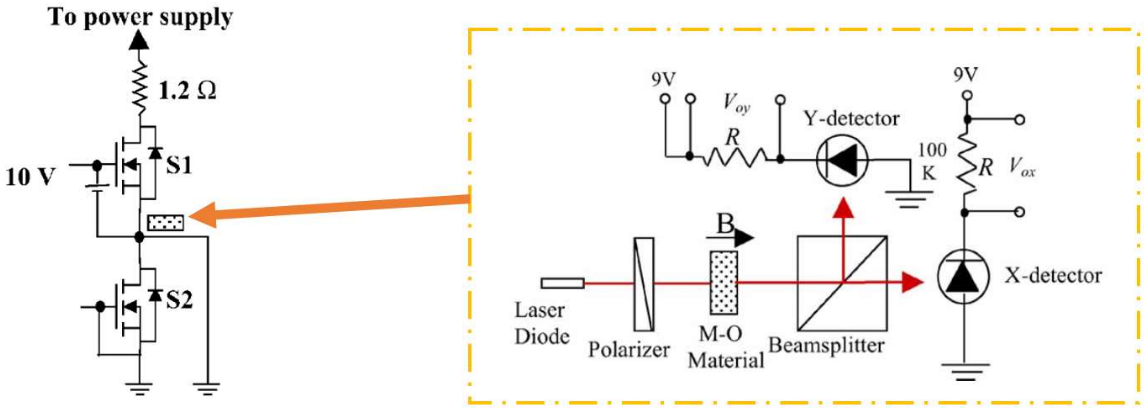

Figure 2.7: Schematic diagram of the optical sensing part placing in a leg test setup [50].

2.3 Current Sensor Integration Concerns in Optimal Power Electronics

Providing a wide range of protection, control, and reliability schemes for power converters that can be utilized for a variety of applications requires accurate electrical current information collected by sensors [23]. The current sensors provide the necessary information to detect and respond to any abnormal current conditions, allowing for the automatic protection of the power converters from overcurrents, undercurrents, and other dangerous situations. They also help to improve the reliability of the converters by providing accurate measurements for precision control. Thus, all requirements of the power converter's current measurements obtained by the sensors should be of sufficient quality to ensure successful integration into these systems. In most cases, the accuracy and reliability of the protection, control, and monitoring methods of the power converter directly depend on the quality of the in-situ current measurement. While it is true that sensors play an important role in power converters, there are other factors that also contribute to the success of these systems. For example, the power converter's control algorithm plays a significant role in determining the overall performance of the system [51]. Even though this is the case, the development of a single current detection scheme suitable for power electronics (especially WBG devices) that can accurately detect a wide range of current types will be extremely challenging due to the restricted geometry/size, the demand for fast sensing speeds, variations in ambient temperatures, and the excessive EMI radiation levels. For example, the high frequencies of modern semiconductor devices cause immense levels of EMI which can lead to false detection and inaccurate measurements from the current sensing scheme. When developing such a current detection scheme, it is important to consider its robustness, reliability, and cost-effectiveness. There have been many current detection schemes developed, but in most cases, they are not of the highest quality, and their use in power converters is compromised.

As an example, an HE current sensor is capable of measuring DC, but is more susceptible to EMI and is not as fast as a CT. Several key concerns related to the integration of current sensing into power converters will be introduced, and the methods described in the previous section that are used for the measurement of single-scheme currents are going to be critically analyzed based on these concerns in this section. This assessment considers the following factors: 1) Isolation, 2) Invasiveness, 3) Size and bulkiness, 4) BW and DC measurement capability, 5) Switching EMI noise immunity, 6) Thermal drift, 7) Accuracy, 8) Sensing range capacity, 9) Power consumption and losses, 10) Cost.

2.3.1 Isolation

Apart from Ohmic (resistive) based current sensing schemes, most current sensing schemes are intrinsically isolated, which does not require a direct electrical connection [36]. A direct electrical connection is not required for inductive, optical, or magnetic-field current sensing schemes, which use energy conversion from one form to another. Therefore, current can be sensed without a direct electrical connection, permitting isolation and safety. Using resistive methods (such as coaxial shunt current sensor), the primary circuits are directly connected to the sensing circuits, which may not be a major concern in low-voltage electronics, however it is of greater concern in power electronics, in which the common mode voltage differentials may be significant between the various circuit components, highlighting the absence of electrical isolation.

The use of shunt sensors or any similar sensor technology such as sense FETs

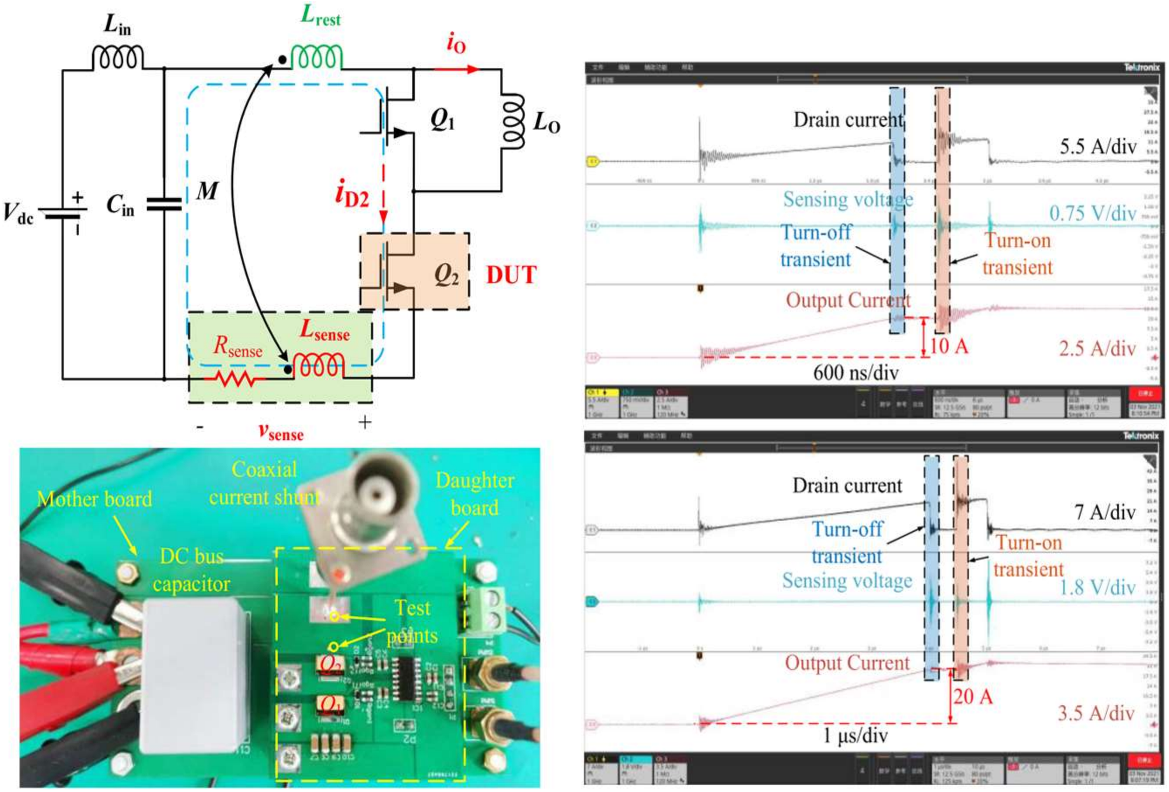

Figure 2.8: Deploying a coaxial shunt sensor in series with low-side switch of a GaN-based DPT setup [37].

(which are special types of Field-Effect Transistors (FETs) designed to measure current flowing through them in applications such as current sensing) is therefore restricted to low-voltage applications or low-side switch current monitoring in power electronics. Sense FETS can, for example, be used in low-voltage converters as a shunt resistor to measure current by connecting in parallel with the low-side switch, while high-side modified sense FETS can be used in low-voltage converters as well. [52] illustrates that isolation requires more complex circuitry. To monitor switch-current in double-pulse testers (DPTs), a shunt resistor could be placed in series with the low-side switch. Also, the shunt resistor can be connected in series with the low-side switch of a half-bridge converter, allowing for accurate current monitoring without the need for isolation. As can be seen in figure 2.8, the coaxial shunt is implemented in series with a low-side switch, to reduce isolation problems.

2.3.2 Circuit Invasion

Invasiveness can be described in terms of the need to pass current electrically through a current sensor to measure it, which requires a connection between the sensor and the circuit, thus invading the electrical circuit to measure the current. A current sensor of this type is considered an invasive current sensor, which must be installed within the electrical circuit, thereby disrupting current flow and electrical properties. For instance, a shunt resistor is an invasive current sensor, as the resistor must be wired in series with the circuit to monitor the current passing through it. Non-invasive current sensing, on the other hand, does not require a connection to the circuit to measure current. It is also possible to measure current using non-invasive or contactless sensors instead of inserting a probe into the circuit as an alternative. As a result, they provide a means to measure current without interfering with the electrical circuit, which is a very helpful feature since it allows more accurate readings and prevents disruptions to the electrical properties in the electrical circuit. A contactless current sensor may, for example, employ MR technologies. The idea is that a current flowing through a conductor will create a magnetic field that can be detected with a magnetometer. In general, a current clamp is referred to as a non-invasive current detector, since it does not require any wiring to the circuit, but instead relies on an electromagnetic field to measure the current. For current sensing (especially in high voltage) applications requiring safety and accuracy, current clamp detectors are the ideal choice, as these aspects are critically important. In addition to this, it may also be worth mentioning that the importance of deploying these contactless current sensors is highlighted by the fact that they don't need to alter the optimal power layouts of power electronics (especially those based on WBG). As an example, a high voltage three-phase inverter utilizing a PCB-embedded RC current sensor can maintain the ideal power layout of WBG semiconductor devices while still providing accurate current measurement capabilities.

Resistive current sensing methods present significant challenges due to their invasiveness (by placing the sensing element in series with the current trace). Besides introducing parasitic elements to the power traces (such as series inductance), these methods can also result in heat loss and power loss (which can limit the element's capacity to sense current) [25, 36-39]. The voltage drops across a shunt resistor, for example, dissipates power as heat, which increases with increasing current flow, and causes the element to heat up as well. While these sensing schemes have been used in a number of specific applications, including DPT for characterization (because of their excellent sensing bandwidth, as shown in figure 2.8), medium-frequency (MF) WBG converters, or small power/voltage applications [53], they are unreliable/integrable for medium/high power converters, due to the absence of isolation, parasitic elements are introduced, nonlinearity is present (due to temperature variation vulnerability, which is extensively discussed later in this chapter), and capacity is limited (due to losses and heat dissipation, which will also be discussed in greater detail later in this chapter). In figure 2.8, an example of the coaxial shunt from [37] is shown to illustrate the issues relating to the integrability of ohmic current sensing approaches within WBG (GaN-based) power electronics converters. This type of shunt is composed of two concentric conductors, with a dielectric material in between. The current that passes through the shunt is measured by the voltage drop across the shunt, which can be integrated into the power electronics converter to provide a current sensing mechanism. This optimized coaxial shunt has a bandwidth of approximately 1 GHz, but it is implemented in series low side switches to reduce isolation problems. In addition, it is possible that the DPT setup selection is related to heat dissipation and power consumption issues. The current waveform illustrates that too much ringing was generated during the switching transient because of the invasiveness of the shunt resistor, implying that too many parasitic values were introduced to the switch power trace.

Inductive, magnetic field, and magneto-optical current sensing methods are intrinsically capable of detecting currents using electromagnetic fields without an electrical connection [25]. Despite this, some integrated circuits (IC), such as HE IC sensors, require current to be passed through them to concentrate magnetic fields. This phenomenon is mainly because HE elements are not as sensitive to small magnetic fields as MR or FG. The issues related to invasiveness, such as altering the power trace path and introducing parasitics, may limit their use within optimal power converter layouts [3], even though they can provide isolation. MR or FG technologies, which are largely non-invasive, may prove more appropriate for use within an optimal power converter layout if their design does not incorporate significant parasitic values. When evaluating inductive current sensing schemes, it may be necessary to insert a CT IC designed for small currents into the primary circuit, comparable to HE ICs. Consequently, CT ICs may present similar problems that HE ICs have when it comes to the electrical insertion of a sensor into a targeted circuit to measure a change in concentrated flux. Moreover, CTs with a large magnetic core may add too much inductance (usually bigger than one micro-Henry) to the primary circuit, even when they are non-invasive electrically, which is known as inductance insertion [27]. It could be argued that PCB-embedded or RC probes would make better alternatives, since they are completely non-invasive, and their inserted inductance is very small (usually not more than a few nano -Henry).

2.3.3 Size and Bulkiness

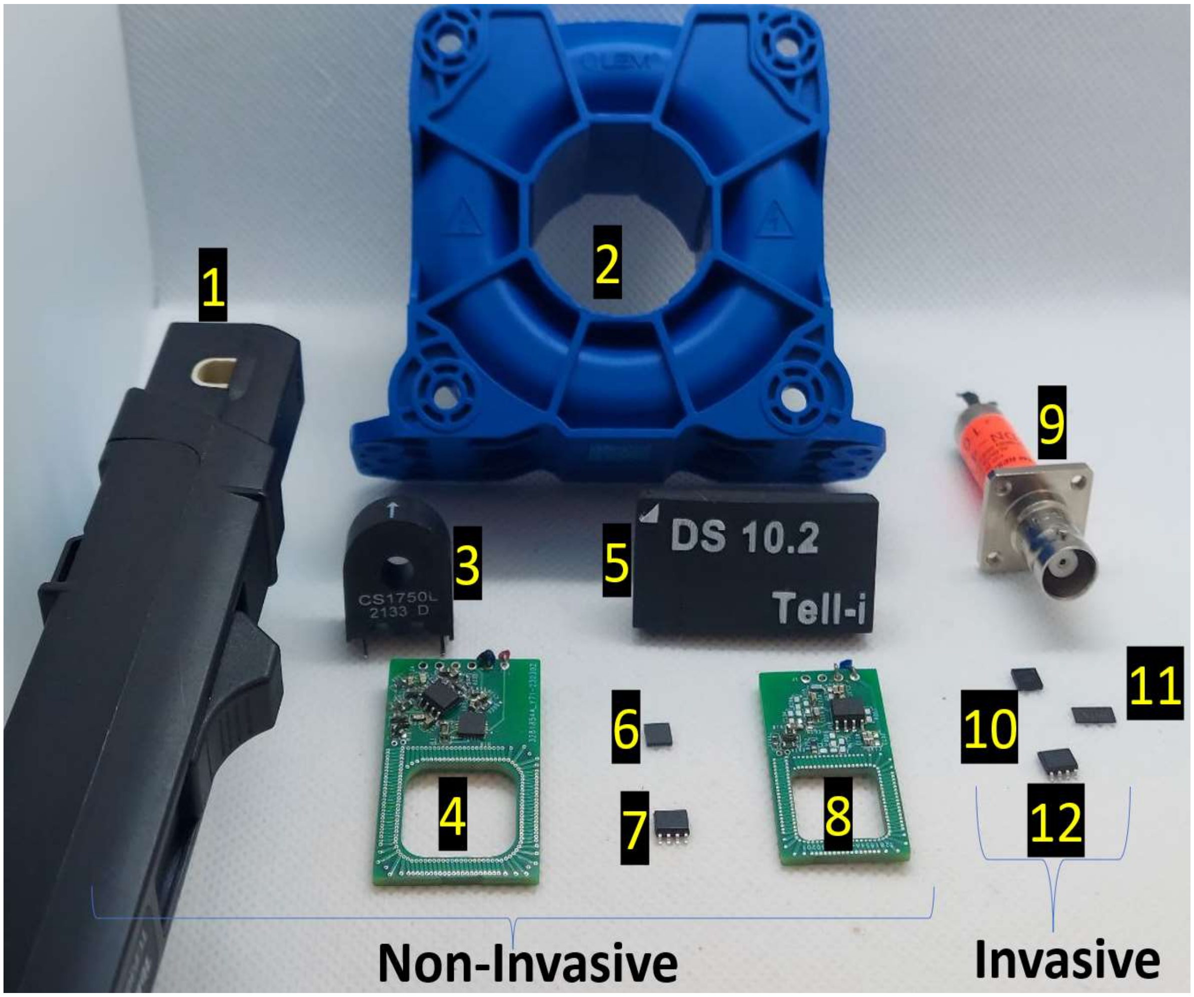

Figure 2.9: Size of different existing current sensors or probes: 1- Tektronix TCP305A, 2- LEM LF 510-S (Closed-loop Hall-Effect), 3-Coil Craft CS1750 (Current Transformer), 4- UNCC's Hybrid (Fluxgate + Rogowski), 5- Tell-i DS10.2 (Coil + MR), 6- TI DRV421 (Fluxgate), 7- HMC 1021S (AMR), 8- UNCC's AC transducer (Rogowski Coil), 9- Coaxial Shunt, 10- Infineon TLI4970 (Hall-Effect), 11- SMD Shunt Resistor, 12- Allegro ACS730 (Hall-Effect) [24].

The size and volume of a current sensor are also critical for integration into optimal power converter layouts, in addition to being isolated and non-invasive. Typically, a non-invasive sensor is an ideal choice if it can be incorporated into the system and takes up as a low space as possible. Keeping the size and volume of a sensor to a minimum allows for greater flexibility in the design and additions to the layout, which reduces the cost and complexity of the overall system [27]. Figure 2.9 displays a visualization of existing current sensors or probes. These can be employed to measure current for specific applications in power electronics, while also considering the amount of space they may require to be installed. Having smaller dimensions offers greater integration flexibility and allows for a greater number of sensors to be integrated, since a smaller volume makes it easier to install and maintain sensors. CT, for example, offers excellent isolation in a non-invasive manner; however, its bulky magnetic core (number 3 in Figure 2.9) may not be adequate for monitoring switch currents, since the bulky core can require a large amount of space, making it difficult to install in confined spaces. An illustration of this issue is provided in Figure 2.10 [54], which displays the height of the electric power trace as well as the length of the overall power trace in the application, showing that too much ringing during switching implies excessive addition of loop inductance because of either the abnormal height of the trace or the insertion of a magnetic core. Also, the non-invasive

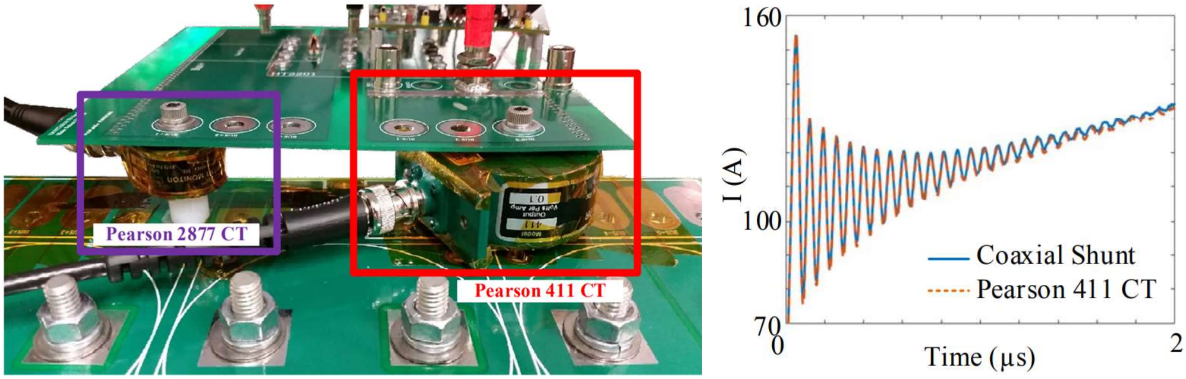

Figure 2.10: Integration of Pearson's current transformers to monitor transient of the switching current [54].

closed-loop HE sensor illustrated as number 2 in Figure 2.9 confirms that incorporating a magnetic core into the sensing structure may not be feasible for integration into small-size converters where bulkiness is an issue.

As a general principle, magnetic cores are problematic in applications requiring limited volume and weight sensing circuitry. Furthermore, it is also important to point out that these converters cannot be equipped with current probes (number 1 in Figure 2.9) for control or protection because of their immense size and cost. There are several different magnetic-field-based current sensors, but MR sensors (specifically AMR and TMR) are contactless magnetometers that are small size ICs (such as number 7 in Figure 2.9), allowing them to be integrated into power converters easier. Due to its PCB/air-core technology (numbers 4 and 8 in Figure 2.9), RC offers an easier alternative to bulky inductive-based circuitry when integrating into a power converter due to its easy embeddability. Furthermore, it is very compact and can also be embedded within a power converter's mother board or gate driver. It has also been reported that magneto-optical (MO) sensors and probes contain sophisticated circuitry (Figure 2.7) that could make them too large, and this could be the same for FG probes in general [25]. Despite this, the on-chip FG solved the size issue (number 6 in Figure 2.9) [34]. A further benefit of on-chip FG technology is that it is more accurate than other magnetometers, and it can be easily integrated with other circuits or sensors, as well as being highly reliable, which makes it suitable for a variety of applications.

2.3.4 Bandwidth and DC Measurement Capability

The current sensing bandwidth refers to the range of frequencies over which a sensor can accurately measure current, and its requirements can vary depending on the application and the specific type of current or equipment being measured. As such, establishing the appropriate bandwidth for an application is essential for accurate

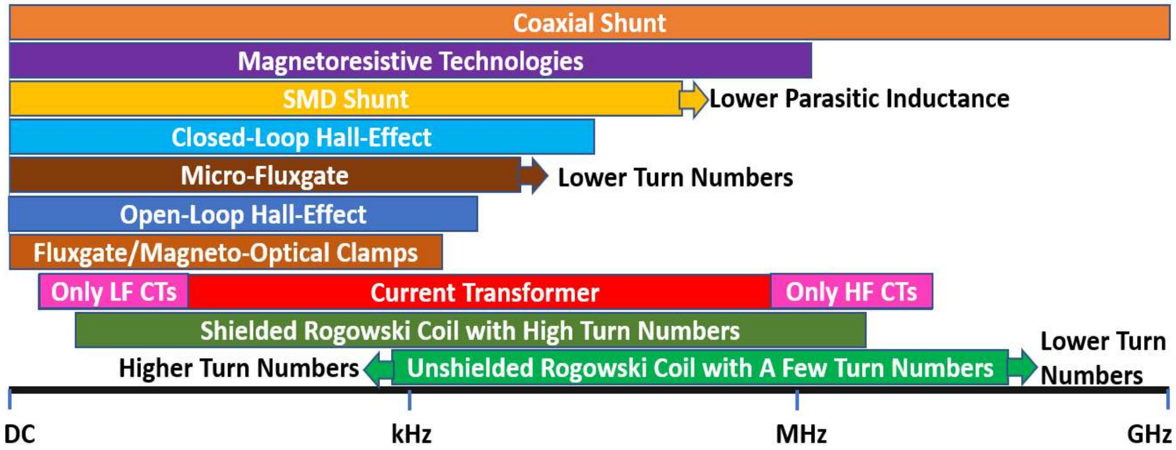

Figure 2.11: Potential bandwidth of different current sensing methods [24].

measurements and results. Typically, higher BW current sensors are required in WBG power electronics due to the faster switching frequency. It is also necessary to meet bandwidth requirements regarding rise time speed, or in other words, the bandwidth should be set wide enough to capture the high frequency components of current waveforms [32]. These factors must be considered when selecting a current sensor for WBG power electronics. The sensor must have a wide bandwidth, fast rise time, and high accuracy to accurately measure current waveforms [25]. For example, a GaN-based PFC can switch at a frequency of several hundred kHz, and to accurately represent the current waveform, a bandwidth of over several MHz is required. As well, the switch-current waveform can be square/trapezoidal with frequency components ranging from DC to extremely high frequencies, and the only single-scheme current sensor capable of measuring DC up to tens of MHz (or GHz) is the coaxial shunt [38], which has integration problems relating to isolation and invasiveness. In addition, in resistive-based current sensors (such as SMD shunt), the skin effect causes higher impedances in high frequencies that is associated with their limited BW as well [25]. A diagram in Figure 2.11 illustrates how potential measurement BWs of SS current sensors may be explained. As shown in Figure 2.11, a CT may be modified to meet the needs of low or high frequency applications [32]. Although both inductive methods (RC and CT) can reach high frequencies in the upper frequency band, they cannot detect DC currents [32, 33]. However, magnetometers (HE, MR, FG) and MO which perform well at DC and low frequencies (LF) are unable to construct a very high BW due to their physical structures [25]. On-chip or micro-FG devices typically limit the excitation signal to 10 to 100 kHz because of the parasitics of the coil and the high magnetization of the core [55]. This is because the core's soft material has the highest permeability and has minimal eddy currents. By reducing the number of coil turns in their IC design, parasitics in the coil can be reduced, thereby improving the frequency range. Despite the limitations of each sensing method, magnetometers, inductive methods, and a combination of the two offer a variety of viable options for measuring current in a wide range of bandwidths. A combination of multiple sensing methods can be used to detect a wide range of frequencies [56], a topic that will be addressed later.

2.3.5 EMI Immunity

One of the most significant obstacles to sensing and signal conditioning in WBG power electronics is the requirement for integrated current sensors capable of handling significant *di/dt* and *dv/dt*. Due to their high frequency switching, they can be subject to high *di/dt* in switching commutation loops that can cause ringing and overvoltage,

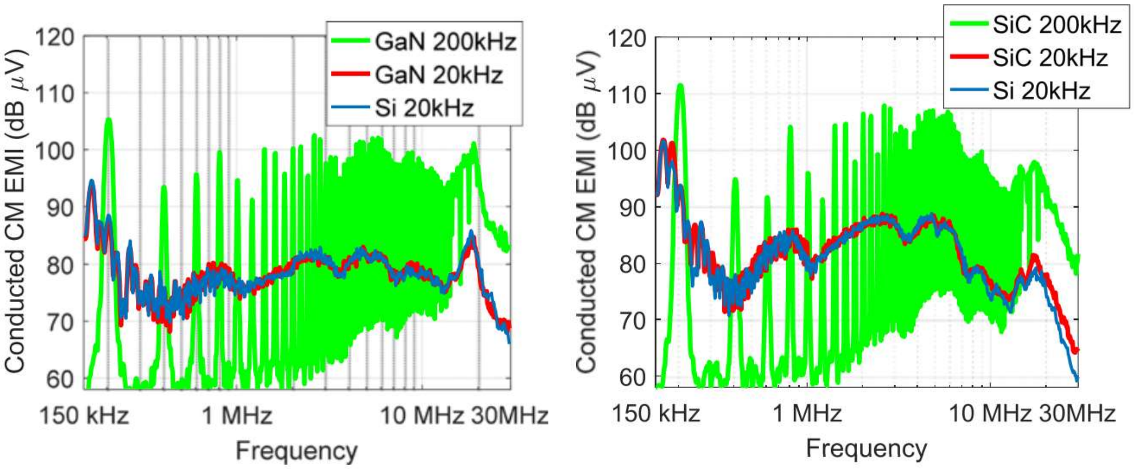

Figure 2.12: Conducted EMI in WBG drives in comparison with Si-based one [57].

resulting in RF emissions, EMI radiation, and additional losses, as well as spurious gate voltages, resulting in crosstalk issues in bridge configurations due to large *dv/dt* [57, 58]. These issues can interfere with the operation of other components in the system and reduce the overall system performance and reliability. For instance, improper turn-off snubbing can lead to a resonance between the bridge leg inductance and the stray capacitance, resulting in destructive transients. These transients can cause circuit malfunctions and harm the system's performance. To mitigate these issues, proper design of sensing circuitry and optimal layout of the converter can reduce the problems associated with high *di/dt*, which is also emphasized in Figure 2.13 [59].

Except for the ways to conduct EMI that can be easily eliminated by isolated sensing circuits, it can also be coupled near the field or radiated, in which EMI noise can be coupled or induced by parasitic inductances and capacitances within the sensing circuit and because of capacitive coupling from *dv/dt* and inductive coupling from *di/dt*, signal processing in the feedback path is especially vulnerable. The amount of coupled noise current can be reduced by reducing stray capacitance (by shrinking the conductor connections and increasing their distance from each conductor), and to minimize the induced EMI noise voltage, the loop inductance of these circuits must be reduced.

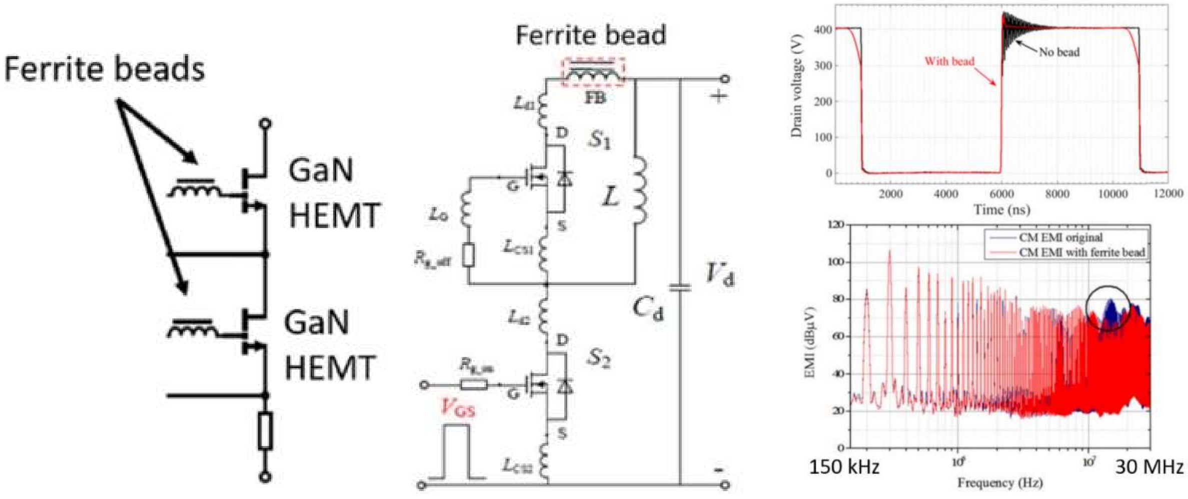

Figure 2.13: An example of layout consideration to reduce radiated EMI [59].

The high radiation potential of EMI is also a reason why non-isolated or invasive current sensors should not be utilized, as parasitics introduced by them into converter layouts can contribute to increased EMI issues, and their considerable amount of

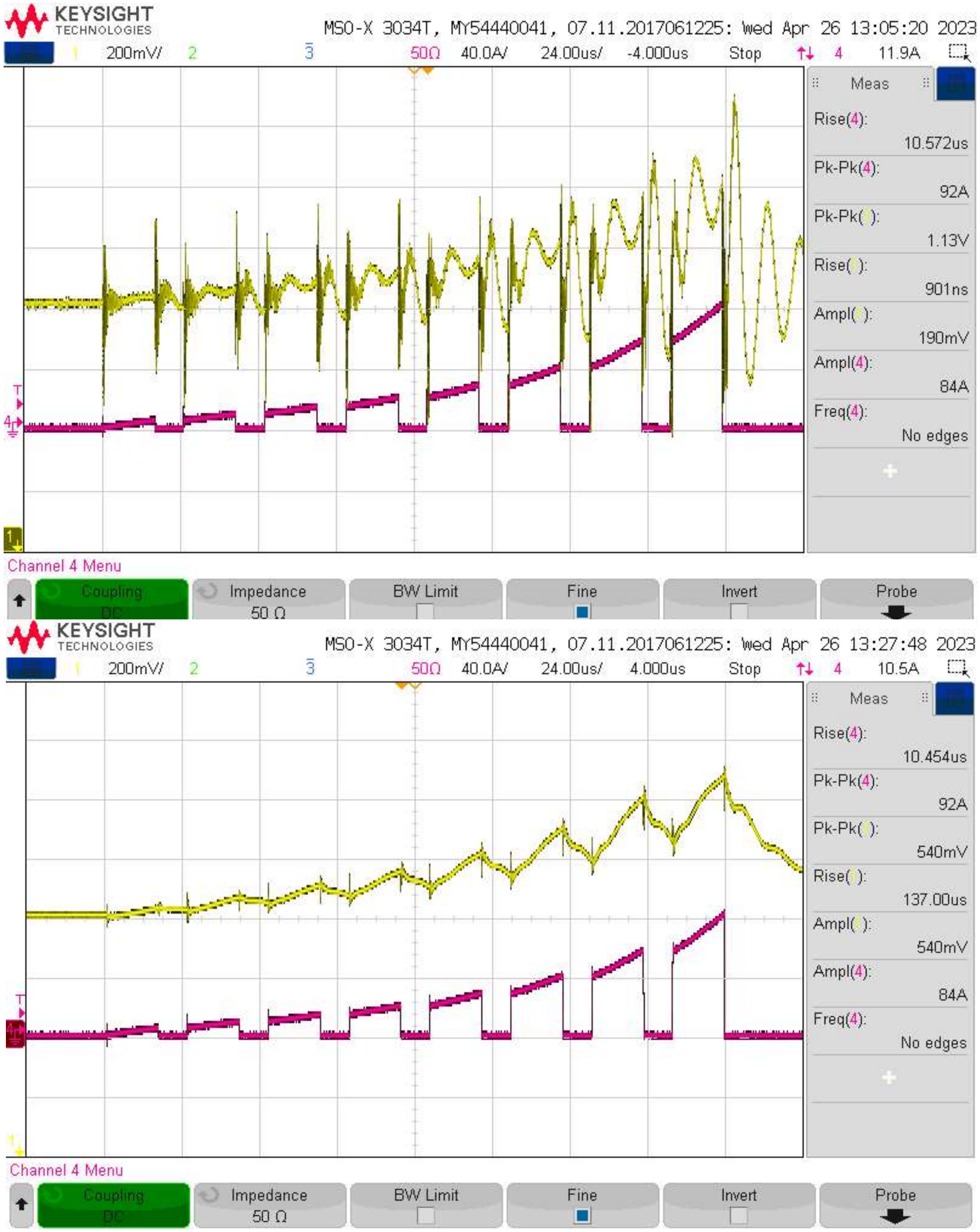

MSO-X 3034T, MY54440041, 07.11.2017061225: Wed Apr 26 13:05:20 2023
1 200mV/ 2 3 50Ω 40.0A/ 24.00us/ -4.000us Stop 4 11.9A
Meas
Rise(4): 10.572us
Pk-Pk(4): 92A
Pk-Pk(1): 1.13V
Rise(1): 901ns
Ampl(1): 190mV
Ampl(4): 84A
Freq(4): No edges

MSO-X 3034T, MY54440041, 07.11.2017061225: Wed Apr 26 13:27:48 2023
1 200mV/ 2 3 50Ω 40.0A/ 24.00us/ 4.000us Stop 4 10.5A
Meas
Rise(4): 10.454us
Pk-Pk(4): 92A
Pk-Pk(1): 540mV
Rise(1): 137.00us
Ampl(1): 540mV
Ampl(4): 84A
Freq(4): No edges

Figure 2.14: TMR's output on a switching node: raw output (Top), lowpass filtered by a passive R-C with a 5 kHz cutoff frequency (Bottom), in which the magenta waveform is the current reference measured by a DC-50 MHz current gun (TCP305A) and the yellow is the output of TMR2111S [24, 60].

conducted and coupled noise can interfere with the system's protection and control systems. The use of inductive current sensors from an EMI standpoint requires avoiding the introduction of excessive inductance into converter layouts, as well as decreasing their stray capacitance as much as possible to avoid the requirement for shielding (to enhance sensing BW), so either very small CTs or RCs embedded on PCBs with very excellent EMI immunity can be implemented. Since HE sensors are either invasive or large/bulky, they do not provide an appropriate representation of magnetometers in terms of EMI immunity.

Furthermore, lowpass filtered outputs are also necessary when non-invasive AMR or TMR ICs are placed near switching nodes (because of coupled and radiated EMI to their metal plates), which further restricts the detection range (or BW) of these devices. Figure 2.14 illustrates that, while TMR has superior sensitivity and BW, it is prone to HF switching EMI, and its output must be cut off with a low-pass filter at a very low frequency (usually less than 50 kHz) in order for the output to remain functional.

2.3.6 Thermal Drift

As a result of temperature fluctuations, thermal drift occurs when the current sensor's output is different, almost under the same electrical conditions, when the differences are not adequately compensated. In temperature-variable systems with ohmic current sensors (shunts), for example, when the temperature of the sensor increases, the output voltage of the sensor increases due to increased resistance, which also results in inaccurate measurements. This can lead to errors in the sensor output, which can be difficult to detect and cause incorrect current measurements. To avoid this, temperature compensation can be implemented in the sensor to ensure accuracy. For example, a closed-loop current measurement system such as FG, MO, or RC (with an inverting integrator) can compensate for any thermal variation, due to their intrinsic feedback system. This, in turn, can lead to greater reliability and accuracy in current measurements, resulting in a higher quality of data. In contrast, current sensing schemes such as open-loop MR or HE are susceptible to such fluctuations. A temperature compensation system can be implemented to reduce calibration needs, which can be accomplished by making the sensing system closed-loop, or by implementing algorithms to compensate for variations in temperature. ppm/K is the unit to quantify the thermal drift of a current sensor, and any value below 100 ppm/K is considered acceptable [25]. It has been found that FG is the non-invasive current sensor with the lowest thermal drift [25, 46], while MO, RC and CT are also able to achieve acceptable values. Accordingly, closed-loop AMR and TMR [46] can have acceptable thermal drift, and closed-loop HE appears to be within a reasonable range as well [25].

2.3.7 Accuracy and Linearity

The accuracy of a current sensor is determined by how closely it can measure the precise value of the target current in the time or frequency domain. There are numerous factors that can affect sensor accuracy, such as temperature, magnetic hysteresis, and electrical noise. Several of the previous concerns associated with current sensor integration could also be associated with reading accuracy, such as BW, thermal drift, and immunity to EMI noise. For instance, CT or RC may not sense accurately if the current has DC or very low-frequency components. Conversely, FG or HE may not be capable of detecting very fast rising currents accurately due to their low BW, so if the sensor is implemented in an application matching its BW, it could be considered accurate. In addition, fluctuations in ambient temperature may cause nonlinear readings (in resistive current sensors) or thermal drift (in magnetic current sensors), which will affect the accuracy of the measurement. Generally, a current sensor needs to have a linear response to any current regardless of temperature variations and the amplitude of the current/magnetic field, to be considered accurate. Depending on the temperature, shunt resistors tend to have different resistance values, which alter their sensitivity, resulting in an inaccurate and nonlinear measurement [25]. In addition, they are prone to be warmed up by passing large currents through them,

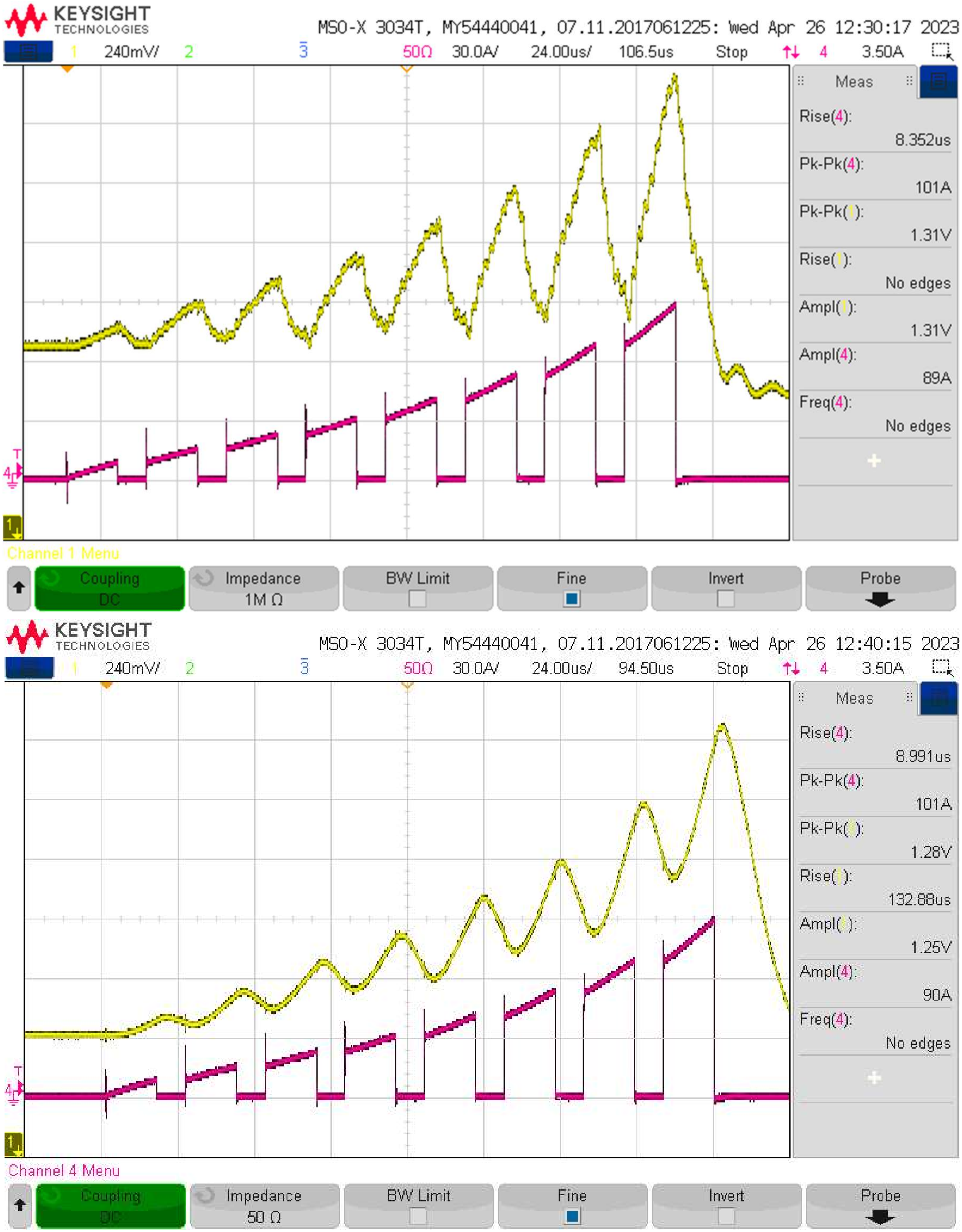

MSO-X 3034T, MY54440041, 07.11.2017061225: Wed Apr 26 12:30:17 2023
1 240mV/ 2 3 50Ω 30.0A/ 24.00us/ 106.5us Stop 4 3.50A

Rise(4): 8.352us
Pk-Pk(4): 101A
Pk-Pk(1): 1.31V
Rise(1): No edges
Ampl(1): 1.31V
Ampl(4): 89A
Freq(4): No edges

MSO-X 3034T, MY54440041, 07.11.2017061225: Wed Apr 26 12:40:15 2023
1 240mV/ 2 3 50Ω 30.0A/ 24.00us/ 94.50us Stop 4 3.50A

Rise(4): 8.991us
Pk-Pk(4): 101A
Pk-Pk(1): 1.28V
Rise(1): 132.88us
Ampl(1): 1.25V
Ampl(4): 90A
Freq(4): No edges

Figure 2.15: Micro-fluxgate’s output on a switching node: raw output (Top), applied an RC lowpass at its output cutting off at 16 kHz (Bottom), in which the magenta waveform is the current reference measured by a DC-50 MHz current gun (TCP305A) and the yellow is DRV425 [24, 61].

changing their sensitivity as well. In CTs, due to the saturation of their magnetic cores as well as hysteresis in case of very large currents or magnetic field changes, there are non-linear readings and a limitation on their capability to provide accurate sensing. However, RC does not contain a magnetic core, so it provides excellent linearity compared to CT. The PCB-embedded RCs are therefore an excellent choice for measuring HF currents since their differential versions are not affected by external magnetic fields, making them an inexpensive, accurate (if the DC lack is compensated), and reliable solution [33].

Except for FG (which can be considered as the most linear and accurate magnetic-based current sensor [25, 46]) most magnetic field detectors have linearity limitations, due to their physics (especially HE and AMR). Moreover, the output of a current sensor should be free of noise when it comes to accuracy, as noisy readings tend to indicate inaccurate measurements. Other than open-loop HE or MR that are prone to thermal drift (which affects their sensing accuracy), HE ICs are usually incapable of noise-free output, while small contactless MR or FG ICs can be low-pass filtered to provide reasonably noise-free outputs (Figures 2.14 and 2.15). As shown in Figure 2.15, a low-pass filter can be used to reduce HF noise and increase the accuracy of the output signal of the micro-FG (DRV425 [61]). The filter can be implemented with a simple RC (resistor-capacitor) network. However, this will reduce the output signal BW. Finally, offset drift (that is usually caused by magnetic hysteresis) is another phenomenon that could affect current sensing accuracy, especially in magnetic field detectors. For instance, the offset drift of a HE sensor (known as one of the poorest magnetometers in this term) can result in false readings that cannot be related to the actual current, resulting in serious accuracy and reliability problems. Not only does it have the best noise immunity and accuracy, FG has the lowest offset drift among other magnetometers, and TMR can be considered as an alternative (but with a much greater offset drift) [46].

2.3.8 Sensing Range Capacity

This term refers to the maximum and minimum currents that can be accurately/linearly sensed by the sensor. The accuracy of the measurement will be affected if the current sensor measures currents outside of this range (also known as the linear operating range), so it is imperative to select the appropriate current sensor based upon the linear operating range required for the application. For instance, a current sensor with a linear operating range of 0-100A would not be suitable for a bidirectional application with a current reading requirement of -50 to +50 A. This linear range can be affected by a variety of factors, as mentioned earlier in this thesis. Among the factors contributing to the linearity limiter of resistive current sensors is heat dissipation, which is a result of the loss of resistance as a function of current passing through it, which heats up the sense element. This causes the resistance to increase with increasing heat, resulting in a nonlinear sensing condition after exceeding the rating current. Core saturation is another linearity limiter in magnetic-based current sensors. Core saturation occurs when the magnetic field generated by the current passing through the core reaches a certain level, and the core becomes saturated with magnetic flux. This saturation limits the current that can be accurately measured, resulting in a nonlinear sensing condition [25]. Due to this phenomenon, all CTs and some HE and MR elements have a limited current sensing range. In other sensing mechanisms such as RC or FG, voltage supply is the sensing range limiter. RC sensors are almost always linear unless they reach their opamp supply voltage. With an RC that has a sensitivity of 10 mV/A and an opamp supply voltage of -5V to +5V, the sensing range will be limited to -500A to +500A [24], which is still significantly greater than the sensing range of a CT of the same size.

Regarding the minimum current sensing range, it is highly dependent on the sensitivity and noise immunity of the current sensor to detect very small currents/magnetic fields, which can once again be a matter of accuracy. It is also dependent upon the ambient noise levels in the environment, as well as the type of current sensor used to be immune to that level of noise. Even very small currents can be detected by high-resolution current sensors due to their high resolution, such as FG detectors [46]. In a nutshell, RC, MO, FG, along with some coreless MR or HE are viable candidates for very high maximum current sensing capacities. With the right current sensor, even the smallest of currents can be detected, allowing for more accurate readings. This enables more reliable data collection and better results. Moreover, with the right sensor, the noise levels of the environment can be compensated for. Shunts, FG, TMR, and AMR can be considered in the case of very small currents [25, 46]. There are several microelectronics current sensing level sensors presented in [62], but most of them have no practical application in power electronics.

2.3.9 Power Consumption

The power consumption of a current sensor may be caused by conduction losses (such as resistive power loss in invasive sensors) or by powering up its processing circuits (such as power supplies in contactless magnetic field sensors). It is important to consider the power consumption of sensors for specific applications, especially when they are susceptible to excessive heat or are located inside high-efficiency low-power converters. It may also be necessary to power the sensor externally (which makes setup more complicated) or consider the cooling system separately. For example, for a sensor that requires 5V and 100mA, an external power source may be necessary to power the sensor,

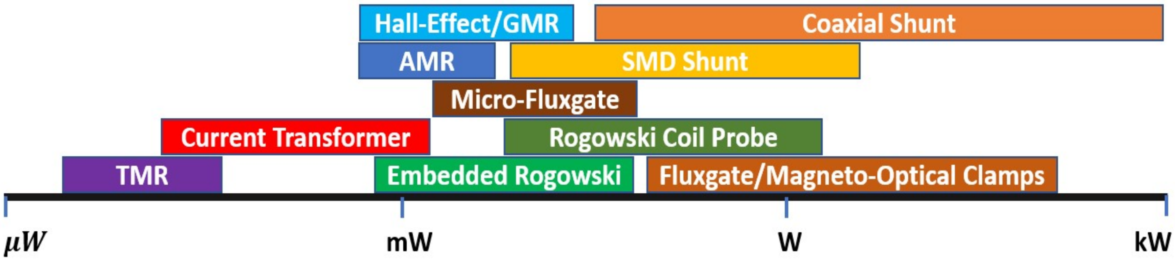

Figure 2.16: Potential power consumption of different current sensing methods [24].

or a heat sink and fan may be needed for cooling. As a result, lossy sensors are not typically applicable to optimal power converters. In such terms, low power sensors are more convenient to integrate since they require minimal power supply and do not require a cooling system, thereby making installation and setup easier, as well as reducing issues associated with power consumption and losses. For instance, low power sensors such as current transformers or Rogowski coils (Figure 2.16) can be used in power converters as they can measure current over a wide frequency range with minimal power consumption. While FG IC has the highest sensitivity, accuracy, and temperature-insusceptibility of all the magnetometers, it has the highest power consumption among them. The reason for this is that Micro FG requires compensation current to equilibrium magnetic fields within its magnetic core to attain a high degree of linearity. Since on-chip FG consumes a great deal of power, they are not suitable for loss-limited conditions, particularly in applications related to the Internet of Things (IoT). According to [55], they designed and implemented an FG IC with only 13 mW power consumption for those applications.

2.3.10 Cost

A major concern with integrating current sensors with power converters is their cost. Sensor technology is rapidly advancing, allowing higher accuracy and lower costs. For example, MEMS sensors have become increasingly popular due to their small size,

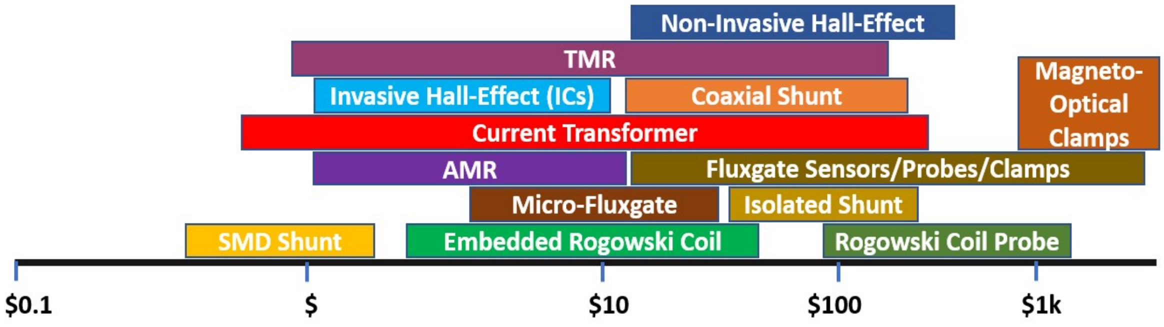

Figure 2.17: Potential cost of different current sensing methods by Summer 2023 [24].

low cost, and high precision. As shown in Figure 2.17, developing FG sensors on the chip results in significant cost savings compared to FG clamps, and this is also true for the development of HE technology, which will also result in substantial cost savings along the way. This trend is likely to continue, as evolving sensor technologies are developed that increase accuracy and reduce costs. This will help businesses become more efficient and reduce costs, resulting in increased profits. Yet, there is no commercial counterpart for RC probes on the market. However, advancements in integrating RC as a PCB-embedded coil at UNC Charlotte and other research institutes show the implementation feasibility of such technology with simple circuitry and similar performance [48]. Figure 2.17 illustrates the cost diagram based on up-to-date market data (from Digikey.com [63]), which can also be compared with the information found in [25] and [29]. According to the information provided, the most cost-effective contactless current sensing schemes are the CT, Embedded RC, On-Chip FG, and MR technologies.

2.4 Current Sensor Selection Based on Application

Integration of current sensors into power converters may be subject to different requirements depending on the application. This requires a deep understanding of the design and operation, which should include the power electronics, the current sensor, and the utilization algorithms. It is important for engineers to consider the complex relationships between these components to guarantee that their designs meet specific requirements and operate as expected, including the design and performance of the power converter layout when choosing the sensors. A particular application may require a variety of current sensors, as well as calibrating and integrating the sensor within the system, which means the optimal selection of a current sensor must be based on the application for which it is intended [23]. This process will require detailed knowledge of the application and its requirements. The current sensor must have the ability to detect and measure the current reliably in the application’s operating environment. Eventually, the selection of a current sensor must be done with care to ensure the system is operating correctly.

Several factors, such as accuracy, dynamic range, size, and cost as well as environmental conditions, have already been outlined in the previous section, which should be taken into consideration when making current sensor selection. The purpose of this section is to introduce a set of applications that employ current sensors in power electronics, along with sufficient details regarding suitable candidates for each application. There are four categories of applications that are examined in this research namely protection, control, reliability, and characterization. Different types of sensors are recommended for each application based on their characteristics and features. For example, current sensors designed for protection should have a super-fast response time, while current sensors intended for control must be super-accurate. The current sensor's flaws will also be discussed in detail with respect to whom they may be compromised depending on the application. For instance, HE sensors are used to measure current in low-level applications, such as motor control, but they have a slow response time and are easily affected by temperature, making them unsuitable for use in protection applications.

2.4.1 Protection

For effective protection against destructive currents, a suitable current sensor is usually required to detect faults when they occur. A current sensor must be able to detect fault currents accurately at high speeds, because the faster the current sensor can detect a fault, the quicker the protection system can act to trip the circuit and prevent further damage from happening. Further, the device must also be capable of handling very high levels of current since fault currents can be very high at times. As well as that, if the current sensors are to be utilized within power electronics protection mechanisms, all other integration concerns that have been discussed previously must be addressed. Despite that, current sensors could have some drawbacks. For example, if the current sensors are not properly calibrated, they can cause false readings that could trip circuit breakers unnecessarily or cause other problems. Current sensors, however, can provide the best interpretation of faults associated with overcurrents and short circuits, which illustrates the importance of calibrating them correctly.

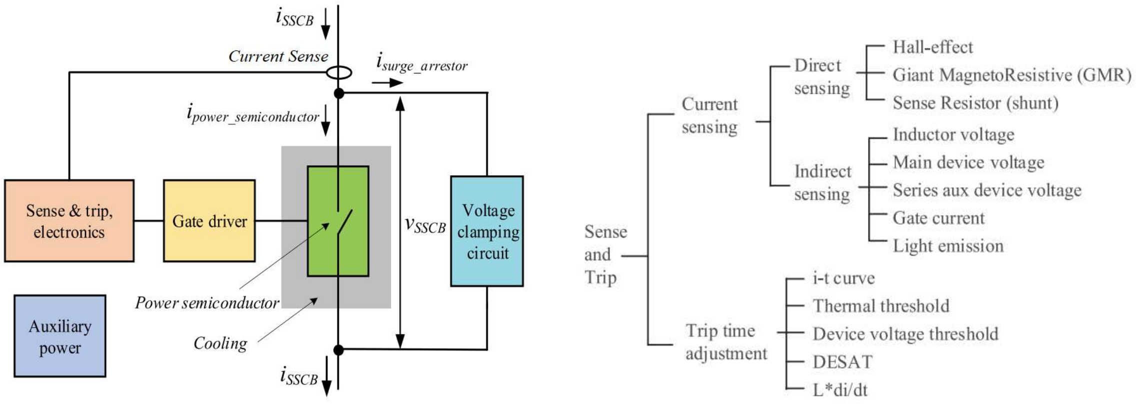

Figure 2.18: Solid-state circuit breaker technology: Key components (Left), Sense and trip adjustment (Right) [64].

There is an increasing use of solid-state circuit breakers (SSCB) in a variety of emerging electrical systems, where power electronics devices perform several at higher speeds than electromechanical mechanisms typically employed by conventional circuit breakers and interrupt fault currents without moving parts [64]. Usually, these devices detect fault currents by sensing them directly or indirectly. The fault current sensor must have a high BW (which also means a fast response time), a low loss (or no loss), and the ability to be integrated into the tripping circuit. Based on the circuit inductance, short-circuit faults can also result in wildly fluctuating current rates. Thus, it is imperative to ensure that the design and implementation of a current sensor are sufficiently robust to operate well across a broad range of current change values. To maintain the highest level of breaker efficiency, the sensor should have a fast response time and lower losses than the main power semiconductor [64]. As shown in Figure 2.18, the literature describes the SSCB key components as well as the mechanism for sensing and tripping. Since a wide range of voltage and temperature changes can cause a false fault to be inferred from indirect sensing methods, they may not be as reliable as direct current sensing. In [65], desat has been compared to embedded RC short-circuit detection to illustrate the differences in accuracy and speed between direct and indirect fault detection methods.

Several upcoming direct current sensing methods, including TMR and micro-FG, can potentially replace HE and GMR soon, as described in the previous section. A CT is generally not suitable for this purpose, mainly because it suffers from core saturation, which makes it difficult to sustain high currents for an extended period. However, embedded RC appears to be a good candidate, particularly if its SSCB fault detection mechanisms do not require DC sensing.

In the case of power conversion, power electronics may be used for a variety of applications (e.g., renewable energy, batteries, or conventional power systems), which may result in facing different amounts of fault currents [66, 67]. Nevertheless, any level of current flowing through a power converter that exceeds the nominal current in its circuits can be considered a fault current, where an overcurrent fault (such as 120% of the power converter's nominal current) or a short circuit (such as reaching two times bigger (or more) than the nominal current in a very short amount of time) must be detected and taken care of. MR and RC (along with their hybrid combinations) have been underutilized extensively when it comes to short-circuit and overcurrent protection for WBG power converters. Because of their small dimensions, these circuits are ideally suited to highly compact layouts [23]. There have been several examples of embedded RCs with a high threshold and BW integrated into the layout design to provide short-circuit/shoot-through protection [68, 69]. MR technologies can be easily integrated into the power semiconductor protection process [70], especially with the development of precise and compact types such as TMR [35, 71]. Due to their high BW, small size, low cost, and non-invasive nature, which have been discussed extensively in the previous section, TMRs are well-suited to protecting power semiconductors.

2.4.2 Control

Many of the control schemes that are used in the field of power electronics rely on current control loops [23, 72]. Using these control schemes, the system can always maintain a desired level of current, regardless of changes in the load or the supply. They are therefore necessary for applications where the current must remain constant, such as motor drives and power supplies. These control schemes are also useful in applications where power regulation is critical, such as solar power systems. In these applications, the control schemes provide an effective and reliable way of regulating the current and maintaining the desired level of power. This helps to ensure the system is running correctly and efficiently, leading to improved performance and cost savings. For current control, high precision and reliability sensors are essential components of the sensing and feedback process [73]. A successful system requires accurate and reliable current control, particularly in industrial applications. Current control sensors must also withstand the harsh environmental conditions of industrial settings, and these systems must be able to operate quickly and accurately to ensure optimal performance.

As a system-level example, typical photovoltaic systems include a DC/DC converter stage followed by an inverter stage (see Figure 2.19). Grid-tied systems require current sensors to ensure grid connection. Current sensors must measure AC and DC currents accurately, but also be dynamically efficient [74]. In a typical inverter configuration as shown in the same Figure, there are several locations where a current sensor might be placed. Integrated current sensors (from the previous section) can be used instead of expensive, high-precision probes/sensors in conjunction with the microprocessor already available for the system. These integrated current sensors can improve the efficiency of the system while reducing the cost and complexity of the overall system. Among the cheapest options for current sensing, non-invasive CT and HE can be used in applications where bulkiness and magnetic insertion/saturation are not important, and shunt and HE ICs can be used in applications where invasiveness is not a significant factor. However, almost none of them are suitable for HF WBG converters' control applications.

The difficulty of integrating current sensors with desirable control functionality has led to the development of control algorithms that eliminate the requirement for current sensors [75], in which they argue that while current sensors can reduce the cost and

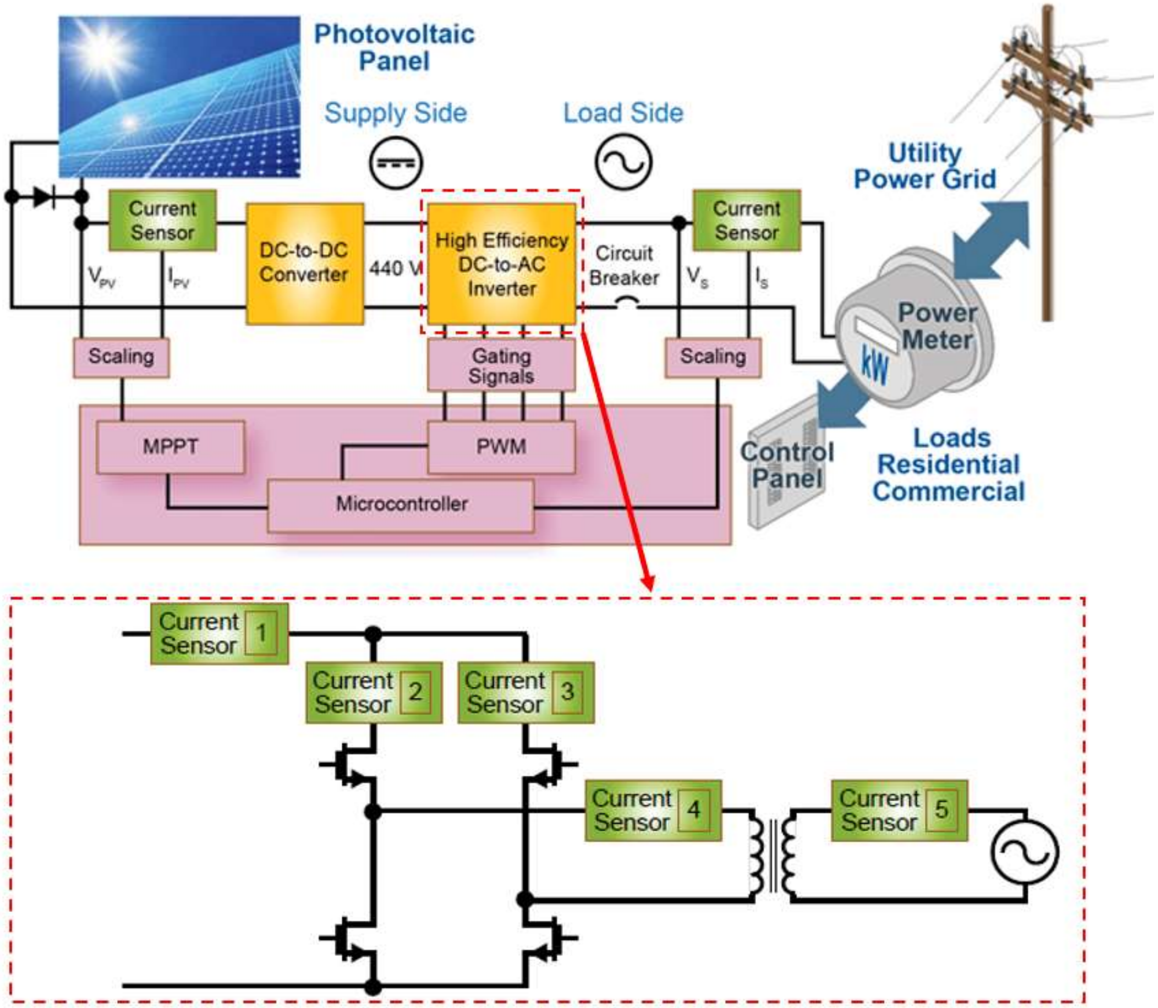

Figure 2.19: Current sensor placement in a renewable grid-tied system for control [74].

complexity of a system, they can also introduce new problems with them [76]. In another example of the use of conventional current sensors to control a system, if the current sensor fails, the system can become unstable, as it would be unstable if the current sensor failed. The latest advances in embedded current sensing technologies, such as RC, MR, and FG, can minimize or eliminate the conventional problems associated with current sensors utilized for control. In addition to offering improved accuracy and stability, embedded current sensing technologies can reduce complexity, size, and cost, and are easier to maintain and calibrate, making them ideal for control applications. According to [68], a PCB-integrated RC (as a switch-current sensor) can be easily modified to control average current and peak current, respectively, and in [70], a bidirectional current controller has been implemented by using a high-quality MR-based current sensor.

2.4.3 Prognostics

Power converters can be made more reliable and resilient if their components are condition-monitored, which will identify potential problems before they become catastrophic, thus reducing power electronics system failures. A condition monitoring system is also capable of extending the lifespan of a converter by monitoring temperature, current, and other parameters. This can result in significant cost savings for power systems, as well as improved safety and reliability [2, 23]. Furthermore, condition monitoring systems may provide useful data for predictive maintenance and analytics. By leveraging real-time monitoring, it becomes possible for engineers to proactively detect potential issues, which can help to avoid system downtime and increase the life expectancy of a converter. A variety of studies and techniques have been developed for monitoring the health and condition of semiconductors and capacitors, since they statistically have the highest failure rate of all power converter components [2, 23, 77]. One of the measurement types whose information can be translated to degradation or aging of swithces or capacitors is current. A high BW current sensor is typically required for this purpose, since most degradation-related current information is obtained from switching transients that have extremely high frequencies [78-80]. The aging detection mechanism can be implemented using current information, such as switching transients, as shown in Figure 2.20. The inherent integrability problems associated with coaxial shunt make embedded RC and MR potentially useful for such applications.

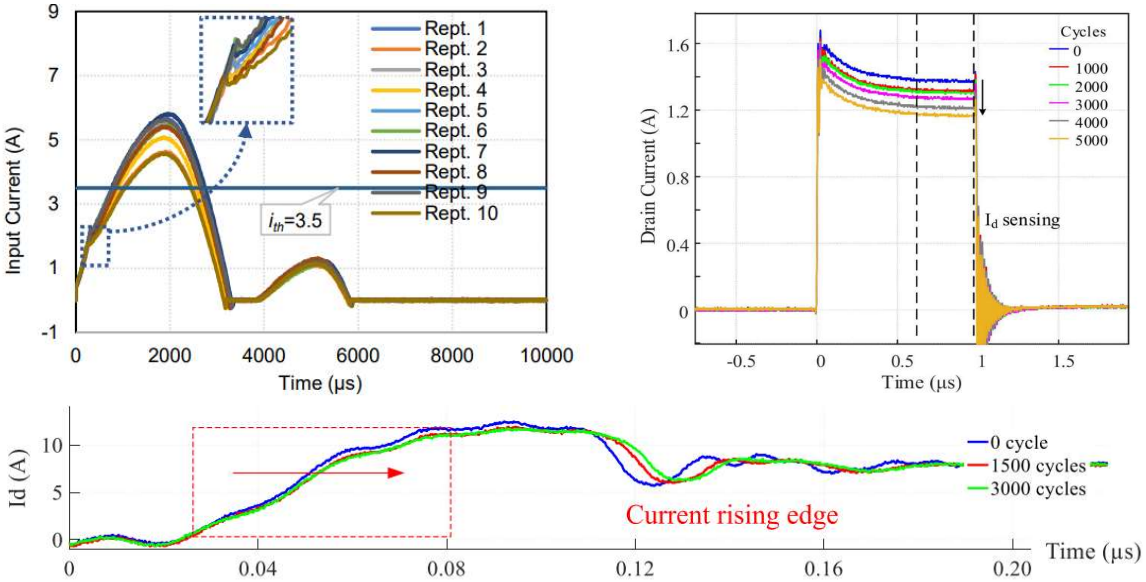

Figure 2.20: Current-based reliability assessment: DC-link capacitor [77] (Top left), Saturated SiC MOSFET [80] (Top right), and SiC in its normal operation [78] (Bottom).

2.4.4 Characterization

It is common practice to use circuits for characterizing semiconductor devices, such as double pulse testers (DPT), to characterize both static and dynamic performances by considering diverse device structures and operating conditions. Analyzing the measured results can provide important insights into device characteristics, a process called device characterization, which is essential for the design and optimization of semiconductor-based converters. In device characterization, switch-current is one of the measurement topics that can be used for a variety of assessment tasks, such as $R_{ds\text{-}on}$ measurement or the analysis of switching transients. Such measurements are usually performed in the laboratory since

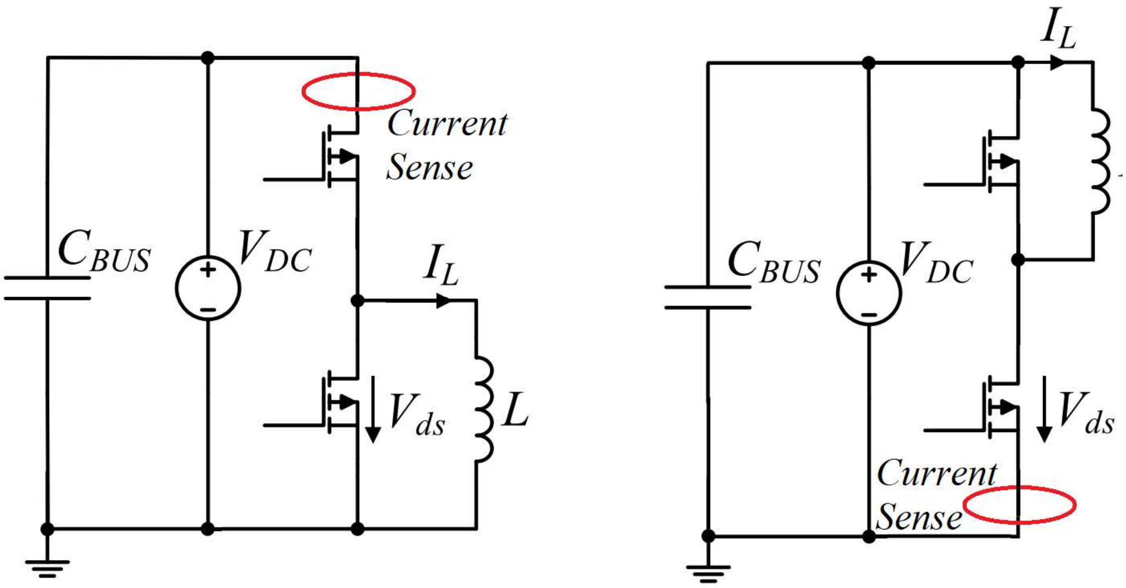

Figure 2.21: DPT testers: High-side DTU (Left), Low-side DUT (Right) [24].

they require expensive instrumentation and careful setup. By measuring switch-current, engineers can optimize the converter layout design for specified applications. As can be seen in Figure 2.21, either the top or bottom switch of a leg can be considered the device under test (DUT). However, since many people use (coaxial) shunt as the switch-current sensor, the low-side switch has been selected as DUT to minimize isolation issues. The use of an invasive current sensor, however, may not be the best option for high compact WBG layouts devices, especially GaN, as this may increase the switching ringing. A non-invasive unidirectional switch-current sensor embedded on a PCB was used in [24] to characterize and test a SiC module for shoot-through protection. The sensor seems promising for use in broader DPT applications.

2.5 Conclusion

Throughout this section of the thesis, the performance of existing single-scheme current sensors has been examined to gain a better understanding of the challenges associated with integrating these sensors into existing or emerging architectures of power converters. Moreover, the potential for developing single-scheme current sensors with desired performance for specific applications has been discussed. For instance, the survey evaluated the performance of single-scheme current sensors in terms of their accuracy, linearity, and dynamic range, as well as the influence of high EMI noise on their performance to be employed for protection, control, or monitoring purposes. In Table 2.1, the current sensing schemes are color-coded [24] in terms of their integration concern, and in Table 2.2, they are scored in terms of their functionality as determined by the four main applications in power electronics systems. The next chapter will discuss the possibility of combining these existing schemes to achieve hybrid sensors with a greater degree of integration for optimal power converter performance.

Table 2.1: Current sensing integration scores [24].

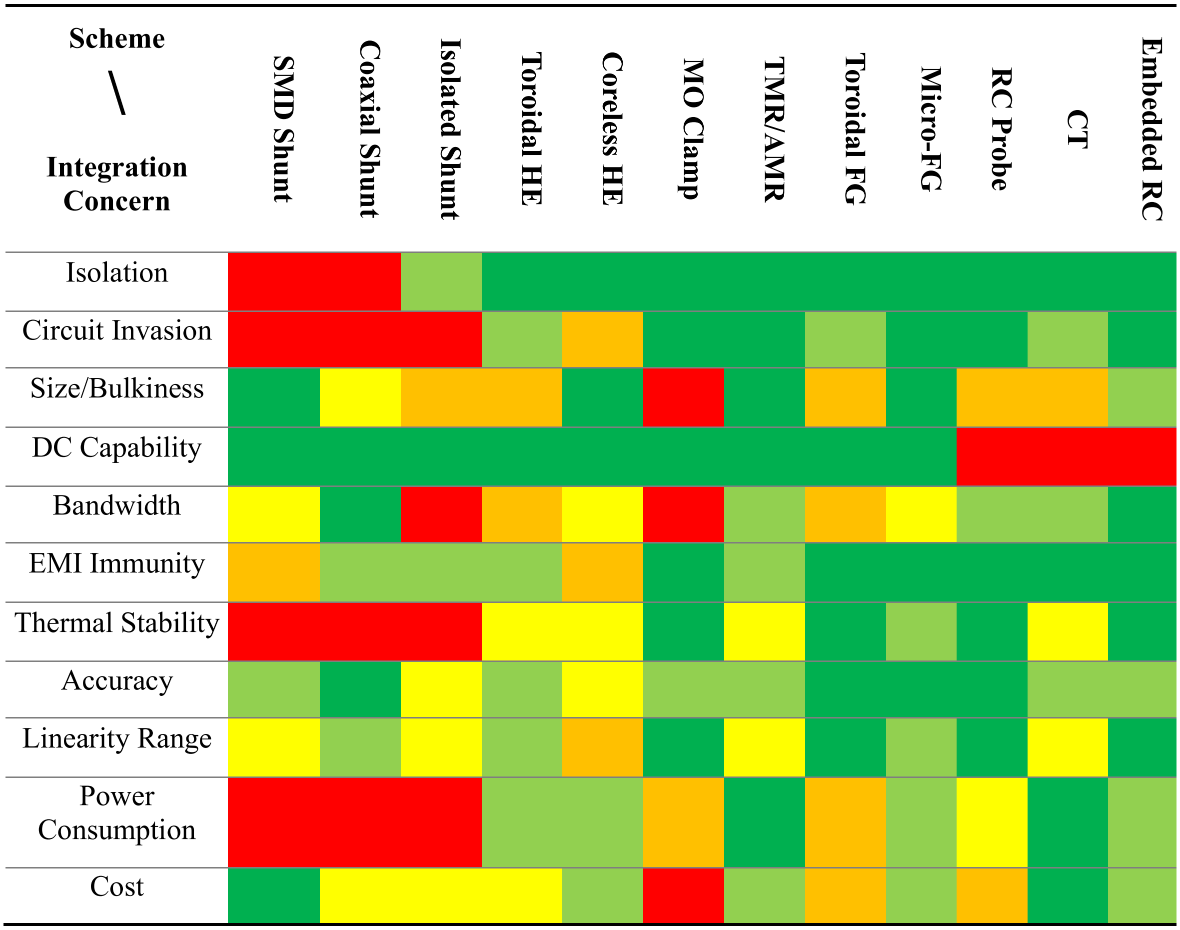

Scheme \ Integration Concern	**SMD Shunt**	**Coaxial Shunt**	**Isolated Shunt**	**Toroidal HE**	**Coreless HE**	**MO Clamp**	**TMR/AMR**	**Toroidal FG**	**Micro-FG**	**RC Probe**	**CT**	**Embedded RC**
Isolation	🟥	🟥	🟢	🟩	🟩	🟩	🟩	🟩	🟩	🟩	🟩	🟩
Circuit Invasion	🟥	🟥	🟥	🟢	🟧	🟩	🟩	🟢	🟩	🟩	🟢	🟩
Size/Bulkiness	🟩	🟨	🟧	🟧	🟩	🟥	🟩	🟧	🟩	🟧	🟧	🟢
DC Capability	🟩	🟩	🟩	🟩	🟩	🟩	🟩	🟩	🟩	🟥	🟥	🟥
Bandwidth	🟨	🟩	🟥	🟧	🟨	🟥	🟢	🟧	🟨	🟢	🟢	🟩
EMI Immunity	🟧	🟢	🟢	🟢	🟧	🟩	🟢	🟩	🟩	🟩	🟩	🟩
Thermal Stability	🟥	🟥	🟥	🟨	🟨	🟩	🟨	🟩	🟢	🟩	🟨	🟩
Accuracy	🟢	🟩	🟨	🟢	🟨	🟢	🟢	🟩	🟩	🟩	🟢	🟢
Linearity Range	🟨	🟢	🟨	🟢	🟧	🟩	🟨	🟩	🟢	🟩	🟨	🟩
Power Consumption	🟥	🟥	🟥	🟢	🟢	🟧	🟩	🟧	🟢	🟨	🟩	🟢
Cost	🟩	🟨	🟨	🟨	🟢	🟥	🟢	🟧	🟢	🟧	🟩	🟢

Table 2.2: Current sensing application scores in WBG converters [24].

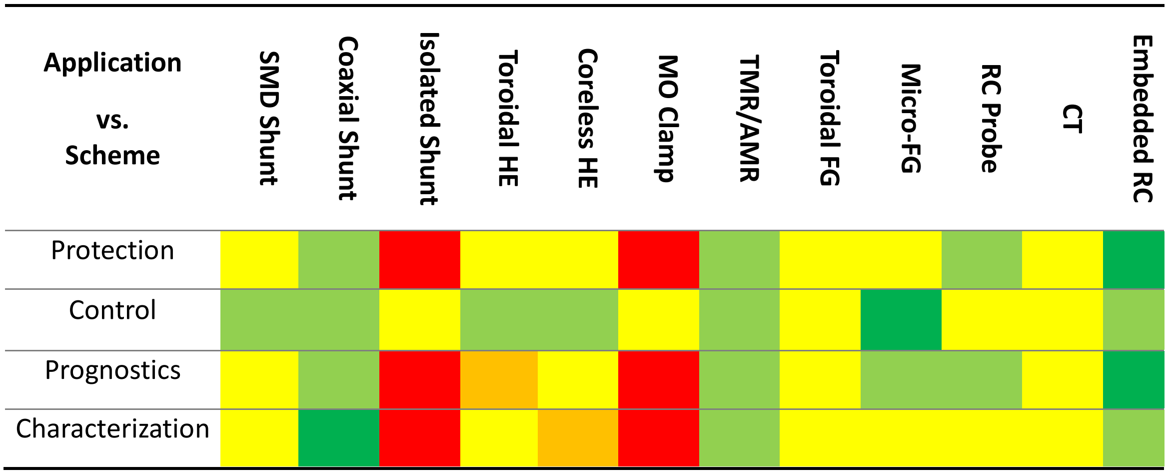

Application vs. Scheme	SMD Shunt	Coaxial Shunt	Isolated Shunt	Toroidal HE	Coreless HE	MO Clamp	TMR/AMR	Toroidal FG	Micro-FG	RC Probe	CT	Embedded RC
Protection	🟨	🟩	🟥	🟨	🟨	🟥	🟩	🟨	🟨	🟩	🟨	🟢
Control	🟩	🟩	🟨	🟩	🟩	🟨	🟩	🟨	🟢	🟨	🟨	🟩
Prognostics	🟨	🟩	🟥	🟧	🟨	🟥	🟩	🟨	🟩	🟩	🟨	🟢
Characterization	🟨	🟢	🟥	🟨	🟧	🟥	🟩	🟨	🟨	🟨	🟨	🟩

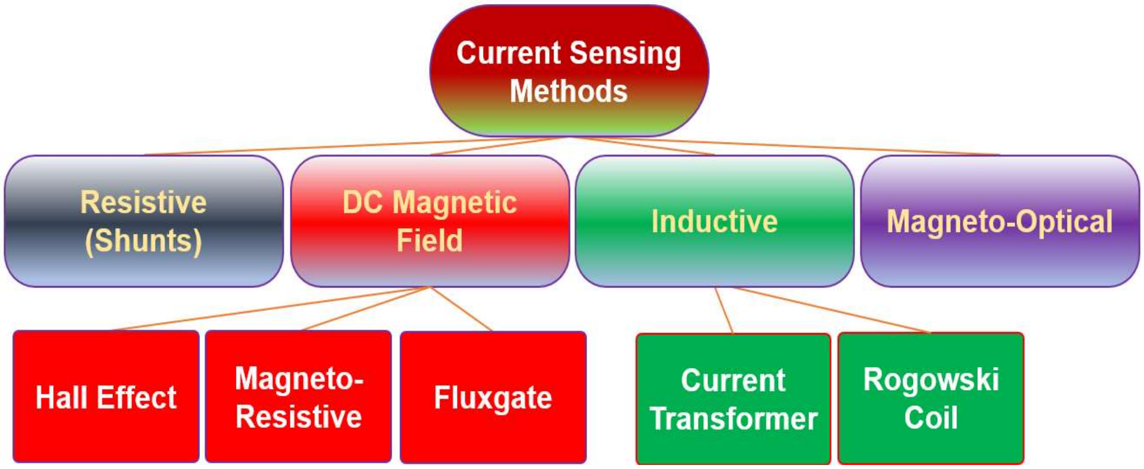

Figure 2.22 Different current-sensing methods in one picture [24].

CHAPTER 3: MULTI-SCHEME CURRENT SENSORS FOR POWER CONVERTERS

3.1 Introduction

Analyzing the information provided in the previous chapter, it becomes evident that there is almost no perfect single-scheme current sensing method with all desirable properties that can be integrated into an optimal power electronics layout. Nevertheless, a combination of different single-scheme methods can be used to achieve the desired performance for a given application. This can range from simple current sensing systems to advanced multi-sensing schemes. Ultimately, the selection of a sensing arrangement should be based on the specific requirements of the application. Historically, hybrid configurations have been underutilized in a variety of applications related to power electronics, in which two single-scheme (SS) sensing methods are combined to compensate for their limited bandwidth. Such hybrid (multi-scheme) configurations can be employed to increase the accuracy, speed, and robustness of a sensing system. This is especially beneficial in high-frequency applications, where the bandwidth of a single sensing method may be insufficient [23].

Additionally, hybrid configurations can provide a more flexible solution compared to an SS sensing system. One disadvantage of hybrid configurations is that they can be more difficult to design and implement than an SS sensing system. Additionally, multi-scheme configurations can be less reliable than SS systems because they rely on the combination of multiple sensing methods, which can introduce errors. As previously discussed in the thesis, the integration challenges associated with current sensors and their application to power electronics have been examined. In this chapter, these challenges and applications are considered in terms of multi-scheme (MS) current sensors, which will result in guidelines for optimally integrated designs after a critical analysis of their design and characteristics. To this end, it is important to understand the proper selection of multi-scheme current sensors in order to improve the integration of these sensors into power electronic systems and to maximize their performance.

3.2 An Overview of Existing Hybrid Current Sensors

The selection of a sensing arrangement for a particular application should be based on its specific requirements and can include simple current sensing systems to advanced MS systems. It may be possible to solve the problem by choosing and integrating compounds in a complementary manner since no existing SS current sensor has been proven to satisfy all the factors required for an optimal power converter. In fact, some SS sensing principles are physically MS, but they are known as SS sensing principles because of their simple integration. The ultra-wideband RC in [24] can be regarded as a hybrid sensor, as it combines the features of a capacitive sensor (or its analog integrator) with those of an air-core current transformer (Figure 2.6). A core-based closed-loop HE can also be viewed as a combination of an open-loop HE with a coil-shunt (Figure 2.2(b)). Consequently, in this chapter, MS solutions are referred to as a combination of the SS principles described in Chapter 2.

Early efforts to develop MS current sensors (around the 1980s) were focused on developing closed-loop HE current sensors, taking advantage of coil/CT technology to improve the wider sensing band [25], and compensating for other issues associated with open-loop HE by developing closed-loop HE sensors, which had been implemented by LEM company (in sensors such as the LA 100-P [82]). This is due to the limited frequency response of open-loop HE sensors, which makes it difficult to achieve a higher measurement range. As also depicted in Figure 3.1, The open-loop HE can be combined with a CT, because the CT can provide a much higher dynamic range than an HE sensor. Additionally, CTs' accuracy is higher than HE sensors. As described in [84], a US patent filed in 1990, an open-loop HE element is included as part of the CT output using this early MS method. The combination of the CT and the HE elements enhances MS performance by providing a smooth transition of the system response across the whole frequency range. The MS method described in [84] is still in use today (it might be using a closed-loop HE rather than an open-loop HE), providing a robust platform for the development of high-performance MS systems. This MS system has been used to great effect in various applications, such as automotive, aerospace, and medical. It has been shown to provide accurate and reliable results with minimal complexity. The MS method is thus a key technology in the development of modern control systems.

In the rest of this section, a criticized analysis of the applied (or applicable) MS current sensors has been conducted based on their 1) BW, 2) Size, 3) Invasiveness, 4)

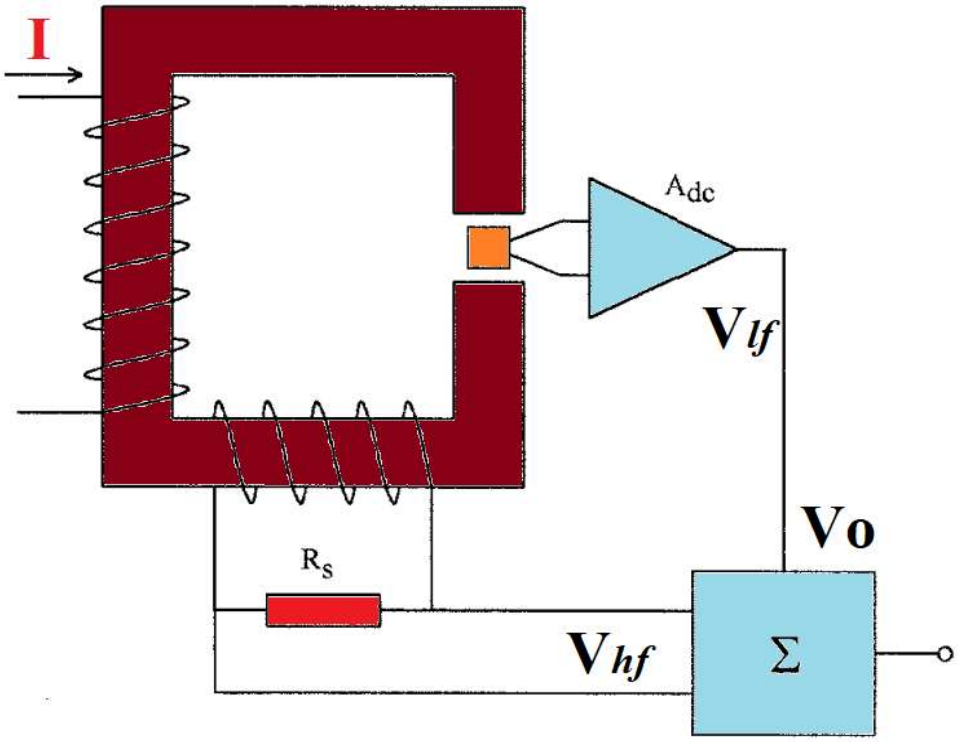

Figure 3.1: Combining a Hall-effect sensor with a current transformer during 1980s [83].

Switching EMI Noise Immunity. As a result of this critical review, we may be able to reach a better solution and design guidelines for MS sensors for the next section.

3.2.1 Bandwidth of Hybrid Current Sensors

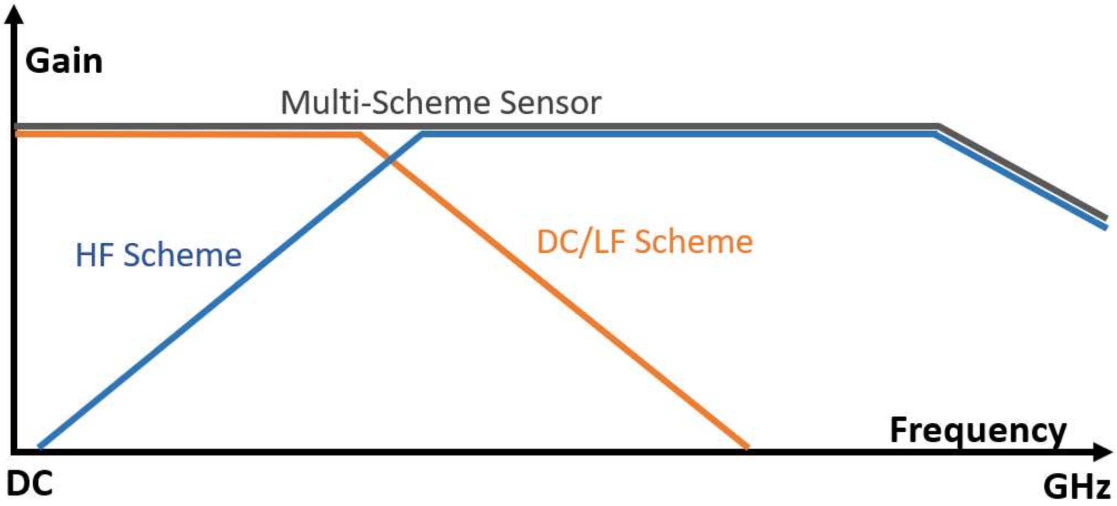

Figure 3.2: Bandwidth enhancement in dual-scheme current sensors.

Most non-invasive SS current sensors do not possess sufficient BW, whether it comes to HF measurement in magnetometers or DC detection in coil-based sensors. From the example provided, an HE sensor will be unable to reach very high levels of BW in contrast to a CT, which does not have DC sensing [23-27], as discussed in the preceding section. Based on the BW combinations, it is possible to compensate for the absence of frequency ranges, and having these compound sensors allows for better performance in terms of BW and dynamic range (Figure 3.2). Combining different schemes for enhancing the BW can thus increase the performance of SS sensors. As a result, both AC and DC currents may be detected using this combination, thus resulting in a more comprehensive output. For this reason, high-quality current sensors/probes (such as Tektronix TCP3001A which has a DC-120 MHz BW) have been widely developed utilizing this method [56]. As an alternative to the LEM technologies and the patent demonstrated in Figure 3.1, which combines an HE with a CT, the proposed method in [85] substitutes a closed-loop HE sensor for the open-loop HE sensor to overcome issues associated with open-loop HE sensors such as thermal drift. Over the years, such HE-CT combinations have been utilized to achieve a BW from DC up to 5 MHz in [86], up to 20-30 MHz in [31, 87], and above 30 MHz in [66, 88, 89].

The Hoka probe is believed to be one of the first current sensing approaches to incorporate an LF sensor, such as HE, in conjunction with an RC to achieve greater BW noninvasively (Figure 3.3) [90, 91]. Also, HE can be replaced with GMR as the initial improvement to this MS method [92-93], but at the same time, the size of the Hoka probe

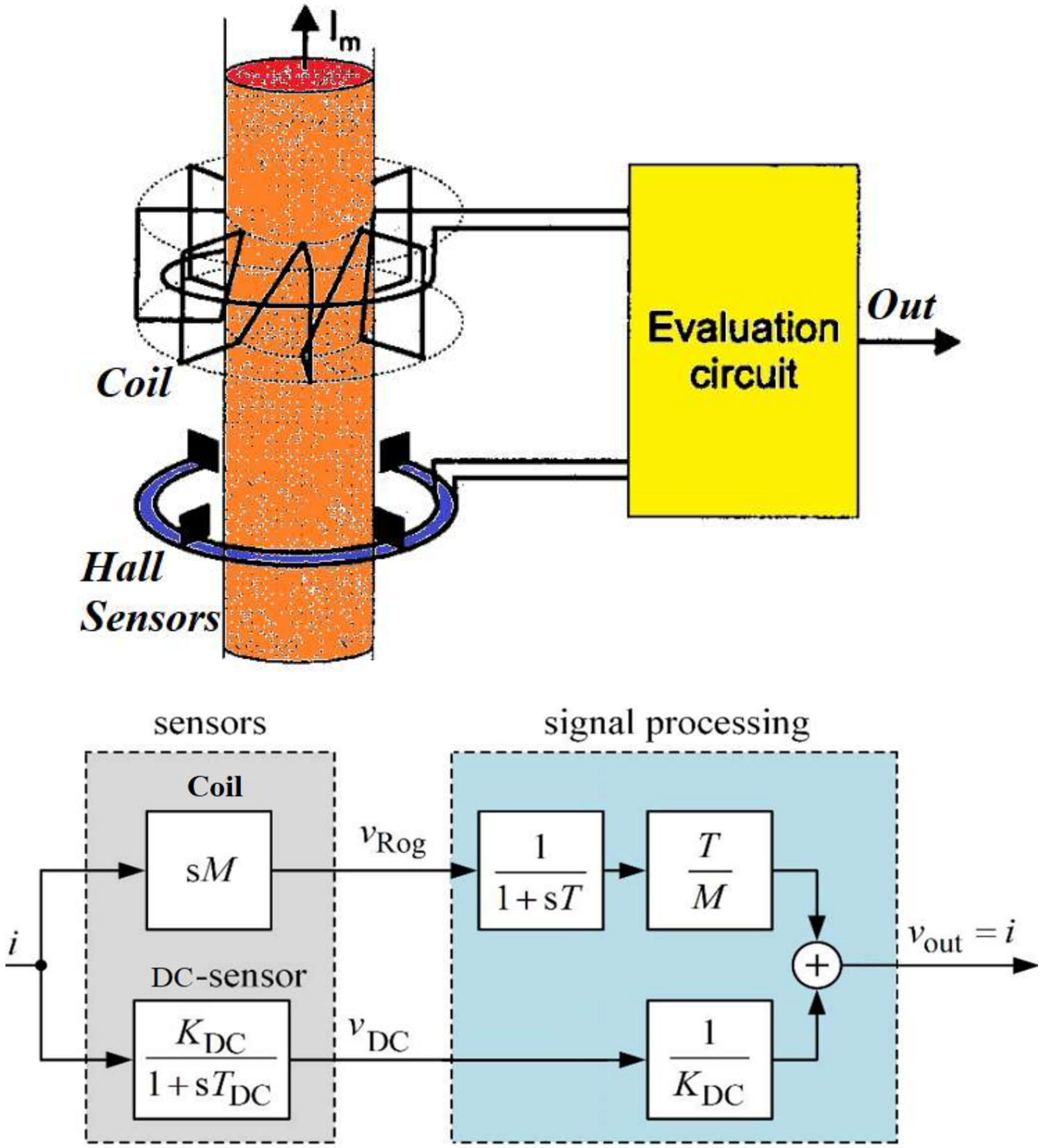

Figure 3.3: Hoka principle of current sensing [90-97].

needed to be improved as well. This refers to the fact that Hoka uses air-core coils rather than magnetic cores when compared with CT combinations, allowing a higher BW while retaining a smaller size and bulk (another factor in IC packaging technology [98-102]), as well as avoiding core saturation when measuring larger currents. Accordingly, several MS current sensors based on the Hoka principle have attempted to replace HE/GMR sensors with smaller/better-quality MR ones (primarily TMRs, due to their improved accuracy, higher BW, and smaller size), in which some of them are also deploying coaxial housing to achieve an ultra-high BW [94-97]. In MS current sensors that use a core-less coil along with HE or MR sensors, [3, 92, 98-101] have a BW of DC up to 1-20 MHz, [94. 102, 103] can go up to 20-100 MHz (up to now, [102] also has the highest BW among on-chip current sensors), and [95-97] have an upper limiting band of over 100 MHz (250, 315, and 240 MHz, respectively). Before the initial Hoka probe, people also attempted in 1995 to create an MS topology using the Rogowski coil core-less size to sense DC-1 MHz, as described in [104]. However, this method required current passing through it due to a shunt

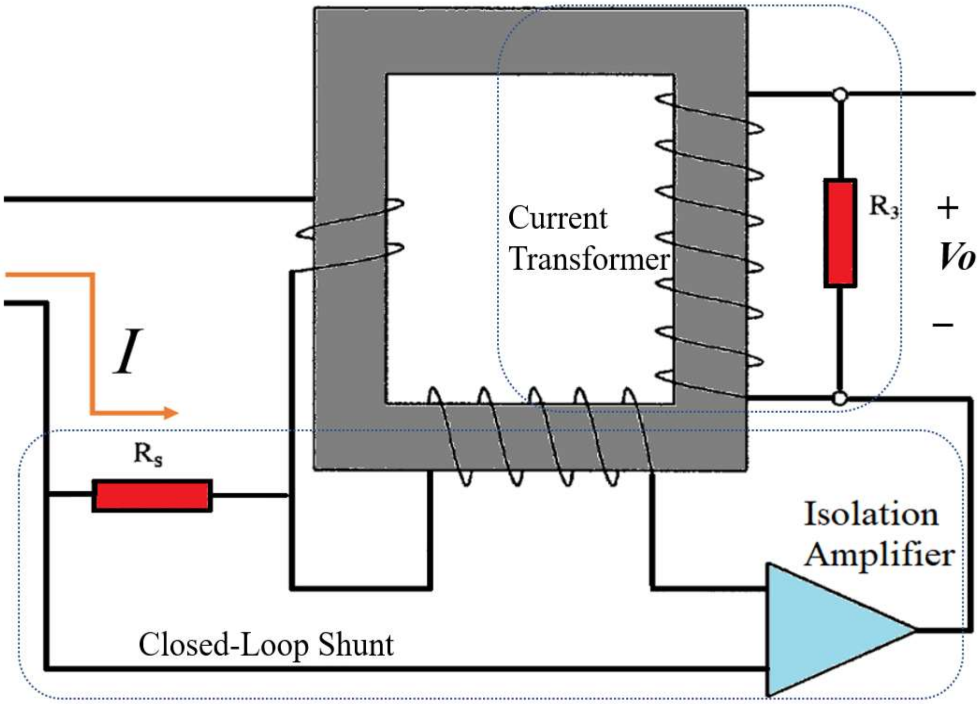

Figure 3.4: DC current transformer idea from [105].

sensing principle, resulting in engineers continuing to look for alternative non-invasive methods.

It is now possible to deploy inductive current sensors (CT/RC) with a variety of coil configurations that extremely cover HF bands without requiring invasive methods of measurement, which makes them necessary to be combined with DC/LF detectors in a wide range of compound sensing systems. Easily used and providing accurate and consistent results, these sensors can be applied to measure current in high-voltage systems with extreme precision and accuracy. In the case of CT, the inventors of [84] (the open-loop HE + CT) and [85] (the closed-loop HE + CT) also collaborated to come up with the idea of a DC CT current sensor in 1999 with a BW of DC-1 MHz [105]. Figure 3.4 illustrates that DC CT replaces the HE sensing element through a closed-loop shunt configuration that the primary current passes through it, which facilitates the mechanical manufacturing process and addresses other issues related to HE sensors [104]. Next, the shunt output is measured by an LF isolator which ensures enough electrical isolation from the primary circuit when the CT output is added to it. It is also possible to apply this DC CT method to a wider range of CTs to cover a wider range of BW. As another example of compounds containing CT(s), [32] (which is proposed by the author of this thesis) presented using a passive method to aggregate CTs with different frequencies (Figure 3.5)

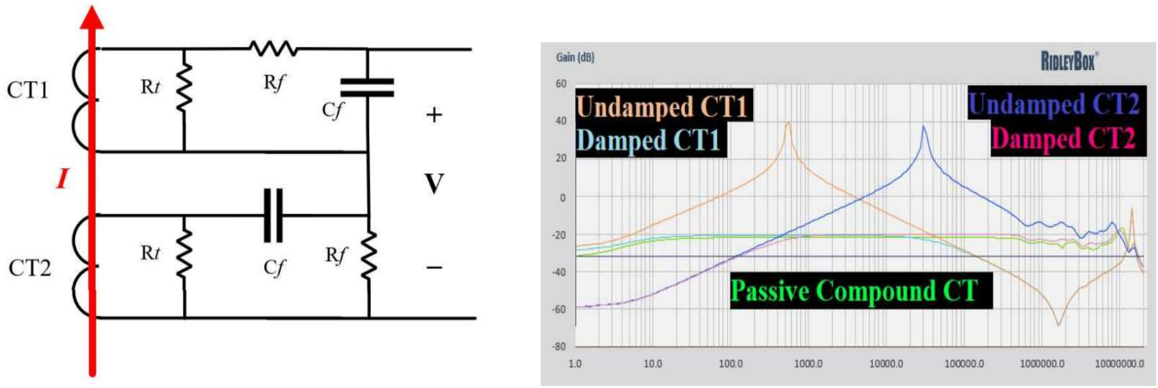

Figure 3.5: Passive Compound CT: The circuitry (Left), The frequency response (Right) [32].

to achieve a much higher BW (in their example 10 Hz to 10 MHz) without electronic components. Even though it cannot detect DC, the method does not require power supplies or invasive sensing, which makes it ideal for some harsh environments that tend to restrict the use of electronics.

Additionally, there is a chain of MS sensors that contain CT and MO sensors, dating back to the early 2000s, that serve as high-voltage/power/current sensors in power systems [106-109], hence there is no significant BW, with a maximum frequency of 5 kHz reported in [108]. Power electronics cannot use these combinations due to insufficient BW, size, and cost. Using micro-FG as the DC/LF detector as depicted in Figure 3.6, another CT combination was demonstrated in [110], achieving a DC-100 kHz BW.

As a follow-up to the discussion of RC, a number of people have attempted to replace the CT in most of the MS examples provided to take advantage of either a higher BW or lighter size (due to the lack of a magnetic core). The RC and MO were combined in [111, 112], but again, they were designed for high-voltage/current applications in power systems, and the BW did not play an important role. A DC-30 kHz BW is suggested in [113] by combining an air-core coil with FG. [114] combines an extended-BW RC with a line-DC detector, in which the DC detector is an invasive HE IC that monitors DC/LF current away from the switching devices. As stated in [114], the final BW is claimed to be DC-250 MHz. However, there is not enough frequency analysis and experiments to

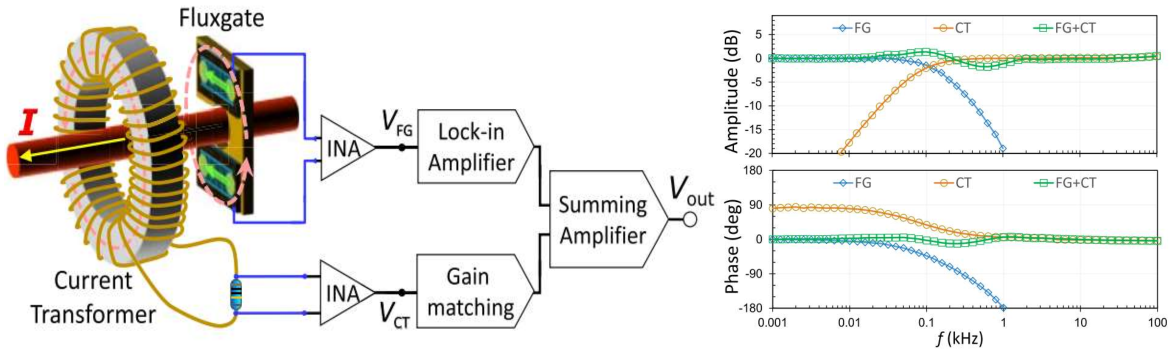

Figure 3.6: Current transformer and micro-fluxgate combined current sensor [110].

support this claim.

According to the examples presented in this section, a DC/LF detector (which is usually a DC magnetic field sensor) with proper physical properties needs to be coupled with an HF current sensor (which is in most cases an inductive-based transducer) in a manner that their gains and slopes match at a particular frequency, as shown in Figure 3.2. Physically, it is difficult to build those sensors in a way that their matching frequency will be the exact same. As illustrated in Figure 3.7, a low pass filter (LPF) at the end of the LF sensor and a high pass filter (HPF) at the end of the HF sensor can be used for better gain/frequency matching [23]. The LF and HF sensors need to have a common frequency band, which allows their overlapped sensing bands to be cut off to the extent needed for specific applications.

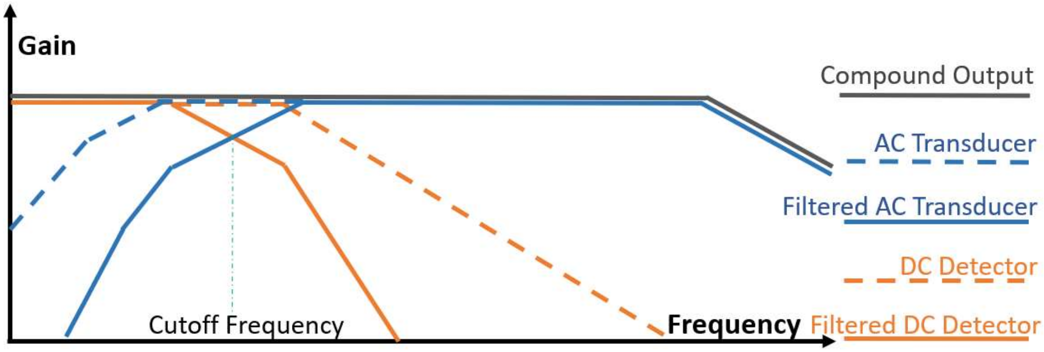

Figure 3.7: Bandwidth enhancement gain matching in multi-scheme current sensors.

3.2.2 Size of Hybrid Current Sensors

Many MS current sensors are built from SS sensors for BW extension purposes [23], however, to integrate them into power converters, speed and BW are not the only considerations. Among the most significant concerns are the size and bulkiness of the MS sensor, which must fit within the dimensions of the power converter. For different applications, even smaller sensors are required in WBG converters. Consideration of the size and weight of magnetic core-containing current sensors can be found in Figures 2.9-

10, as well as in Figure 3.8, in which some core-based MS current sensors are illustrated. As can be seen in Figure 3.8(a, c-f), all sensors have considerable bulk and volume that makes them difficult to integrate within optimal power converters' layout. The sensor in Figure 3-8(b) with the smaller height and volume senses the current invasively (although it provides isolation, we will discuss the issue of sensing invasively in the next subject).

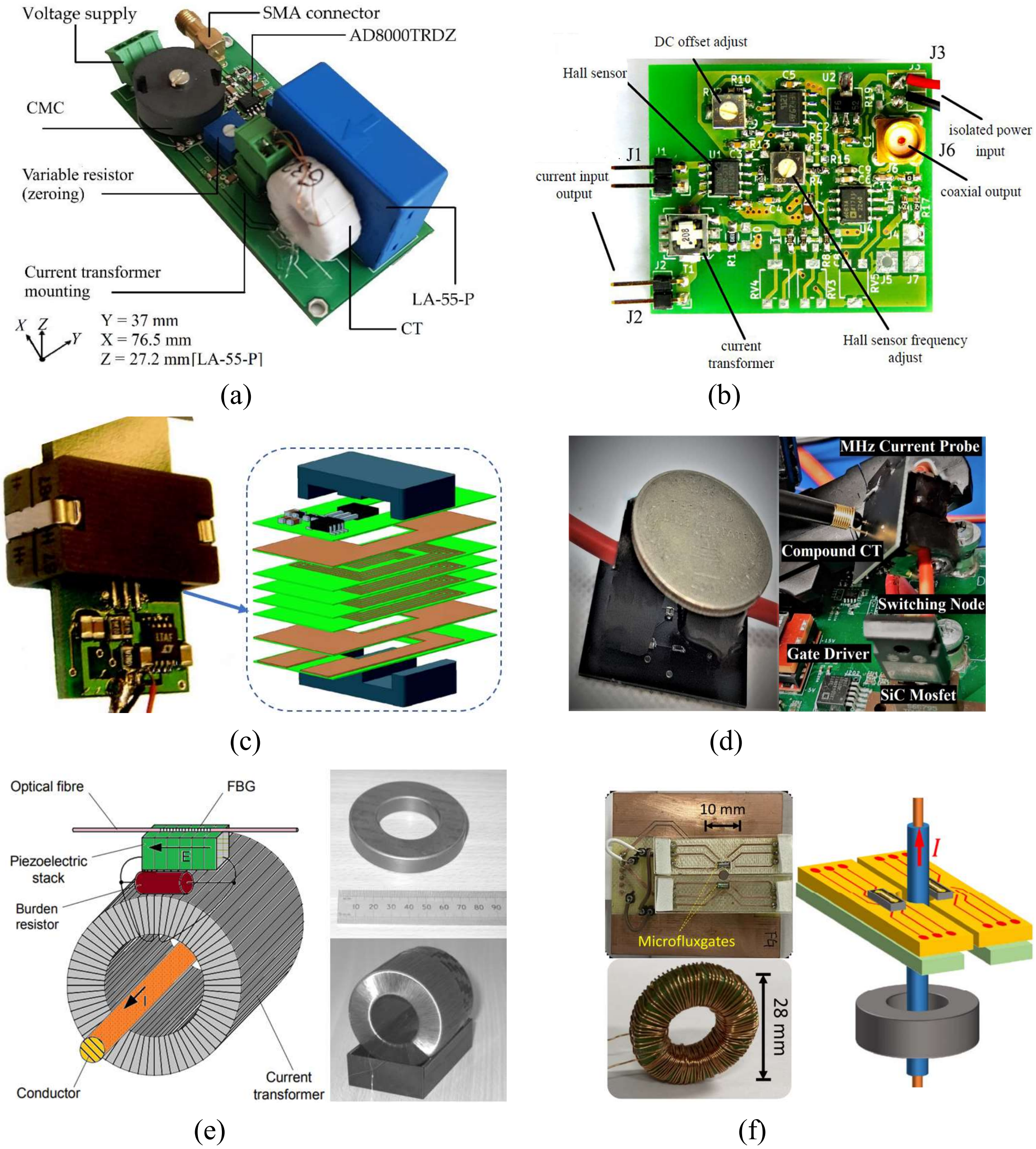

(a) (b)

(c) (d)

(e) (f)

Figure 3.8: Depiction of core-based multi-scheme current sensors: a) [56], b) [86], c) [31], d) [32], e) [109], f) [110].

Air-core coils can be used for HF sensing to reduce the size of MS sensing methods such as Hoka, however, Figure 3.9 illustrates that some of these MS current sensors are too large to be integrated into WBG power electronics. It is clear from Figure 3.9(a) that the

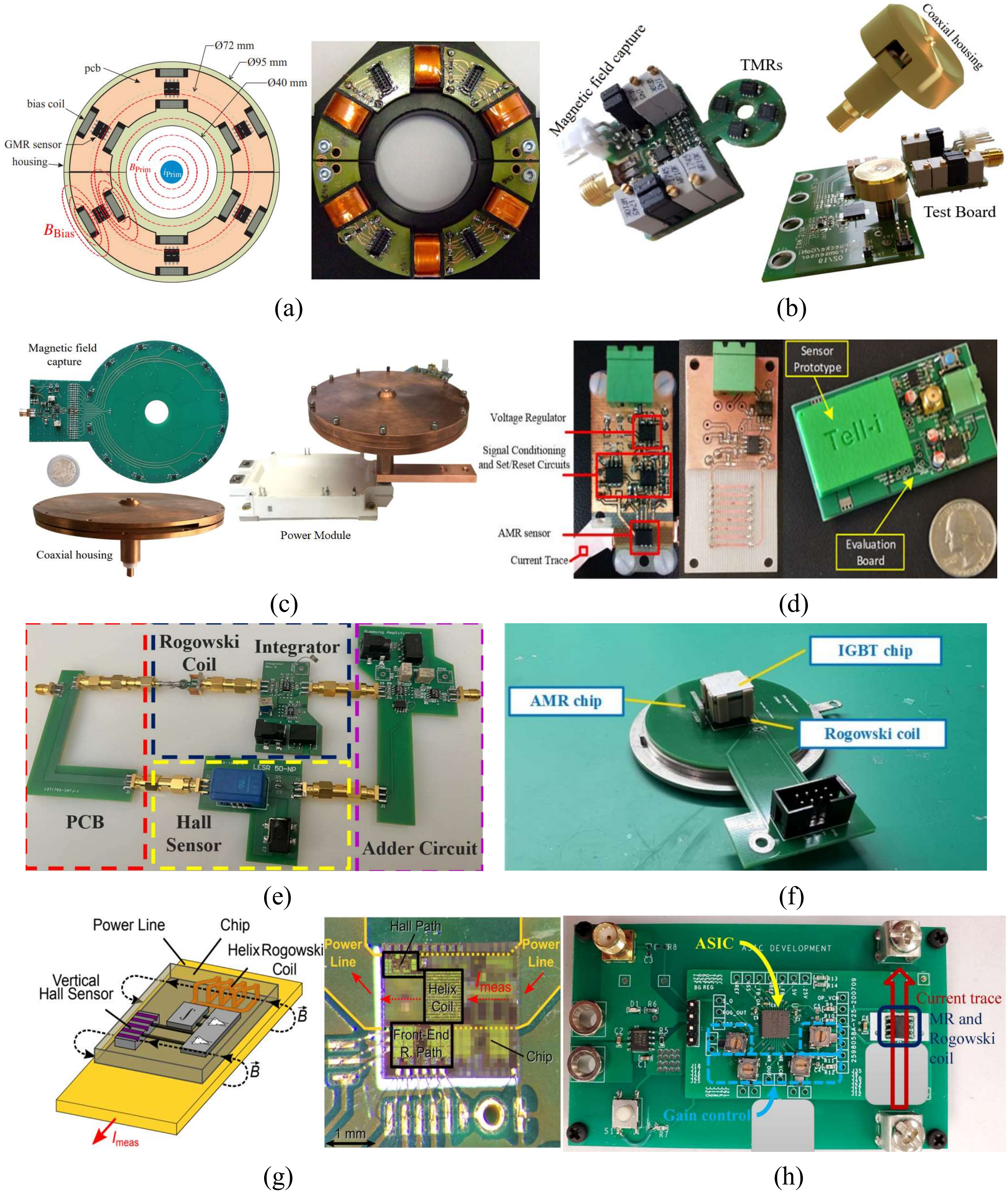

(a) (b)

(c) (d)

(e) (f)

(g) (h)

Figure 3.9: Depiction of core-less hybrid sensors: a) [93], b) [96], c) [97], d) [3], e) [114], f) [115], g) [101], h) [116].

head is too large due to the size of the coils and GMR sensors, while Figures 3.9(b-c) demonstrate excessive sensor dimensions due to the shape of the coaxial housing or the number of integrated HE/TMR sensors. Hence, alternative solutions have been extended to meet size requirements, including designing sensors with integrated circuitry (Figures 3.9(g)), readout interface IC for signal processing (Figure 3.9(h)), press-stacking technologies (Figure 3.9(f)), or embedding them into PCBs (Figures 3.9(d-e)).

Compact sensors have been developed to accommodate the tight confines of WBG converters, which are smaller and more compact than core-based sensors. In Figures 3.9(d-f), RC is embedded on each PCB together with AMR [3, 115, 117] or HE [114], and Figures 3.9(g, h) show IC packaging with RC plus HE [101] or readout interface for MS

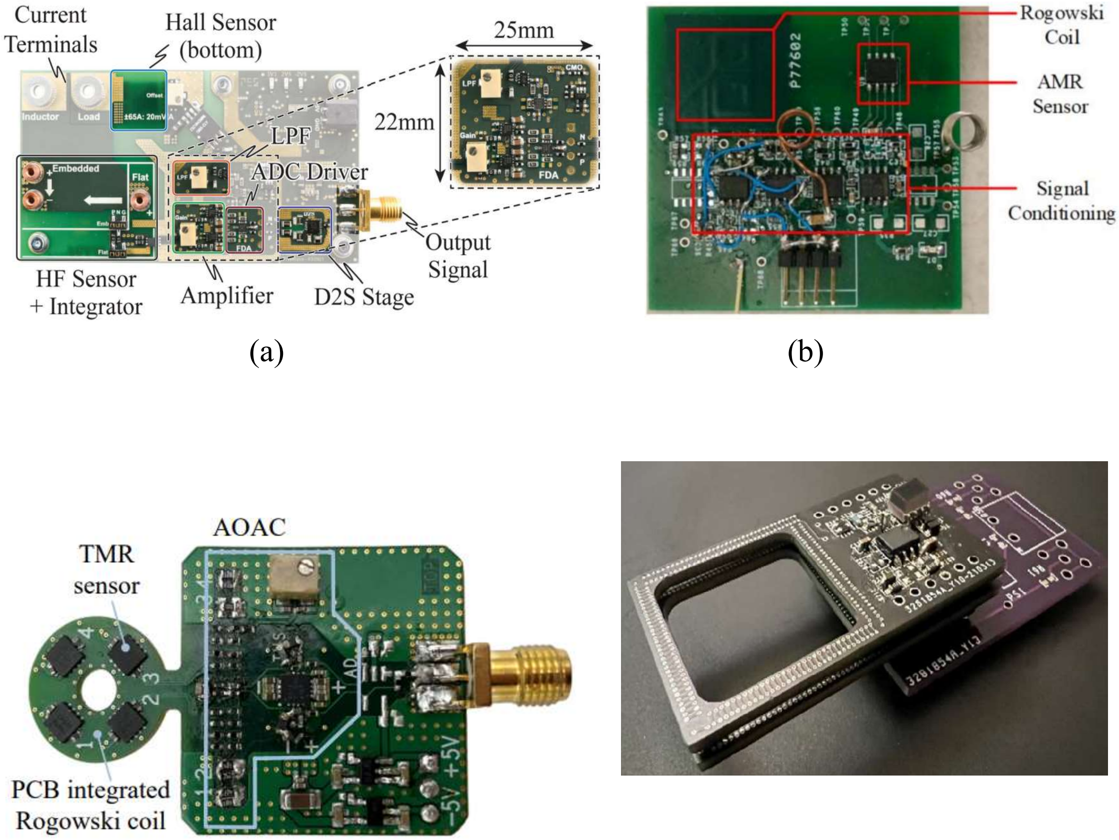

(a) (b)

(c) (d)

Figure 3.10: More examples of PCB-embedded hybrid current sensors: a) [103], b) [117], c) [118], d) [33].

sensors [114, 119]. Further examples of MS PCB-embedded current sensors can be found in figure 3.10 as well as on-chip die-level capture examples can be found in Figure 3.11.

Figure 3.10(a) shows the coil is integrated into the HF sensing part, and all the RC, HE, and processing circuits have been integrated into a single PCB. For contactless on-trace current sensing, the PCB-embedded RC is coupled with the top-mounted AMR, as pictured in Figure 3.10(b). The RC and TMR components shown in Figure 3.10(c) are integrated into a small PCB area that allows differential current measurements within the central hole. Figure 3.10(d) depicts how the RC pair substitutes the DC/LF sensor with another RC, whose output will be rectified using an Opamp precision full-wave rectifier [33], and then added to the AC-RC output to construct the switch-current unidirectionally [24] for semiconductor modules.

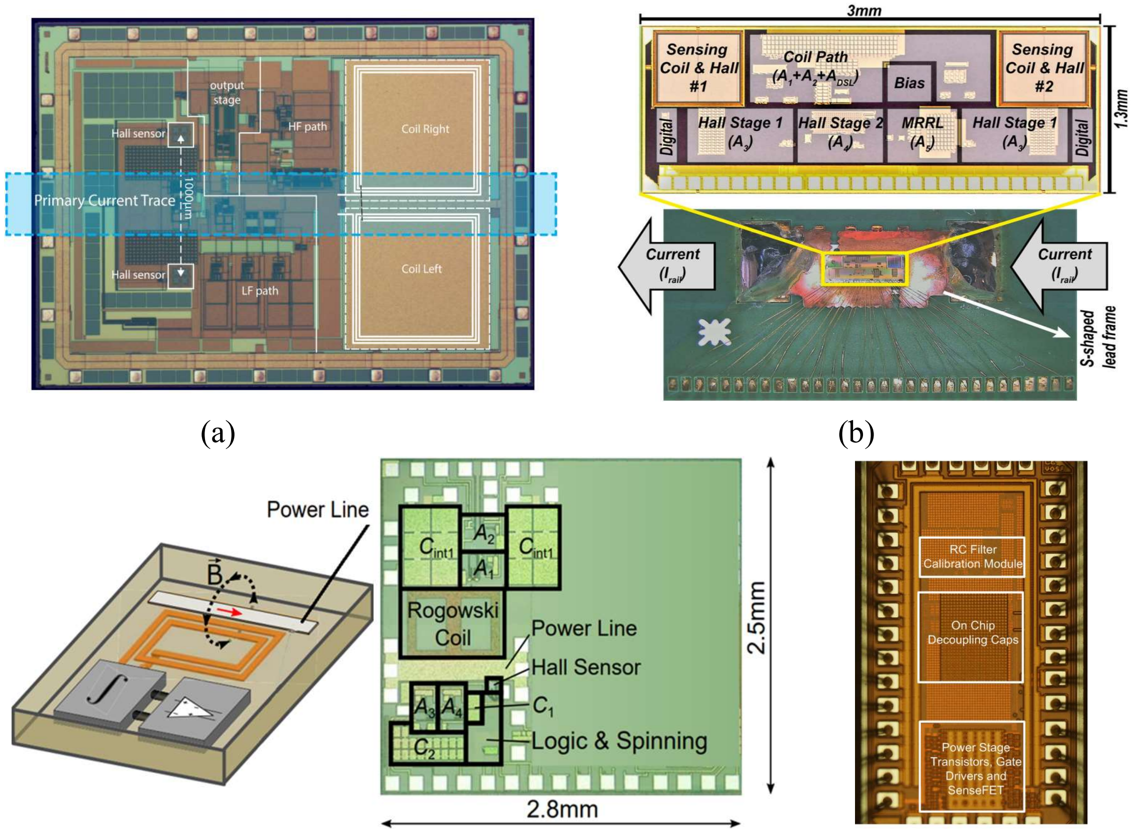

(a) (b)

(c) (d)

Figure 3.11: More examples of die-level hybrid current sensor ICs: a) [99], b) [102], c) [98, 100], d) [120].

In Figure 3.11, most IC-packed MS sensors employ a combination of HE and RC [98-102]. A chip-level integrated hybrid current sensor is also shown in Figure 3.11(d) equipped with RC filters and sense FETs with a novel self-calibration method is employed based on two-point measurements of high under-sampling rates to measure inductor current within integrated HF DC-DC converters [120].

In general, MS current sensors are designed for BW extensions, however, Figure 3.12 illustrates different types of compound/array current sensors whose point of combination is not (only) based on BW extensions. It is possible to use the same sensors for numerous purposes other than BW extension, including busbar current sensing (Figures 3.12(a-c)) and differential measurement and optimization of field-sensing functions (Figure 3.12(d)). As presented in Figure 3.12(a), an array of eight HE sensors can measure high currents from a rectangular busbar by forming a DC-5 kHz current transducer; however, there is a trade-off between the size of the array (fewer sensors) and its accuracy [121]. Closed-loop measurements have been applied to a circular array of both HE and FG current sensors (Figure 3.12(b)), resulting in a significant decrease in measurement error when FG sensors are chosen instead of HE sensors [122]. The same size scenario (with Figure 3.12(a)) applies here as well. As shown in Figure 3.12(c), a PCB-mounted MS current sensor using TMR devices can break the tradeoff between sensitivity and detection range, and the results of [123] indicate that the sensor, consisting of two TMRs with varying degrees of sensitivity integrated into one current sensor module, is capable of measuring currents in the range of 2 mA to 100 A with a dynamic range of approximately 93 dB, and has a very small size because the TMRs are surface mounted. Figure 3.12(d) represents another compound ultra-sensitive current sensor derived from GMR as another attempt to improve sensitivity by utilizing MR sensors. By combining a multi-trace current trace system with a dual differential GMR detection system, this system effectively constitutes a planar coil that maximizes the magnetic field available to single GMR sensors

[124]. This approach enables the current sensor to detect very small currents and provide a much higher sensitivity than conventional SS current sensors.

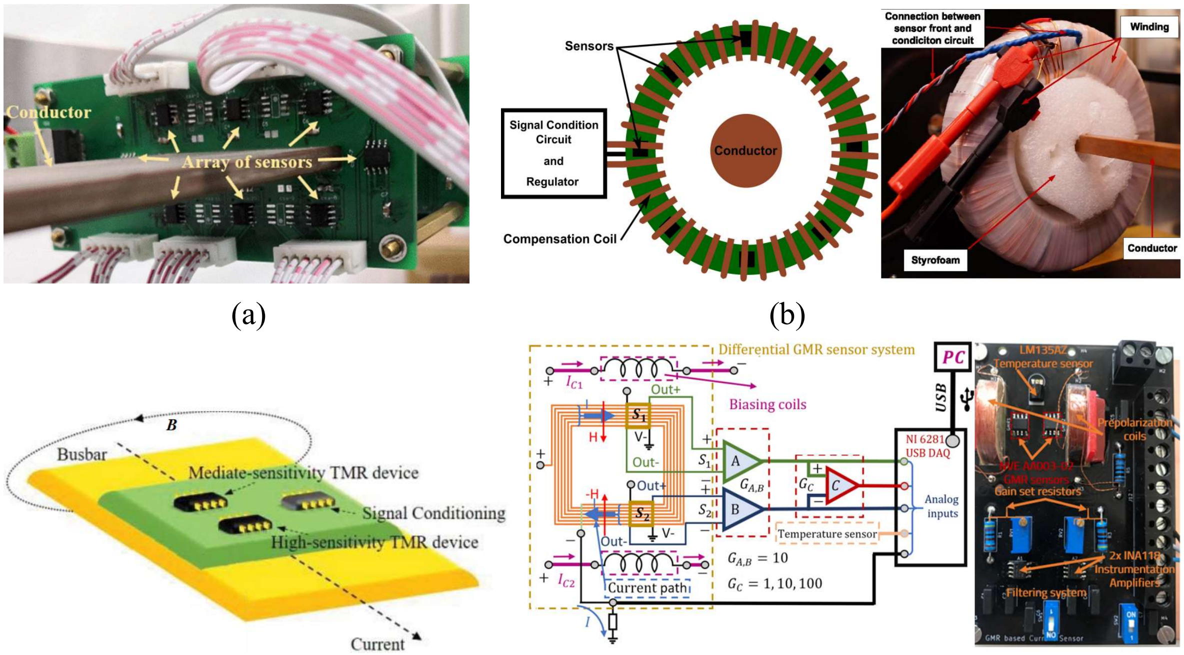

(a) (b)

(c) (d)

Figure 3.12: Examples of current sensor arrays: a) [121], b) [122], c) [123], d) [124].

Overall, it appears that deploying core-less coils or exploiting a more modern magnetometer (such as MRs) together with compact PCB, stack or IC design may contribute to maintaining acceptable final dimensions in MS current sensors within context of newer generation power converters.

3.2.3 Circuit Invasion of Hybrid Current Sensors

As the term invasive measurement implies, the target current is passed electrically through the measurement device. This involves connecting the sensor to the circuit electrically, in which the current sensor invades the original circuit layout and its electrical properties. Due to altering the electrical properties, someone may view other alterations, such as the magnetic core of a contactless CT introducing an excessive amount of parasitic inductance into the original circuit, as invasive, but all contactless current sensors are considered non-invasive in this thesis. Approximately 44 MS techniques have been discussed in the last two sections, and in this section, they will be classified into two groups: those that require electrical connections to the target circuit (invasive) and those that do not (non-invasive). Among the MS current sensors presented, [3, 31-33, 56, 83-85, 87, 89-93, 99, 106-113, 115-117, 121-125] are non-invasive (or electrically contactless). Other presented current sensors are considered invasive due to one of the following situations: 1) the use of an ohmic sense element [104, 105, 120], 2) coaxial housing for current commutation [94-97], 2) the use of invasive HE current sensors as DC/LF detectors [86, 88, 103, 114], and 4) the integration of an HE element into the IC packaging for improved current sensing accuracy [98, 100-102].

Even though most of the invasive MS current sensors can provide enough electrical isolation, altering the original optimal layout of power converters (especially the ones close to semiconductor switches and decoupling capacitors) is the most challenging aspect of integrating them into such applications, usually as a result of adding parasitics to the layout. The parasitic inductance from the sensor leads can cause high current ripples and oscillations in high-frequency power converter applications, which can also increase power losses, decrease efficiency, and increase radiated EMI. Therefore, extra care should be taken when designing these layouts, to minimize the impact of extra parasitics. To achieve this goal, light-sized non-invasive compounds, such as those containing RC, small MRs, and micro-FG, will certainly contribute significantly.

3.2.4 Hybrid Sensors' EMI Immunity

Since WBG power electronics operate at high switching frequencies, integrated current sensors must be capable of handling extremely high levels of electromagnetic interference (EMI) radiation and coupling. It is known that high di/dt near switching nodes can cause sensors to be exposed to ringing and over-voltages, resulting in RF emissions, EMI radiation, and false output information, as well as destructive circulating currents due to large levels of di/dt. In MS current sensors, the situation can be adversely affected in comparison to SS sensors, since 1) there are multiple sensing elements whose exposure conditions may require different methods of noise rejection in differential and common modes, 2) larger conditioning circuits and traces, and other conductor components (which implies larger parasitic capacitances and inductances), and 3) their intended placement and application within WBG power converters. For example, the immunity of the multiple sensing elements to the common-mode noise in MS current sensors can be easily impaired by the large capacitance between the traces and the parasitic capacitance of the current sensing circuit. This section examines several examples of MS current sensors along with the waveforms of their outputs near the switching nodes to gain a better understanding of designs and topologies that can be placed easily near noisy semiconductors to generate clean results.

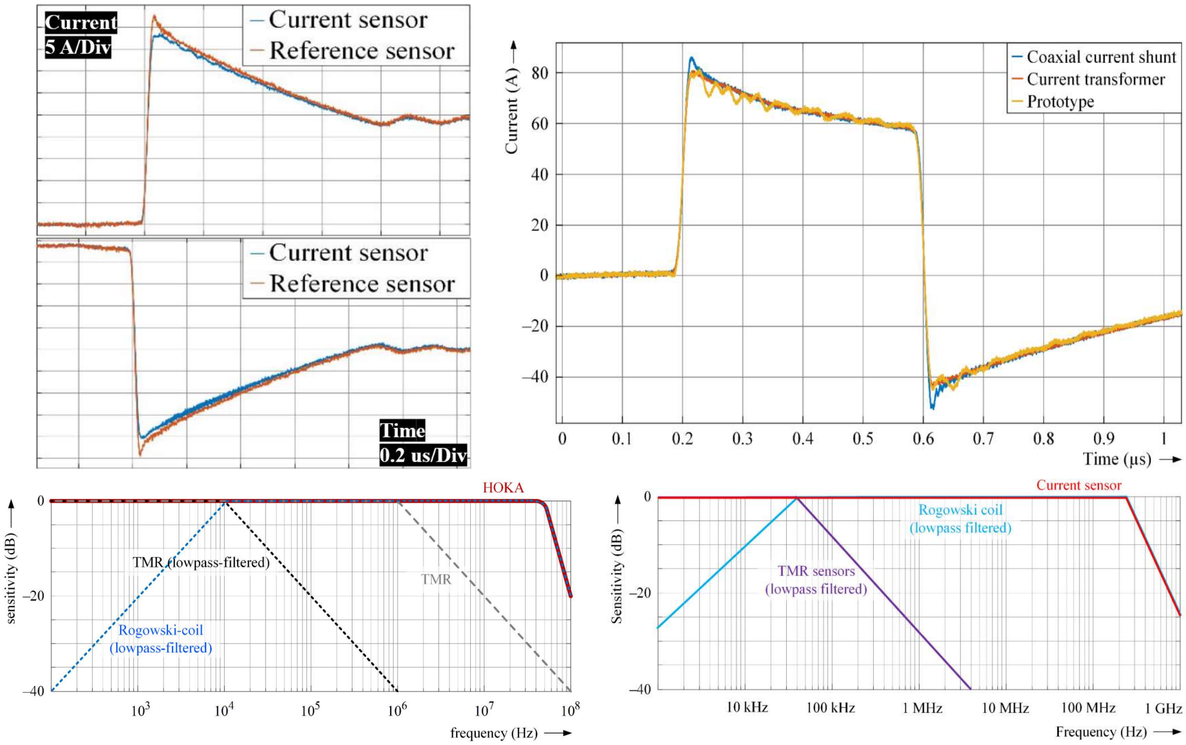

(a) (b)

Figure 3.13: Switch-current waveforms and Bode plots of: a) [94], and b) [95].

A comparison is made between the results of two current sensors using the same Hoka principle and coaxial housing, one with a BW of 50 MHz [94] and the other with a BW of 250 MHz [95]. Figure 3.13(b) shows a ringing of approximately 10 Ap-p at a frequency of approximately 30 MHz that is not present in its reference waveform (the blue waveform), and a much smaller ringing with a similar frequency (or a bit less) is also visible in Figure 3.13(a). As [95] stated, coupling noise is the source of unwanted ringing in coaxial housing, yet both sensors have similar coaxial housing conditions, and although these two sensors are designed to operate within two different frequency bands, the existing ringing is within both sensors' BW. The one that is designed to operate at 200 MHz above the other might have different coil design characteristics, making the stray capacitance of the RC a potential source of error. Another difference might be causing the problem, as one has a 10 kHz TMR cutoff band and the other has a 40 kHz. Under the

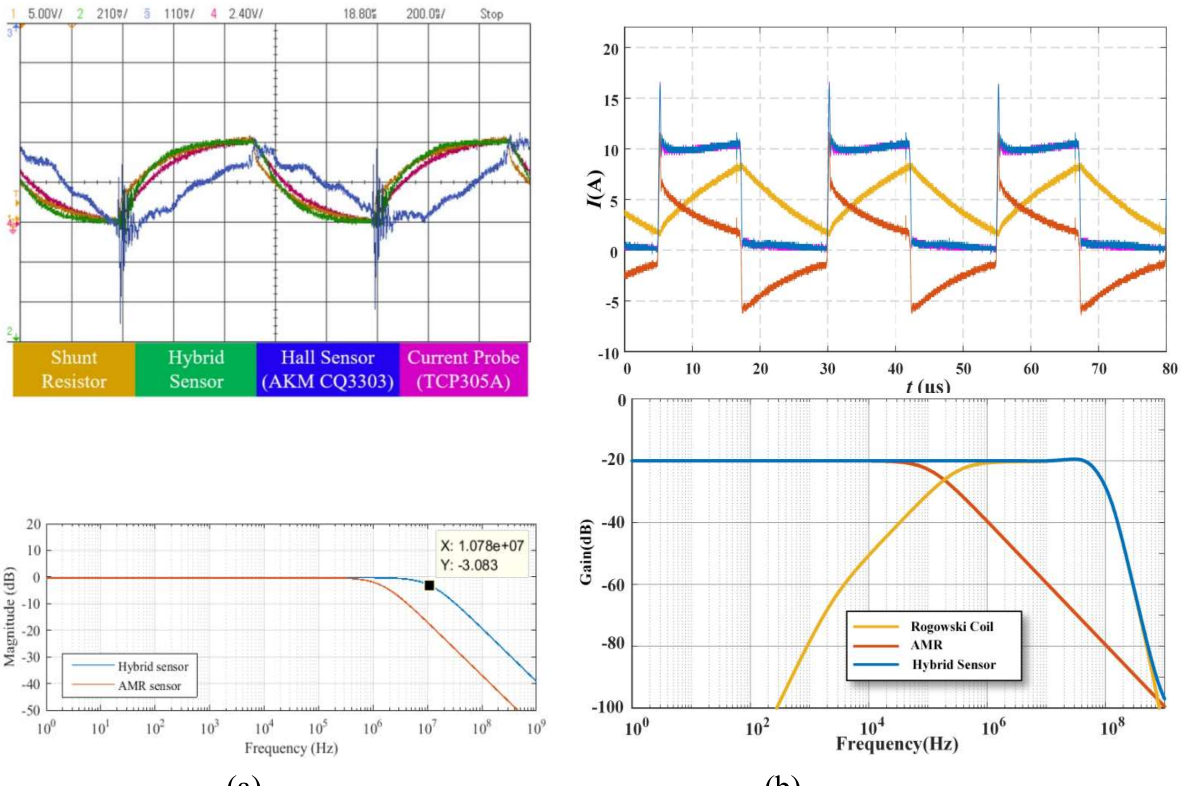

(a) (b)

Figure 3.14: Different sensor reading waveforms and Bode plots of: a) [3], and b) [115].

subject of switching EMI noise effects on current sensing integration, it was demonstrated in Figure 2.14 that TMRs need to be filtered at a low cutoff frequency to minimize EMI interference. Therefore, the 10 kHz TMR cutoff band should be more effective in reducing EMI interference than the 40 kHz TMR cutoff band. This might be the reason why one MS sensor is experiencing more EMI interference than the other.

Figure 3.14 illustrates examples of DC/LF detection using AMR in which the testing condition, current type, and sensor topology are not exactly the same. The current type is the inductor current in Figure 3.14(a), but it is not as clean as the measured switch-current in Figure 3.14(b), since inductor currents are easier to measure than switch-current types (In fact, Figure 3.14(a) deals with a much higher switching frequency than 3.14(b), still inductor current can be measured cleaner). Their design and testing conditions differ greatly, but it is apparent from their Bode plots that the sensor in [3] uses AMR up to its maximum frequency band without lowpass filtering, whereas the sensor in [115] cuts off

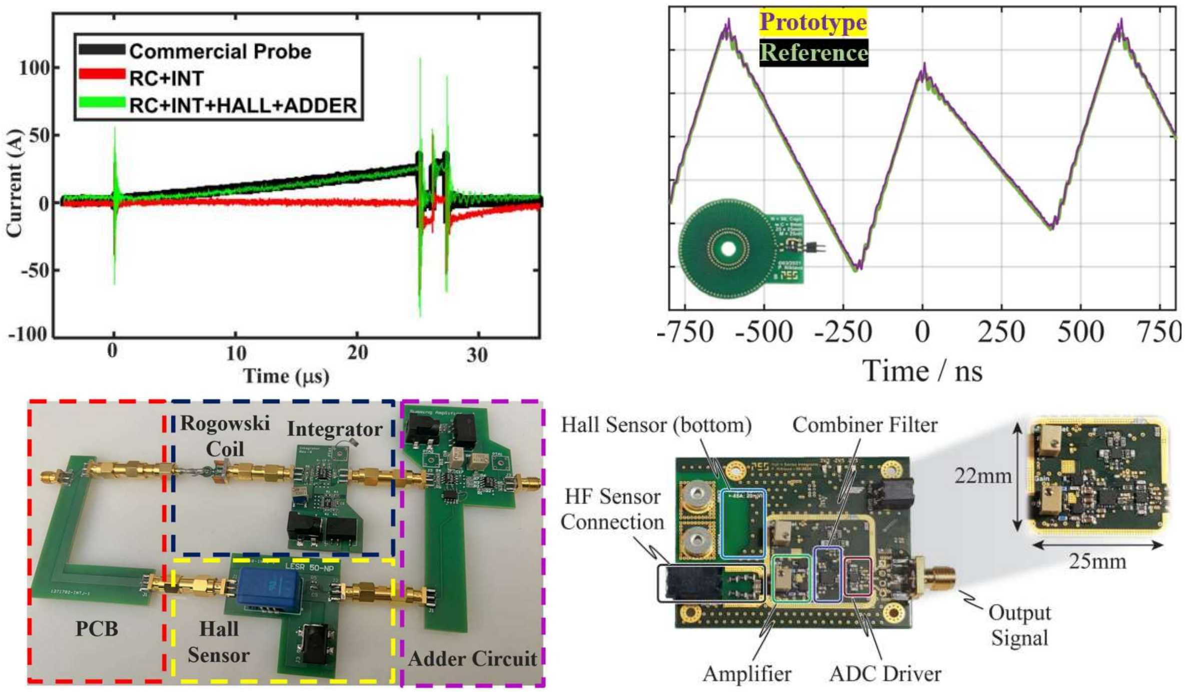

(a) (b)

Figure 3.15: Different sensor results with different layouts: a) [114], and b) [103].

the AMR output at 100 kHz. In a similar manner to TMR examples, excessive noise may be caused by the cutoff frequency of the AMR, due to the design choice to minimize AMR output noise. There is also the possibility that the current sensor is more sensitive to external noise sources, in particular, the layout of the MS may play a role in this regard.

The layout designs of [3] and [115] are not further described, but the examples in Figure 3.15 would provide some insight into that as well. Careful evaluation and selection of layout designs can help to minimize coupled EMI from external noise sources, allowing for better MS sensing performance. Additionally, noise-canceling techniques and materials can help reduce the sensing system's inaccuracies. The example in Figure 3.15 illustrates how shorter sensing traces combined with an optimal sensing PCB layout can produce much cleaner outputs. This helps to reduce the amount of interference that can impact the accuracy of the sensing system. Shielding can also be used to protect the sensing system from external noise sources. The overall performance of the system can be improved by taking the time to properly design the sensing layout, selecting the appropriate electronics, bringing down the cutoff frequency, and utilizing noise-canceling techniques.

Generally, MS systems are the preferred choice for high-frequency applications. For example, the same sensor used in [3], [117] is applied in [125], in which the MS current sensor measures the decoupling capacitor current and infers an excessive fast current as a short circuit problem. This way, the MS system (consisting of RC + AMR) can detect faults faster than the single AMR sensing system. This feature is particularly useful in time-critical applications. Also, a review of all presented MS current sensors in this section is provided in the conclusion of this chapter.

3.3 Multi-path Enhanced Current Sensor Topology

Depending on the application, a sensing arrangement can range from simple current sensors to advanced MS systems. It may be possible to solve issues with SS current sensing methods by choosing and integrating compounds in a complementary manner since no existing SS current sensor has been proven to satisfy all the factors required for an optimal power converter. By reviewing the feasible combinations and their pros and cons in the last section, we were able to arrive at a better solution and develop design guidelines for MS sensors as a result of this critical review. Although there were some combinations such as arrays of magnetometers for busbar differential readings, most MS current sensors are built upon BW compensation of SS methods, as no non-invasive SS current sensor has sufficient BW, whether possessing high BW in magnetometers or reading DC in inductive-based sensors. Figures 3.2-15 provide good insight into sensor selection based on BW, size, noise immunity, etc., which can be utilized here for general guidelines regarding the design and manufacture of MS current sensors.

The sensor must be able to measure a wide range of currents reliably, accurately, and quickly. It also needs to be relatively small and low cost to ensure the overall design is effective and cost-efficient. Good quality sensors are essential for any successful design. This section will provide sufficient information regarding signal circuitry, dimensions, and geometry, as well as SS sensor selection. The information should be used to ensure the best sensor design and guarantee the design is reliable and cost-effective as well as if the sensor is able to measure a range of currents accurately and quickly and meets the requirements of the design.

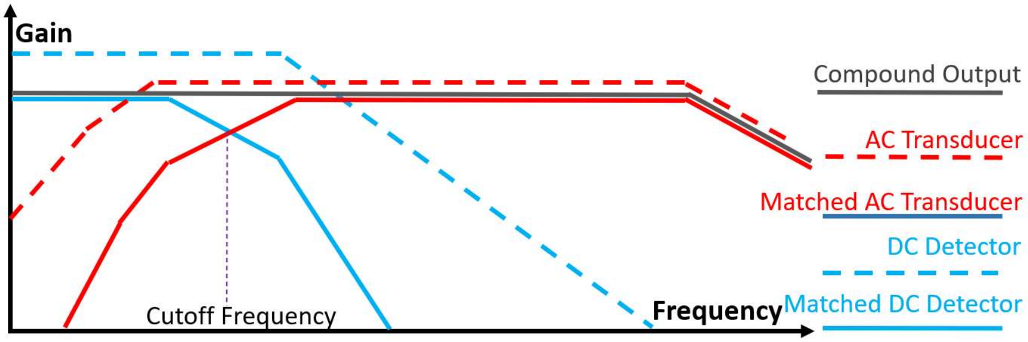

Figure 3.16: Optimal bandwidth matching in a hybrid current sensing combination.

3.3.1 Signal Mapping and Circuitry

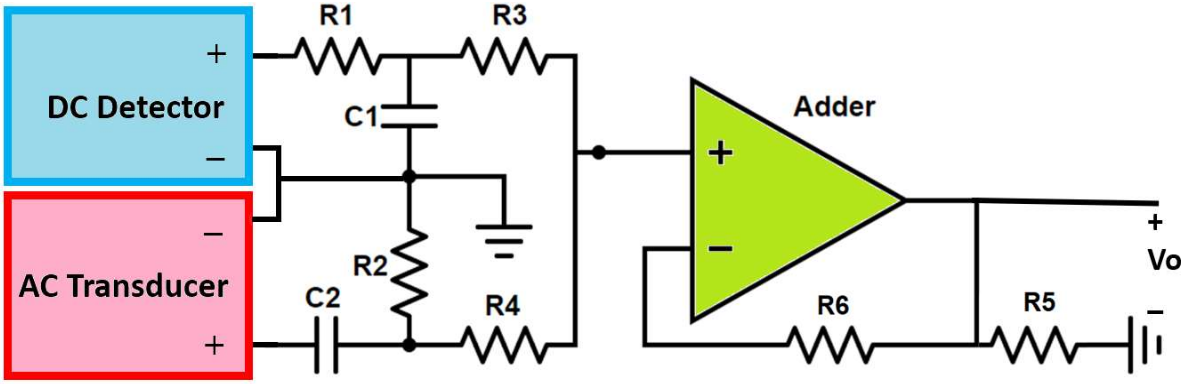

Figure 3.17: Gain/frequency matching circuitry using active adder and passive filters.

Since SS current sensors do not meet all of the necessary criteria for a power converter to operate optimally, complementary combinations of SS current sensors may be able to overcome the challenges associated with SS current sensing. The majority of MS current sensors have been constructed using BW compensation of SS methods in the absence of a noninvasive SS current sensor with sufficient BW. As part of our methodology, the BW extension is once again the basis of the combination, with an emphasis on optimizing the size and quality of the sensor's output signal. Figure 3.7 presents a more practical approach of dual current sensor compounds compared to Figure 3.2. For maximum flexibility when selecting the cut-off frequency, both SS sensors should have the same gain and phase in their own BW, and their BWs should overlap for at least a decade. Compared to Figure 3.7, Figure 3.16 shows an overall picture of BW matching in which two SS sensors have two different gains while they share a band of frequencies. The Bode plot in Figure 3.16 can only be obtained using tools that match gain/phase versus frequency, and Figure 3.17 illustrates an excellent example of such a tool that can match gain and cutoff frequencies. A low-pass filter is constructed by R_1 and C_1 for the DC/LF detector and a high-pass filter is constructed by R_2 and C_2 for the HF SS sensor. A cutoff frequency should be set for both filters at the same frequency, which means that the resistors and capacitors can also have the same value. The noninverting adders' resistors R_3 and R_4 can be adjusted if there is a gain mismatch. Moreover, R_5 and R_6 can also be used to match the output gain, particularly the final gain. This relationship between filtered outputs of LF and HF in an opamp network can be found in (3.1):

$$Vo = \frac{R5 + R6}{R5(R3 + R4)}\left(\frac{Vhf.R3 + Vlf.R4}{R3.R4}\right) \qquad (3.1)$$

Where V_{hf} represents the filtered output of the HF sensor and V_{lf} represents the filtered output of the LF sensor. Moreover, it is obvious that equation (3.1) can be simplified into equation (3.2) when $R_{3\text{-}6}$ are equal:

$$Vo = Vlf + Vhf \qquad (3.2)$$

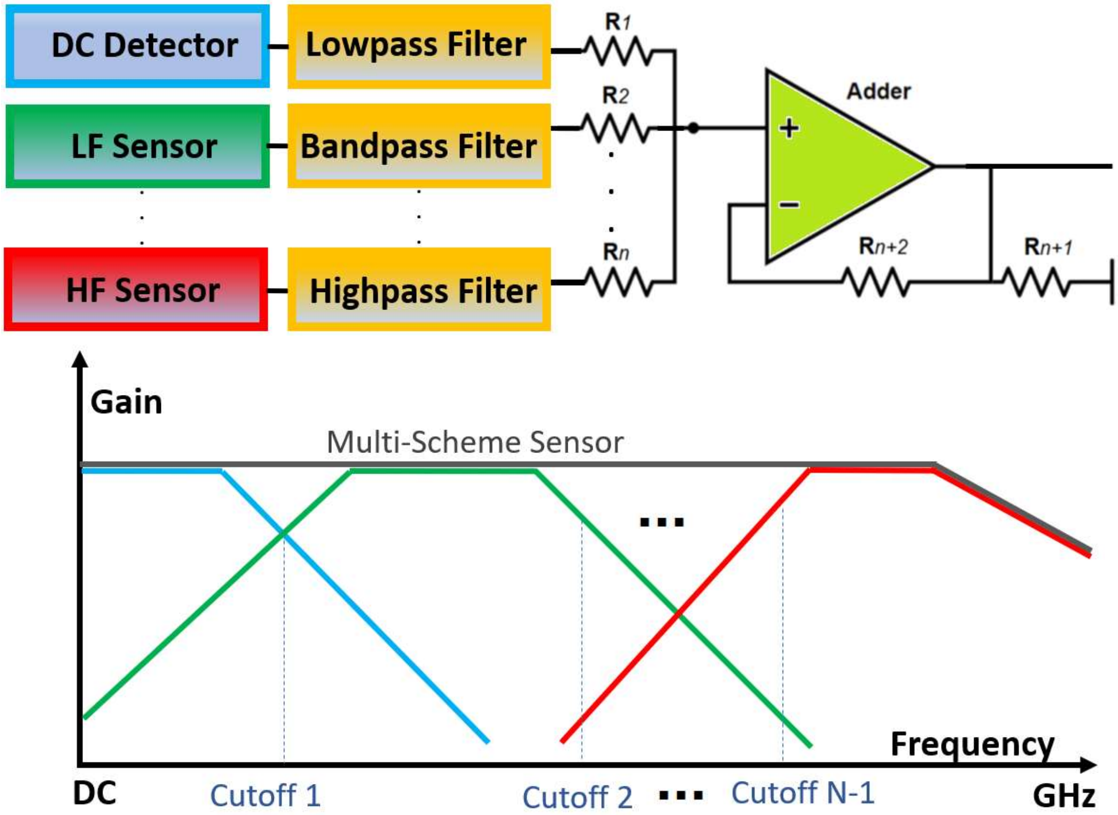

Figure 3.18: General matching circuitry using active adder and passive filters for multi-scheme sensors.

Also, equal adder resistors can be used if both sensors have the same gain in the same frequency band. Up to now, it has been mostly about dual-scheme current sensors whose BW was extended using a complementary SS sensor BW. However, there may be a large number of sensors that can be combined based on BW extension. Detailed block diagram and gain-frequency plot of such a system can be seen in Figure 3.18. An extended version of equation (3.1) can be seen as (3.3) for the circuit in Figure 3.18:

$$Vo = \frac{R(n+1) + R(n+2)}{R(n+1)(R1 + R2 + \cdots + Rn)}\left(\frac{V1}{R1} + \frac{V2}{R2} + \cdots + \frac{Vn}{Rn}\right) \tag{3.3}$$

in which V_1 through V_n are the filtered output of Sensor 1 to N.

3.3.2 Geometry

Designing an optimal layout for MS current sensors requires consideration of the geometry and dimensions of the final assembly, among the most significant concerns along with the BW of the MS sensor. There are even smaller sensors required for different applications in WBG converters, whose dimensions must match within the converter. The disadvantage of altering power traces also makes non-invasive current sensors preferable. The allowed space for installing different sizes/geometries of sensors may vary depending on the size of the converter, the specific node/branch, and the type of current. Specifically, line and input/output currents of power converters do not limit the dimensions of the current sensors in the same way that switch-current sensing space is limited. The reason for this is because current sensors can be assigned a large amount of space within the converter's input and output cables, whereas the optimal layout of the traces within the converter, especially in HF WBG power converters, limits the amount of space and geometry available to measure the current of any switch, inductor, or capacitor inside the converter. Such problems can be solved by some integration method, such as embedding a current sensor into the converter PCB for switch-current measurement. Consequently, the current can be measured more accurately, and the power layout of the converter can be optimized, thus reducing its cost and size. In power electronics, switch-current is without a doubt the most difficult type of current to measure due to its constrained measurement size and geometry, excessive EMI radiation/coupling, and required ultrawide BW. Other than

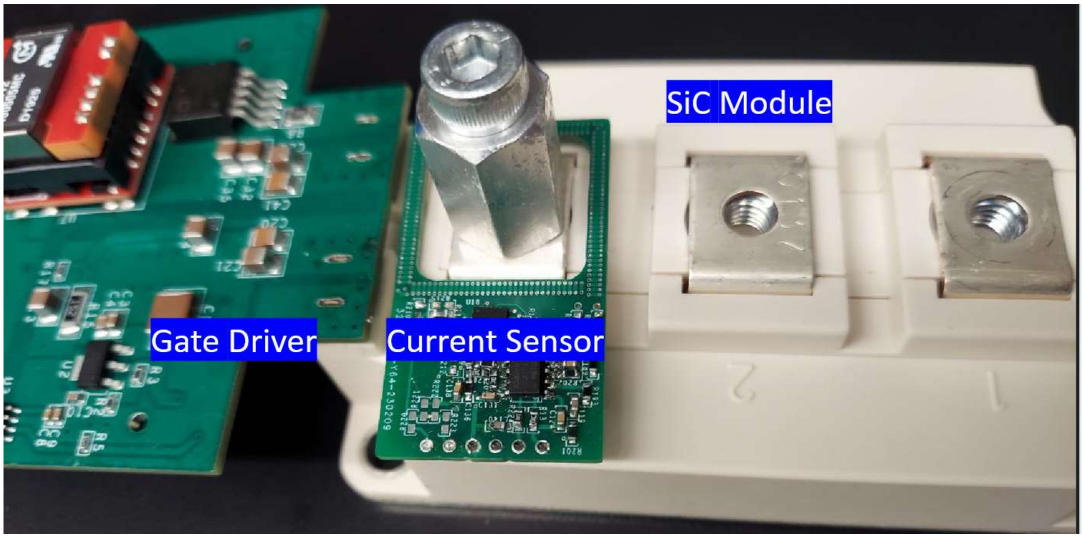

(a)

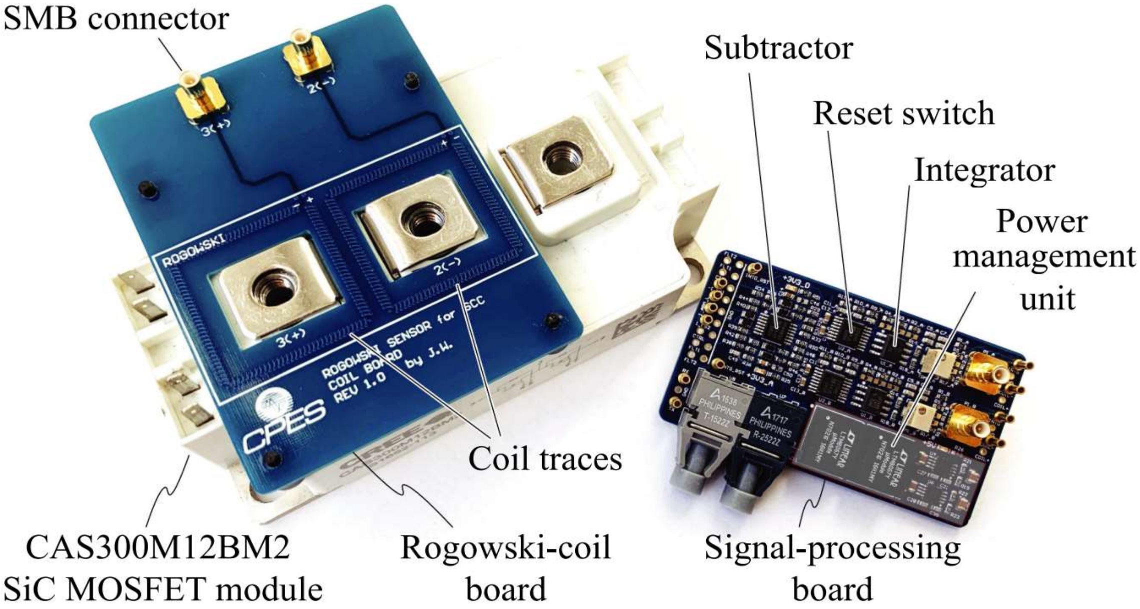

(b)

Figure 3.19: A light-size switch-current sensor design for a SiC module (FF3MR12KM1HOSA1 [126, 204] (a), and the gate-driver-embedded switch-current sensors [68] (b).

BW optimization and EMI reduction techniques, the size of MS current sensors have been extensively discussed previously. Current sensors for the measurement of the current at internal nodes (switches, capacitors, etc.) should have a light size and compatible geometry. In this section, examples of the best size and geometry options for these sensors are provided. In Figures 3.9(c) and 3.10(d), you can see examples of MS sensors designed for high-current power modules. A coaxial housing such as that shown in Figure 3.9(c) is an appropriate choice for mounting the sensor on an IGBT module. In Figure 3.10(d), the square shape of the coil and its light height make it suitable for mounting on a high-power SiC module. A similar approach is depicted in Figure 3.19(a), in which our custom-designed current sensor is intended to be used as a switch-current sensor for an Infineon SiC module (FF3MR12KM1HOSA1) [126]. As shown in Figure 3.19(b), they have integrated two switch-current sensors for ease of integration into a single PCB. Pick-up coils and any other small PCB-embedded coil are favorable for smaller semiconductors. Figure 3.20 illustrates more geometry to consider for the design of the most suitable MS sensors. In Figures 3.20(d-f), for example, MRs are used non-invasively close to semiconductor devices. A good example of stacked current sensors and stacked IGBT chips can be seen in Figure 3.20(b). Figure 3.20(c) is a lateral GaN version of the SiC Mosfet in Figure 3.20(a) using pick-up RC coils as the switch current sensor. Clearly, the coil is embedded using a limited amount of internal layer space, which can result in a significant improvement in contactless current sensing for tight-layout lateral GaN power switches.

In summary, stacked or PCB-embedded solutions that do not add a significant amount of height or bulk to the converter layout should be preferred. Since people usually use a DC/LF detector in conjunction with a coil-based current sensing scheme in MS sensors, contactless magnetometer ICs (such as MRs or micro-FG) are an excellent choice due to their ease of PCB mounting and desirable output quality. For higher frequencies, PCB or coreless coils are an appropriate choice, in which the coil's number of turns should be optimized to reduce the size and maintain accuracy. Furthermore, the coil should

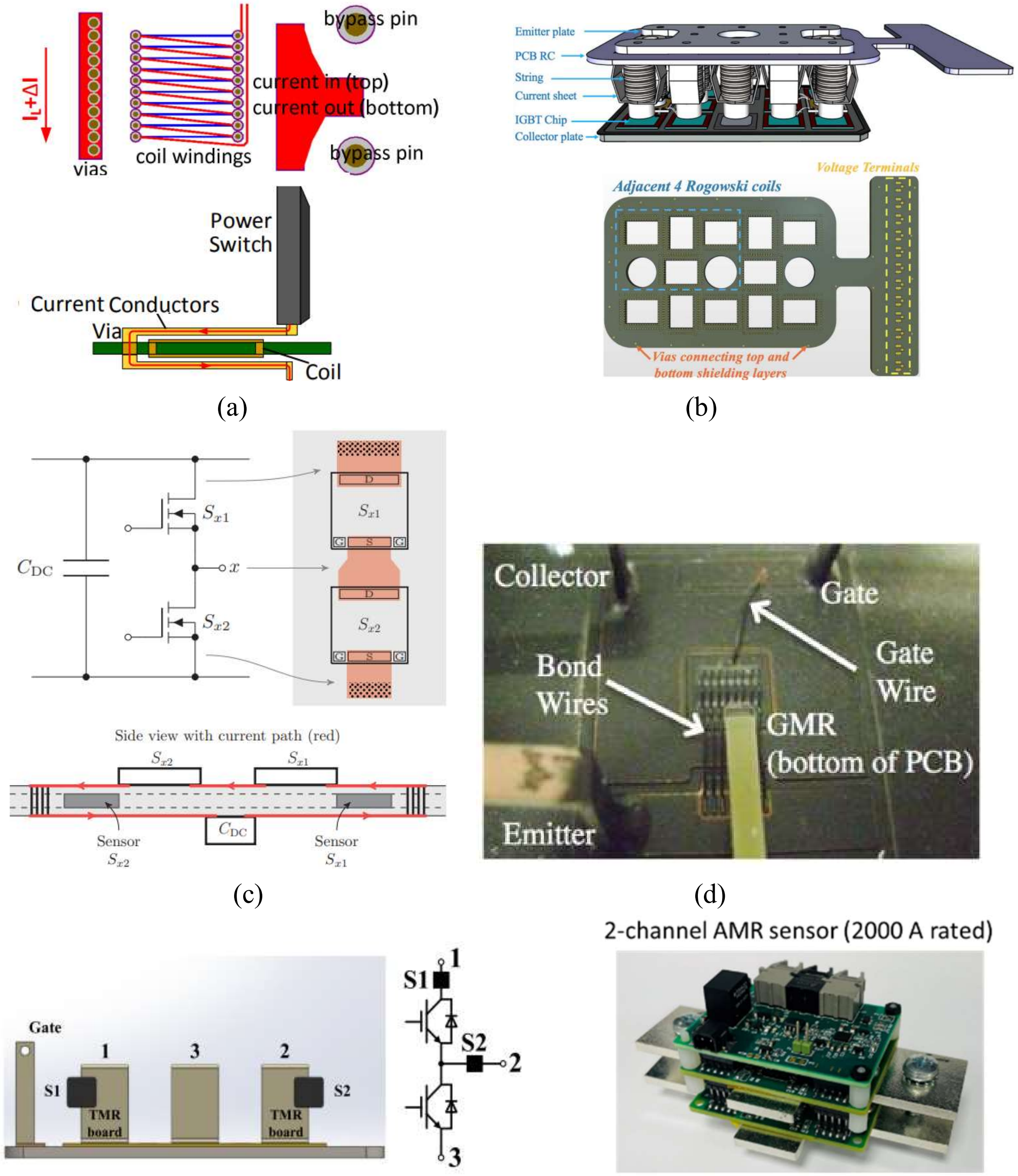

(a) (b)

(c) (d)

(e) (f)

Figure 3.20: More geometry examples of embedded current sensors: a) [127], b) [128], c) [129], d) [130], e) [35], and f) [131].

provide a low-impedance path for measuring the current, and its design should consider the strength of the magnetic field and its intended performance. If space allows, such as in power modules or vertical power switches, relative-size toroidal/square PCB-embedded coils can be implemented, which is not the case for most GaN switches, due to their lateral geometry. The use of a pick-up coil or surface coil is much more suitable for lateral GaN readings as well as on-trace DC capacitor or inductor current measurements.

3.3.3 DC and Low-Frequency Magnetometer Selection

According to Figures 3.16-18, a reliable DC/LF detector is always required in such schemes. A power electronics integration application requires a DC detector that is contactless (non-invasive), accurate, and EMI-immune, in addition to being of reasonable size, power consumption, and cost. Thus, there is a need for a suitable and robust DC detector that can meet all the requirements of a power electronics integration application. Such a detector should be able to detect both LF and DC current accurately and with minimal interference. To see what our options are for different SS techniques, one can refer to chapter II. As a recap, there are three facts: 1) inductive-based current sensors cannot detect DC current in any condition [24], 2) the MO current sensing scheme is too large, too expensive, and too complex for power electronics integration [25], and 3) resistive SS current sensors cannot provide thermal invariance, isolation, and contactless measurement [23-26]. HE, MR, and FG magnetometers are the only remaining types of current sensors. These sensors are able to measure the flux density (B) around their sensing system, and we can convert the flux density into electrical current by utilizing formula (2.1). In addition to their DC measurement capability, ease of application, low cost, and good isolation, magnetic field detectors are advantageous as current sensors. It is usually the case that these sensors are susceptible to EMI noise and interference with external magnetic fields (particularly when using metal plates as sensing receivers), and they have a limited BW (which can be compensated for in an MS sensor topology) that may be sacrificed (or cancelled) when integrated into power electronics. This can lead to reduced accuracy in the sensor readings and may result in incorrect system operation. In order to mitigate these issues, the sensors can be placed in an environment that is EMI-shielded and has a low external magnetic field. Additionally, the sensor should be calibrated regularly to ensure accuracy. Among them, HE has the lowest accuracy of all the remaining options, which makes most of its integrated products invasive, given their extremely weak sensitivity to small magnetic fields and currents. Even though people have successfully integrated invasive HE ICs to cleanly (with the proper sensor PCB layout [132]) read DC currents, HE is not ideal for HF devices due to its invasiveness, inaccuracy, and EMI proneness.

MRs have been discussed extensively, including several successful combinations that have been established using AMR, TMR, and GMR. Since MRs are more accurate, smaller, consume less power, are more affordable (not always), and have a higher BW than HE, and also because of their superior accuracy, they can read currents non-invasively. In some instances, they have been shown to be prone to EMI; however, lowering their lowpass filter cutoff frequency may help to overcome that potential issue.

FG magnetometers are typically considered to be the most accurate sensors among all the different magnetic field detectors available today [25, 46]. Big FG probes or sensors often have many issues, such as huge size or bulk, extremely high cost, or excessive power consumption [25]. With the advent of FG ICs, these issues have been overcome [34]. The DRV425 from Texas Instruments is one of the latest on-chip FG sensors available on the market with reasonable size, accuracy, price, and linearity [61]. In Figures 2.14-15, it is evident that micro-FGs can be much more noise-immune and accurate than TMRs, in that they do not require a very low cutoff frequency as TMRs do, which will be proven further in section 5.3.

3.3.4 High-Frequency Transducers for Broadband Extension

As a quick flashback to SS current sensors, the only non-invasive method that can achieve very high sensing frequencies is inductive-based method. Ohmic sensors cannot be used due to their invasiveness and also, MO and magnetometers cannot achieve a very high frequency (MRs may achieve a few MHz (which is still not so high), but they can also

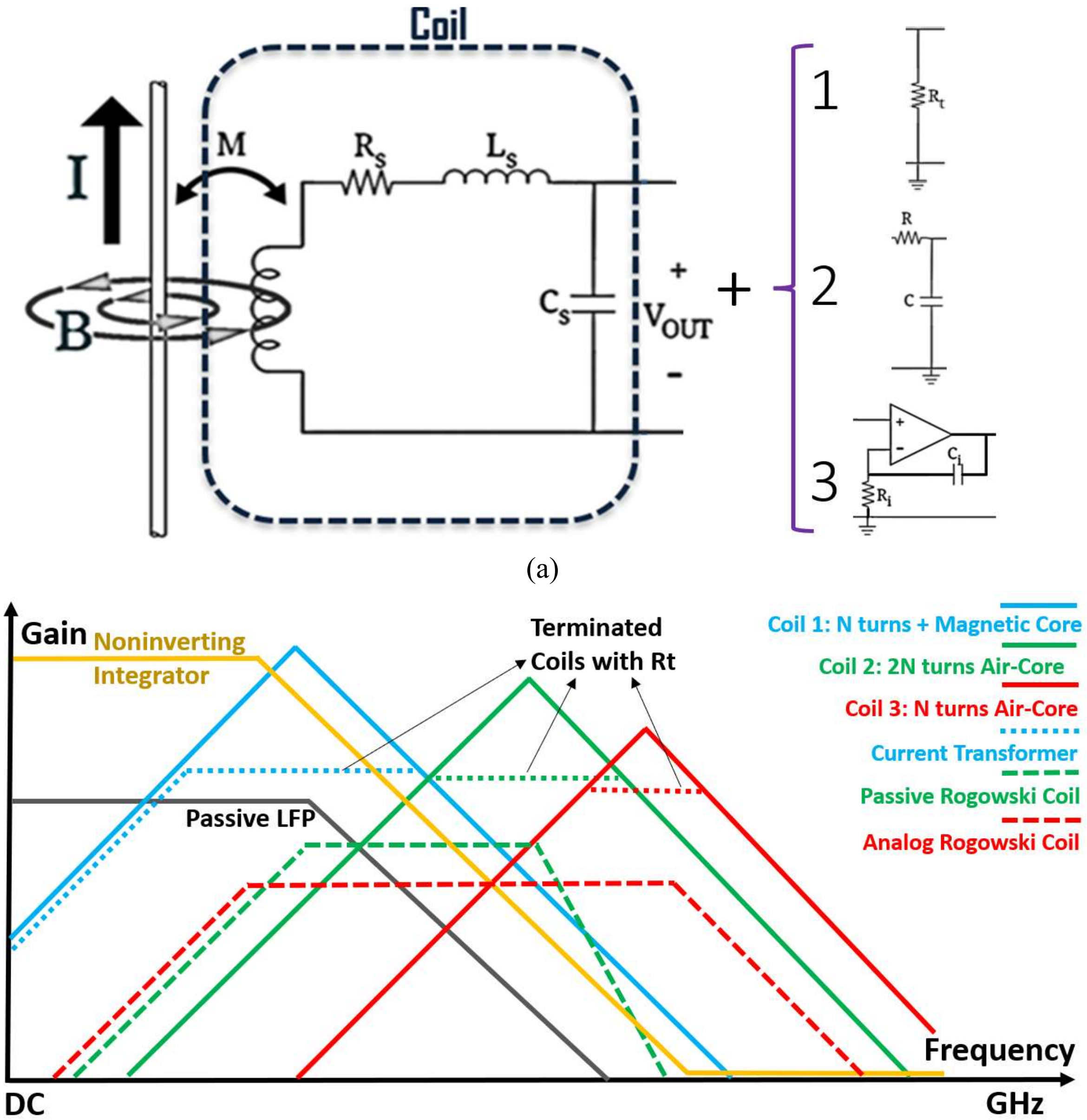

(a)

(b)

Figure 3.21: Different coil realizations as a current sensor (a), and their gain-frequency Bode plot (b).

have EMI issues if used for higher frequency currents [23-26]. In contrast, inductive-based sensors can reach frequencies up to several hundred MHz, and are non-invasive, making them a great choice for high-frequency current sensing [32, 33].

To use a coil as a current sensor, the output signal of the coil needs some signal processing either passively or actively (Figure 3.21(a)). It is possible to force the coil output to operate according to CT principles by terminating it with a single passive resistor [32]. A magnetic core is required in order to provide much higher mutual inductance to work at lower frequencies since air-core coils do not possess a significant mutual inductance. Figure 3.21(b) illustrate this with details as in the blue plot. However, it has been asserted previously that core-based current sensors can occupy a large space which is not ideal for new power electronics.

There is another way of coil passive compensation for current sensing, in which the rising slope of the coil before the coil's natural resonant frequency will be cancelled with the falling slope of an RC low-pass filter at its output. Technically, most sensors based on Hoka probe deploy this compensation method. Likewise, since air-core coils have a low mutual inductance, the sensor starting band might not achieve frequencies below 10~50 kHz [94-96]. In this case, there will be a problem using DC magnetometers in MS topology, since they must use a lower cutoff frequency to minimize EMI effects. Figure 3.21(b) illustrates this by intersecting the gray line (passive LPF) with the green coil plot.

PCB-embedded RC coupled with active electronics circuitry (which is a noninverting opamp-based integrator in Figure 3.21) may be a better solution than the last two compensation methods, since opamp integrators can provide a higher gain for RC beginning at much lower frequencies than the passive integrator (LPF). By providing a BW at lower frequencies, DC/LF detectors can also be cutoff at lower frequencies, while maintaining a light size and ease of integration. This makes PCB-embedded RC coupled with active electronics circuitry a more viable option for MS topology. It also has the potential to reduce the size of the circuit, as well as integration complexity. The design and performance of PCB-embedded RC coupled with active electronics circuitry can be further enhanced to achieve higher levels of accuracy and reliability, which can enable the development of highly efficient current sensing systems, with wider frequency ranges and improved performance. A full discussion of PCB-embedded RC for ultra-wideband current sensing within WBG power converters will be presented in Chapter 4.

3.4 Conclusion

An MS configuration can offer a more flexible solution than an SS sensing system since different SS methods can be used to achieve the desired performance for any given application, resulting in a more customized solution than an SS sensing system. Accordingly, a sensing arrangement must be selected based on the application's specific requirements. Especially in high-frequency applications, a single sensing method may not provide the necessary BW. To take advantage of the higher BW of MS systems, multiple SS sensing methods can be combined, providing a more comprehensive sensing solution. MS systems are therefore the preferred choice for high-frequency applications.

he MS system can also detect smaller current changes than the SS system, allowing for superior precision. Table III presents an overview of MS sensors, which includes a brief discussion of their BW, invasiveness, size, EMI immunity, and their possible applications. The table helps to compare and contrast the various MS sensors and provides useful insights into the design of new MS systems. Furthermore, the information in the table can be used to identify the most suitable MS sensors for specific applications. The table also helps to identify potential limitations of MS sensors, such as size, BW, and invasiveness, allowing for the design of more efficient and effective MS systems. Additionally, Table 3.1 provides useful information to researchers and engineers in selecting the most suitable MS sensors for their applications. As a result of the literature review, all the optimal aspects of the configuration of MS current sensors were covered in detail, including gain and frequency matching circuitry, BW extension schemes, ideal geometries, and dimensions, as well as the selection of SS current sensors.

Table 3.1: A literature review on properties of existing hybrid current sensor/probes.

Reference	**Technique**	**Achieved Bandwidth**	**Isolated/ Invasive**	**Size**	**EMI Immunity**	**Sensing Range**	**(Possible) Application(s)**
[83, 84]	HE + CT	-	Yes/No	Big	Fair	-	Control
[56]	HE + CT	DC-38MHz	Yes/No	Big	Good	± 40A	Monitoring/Control
[85]	HE + CT	DC-300kHz	Yes/No	Big	Good	-	Control
[86]	HE + CT	DC-5MHz	Yes/Yes	Fair	Fair	± 20A	Characterization
[31]	HE + CT	DC-30MHz	Yes/No	Big	Excellent	± 40A	Monitoring/Control
[87]	HE + CT	DC-20MHz	Yes/No	Big	Good	± 50A	Control
[88]	HE + CT	DC-35MHz	Yes/Yes	Fair	Good	-	Control
[89]	HE + CT	DC-50MHz	Yes/No	Big	Good	± 100A	Monitoring/Control
[90, 91]	HE + RC	DC-MHz	Yes/No	Fair	Good	± 200A	Control/Protection
[92. 93]	GMR + RC	DC-10MHz	Yes/No	Fair	Good	± 800A	Protection
[94]	TMR + RC	DC-50MHz	Yes/Yes	Big	Good	-	Monitoring
[95]	TMR + RC	DC-250MHz	Yes/Yes	Big	Good	± 100A	Monitoring
[96]	TMR + RC	DC-315MHz	Yes/Yes	Big	Good	± 100A	Characterization
[97]	TMR + RC	DC-240MHz	Yes/Yes	Big	Good	± 1200A	Characterization
[3,117,125]	AMR + RC	DC-10MHz	Yes/No	Fair	Fair	± 50A	Protection/Monitoring
[98]	HE + RC	DC-1.8MHz	Yes/Yes	IC	Low	± 25A	Integrated Control
[99]	HE + RC	DC-3MHz	Yes/No	IC	Fair	-	Integrated Control
[100]	HE + RC	DC-5MHz	Yes/Yes	IC	Low	± 51A	Integrated Control
[101]	HE + RC	DC-15.3MHz	Yes/Yes	IC	Low	± 60A	Integrated Control
[102]	HE + RC	DC-75MHz	Yes/Yes	IC	Low	± 50A	Integrated Control/Protection
[103]	HE + RC	DC-100MHz	Yes/Yes	Fair	Good	-	Monitoring/Control
[104]	Shunt + RC	DC-1MHz	Yes/Yes	Big	Low	± 1000A	Protection
[105]	Shunt + CT	DC-1MHz	Yes/Yes	Big	Good	-	Control
[32]	LFCT+HFCT	10Hz-10MHz	Yes/No	Big	Excellent	± 100A	Characterization/Monitoring
[106-109]	MO + CT	DC-kHz	Yes/No	Big	Excellent	± kA	Line Protection
[110]	MicroFG+CT	DC-100kHz	Yes/No	Fair	Excellent	±10A	Characterization/Control
[111,112]	MO + RC	DC-kHz	Yes/No	Fair	Excellent	±30kA	Protection/Monitoring
[113]	FG + RC	DC-33kHz	Yes/No	Light	Good	-	Control/Protection
[114]	HE + RC	DC-250MHz	Yes/Yes	Fair	Low	>±120A	Protection/Monitoring
[33]	Rec-RC+RC	DC-120 MHz	Yes/No	Light	Excellent	0-500A	Protection/Characterization
[115]	AMR + RC	DC-30MHz	Yes/No	Light	Excellent	± 25A	Characterization/Control
[120]	FET + RC	DC- MHZ	No/Yes	Light	Good	-	Control/Monitoring
[121]	Array of HEs	DC- 2.5 kHz	Yes/No	Fair	Fair	± 200A	Protection/Monitoring
[122]	Array of HE/FG	-	Yes/No	Big	Good	± 2000A	Line Protection
[123]	A pair of TMR	DC-MHz	Yes/No	Fair	Excellent	±0.01-100A	Characterization/Monitoring
[124]	GMRs + Coil	DC-50kHz	Yes/No	Fair	Excellent	±2-300mA	Protection/Monitoring

CHAPTER 4: ULTRA-WIDEBAND PCB-EMBEDDED AC CURRENT SENSORS

4.1 Introduction

Since current is an essential parameter in a power electronic converter, and as mentioned earlier, it can be utilized to control, diagnose, prognosis, and protect circuits and systems, current sensing must undergo significant improvements to keep up with advances in high frequency power electronics. Further, it has been demonstrated that most traditional current sensing techniques cannot be used to monitor currents in modern power converters while maintaining a high level of efficiency and keeping a small footprint. In order to measure current in HF WBG power electronic converters, ultra-wideband current sensing methods are necessary. High frequency applications require these ultra-wideband current sensors to provide accurate and efficient current measurement, while also being small and easy to install, making them ideal for power converters. For example, a planar Rogowski coil is a suitable current sensor for HF WBG power converter applications due to its small size, wide bandwidth, and high accuracy [133]. These current sensors are used to sense current in the high frequency range, from kHz to GHz, as well as low frequencies. In addition, they are capable of measuring high currents in a range of up to hundreds of amps.

4.1.1 Various Types of Current in Power Electronics

For a variety of applications, different topologies of power converters are required to include current monitoring for different device/power traces. These current sensors can be used for a variety of applications such as power management, motor control, and automotive systems. They are also used in applications where current monitoring is essential, such as in medical devices, renewable energy systems, and industrial machinery.

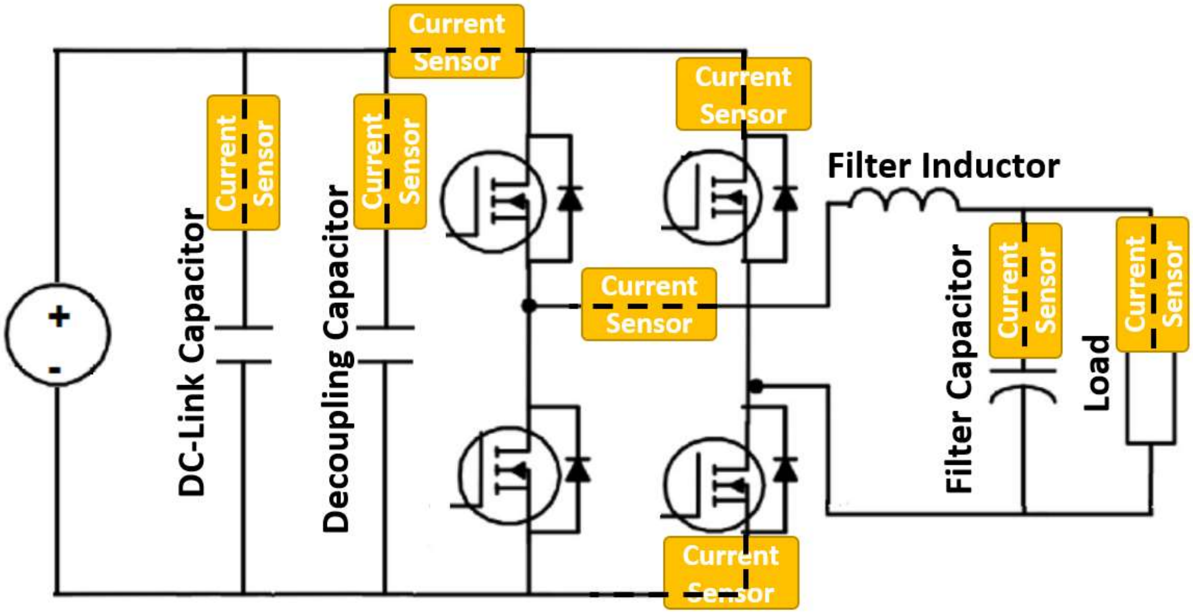

Figure 4.1: A single-phase inverter (H-bridge) equipped with eight different current sensors.

According to Figure 4.1, a single-phase DC to AC converter is shown, with different types of current sensors that can be used to monitor the current flow through its various branches and devices. All capacitors, inductor, H-bridge input, and switch currents can be equipped with current sensors as shown, which can provide a reliable way to detect faults, overloads, and sudden changes in current, allowing for better control of the system and improved safety. Additionally, these sensors also provide feedback for the system's control loops, enabling efficient control of the converter's output.

A simulation of the same circuit using Simulink has been performed and its results are included in Figure 4.2. The first thing one notices about them is that none of them have a DC component other than the switch current. There will be DC values for load, inductor, and leg/H-bridge/half-bridge in DC-DC converters, but capacitor currents will always be AC, due to the fact that capacitors have DC impedances of infinity and therefore cannot pass DC currents. Also, for the load current from Figure 4.2, there would not be any specific middle or high frequency current component. While the inductor current sensor requires a larger BW than the load current sensor, its frequency components are not as high as those of the switch or capacitor current sensor. H-bridge currents are similar to switch currents, with the exception of having a DC value. While DC side capacitors have ultrahigh frequency components, filter capacitors do not need very high BWs. Finally, the ultrahigh frequency part of switch-current is caused by very sharp rising and falling along with HF ringing during those transients. In general, switch-current needs ultra-high BW starting with DC to ultra-high frequency to be detected. This ringing (which is also a sign of EMI radiation level) can be attenuated by increasing decoupling capacitors and lowering

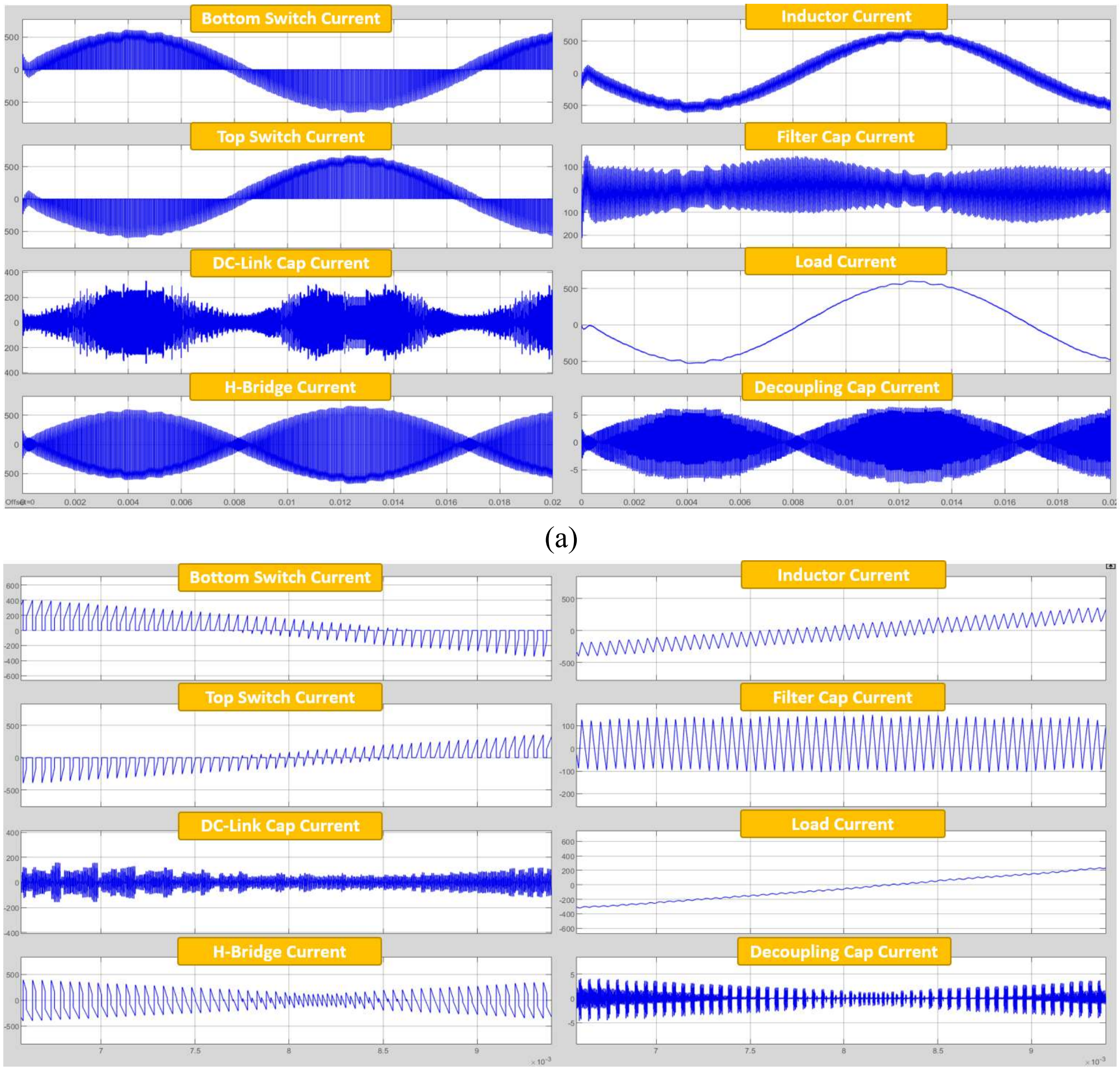

(a)

(b)

Figure 4.2: Different current types in an inverter: Zoom-out (a), Zoom-in(b).

the loop inductance on switch traces. This implies that light-size and non-invasive current sensors should be placed near power switches in order to minimize EMI radiation. Combining all this information, it appears that switch current is the most critical current type to detect, which is why a more detailed discussion of switch current characteristics and sensor selection will be provided in the next section.

4.2 Switch-Current Sensor Requirements

Apparently, among all the different types of currents in a power converter discussed, the switch-current type is the most challenging because 1) it usually requires a very high BW for detection, 2) it can contain significant amounts of EMI radiation and coupling with nearby circuits, and 3) a current sensor is very limited in terms of space and location to be assigned for that purpose. These challenges can be mitigated by careful design of the converter circuit and the current sensing circuitry, as well as by selecting suitable components with high accuracy. Moreover, good PCB layout practices can reduce the amount of EMI radiation and coupling. The switch-current characteristics will be discussed in the following sections, along with attributes of a suitable switch current sensor, in order to explain the application of an ultra-wideband embedded Rogowski coil to many situations requiring the detection of switch currents. It can also be optimized in the coil design and electronic circuitry so that the readings are more accurate, and this can be done while minimizing the system's size and eliminating the need for external leads by matching the required BW of the current waveform.

4.2.1 Characteristics of Switching Current Waveforms

The frequency spectrum of switch-currents ranges from DC to several hundred megahertz, with HF ringing usually occurring at the transient moment due to sudden rises and falls in frequency at the transient moment. The EMI radiation level determines the overshoots and undershoots in the switch-current (which is caused by the loop inductance

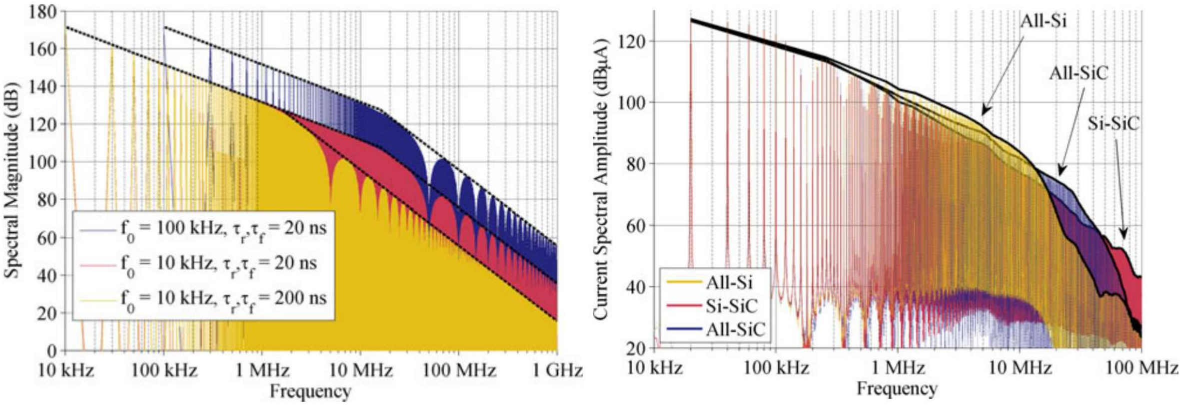

Figure 4.3: Fourier analysis of switching waveforms: Trapezoidal spectrum(a), Current waveforms(b) [134].

at the switch node and the decoupling capacitor path), making the switch-current the most challenging current type to detect. EMI/EMC analysis of switched-mode power converters is often based on idealized waveforms, since switching waveforms closely resemble trapezoidal waveforms [134], which simplifies the analysis, but it is not always accurate. To get more precise results, a more realistic model of the system should be used, which requires considering the actual waveform of the switching current.

According to Fourier analysis, the rise/fall of the trapezoidal waveform is directly related to its high-frequency spectral amplitude, confirming the widely observed correlation between high switching speeds (*dv/dt, di/dt*) and EMI. This result can be used to provide guidelines for high-speed switching systems sensing design. As compared to the

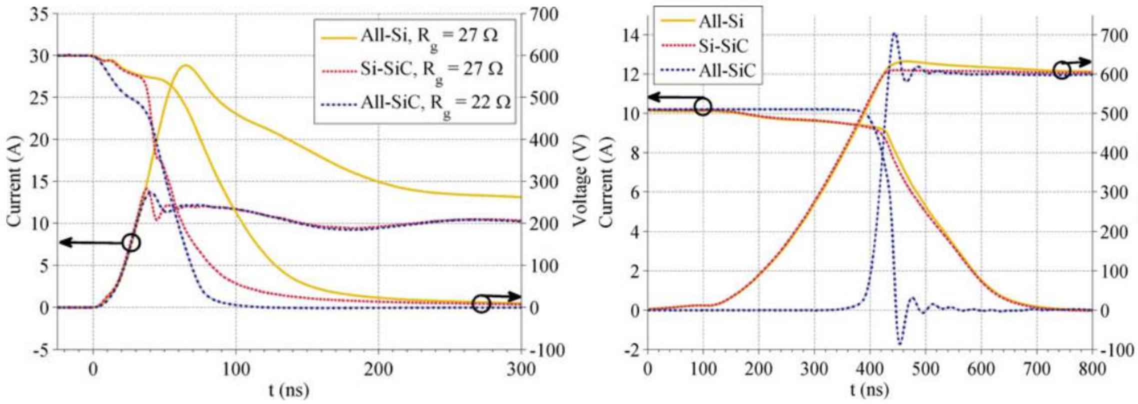

Figure 4.4: Transient moments of switching waveforms: Turn-on(a), Turn-off(b) [134].

other waveforms in the study, Figure 4.3 shows the magnitude spectra and envelopes of three symmetrical trapezoidal waveforms of the same amplitude and duty ratio, with different fundamental frequencies and rise/fall times. These waveforms can be used to measure the performance of the sensing systems under different conditions. This result provides useful insight for designing high-speed switching systems for future applications. Figure 4.4 shows the actual rising and falling moments of semiconductors' waveforms in [134]. Waveform analysis helps to understand the dynamic behavior of the devices under different conditions. This technique can be applied to various types of sensing systems. It can also be used to optimize the performance of the system. For example, by analyzing the waveforms, designers can identify the best operating frequency range and the optimal switching speed to match the requirements of the system.

4.2.2 Suitable Switch-Current Sensors

A high precision/BW, reasonably light, and electrically contactless current sensor is essential to be employed as a switch-current sensor [24]. This sensor should have a high dynamic range and wide frequency response for accurate current sensing. The switch circuit must also have low (or no) parasitic insertion and should also be robust enough to

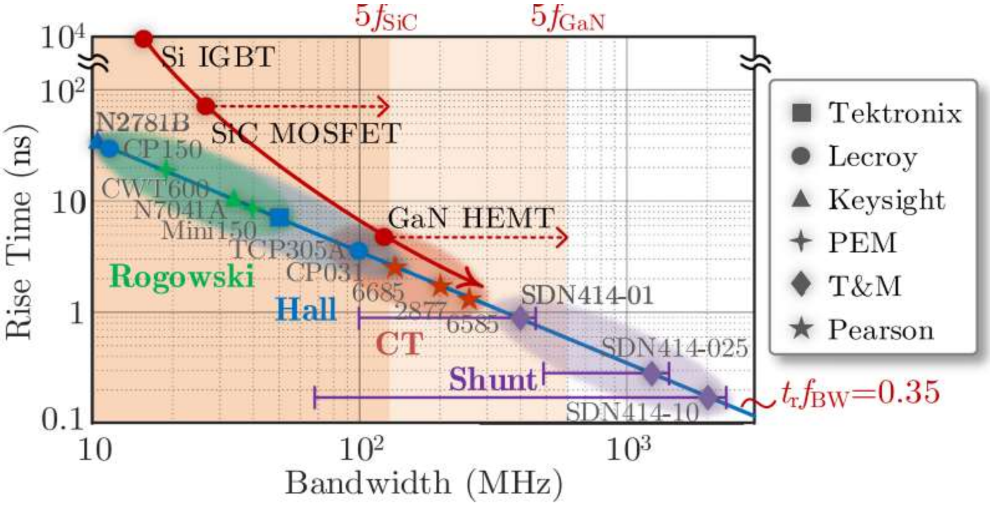

Figure 4.5: Some commercial current sensors for WBG devices [136].

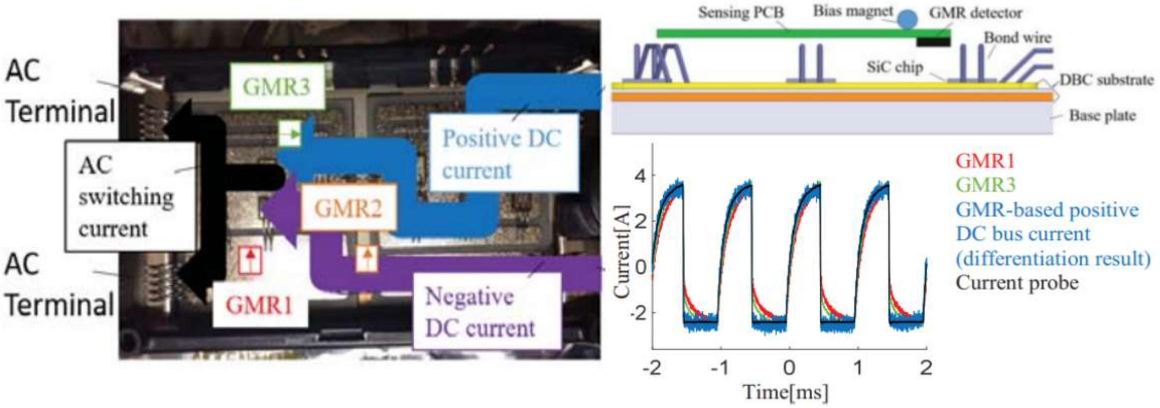

(a)

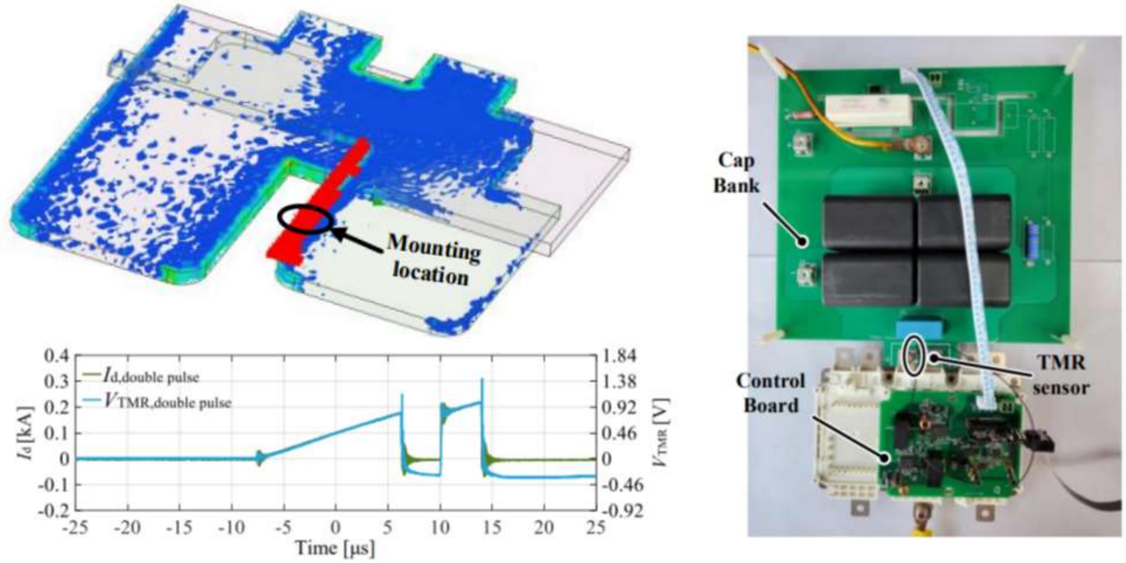

(b)

Figure 4.6: Magnetoresistive sensors for device-level sensing: GMR [137](a), TMR [138](b).

operate in potentially harsh environments. In spite of the high-BW current sensors achieved by coaxial shunt resistors, they have to be inserted into the switch circuit, which, in addition to losses and a need for extra isolation, can also lead to excessive EMI emission due to parasitics inserted in some cases (specifically GaN-based converters) [58, 135], and its height is not suitable for the WBG power electronics industry. Figure 4.5 also demonstrates some commercial current sensing products in general that are suggested for WBG device sensing. It has been unearthed that MR products (GMR [137] and TMR [138]) can also be used as switch current sensors within module packaging (Figure 4.6), where they are likely subject to issues such as offset drift that can reduce their BW below a few MHz.

While RC has the disadvantage of drooping due to the lack of DC and LF components in switch-current, it has been suggested that the PCB-embedded RC current sensor, which can have a BW of over tens of MHz and is noise-immune, can often be used as switch-current sensors by either combining/compensating their outputs or using them as SS sensors for specific applications (such as DPT with short pulses) [139-144]. This allows for high-precision current detection, as RC current sensors have high sensitivity and low loss. Moreover, these RC current sensors can also be used to reduce the size of the entire system, resulting in a more streamlined design. Therefore, these embedded RC sensors can be used for detecting high-frequency current components and can be potentially used in next-generation power modules. As shown in Figure 4.7, some switch-current examples

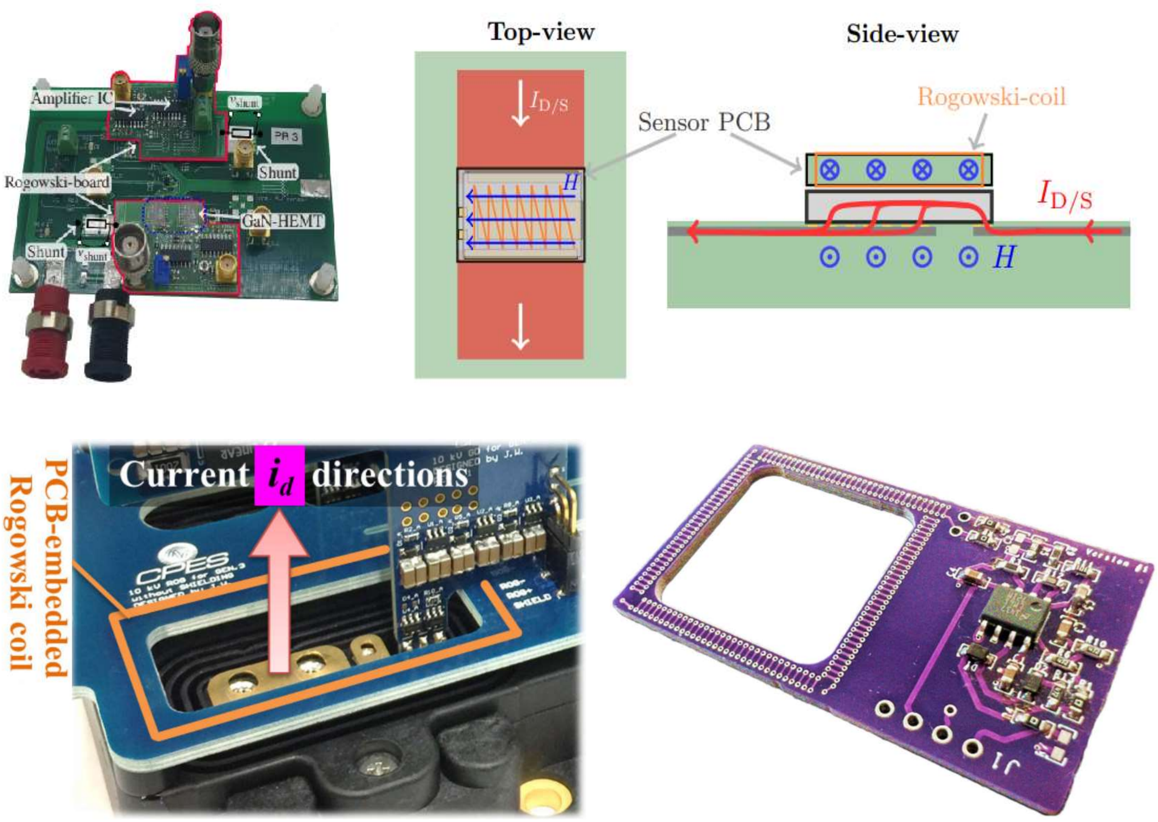

Figure 4.7: Some examples of PCB-embedded Rogowski coil switch-current sensor [141-144].

have been implemented using PCB-embedded RCs for WBG devices. The next step will be to explain in detail the design methodology and compensation methods of PCB-embedded RC switch-current sensors.

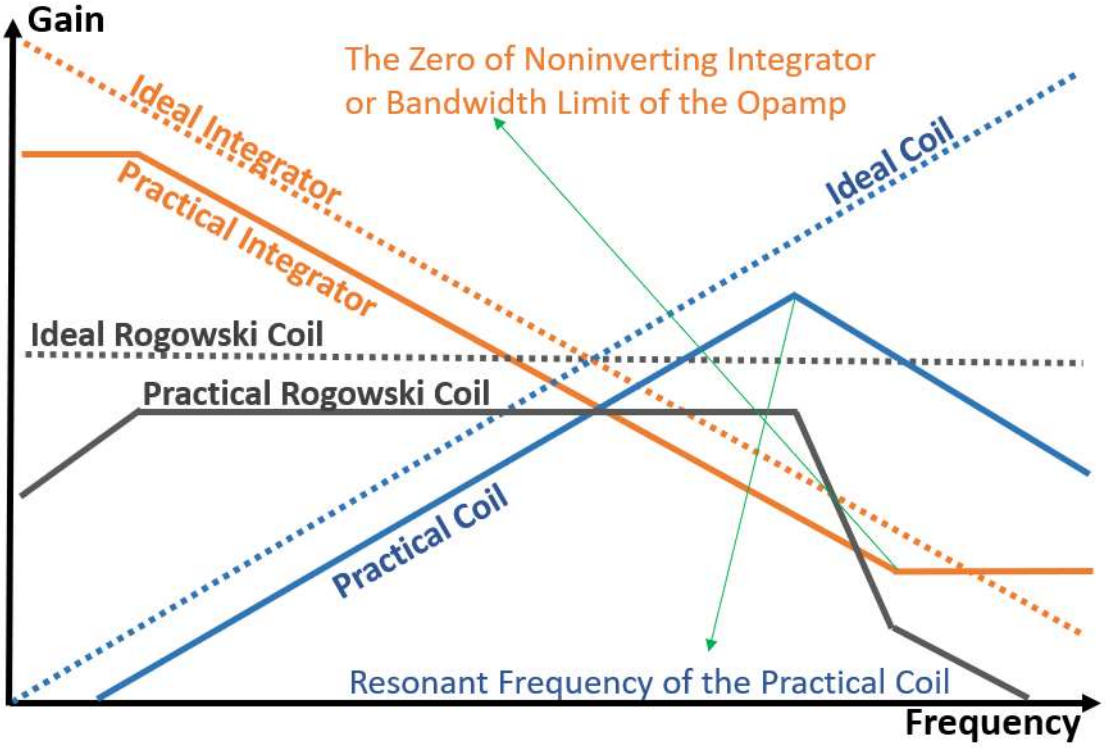

Figure 4.8: Bandwidth constitution of ideal and practical Rogowski coil current censors.

4.3 PCB-Embedded Rogowski Coil

A brief discussion of the working principle of RC current sensors has been provided in sections 2.2.3 (Inductive-Based Sensing Schemes) and 3.3.4 (High-Frequency Transducer Selection). RC manufacturing is feasible with an air or PCB coil added to either a passive (RC LPF) or an active (OPAMP-based) integrator, and among them the electronics RC can be modified easier to achieve better LF gain. When it comes to PCB-embedded RC, the coil needs to be embedded into the PCB of the motherboard/gate driver or the sensor platform PCB, along with its integrator and signal conditioning circuitry. By using PCB-embedded RCs, an advantage of cost-effectiveness and higher integration is

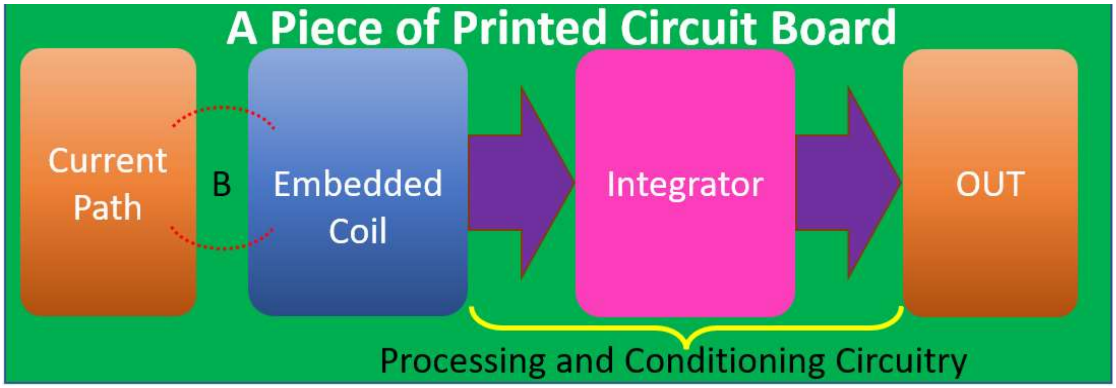

Figure 4.9: Block diagram of contactless PCB-embedded Rogowski current sensor.

achieved, rather than using air coils, in which the coil's physical characteristics and the layout quality of the sensing system determine the accuracy of the performance. As shown in Figure 4.7, the top example uses embedded pick-up coils in a passive RC switch-current topology, whereas the bottom examples use modular (square-shaped) embedded coils with Opamp integrators for monitoring switching currents in power modules. A comparison of the ideal and practical (electronic) RCs in terms of their BW constitution can be seen in Figure 4.8, where the LPF (opamp integrator) non-idealities along with the coil resonant frequency limit the total BW. The trade-off between Opamp integrator BW limitation and flexibility of coil/electronics integration into PCB should be considered carefully while designing the system. Also, the block diagram of a PCB-embedded RC current sensor is depicted in Figure 4.9. An optimized design based on system requirements and restrictions should be adopted. In addition, the PCB design should be carefully considered for reducing the EMI effects on the processing circuitry. It is desirable to have the system with the highest precision and smallest size possible. Physical and mathematical details about the PCB coil design, coil termination, and integrator will be presented next.

4.3.1 PCB-Embedded Coil Design and Manufacturing

According to the Faraday law of induction, variable (AC) currents can induce a voltage at any coil's terminals. The magnitude of the induced voltage is determined by a combination of mutual inductances between the coil and the current carrying conductor as well as the amplitude and frequency of the observed current (see equation 2.2). The induced voltage can be useful in the design of electrical equipment such as transformers, relays, and generators. It can also be used to detect the presence of an AC current in a circuit. In the case that the observed current amplitude and frequency components are kept at the same level, by increasing *M*, the magnitude of the induced voltage can be increased to have better current sensing resolution. Therefore, when designing the coil, the parameters that affect inductance are imperative to optimize (and the detailed formulation for obtaining *M* in different coils will be presented further). This implies that special techniques are necessary for PCB-embedded coil design for RC switch-current sensors since these parameters can be difficult to optimize (for example, the PCB height cannot generally be changed). In the examples of Figure 4.10, one or several layers of PCB can be underutilized to implement the windings for these integrated coils.

In the examples of figure 4.10, one or several layers of PCB can be underutilized to implement the windings for these integrated coils. As shown in Figure 4.10(a), most winding schemes can be implemented with two layers of PCB (top and bottom), with the exception of those that require a return path in the middle of the forward winding path (which will be discussed further below) for differential current sensing. The same could be said for micro windings shown in Figure 4.10(b), where the return path is placed in the middle due to their small size. in Figure 4.10(c), pickup coils that read the magnetic flux in/out of the page direction can be fabricated in a single layer, unless they are meant to measure differentially [pascal] which makes them to need two layers, in which the second layer is needed for electrical connection of the two symmetrical coils (such as the coils on the left side of Figure 4.10(c)). Figure 4.10(c) also demonstrates spiral pick-up coils (the two on the right side) that require at least two layers, with the two layers connected by a via, allowing the induced voltage built up from the first layer to be transferred to the next

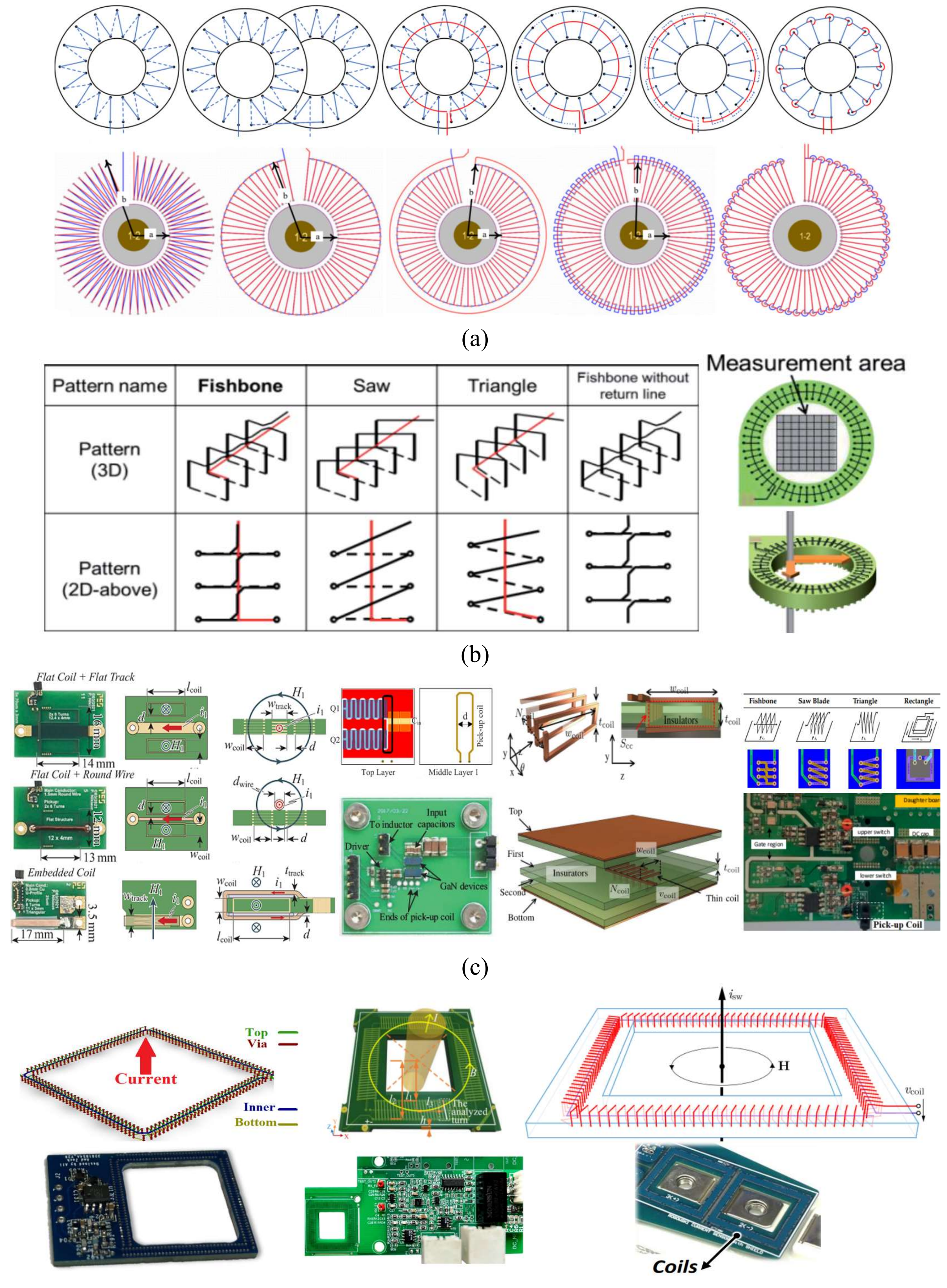

(a)

(b)

(c)

(d)

Figure 4.10: Embedded coil geometries: a) Helical with circular shape [145-147], b) Micro helix [148], c) Pickup coils [103, 149-151], d) Helical with square shape [24, 68, 152,153].

layer and circulated continuously. This increases mutual inductance and allows for more efficient signal pick-up, as well as a higher signal to noise ratio. The pick-up coils can be placed on the inner or outer layers of the PCB, depending on the design of the system. Depending on the available space (which can be the case for power modules or vertical/bigger semiconductor switches), the helical shape can be more flexible for optimizing coil parameters, such as square shape of coils shown in figure 4.10(d). The winding of the pick-up coils can be designed to be customized for different applications. This allows for improved performance of the system by optimizing the coil parameters. It also ensures that the coils are optimally placed to pick up the signal.

Designing a coil involves optimizing two main factors: 1) The occupied space/shape/geometry, and 2) The electrical and magnetic properties. Both of these factors are interrelated, so any change in one will affect the other. A coil's shape/size is determined by the PCB/converter's available space, whereas its electrical parameters are determined by its dimensions and distances (in relation to the current carrying trace/conductor) along with its winding arrangement. This means that when designing a coil, a trade-off must be made between electrical and magnetic properties, and the available space/shape/geometry. The chosen design must ensure that the coil meets the desired performance while still fitting in the allotted space. This can be a difficult balance to strike, but with careful consideration, a

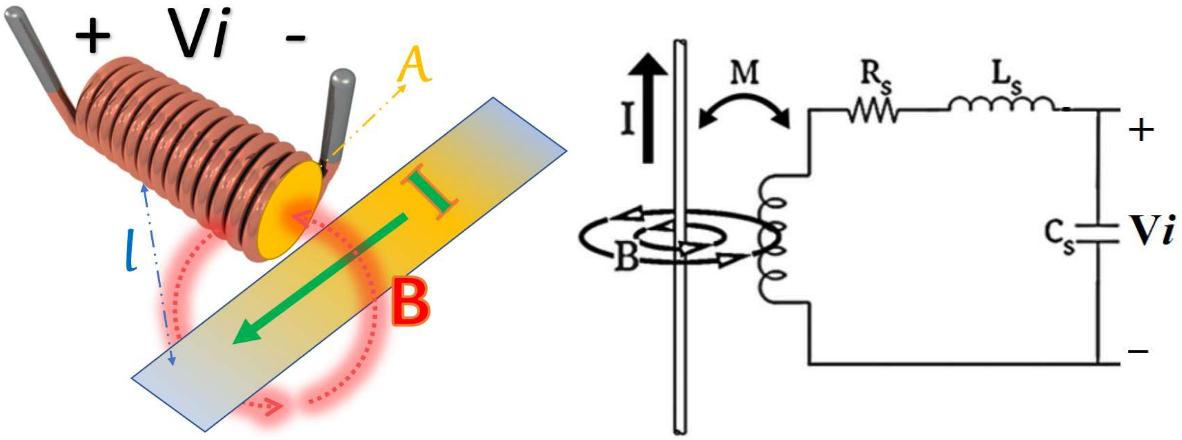

Figure 4.11: A simple 3-D spiral coil with its simplified equivalent circuit.

design that meets all of the criteria can be achieved. Additionally, modern simulation tools can be used to optimize the design of the coil to ensure the best possible performance. Starting from the coil's (simplified) equivalent circuit, the optimization can be performed by examining the relationship between electrical parameters (*RLC*) and physical dimensions and properties. Figure 11 shows a simple coil with its simplified equivalent circuit, in which M is the mutual inductance between the coil and the conductor, L_s is the self-inductance of the coil, R_s is the winding resistance, and C_s is the stray (or parasitic) capacitance between the windings themselves and also between winding and other nearby conductors. Using Electromagnetics laws [154-157] (specifically, Ampere's law in (4.1)), one can obtain the flux density (B) inside the coil's turns:

$$\oint_C B.dl = \mu_0\, I \qquad (4.1)$$

in which I is the current inside the conductor and μ_0 is the magnetic permeability of the air. To simply the integration, the closed circular path around the conductor carrying current I that passes through one of the winding turns with a distance of l form the conductor can be considered, which defines the magnetic flux density (B) as in 4.2:

$$B = \frac{\mu_0\, I}{2\pi l}\ (T) \qquad (4.2)$$

In the complete form of the Faradays law [153-156], any magnetic field variation in time produces an electrical field (4.3) and in case of having a winding turn (with some approximation about the field distribution), it will be an induced voltage to the coil’s terminals (4.5):

$$\oint_C E.ds = -\frac{d}{dt}\int_S B.da \qquad (4.3)$$

$$\Phi = \int_S B.da = B.A\ (Wb) \qquad (4.4)$$

$$V_{single-turn} = -\frac{d\Phi}{dt} \qquad (4.5)$$

E is the induced electric field around the closed counter of *C* and the area of *S* can be considered as the effective area of the coil that has the flux density of *B* (which was considered as a constant distribution for simplicity). Magnetic flux, from (5), is a scalar dot product of *B* (flux density) and *A* (area). Now, by combining (2.1) and (4.5), the relation between *Φ* and the *M* of a single turn of the coil winding can be disclosed as in (4.6):

$$\frac{d\Phi}{dt} = -M_{single-tur} \cdot \frac{di}{dt} \qquad (4.6)$$

$$M_{single-tur} = \frac{\Phi}{I} = \frac{BA}{I} = \frac{\mu_0 A}{2\pi l}\ (H) \qquad (4.7)$$

Thus, the larger the cross-section area (big *A*) and the shorter distance to the conductor (small *l*), the bigger *M* and the larger induced voltage to sense. To obtain the total *M*, the summation of each turn's *M* can be stated as in (4.8):

$$M = \sum_{k=1}^{N} M_k = \frac{\mu_0 A_k}{2\pi l_k} = \frac{\mu_0}{2\pi}\sum_{k=1}^{N}\frac{A_k}{l_k}\ (H)(4.8)$$

in which *N* is number of turns. In most helical and spiral coils, the effective cross-section of all coils is the same, which simplifies the equation (4.8) to the form of (4.9):

$$M = \frac{\mu_0 A}{2\pi}\sum_{k=1}^{N}\frac{1}{l_k}\ (H) \qquad (4.9)$$

Also, if the distance of all turns are the same from the conductor (such as in circular helical coils), the *M* of those coils can be obtained from a more simplified form as in (4.10):

$$M = \frac{\mu_0 NA}{2\pi l}\ (H) \qquad (4.10)$$

It is only *M* that improves sensitivity in current sensing among electrical properties in the equivalent circuit of the coil. Three additional *RLC* elements are considered parasitic values of the coil, which also limit the range of frequencies and currents that can be detected by the coil. As a result, parasitic elements can also reduce the signal-to-noise ratio of the coil since they dampen the signal at specific frequencies. Based on the circuit in Figure 11, the coil's transfer function can be expressed as follows in (4.11):

$$\frac{V_{coil}(s)}{I(s)} = \frac{-M.s}{L_s C_s\, s^2 + R_s C_s s + 1} \qquad (4.11)$$

Apart from the zero at s=0, since the absolute values of L_s and C_s are billions of times smaller than R_s, there is a double pole at F_r with a good approximation of (4.11):

$$F_r = 1/2\pi\sqrt{L_s C_s} \qquad (4.12)$$

which means the coil's gain increases with a slope of +20 dB/dec starting from frequencies close to DC until it reaches the resonant frequency of F_r, then it decreases with a slope of -

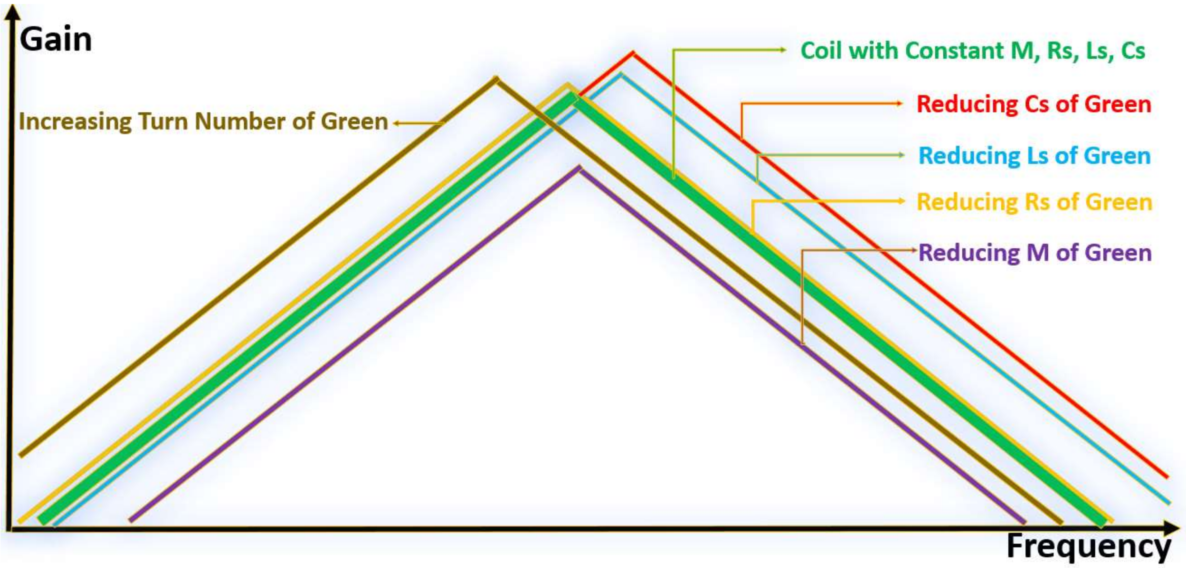

Figure 4.12: Gain Bode plot of a raw coil with changing its electrical parameters [24, 32-33].

20 dB/dec. Figure 4.12 is a comprehensive Bode plot that illustrates the effects of changing each coil’s electrical parameter on its gain-frequency response (from 4.11) and overall BW to clarify this point. This plot can be used to identify the optimal combination of parameters to maximize the coil's signal-to-noise ratio. Additionally, the plot can be used to adjust the coil parameters for specific applications that require a specific frequency or BW response. Thus, similar to what has been previously done for *M*, the relationship between parasitic *RLC* and physical properties and dimensions can be examined in order to gain a deeper understanding of how the coil's physical design has been optimized so that parasitic negative effects on the desired frequency spectrum are minimized, allowing the coil to be used for a variety of applications that require specific BW to be satisfied.

The self-inductance (L_s) of a coil can be determined by applying a current to it, calculating the turn-flux (summation of the flux generated by each winding turn or $N.\ \Phi$), and dividing that by the magnitude of the current that caused it [154-157]. When the current *I* is applied to the coil in Figure 4.11, *B* of *N* circular turns with a total length of *l* can be calculated as follows in (4-13):

$$B = \frac{\mu_0\, NI}{l}\ (T) \qquad (4.13)$$

From (4.4) and with a cross-section of *A*, the flux inside the coil can be determined by (4.14):

$$\Phi = B.A = \frac{\mu_0\, N.I.A}{l}\ (wb) \qquad (4.14)$$

Now, with dividing the flux-turn by the current, one can obtain the L_s as in (4.15):

$$L_s = \frac{\Phi.N}{I} = \frac{\mu_0\, N^2 A}{l}\ (H) \qquad (4.15)$$

Therefore, many factors contributing to M will also contribute to L_s, such as the cross-sectional area of the coil and its turn number, of which N will affect L_s more than M due to its squared nature. Among mutual and self-inductance contributor differences, the only difference is the length of the coil, which does not affect M, and the distance between the coil and the current carrying conductor, which does not affect L_s. In order to minimize L_s while keeping a similar M, the coil needs to have a shorter length, which requires denser winding distribution. Similarly, rather than increasing N for a better M, it is better to keep the coil as close as possible to the current carrying conductor and if necessary, slightly increase the area (A).

Once the factors that affect L_s in coil design have been examined, stray capacitance (C_s) should be analyzed in relation to the coil's physical design, because C_s also negatively impacts the coil's upper frequency range. Changes to the physical design that reduce C_s can improve coil performance. According to PCB design practice, conductor gaps and trace spacing should be kept minimized to reduce parasitic capacitance, which can also be applied to coil design to better understand how to minimize its stray capacitance. However,

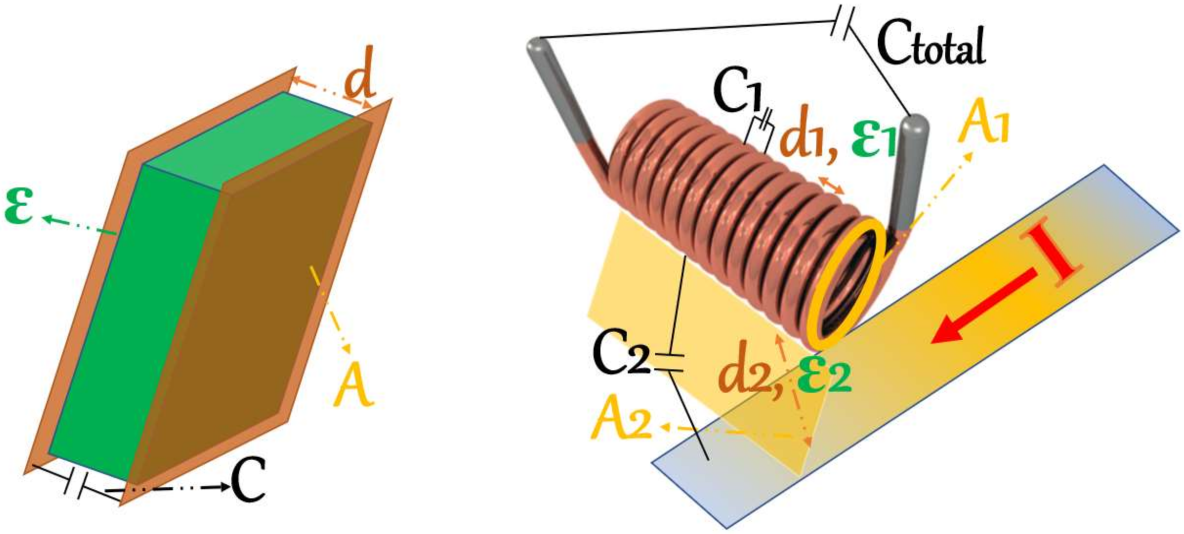

Figure 4.13: A simplified 3-D model of forming a capacitor (Left), and possible coil capacitors forming (Right).

it is worthwhile to remember that there is a limit to how much C_s can be increased. As a result of too large gaps and trace spacing, the resultant large coil may be less effective, due to its reduced M and increased L_s. Additionally, materials such as dielectrics with low dielectric constants (ε_r or κ) can be used to further reduce capacitive losses caused by a big C_s. An example of a simple capacitor forming process is shown in Figure 4.13, in which two conductors are separated with dielectric material. As shown in (4.16), the capacitance value can be calculated using the simplest classical electromagnetic rules [154-157]:

$$C = \frac{\varepsilon . A}{d} \, (F) \qquad (4.16)$$

in which A is effective coupling area, d is the distance between two conductors, and ε is the permittivity (which is the product of the air permittivity (ε_0) and the dielectric constant (ε_r)) of the gap. Taking this capacitance calculation into account, it is possible to calculate C_s of the coil by adding all the capacitances formed between nearby conductors. The dielectric materials used in this process can be air or FR-4 (in most PCB forms). The capacitance is determined by the dielectric material size and thickness, which can be modeled and calculated using the distributed capacitance model. The distributed capacitance model assumes that each of the formed capacitors between conductors is proportional to the distance between them. Specifically, parasitic capacitance is the accumulation of capacitance between windings or traces adjacent to each other, and between windings and nearby conductors, including the circuit carry conductor, the ground plane, the shielding, and the coil's return path. This parasitic capacitance can significantly affect the performance of the coil, so it is important to consider this when designing such circuits. In addition, the capacitance of the coil should be taken into consideration when calculating the total capacitance of a circuit. Two examples of these capacitances are illustrated in Figure 4.13, where C_1 represents the capacitance created between adjacent windings and

C_2 represents the capacitance formed between the coil windings and the current carrying conductor. A general formula for C_s can be expressed as (4.17):

$$C_s = \sum_{k=1}^{X} C_k = \sum_{k=1}^{X} \frac{\varepsilon_k A_k}{d_k} \quad (F) \qquad (4.17)$$

where X represents the number of possible capacitors formed between all conductors within the coil. C_s can be minimized by extending the windings as far as feasible and reducing the intersection areas between the windings as much as possible. Also, other factors can be to avoid close-by intersections with external conductors and not to use extra conductors for shielding, screening or the return path. As a consequence, all of those facts demonstrate the difficulty in keeping minimum C_s while maintaining the necessary M and minimum L_s, as well as other integrated matters such as differential sensing.

As a final parameter to consider is the winding resistance (R_s), which may not be as significant as L_s or C_s since it only impacts the lower band of frequency (Figure 4.11) and the physical factors to minimize it are already considered when optimizing other electrical

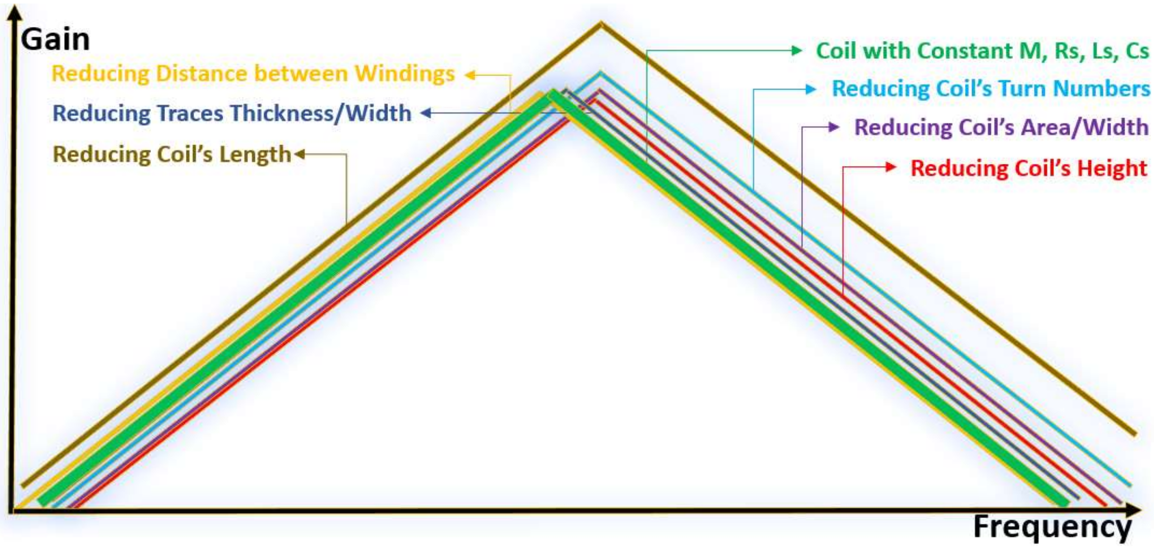

Figure 4.14: The coil's physical properties alteration impact on its bandwidth [33].

properties. However, it should not be overlooked as it can still impact on the overall system performance. Based on general rules in electricity, the resistance of a conductor can be calculated using (4.18):

$$R = \frac{\rho . A}{l} \quad (\Omega) \qquad (4.18)$$

in which A is the cross-section of the conductor, l is the length of the conductor, and ρ is the resistivity of the conductor material. For a coil conductor to minimize R_s, it should have a large cross section while maintaining a minimum length.

Table 4.1: Effects of coil physical properties on its electrical properties.

Effect of Increasing … on	Number of Turns (N)	Distance to the Target Current	PCB Height	Coil Cross-Section Area/Width	Coil Length	Trace Width	Trace Thickness	Adjacent Traces Distance	Internal Return Path Width	Return Path Length	Adding Shields
M	↑	↓	↑	↑	↓	-	-	-	-	-	-
L_s	↑↑	-	↑	↑	↑	↓	↓	↑	↓	↑	-
C_s	↑	↓	↓	↑	↑	↑	↑	↓	↑	↑	↑
R_s	↑	-	↑	↑	↑	↓	↓	↑	↓	↑	-

Table 4.1 and Figure 4.14 are useful tools for translating physical changes that affect electrical properties and the overall BW of the coil into PCB layout design terms. By doing so, it becomes easier to optimize the parasitic values in a PCB-embedded coil design, which also allows the identification of the design parameters that have the greatest impact on electrical attributes and overall coil BW. Combining the parasitic effects on coil

BW analysis with the relationship between physical coil parameters and its electrical parameters is an effective method of designing PCB-embedded coils for current sensing in an efficient manner, thereby identifying trade-offs in terms of size and complexity of the

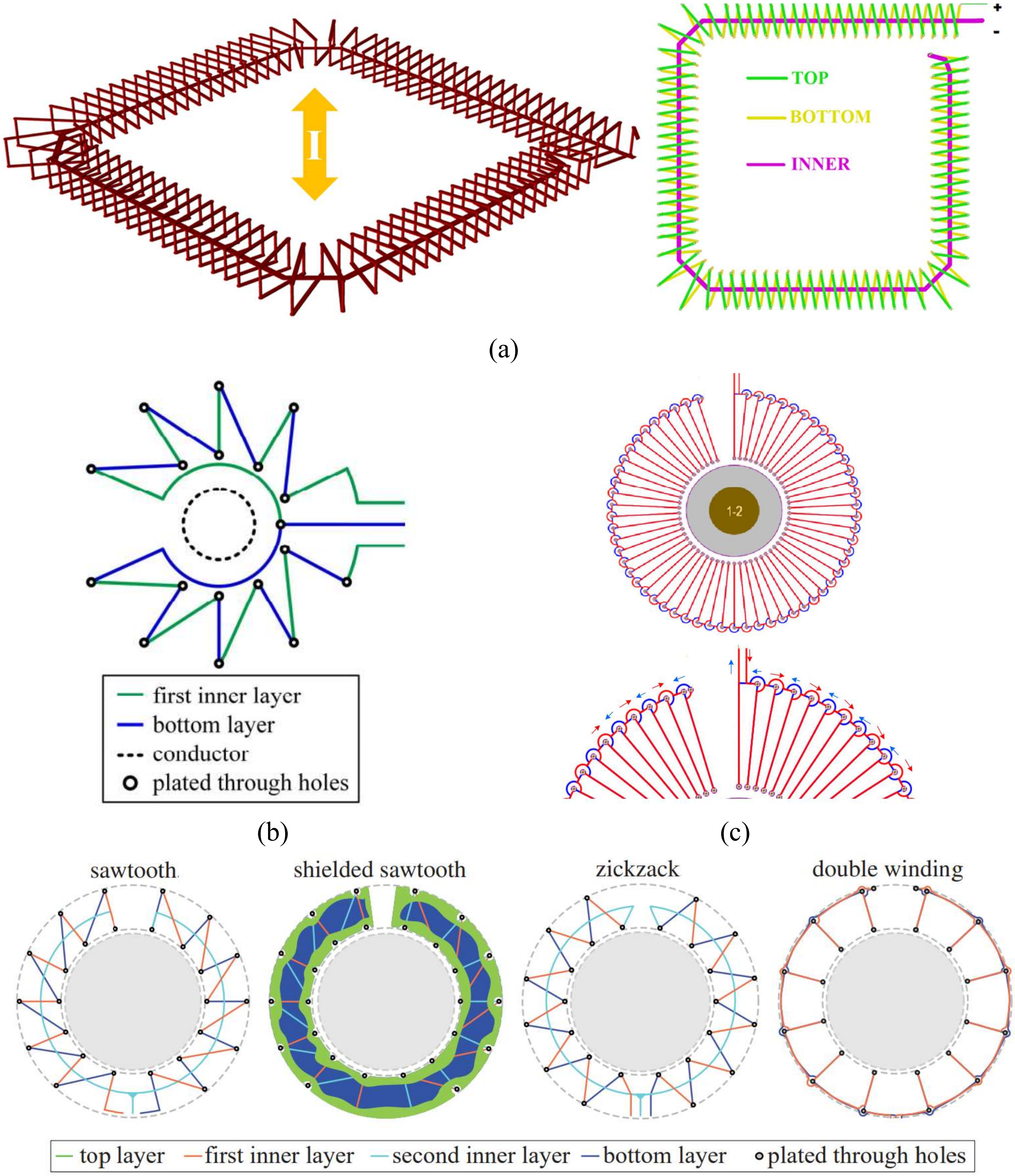

(a)

(b)

(c)

(d)

Figure 4.15: Helical winding: a) With an internal return path, b) Minimized return path [97], c) Embedded return path in windings (double winding) [147, 158], d) Winding method comparison based on stray capacitance [159].

coil design. It can, for example, be inherent in helical coils for differential current sensing to have a return path, as shown in Figure 10.

A return path is necessary to ensure accurate results, as its absence may result in measurement errors and incorrect readings. In particular, the path is designed to cancel induced signals generated by external (or outside the coil's loop) sources, improving the accuracy and noise immunity of a coil-based current sensor. This trace loop can be provided in several ways, such as by connecting a single-turn internal return loop inside the coil or by electrically connecting the shielding to one of the coil's terminals. Additionally, the return loop trace should be as close to the current-carrying path as possible to reduce external magnetic fields. Therefore, parasitic effects of the return path must also be taken into consideration when designing PCB-embedded coils. This will allow for more accurate current sensing and the optimization of the coil design. This presents a challenge for differential sensing applications as the return path needs to be re-designed to allow for differential current, in which an entirely different return path strategy may be proposed to enable differential current sensing in helical coils. Figure 4.15 shows some common and optimal helical coils with a return path for a more precise analysis. Most existing RC current sensors embedded on PCBs employ a square/toroidal distribution scheme with a simple internal return loop, as shown in Figure 4.15(a).

A major issue with the internal return path is that 1) it adds a long conductor to the coil, resulting in an increased parasitic resistance and self-inductance, 2) the internal conductor has a large total coupling area with all coil windings, which results in excessive parasitic capacitances. In the case of a narrower conductor, reducing the internal trace width may result in a lower C_s; however, the narrower conductor adds even more R_s and L_s to the overall coil. Figure 4.15(b) addresses the issue by placing the return path within an inner loop and outside of the coil itself, which somehow reduces the C_s, but two problems remain: 1) the return path still constitutes coupling with vias of the windings, so parasitic capacitances have not yet been minimized, 2) the return path is still an additional conductor of the coil that adds loop inductances and resistances. This creates a need to find a more complex solution that reduces these parasitic elements and still follows the design rules that are applicable to the particular application. As illustrated in Figure 4.15(c), the double winding method tries to embed the return loop within the coil system as a winding [147, 158, 159]. Although the double winding may result in smaller parasitics than the last two methods, the way in which the traces are wound adds an additional length to the conductor of the overall coil, as well as the possibility that there will be a large coupling when the different direction turns are positioned around opposite ways, resulting once again in an unnecessarily large C_s. This can lead to the need for fewer turn numbers to achieve the desired parasitic values, resulting in a smaller mutual inductance and less SNR. In addition, since the original scheme was implemented using only two layers of PCB, it may be necessary to compensate for this technique by underutilizing more layers in the manufacturing process. [159] provides a decent reference on the effect of a coil's C_s on its BW and performance. Using the winding methods examined in Figure 4.15 (d), it is evident that there is a trade-off between L_s and C_s for different winding schemes, where shielding is not recommended at all (due to the large parasitic capacitance) and methods utilizing shorter conductor lengths are recommended.

Although the double winding idea (employing the coils winding themselves as the return path) seems fascinating, they did not achieve the best minimized parasitic results [159], due to PCB manufacturing physical limitations. A better solution would, however, be to use more PCB layers and optimize the winding scheme to reduce its parasitic capacitance and inductance. Figure 4.16 illustrates how this thesis winding scheme (which is a combination of Figures 4.15(a) and 4.15(c)) can be used to detect ultra-wide frequency spectrums and bidirectional switch currents. This coiling scheme can significantly reduce the overall coil length as well as its parasitic values. This makes it a more viable solution for differential current measurement that can reach very high frequency upper bands. It is evident that the reduced total length of the coil's conductor results in a lower R_s and L_s while maintaining the same turn numbers. This, in turn, reduces the total equivalent inductance and improves the common-mode rejection ratio of the system. In summary, this coiling scheme improves the performance of differential current measurement systems and is a more suitable option for high frequency applications. Indeed, due to the reduction in the number and area of intersection between the forward and return path windings, as well as the greater distance between adjacent and parallel coil windings, the overall C_s of the coil will be much smaller than the original coil with an internal return path. This could result in the coil having a higher self-resonance frequency and a wider operating frequency range, resulting in improved performance.

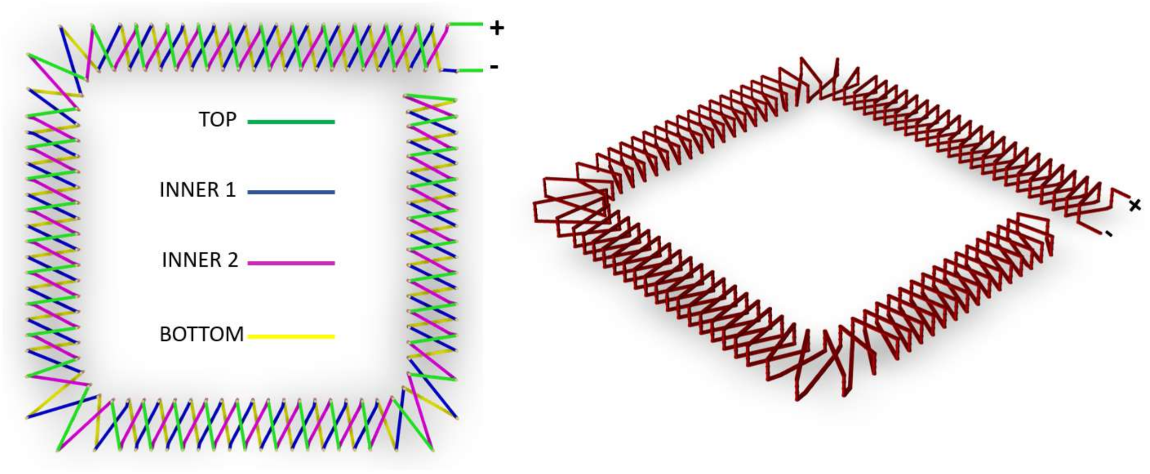

Figure 4.16: Proposed coil by combination of the coils in figure 4.15(a) and 4.15(c).

Using internal layers for each direction winding may result in a lower mutual inductance than the original coil with an internal return path (M is 10~25% less than the original value due to the smaller coil's cross-section area). If the internal layers are replaced with conductors placed only on the top and bottom layers, the issue can be resolved.

The problem with such a replacement is that the induced signals of coils in opposite directions will cancel each other out (as shown in Figure 4.17(a)). Figures 4.17 (b, c) illustrate how the ends of two opposite coils can be connected to overcome this cancelling effect. This will ensure that the signal from both coils is added, significantly increasing the signal strength. Even though the new scheme has a higher *M*, the parallel traces are placed closer, which results in a higher C_s, which is still lower than the C_s in the original coil with

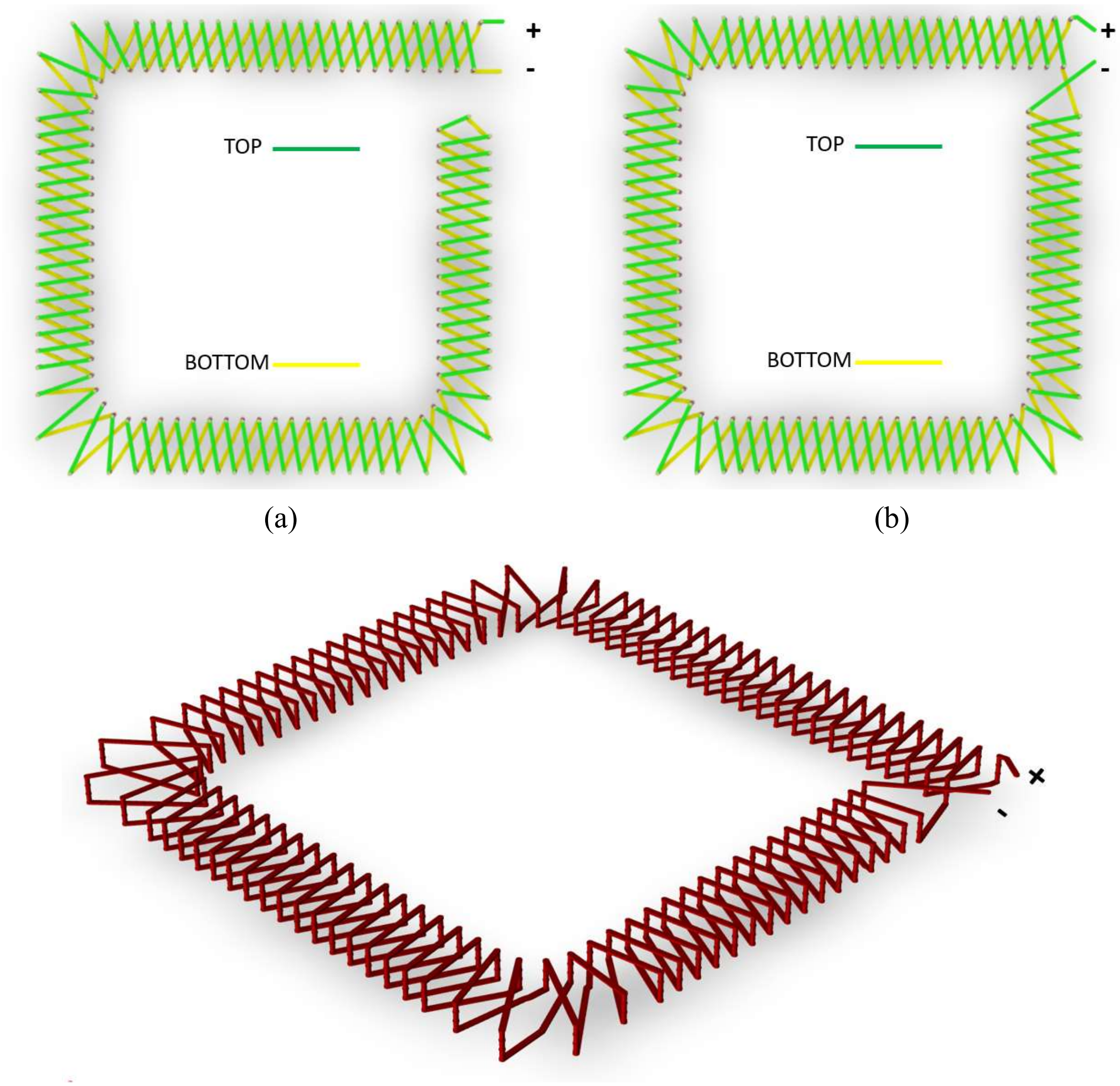

(a) (b)

(c)

Figure 4.17: Two layers version of the proposed coil: a) False termination, b) Correct termination and its 3D (c).

an internal return loop. The proposed coils in Figures 4.15(a), 4.16, and 4.17 (b) all have 82 turn numbers, a side length of 24 mm, trace width of 10 mils, coil width of 3 mm, PCB height of 1.6 mm, and thickness of 1 oz (FR-4). Table 4.2 contains the electrical parameters of these three coils, with the mutual inductance being calculated using (4.9), and the parasitic *RLC* element values being derived using OrCAD Allegro PCB design software.

Table 4.2: Electrical element values of proposed coils.

Electrical Value	**Mutual Inductance**	**Self-Inductance**	**Stray Capacitance**	**Resistance**
Figure 15(a)	10 nH	448 nH	42 pF	0.58 Ω
Figure 16	9 nH	364 nH	29 pF	0.58 Ω
Figure 17(b)	10 nH	404 nH	38 pF	0.56 Ω

Both proposed windings have better (smaller) parasitic results than the coil with internal retuning path, as shown in Table 4.2. Despite the lower *M* of the coil in Figure 4.16, its resonant frequency was shifted up by around 10-20 MHz by reducing L_s and C_s, where the smaller *M* value is a result of using less coil winding area than two other methods, which could be compensated by using 2 mm PCB height instead of 1.6 mm. The coil BW can be optimized by combining the results from Tables 4.1 and 4.2. In particular, the coil resonant

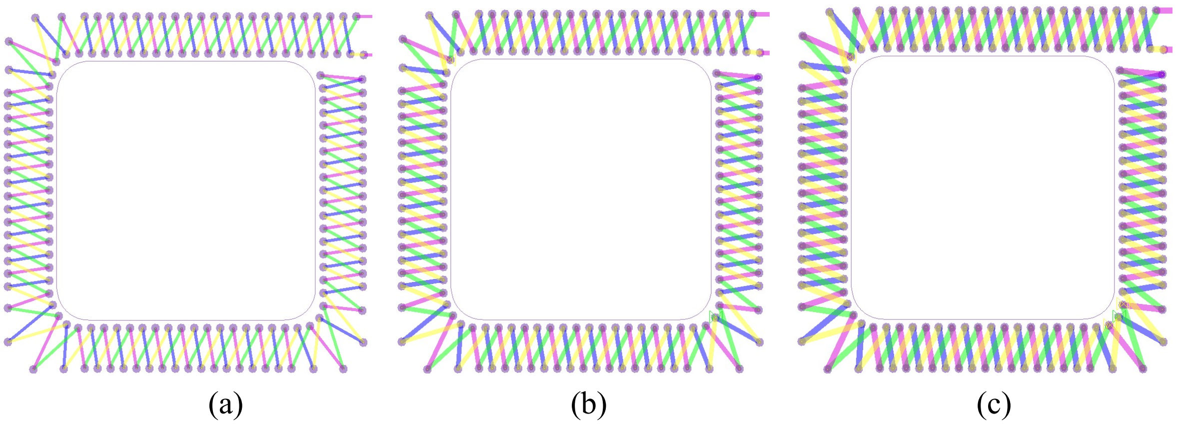

(a) (b) (c)

Figure 4.18: Coil in Figure 16 with different PCB trace width: a) 6 mm, b)9 mm, c) 12mm.

frequency (F_r from (4.12)) can be considered when optimizing the coil parasitic *RLC* values. For instance, with having the same coil as Figure 4.16, its winding PCB trace width can be altered to find the optimal values for coil electrical parameters. As shown in figure 4.18, the same coil is shown with three different trace widths, yet it has the same number of turns and dimensions (meaning the *M* value is the same). According to Table 4.3, the parasitic values of the coil as well as their natural resonant frequency are provided.

According to the trace width optimization (based on resonant frequency), the coil shown in figure 16 is the most optimal. Nevertheless, the optimization objective can vary depending on the application. For example, for bidirectional sensing (which will be discussed in detail further) and ultrahigh frequency applications, C_s must also be a minimum, or for LF applications, better gain and resolution in lower frequencies is required, meaning minimum L_s may be desirable in such applications.

Table 4.3: Electrical parasitic values of the proposed coil with different trace widths.

Electrical Value	**Trace Width**	**Self-Inductance**	**Stray Capacitance**	**Winding Resistance**	**Resonant Frequency**
Figure 18(a)	6 mm	394 nH	27 pF	0.96 Ω	48.7 MHz
Figure 18(b)	9 mm	370 nH	28.6 pF	0.62 Ω	48.9 MHz
Figure 16	10 mm	364 nH	29 pF	0.58 Ω	49 MHz
Figure 18(c)	12 mm	354 nH	31 pF	0.52 Ω	48 MHz

Recalling Figure 4.10, helical coils are more suitable for (SiC/Si MOSFET or IGBT) power modules and vertical power switches, such as vertical SiC Mosfets, due to their size (for current sensor installation) and BW requirements. However, this may not be the case with lateral GaN switches with very tight layouts and ultra-high switching speeds. Many PCB-embedded RCs designed for GaN switch-current sensors incorporate pick-up coils, which can be easily embedded within one or two layers of the internal PCB of the

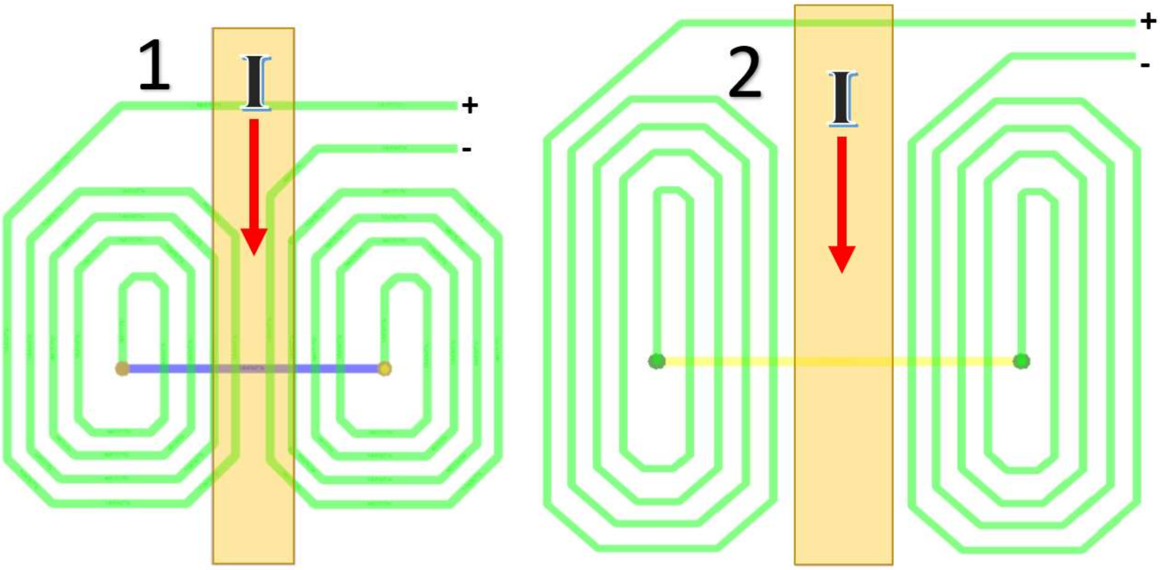

Figure 4.19: Differential pick-up coils having different coupling with the current carrying conductor.

power converter and generally have smaller parasitic values than helical coils. To make them differential for current sensing, one can use examples from [103] that are also shown in (left side of) Figure 4.10(c).

Table 4.4: Electrical elements values of proposed pick-up coils.

Value of	**M**	**L_s**	**C_s**	**R_s**
Coil 1	16 nH	141 nH	9.2 pF	0.42 Ω
Coil 2	16 nH	172 nH	7.8 pF	0.63 Ω

An example of differential coils embedded in an internal layer is shown in Figure 4.19, where two similar coils are connected differentially by another layer trace. A coil of this type has a higher *M* (because it is located closer to the conductor carrying current) and a lower parasitic (because it has fewer turns than most helical coils). As space is limited, the winding traces should be distributed in a way to ensure that enough turns can be placed with sufficient space between them. A further aspect of helical coils that can be overlooked (since they are situated much further from the conductor carrying current) is the coupling between the coil and the conductor, but it must be considered during the design of pick-up coils. This is a tradeoff between having a larger mutual inductance by placing the windings closer to the current conductor, which increases, particularly, the coupling capacitance and adds to the coil's parasitics and limit in the higher frequency band, which in turn reduces the coil's BW. Consequently, the design must be balanced between gain and noise figure of the coil in lower and higher frequency bands. Two coils displayed in Figure 4.19 have different winding distribution and spacing. While one coil turn loop is located much closer to the current carrying conductor, the other attempt to replicate the mutual inductance by employing larger coil turn loops but far from the current carrying conductor, which results in a much smaller coupling capacitance with the power trace, but instead increases the length of the coil windings, thus increasing the coil's L_s. Similarly, pick-up coils may be optimized for their intended applications as was the case with the last optimization approach for helical coils. Table 4.4 contains the electrical values of the two coils.

Although coil 2 occupied a bigger space to minimize its parasitic capacitances, the excessive self-inductance causes a lower resonant frequency in comparison with coil 1. Again, depending on the application, each may be more suitable than the other one to integrate to the converter’s PCB layout.

4.3.2 Analog Integrator Design

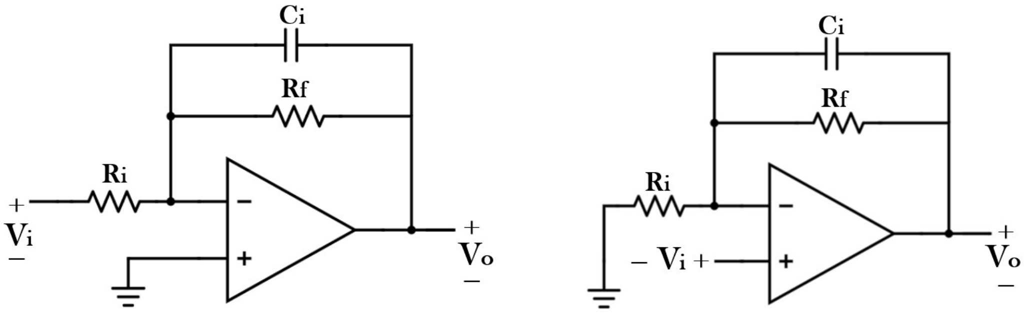

(a) (b)

Figure 4.20: Op-amp-based integrators: a) Inverting, b) Noninverting.

The coil in RC do not have a magnetic core, which means their mutual inductance is generally insufficient to work passively (as a CT), whereas PCB-embedded coils cannot provide a constant gain below a few MHz with passive/resistive termination. The integrated differentiating frequency region could be integrated using an integrator circuit to increase the lower-band frequency gain (Figure 4.8). The amplifier's order of integration is designed to provide the desired gain and frequency response characteristic. The gain of the amplifier is designed to be sufficient to drive the RC or PCB-embedded coils. The circuit is then tuned to achieve the desired frequency response. The integrator circuit can be passive or active. It is possible to use either an analog or digital integrator as an active integrator [33].

As discussed in section 3.3.4 and Figure 3.21, an analog opamp-based integrator is well suited to many situations, as it is able to provide enough gain at low frequencies [160] while having a flexible frequency region (in contrast to passive integrators and does not deal with HF noise as much as digital integrators do [33]). As the amplifier gain drives the embedded coils or RC, and the circuit is tuned to achieve the desired frequency response, this order of integration gives the desired gain and frequency response characteristics. The integrator circuit is a fundamental building block for many other electronic circuits, such as signal filters and oscillators. It is also widely used in instrumentation, control systems, and audio applications. For choosing an electronic integrator, as shown in Figure 4.20, two different opamp-based integrator models are available: inverting and noninverting [160-167]. The inverting integrator model uses an opamp in an inverting configuration, where the output signal is 180 degrees out of phase with the input. The noninverting integrator model uses an opamp in a noninverting configuration, where the output signal is in phase with the input. Both integrator models have a resistor and a capacitor in the feedback loop, which is what gives them the desired frequency response characteristics. The resistor and capacitor values can be adjusted to control the frequency response of the integrator, thus enabling the integrator to be tuned to meet the requirements of a particular application.

Inverting and non-inverting integrators differ primarily in the following ways: a) the gain polarity, b) an extremely high input impedance of the non-inverting integrator, versus a limited input impedance of the inverting integrator (R_i), c) although both have negative feedback, the feedback is not connected to the ground of the inverting integrator, d) the gain of noninverting integrators is always greater than 1, indicating that they are ineffective at ultrahigh frequencies, whereas the gains of inverting integrators can be lower than one, e) The noninverting integrator delivers greater gains than the inverting integrator, particularly at lower frequencies [163-166]. In order to analyze these integrators in more detail, the transfer functions are shown in (4.19) and (4.20) for inverting and noninverting integrators, respectively:

$$\frac{V_{oi}(s)}{V_i(s)} = \frac{-R_f}{R_i(R_f C_i s + 1)} \qquad (4.19)$$

$$\frac{V_{on}(s)}{V_i(s)} = \frac{R_i + R_f + R_f R_i C_i s}{R_i(R_f C_i s + 1)} \qquad (4.20)$$

$$S_{pole} = \frac{1}{R_f C_i} \quad (rad/s) \qquad (4.21)$$

where R_i and C_i are the integrator's resistors and capacitor, respectively, and R_f is the integrator's feedback resistor. As can be seen from the transfer functions, both integrators exhibit a pole derived from (4.21), which indicates that the larger the R_f, the lower frequency at which the integration can be initiated, or, in other words, the R_f value will limit the lower band of the integration process. As a result, the larger the R_f value, the higher the gain at low frequencies. This means that the lower band of integration can be amplified at low frequencies through increasing R_f, in which the integrators will be able to

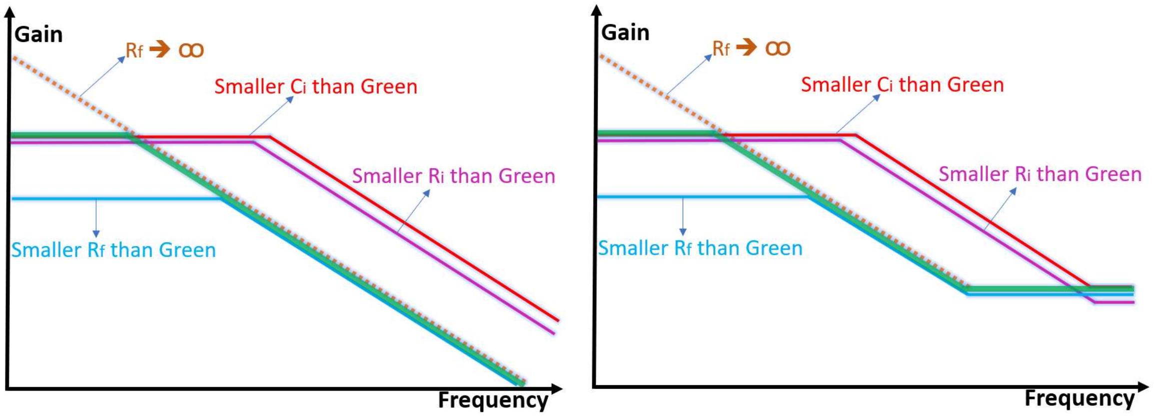

(a) (b)

Figure 4.21: Gain-Bode plots of OP-amp-based integrators: a) Inverting, b) Noninverting [202].

integrate signals with lower frequency. Aside from the 180-degree phase difference between the two integrators, the noninverting integrator has a zero (which can be derived from (4.22)) that is not present in the inverting integrator:

$$S_{zn} = \frac{R_f + R_i}{R_f R_i C_i} \quad (rad/s) \qquad (4.22)$$

Due to R_f being much larger than R_i, in practice, the pole of noninverting integrators will occur at very low frequencies, while the zero of noninverting integrators will occur at very high frequencies. Based on the assumption that $R_f >> R_i$ (which is an assumption that most of time is true in higher frequencies), equation (4.22) can be simplified into equation (4.23):

$$S_{zn,HF} = \frac{1}{R_i C_i} \quad (rad/s) \qquad (4.23)$$

The presence of a HF zero in an integrator frequency response can be either an advantage or a disadvantage, as the zero can control the higher band of the integrator while it can also limit the higher band in applications that require high upper bands. In other words, the non-inverting integrator is more suitable for applications in which the upper frequency band of integration must be limited, while the inverting integrator is more

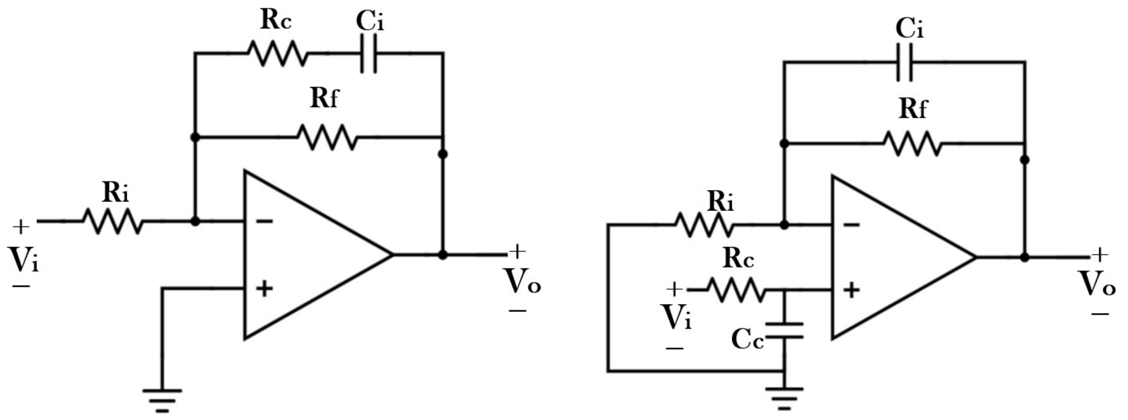

(a) (b)

Figure 4.22: Circuitry of compensated integrators: a) Inverting, b) Noninverting.

suitable for applications in which the upper frequency band is not limited. Figure 4.21 illustrates Bode plots of integrators from (4.20) and (4.21), illustrating possible compensations for non-compensated integrators in which everything is almost identical except for the effect of zero at HF in noninverting integrators. In reality, the integrating slope of inverting integrators will be limited by the opamp upper frequency of the unity gain. RC compositions require the integration of the coil's differentiating slopes up to a specific frequency, which means controlling the upper band of the integrator is a must. However, affecting the whole frequency band with R_i alteration may not be desirable since it contributes to the overall sensitivity of the sensor. A pre-shoot effect associated with inverting integrators at higher frequencies is another issue associated with these devices. Since the inverting integrator has a small input impedance, the input signal can be directly connected to the output. Additionally, its capacitor is very close to being short at ultra-high frequencies, resulting in an undershoot for switch-currents as well [160-162].

Figure 4.22 establishes a simple adjustment technique for both inverting and noninverting integrators. R_c adds a zero after the integrator input terminal in the compensating inverting integrator, which limits the integrating slope at high frequencies, as well as reducing the bad effects of pre-shoot issues. Using R_c and C_c, a passive LPF extends the integrating slope in the compensated noninverting integrator. Figure 4.22 shows a simple compensating technique for both inverting and noninverting integrators. In the compensated inverting integrator, R_c adds a zero after the integrator input terminal to limit the integrating slope at HF. Using R_c and C_c, a passive LPF extends the integrating slope in the compensated noninverting integrator. For inverting and noninverting integrators, equations (4.24) and (4.25) describe the transfer functions of compensated integrators:

$$\frac{V_{oci}(s)}{V_i(s)} = \frac{-R_f(R_cC_is+1)}{R_i((R_f+R_c)C_is+1)} \qquad (4.24)$$

$$\frac{V_{ocn}(s)}{V_i(s)} = \frac{R_i+R_f+R_fR_iC_is}{R_i(R_fC_is+1)(R_cC_cs+1)} \qquad (4.25)$$

In addition, as can be seen from TF of a compensated inverting integrator, R_c affects the existing pole, meaning that a new pole will be defined at a slightly lower frequency according to (4.26):

$$S_{new\ pole} = \frac{1}{(R_f+R_c)C_i} \quad (rad/s) \qquad (4.26)$$

Since values of R_f is always much higher than R_c, this will not be a very significant shift for the original pole frequency. Moreover, it is now possible to modify the upper band of inverting integration easily by selecting a fit R_c in the manner described in (4.27):

$$S_{zi} = \frac{1}{R_cC_i} \quad (rad/s) \qquad (4.27)$$

Furthermore, the pole of the passive LFP can cancel the zero of the noninverting integrator, which extends its integration slope to ultra-high frequencies in order to make it suitable for HF applications. This compensated integrator is also called “hybrid integrator” due to

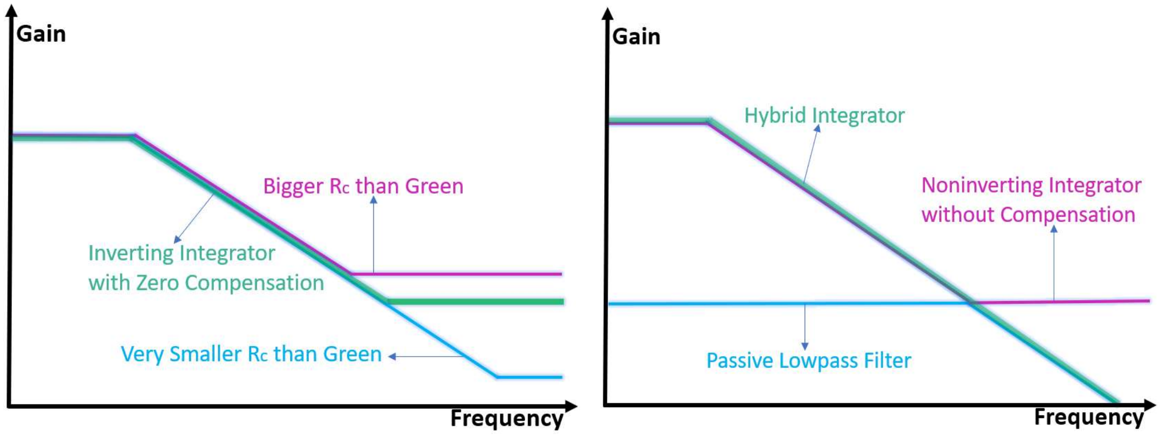

(a) (b)

Figure 4.23: Gain-frequency response of compensated integrators: a) Inverting [202], b) Noninverting.

combing an electronics integrator with a passive one [146, 160, 168]. This can be achieved by selecting the passive LPF's pole at the same frequency as the noninverting integrator's zero as described in (4.28):

$$\frac{1}{R_c C_c} = \frac{R_f + R_i}{R_f R_i C_i} \qquad (4.28)$$

As R_f in integrator systems is typically much larger than other resistors (to use the lower band of the integration), the approximation of (4.23) can be applied to (4.28), yielding (4.29):

$$R_c C_c = R_i C_i \qquad (4.29)$$

As a result of compensations, sensors can be designed using integrators for LF to ultra-HF (UHF) applications, providing additional design flexibility. Figure 4.23 illustrates potential Bode plots for both compensated circuits, in which either frequency limiting, or extension is also emphasized. This provides tools to customize the responses in accordance with the circuit's desired output. A high-frequency response, for example, can be achieved using an integrator, which extends the frequency range beyond what is provided by passive components. In a similar way, if low-frequency response is desired, the integrator can be used to limit the frequency range below what the passive components provide.

There are many specialized analog integrators for RC operation available in the literature, and Figure 4.24 illustrates a few examples of them. In Figure 4.24(a), the integrator achieves much longer integration times when measuring pulse currents but suffers from poor compensation when the input signal is not centered around *Vcc/2* [169]. In Figure 4.24(b), a differential long-term integrator works with a special type of RC designed to measure plasma pulse currents, in which switches in the integrator let the remaining electrical charges on the integrating capacitors go once the measurement has been completed, thus canceling errors accumulation by repeating measurements [170]. Figure 4.24(c) shows that the filtered signal will be differentially amplified with an instrumentation amplifier, then integrated with a noninverting integrator in order to reduce the effect of common mode switching noise [158]. In Figure 4.24(d), an integrator circuit receives a current sensor signal and outputs a voltage signal, with a high-pass filter connected to the integrator output to remove DC content. Further, the feedback loop also provides DC content to the inputs of the integrator and high-pass filters, as well as an output containing DC content of the voltage signal, which detects large current steps as well as faults by monitoring line conductors [171]. As illustrated in Figure 4.24(e), the type of integrator's feedback compensation will allow the integrator to eliminate DC/LF measurement errors by reducing the very LF gain of the overall integrator [152]. In Figure 4.24(f), the integrator filters the output by passive LFP, then passes it on to a capacitor and follower for load-bearing capacity, followed by an inverting amplifier to attenuate the signal. The processed signal is then connected to an integrator input, resulting in an inverting feedback adder that corrects measurement errors [172]. As with the integrator in Figure 4.24(e), the integrator in Figure 4.24(g) utilizes a resistive feedback system to alter the lower integration band [173].

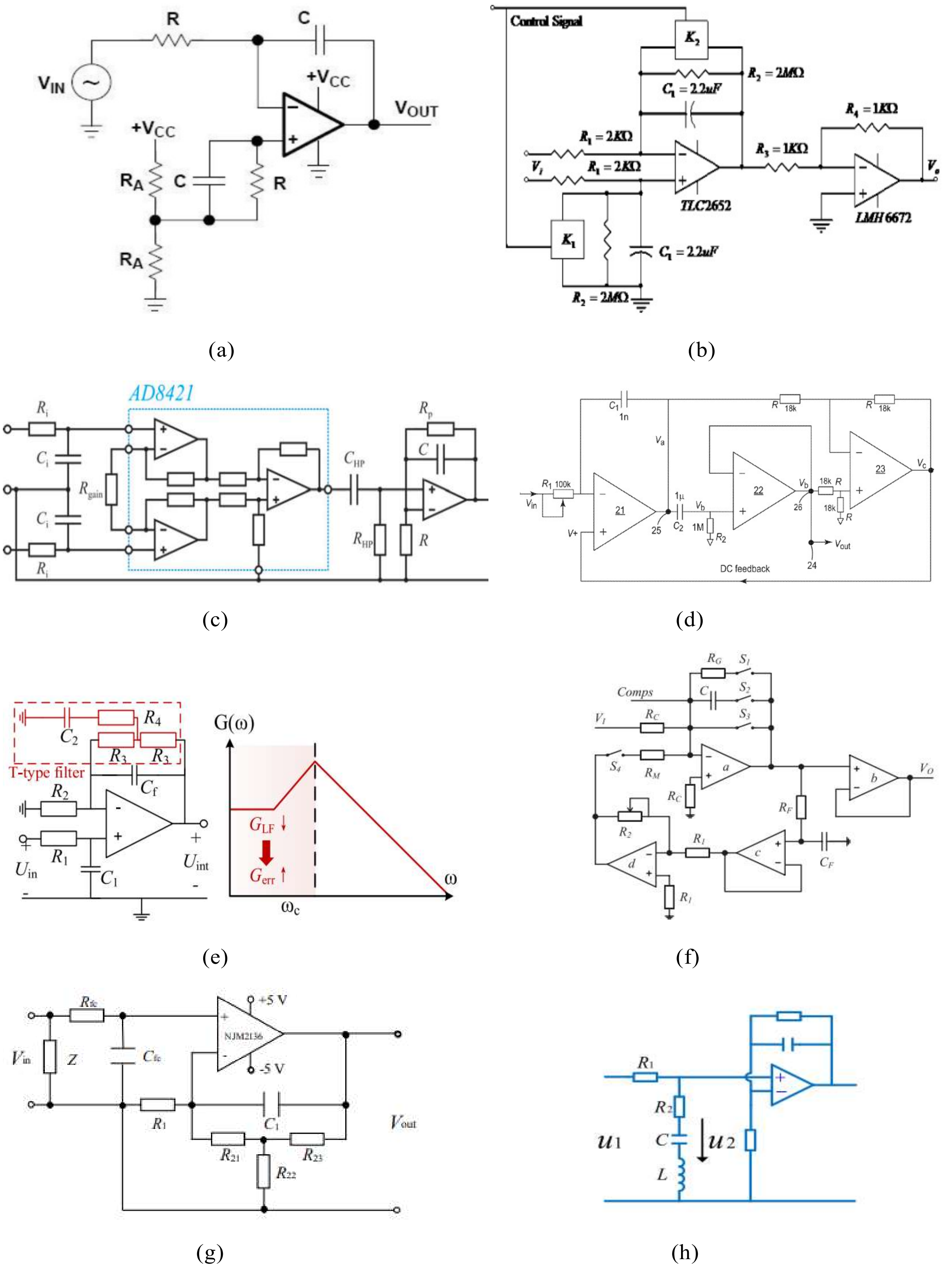
(a)
(b)
(c)
(d)
(e)
(f)
(g)
(h)

Figure 4.24: Specialized integrators: a) Inverting integrator with drift compensation [169], b) Plasma current measurement with differential integrator in J-TEXT [170], c) Differential/split integrator with instrumentation amplifier [158], d) Impulse current measurement [171], e) Low droop distortion [152, 161, 162], f) Integrator with capacitive leakage error compensation [172], g) Hybrid integrator with lower band alteration [173], h) Hybrid integrator with sharper [174].

For RC BW extension, the hybrid integrator in Figure 4.24(h) replaces the *RC* LPF with an *RLC* branch, which alters the frequency response characteristics of the integrator about coil frequency response [174]. Integrators based on opamps often suffer from undesirable offsets at their output due to opamp non-idealities. Figure 4.25(a) shows the general non-ideal characteristics of an operational amplifier. Due to the bias currents and their resulting input offset voltages, a voltage offset is caused at the output. Figure 4.25(b) illustrates how bias currents can be cancelled out by using two identical input resistors in opamp integrators [139, 177]. In opamp integrators, offset voltages may also be minimized by reducing R_f [175], although this will limit the lower integration band as demonstrated previously. Additionally, [175] mentions that resetting the C_i (or C_f in their terminology) (which is one method that can be used to compensate for droop issue in switch-current caused by the inability to read the DC component of the switch current) may help to resolve the problem. However, resetting may not be applicable to HF switch-current sensing, which will be discussed in more detail, and compensating for offsets solely

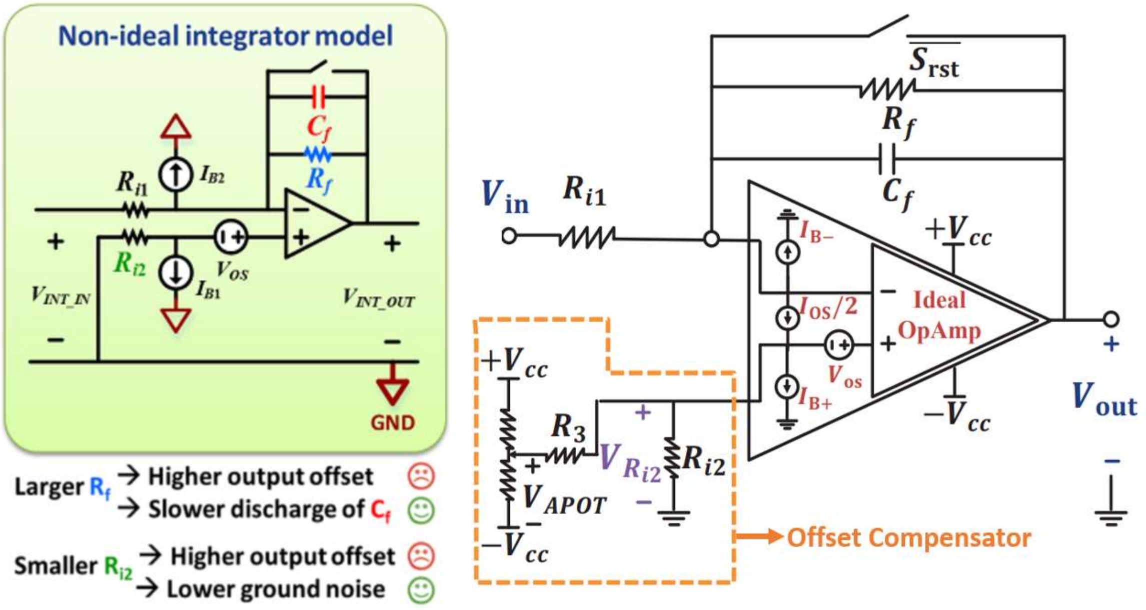

(a) (b)

Figure 4.25: Op-amp offset issue: a) non-idealities that cause offset [175, 176] and b) classical cancelling method [139], [177].

through resetting may result in different sensitivities with different sensors having different offsets, as non-ideal opamps have limited slew rates. Also, the classical technique presented in [139] or [177] might not be desirable, since different sensors can have different offsets, which means that all of them need to be tuned manually this way. Furthermore, a harsh environment might further alter the offset while the sensor is still under operation, and the technique will not be dynamic enough to correct errors if this occurs. The issue has also been addressed in a more dynamic manner than through these classical methods.

Figure 4.26 shows some examples of how offsets may be removed dynamically using electronics or digital signal processing. A fully analog circuit can be implemented with the method presented in Figure 4.26(a), whereas the other two require the use of a

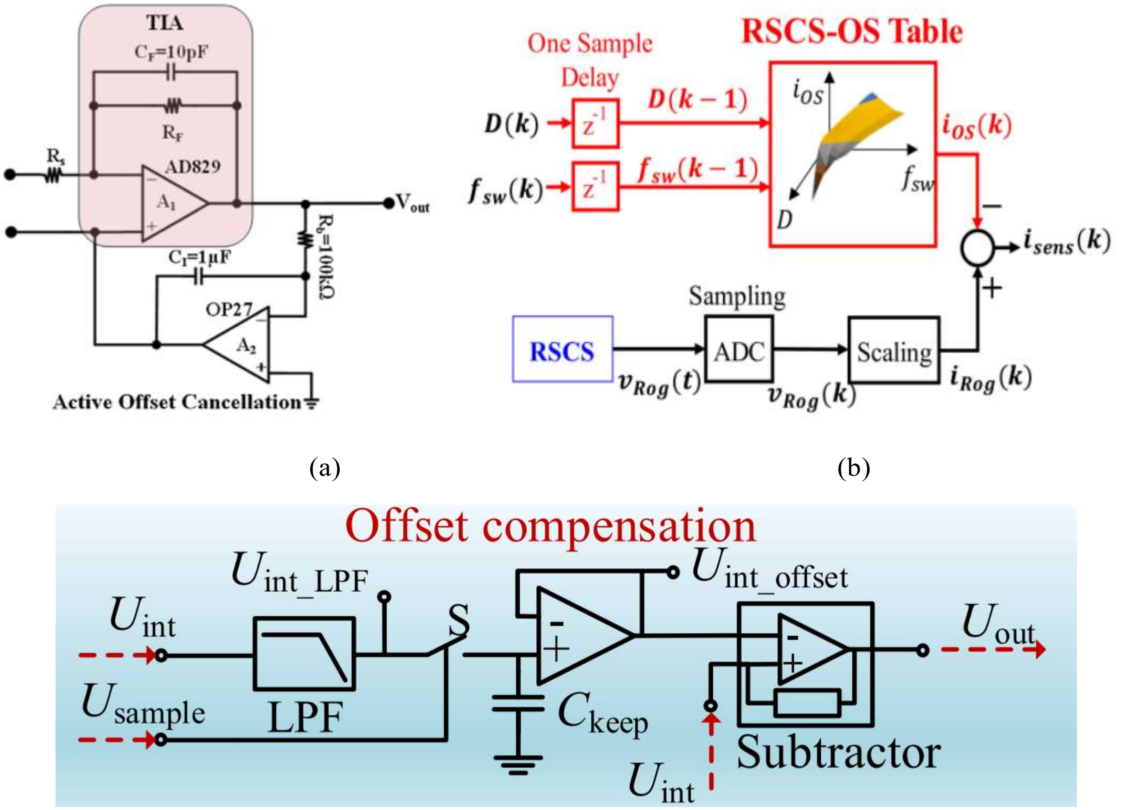

(a) (b)

(c)

Figure 4.26: Dynamic offset cancellation: a) Active positive feedback [178], b) Sample-based correction inside micro-controller [179], and c) sample-filter-hold method by having a feedback from microcontroller [152].

microcontroller, increasing the complexity of the whole sensing system, especially in case of dealing with HF noise due to extremely high EMI emission within WBG power converters. This complexity can lead to system errors, if not implemented correctly. Therefore, it is paramount to choose the right method to reduce offsets to ensure signal accuracy. By selecting the correct type of integrator and filtering as well as selecting the right components (such as an opamp), the offset value can inherently be reduced. It has been shown in Figures 4.24(b) and 4.24(c) that a differential integrator is applied to achieve the advantage of both inverting and noninverting integrators, in which the offset value can also be reduced. The differential integrator's circuit is shown in Figure 4.27 (assuming that R_f is open) to illustrate its advantages and disadvantages. The TF of the circuit in Figure 4.27 is described in (4.30):

$$\frac{V_{od}(s)}{(V_2 - V_1)(s)} = \frac{1}{R_i C_i s} \tag{4.30}$$

in which both capacitors and resistors need to have the same value so that the internal pole and zero can cancel each other and yield a unified integration factor throughout the desired frequency band. A differential integrator may provide cleaner integration by canceling

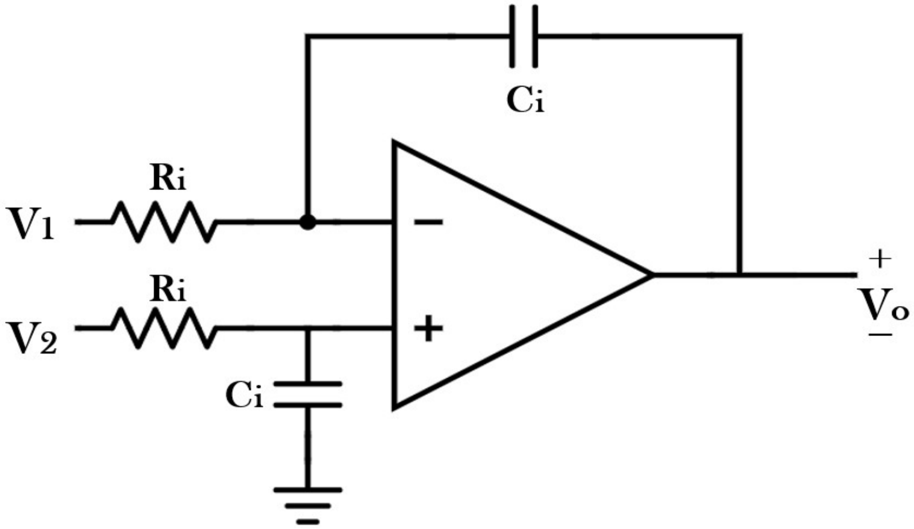

Figure 4.27: Differential Integration method [139, 177].

common mode noises [180]; however, it is difficult to control its upper frequency band. To overcome this issue, an active filter is necessary to limit the upper frequency band and stabilize the system. It will be possible to accomplish this by adding an op-amp circuit which will increase the complexity and utilization of electronic circuits, thereby reducing the system's immunity to noise.

The implementation of a passive dynamic offset compensator may be advantageous since fewer active electronics components are more desirable. The passive dynamic offset compensator may also provide valuable benefits such as improved accuracy and stability. Consequently, the circuit may be more reliable and perform better, which may reduce its complexity and cost. It is earlier shown that integration always happens after a specific frequency and analog integrators cannot integrate very LF components, due to a finite feedback resistor. As a result, a passive HPF with a cutoff frequency below the integration band can be used at the opamp output terminal (Figure 4.28) in order to eliminate all DC and LF components outside the measurement band (such as an undesirable opamp offset) [24, 33, 143, 144]. The cutoff frequency of R_h and C_h (resistor and capacitor of the HPF) should be smaller than the first pole of the integrator (from (4.21)) as described in (4.33):

$$HPF\ Transfer\ Function = \frac{R_h C_h s}{1 + R_h C_h s} \qquad (4.31)$$

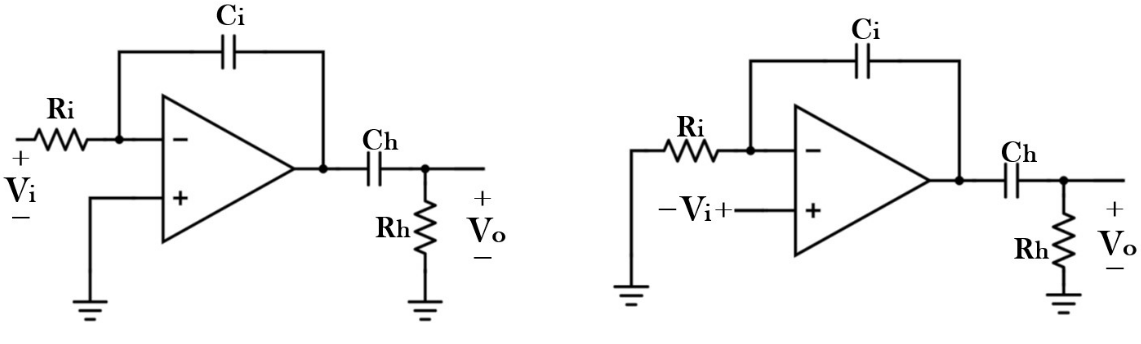

(a) (b)

Figure 4.28: Passive offset compensations for integrators: a) Inverting, b) Noninverting.

$$S_{cutoff,HPF} = \frac{1}{R_h C_h} \quad (rad/s) \qquad (4.32)$$

$$S_{pole,int} > S_{cutoff,HPF} \; or \; R_h C_h > R_f C_i \quad (4.33)$$

As a final challenge when implementing analog integrators, opamp selection is also a major concern. With simple forms of integrators (such as those illustrated in Figures 4.20, 22, or 28), and voltage-voltage amplification (such as in simple RC construction to integrate the coil voltage and deliver a voltage that represents the primary sensed current), a voltage-feedback opamp may be a good choice if it has the following characteristics:

1) The slew rate should be high enough because pulses and switch currents require ultra-high signal rise time [144]. Depending on the defined sensitivity and BW, a slew rate of 200-1000 V/us might be the minimum requirement.

2) A high-enough internal feedback resistor is necessary, as earlier it has been shown that the higher the Rf, the better the lower integration band can be achieved.

3) A sufficient BW is required for an opamp (not too high or too low compared with the required BW), whereby the required BW of the opamp is typically one or two decades greater than the upper band of the active integrator; for example, if the upper band of an analog integrator is 1~2 MHz, an opamp with a BW of 40~100 MHz should be sufficient. It is better to avoid using ultrahigh BW opamps if it is not necessary, since higher-BW opamps might be more prone to EMI noise distortions, as well as their internal feedback resistor is usually smaller than lower-BW opamps.

4) Opamps with very low harmonic distortion are a better choice, since the integration slope and final sensitivity need to be uniform throughout the whole defined BW of the integration process.

Based on these four characteristics, LM6172 [181] and LM7372 [182] are very suitable options. A detailed discussion of the coil and integrator combination for the composition of an ultra-wideband RC will be provided in the next section.

4.3.3 Ultra-Wideband PCB-Embedded Rogowski Coil

Following the information provided regarding the coil and the analog opamp integrator, it is now possible to consider their possible composition as ultra-high BW AC current transducers. When used as an AC ultra-wideband current transducer, it must be capable of providing a unified gain for frequencies as low as 100 Hz~ 1kHz or as high as 10~100 MHz. As such, the coil and opamp integrator must be carefully chosen and configured in order to achieve the desired performance. Furthermore, signal conditioning circuitry should also be considered to ensure the output is suitable for further processing.

As described in the coil design section, a raw coil is capable of providing a differentiating slope at frequencies below its natural frequency (F_r from (4.12)), which was known as the upper frequency limit of a coil for current sensing. Nevertheless, it is possible to terminate a coil using a simple small resistor (or R_t) to obtain the CT working principle, also referred to as passive or self-integration, in which the *RL* circuit passively

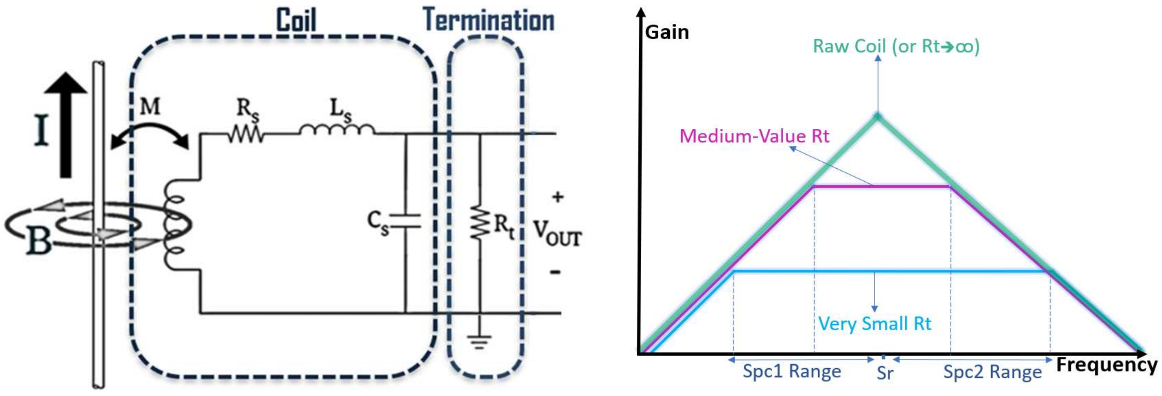

(a) (b)

Figure 4.29: Self-integration in current transformer: a) Terminated coil circuit and b) Its gain Bode plot.

integrates the coil output [32]. As shown in Figure 4.29 is the equivalent circuit of a terminated coil together with a possible plot of its gain and frequency. Terminated coil signal TF is described in (4.34) [24, 32, 33, 178]:

$$\frac{V_{coil}(s)}{I(s)} = \frac{-MR_t.S}{L_s R_t C_s\, S^2 + (R_s R_t C_s + L_s)S + R_s + R_t} \quad (4.34)$$

As can be seen from the figure and TF, the termination resistor converts the coil's double pole at resonant frequency (S_r or $2\pi F_r$) into two poles at S_{pc1} (lower band of CT) and S_{pc2} (upper band of CT). *RL* integration produces a nearly constant phase and output gain in the band between these two single poles. It is possible to derive the self-integration gain and frequency of these two poles from (4.35-37) using a simple approximation of (4.34):

$$Gain_{CT} = \frac{MR_t}{L_s} \ (V/A) \qquad (4.35)$$

$$S_{pc1} = \frac{R_s + 2R_t}{2L_s} \ (rad/s) \qquad (4.36)$$

$$S_{pc2} = \frac{1}{R_t C_s} \ (rad/s) \qquad (4.37)$$

The smaller the R_t, the wider the coil's BW. On the other hand, a smaller R_t will result in reduced sensitivity. Moreover, a smaller C_s value (as well as a smaller R_t value) would have the effect of extending the upper band of frequency, while a smaller L_s value would result in a greater coil sensitivity.

In accordance with the coil design section, the more turns are used, the higher the *M* value (for improved sensitivity and SNR), but at the same time, the L_s value will also rise, as well as a larger value of C_s, which is capable of causing capacitive coupling with large currents and voltages, so a minimum value of C_s is required to prevent capacitive coupling. Technically, HF EMI and HF currents generated by high *dV/dt* can be dampened to a large extent by terminating the coil with a low R_t. Thus, the coil design should be carefully studied to ensure a balance between these parameters. Ideally, the coil should have the right number of turns and the right values of L_s and C_s, which can be terminated with a low R_t in order to prevent HF EMI and capacitive coupling while achieving high BW and SNR.

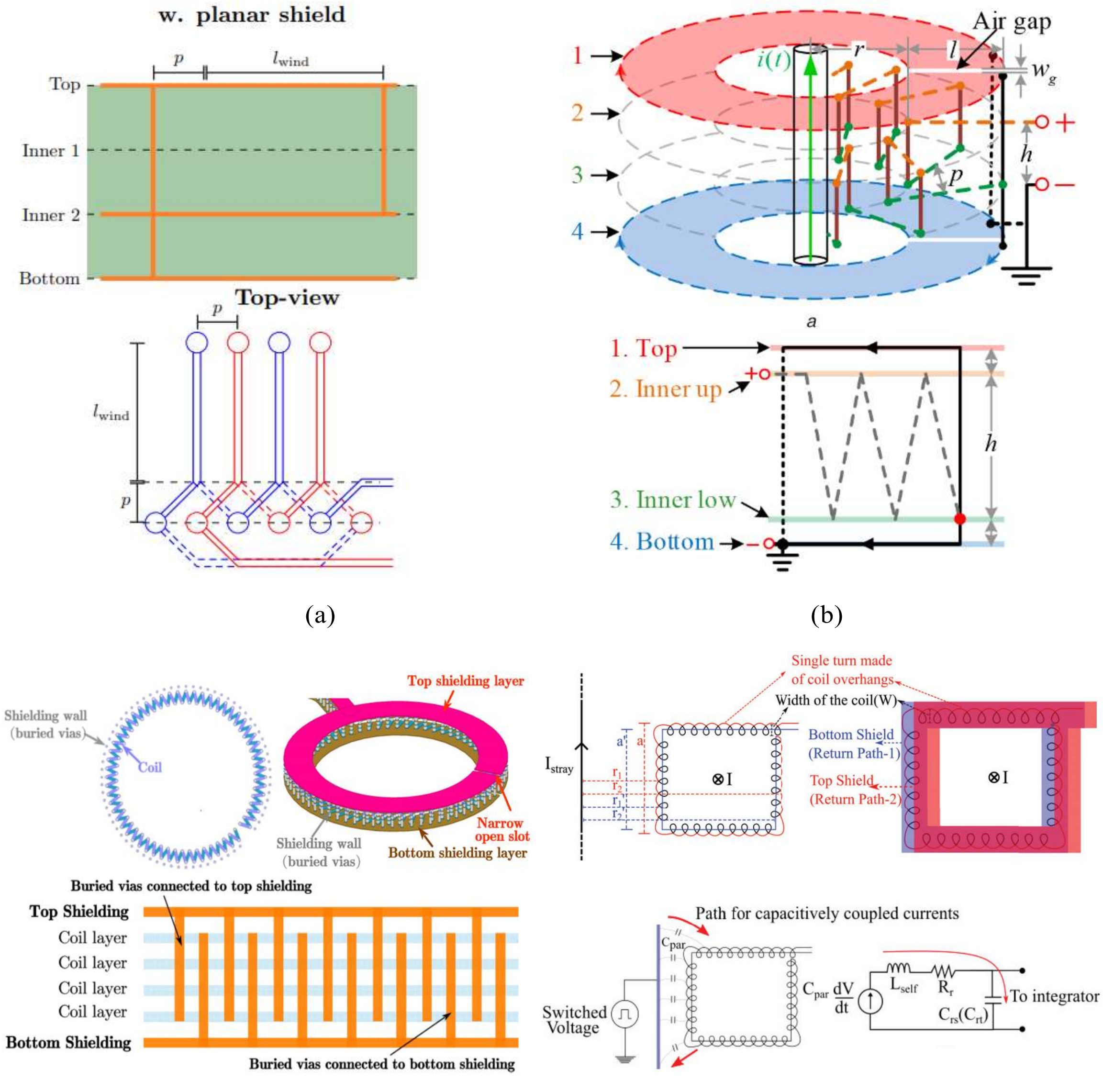

(a)

(b)

(c)

(d)

Figure 4.30: Shielded examples of PCB-embedded coils: a) Planar shielding for pick-up coils [141], b) Screen-returned differential coil (the return path is the screen shielding) [162, 183], c) All-round shielding through buried vias [184], and d) Physical and electrical model for capacitively coupled noise [185].

There is substantial evidence of EMI coupling at HF near power switches or switching nodes, as noted in sections 2.3.5 and 3.2.4. These noises can be induced/coupled through the coil's C_s and L_s (even with the best differential coil structure), resulting in inaccurate HF voltage components across the coil terminals which can be dampened by externally shielding the coil [146]. This can be accomplished by using a metallic shield around the coil. It can also be accompanied by additional filtering components such as capacitor dividers. For such corrections, Figure 4.30 shows examples of shielded PCB-embedded coils. Figure 4.30(b) shows that it is possible to reduce noise by the way of connecting the shield to the ground. Although it has been practiced by means of screen shielding as a return loop as well to help minimize the stray capacitance caused by the return loop [146, 162, 183], the shielding itself will add a coupling capacitor to the windings, as shown in Figure 4.30(d), resulting in multiple resonant frequencies to the coil output and thereby decreasing the coil's BW. As a practical alternative to shielding, terminating the coil with a small resistor is preferred, as this significantly lowers the near-resonant frequency components induced with a similar level of sensitivity to the lower frequency components, thus dampening induction and near field coupling associated with HF EMI. Furthermore, it is beneficial to use lower BW opamps for active integration that are less prone to EMI noises, since R_t reduces the self-integration of lower bands (S_{pc1}) [24]. As in Figure 4.31, a small resistor of R_t is used to terminate the coil so that the coil can be used in HF (above a few MHz), which also contributes to dampening a large amount of induced/coupled noise in HF. Consequently, the integrator is only required to integrate the coil output signal up to a few MHz (or just below 1 MHz) for a clean integrated output, as mentioned earlier. This ensures that the integrator does not have to process any HF noise, which allows it to accurately integrate the input signal. R_t also limits the ringing of the coil, thus preventing overshoot and reducing the distortion of the input signal. By combining the compensated inverting integrator (from Figures 4.22 and 4.28)

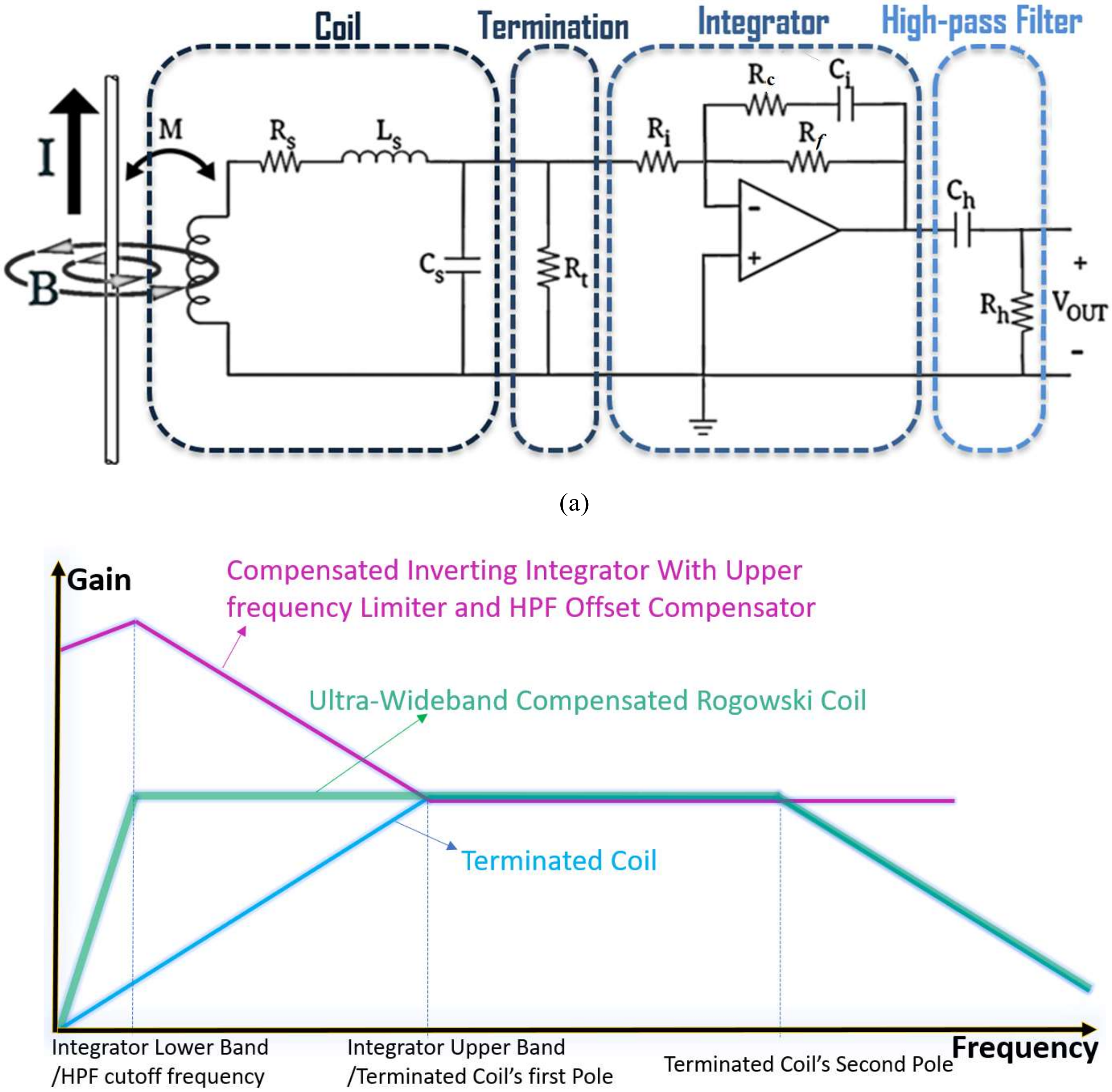

(a)

(b)

Figure 4.31: Ultrawideband Rogowski coil: a) Circuitry [48] b) Its gain Bode plot [202].

and the terminated coil from Figure 4.29, the composed RC AC current transducer can cover a range of frequencies from a few hundred Hz to tens (or hundreds) of MHz (Figure 4.31(b)) [24, 33]. The resistor also helps to minimize the phase shift between input and output signals. When combined with the compensated inverting integrator, the RC AC current transducer is able to provide accurate and reliable measurements over a wide range of frequencies. In order to obtain the TS of the whole current sensor, one needs to combine the TFs of these four blocks (4.24), (4.31), and (4.34) as in (4.38):

$$\frac{V_{out}(s)}{I(s)} = \frac{MR_tR_fR_hC_h(R_cC_i.S+1)\,S^2}{R_i((R_f+R_c)C_i.S+1)(L_sR_tC_s\,S^2+(R_sR_tC_s+L_s)S+R_s+R_t)(R_hC_h.S+1)} \quad (4.38)$$

For frequencies before self-integration begins (S_{pc1}), the integrator compensates for the rising low gain of the coil. Therefore, the integrator's zero (S_{zi}) should coincide with the first pole of the coil (S_{pc1}). It is imperative that a continuous gain is maintained throughout the sensor's operational range, which requires that the phase and gain of the integrator be adjusted in order to match the coil gain at S_{pc1}. In this way, it is ensured that the gain of the complete sensor is equal to the gain of the passive coil's self-integration, in which case the best value for R_c is determined by matching the gain and corner frequency of the coil (S_{pc1}) and the integrator (S_{zi}) as explained in (4.39):

$$S_{zi} = S_{pc1} \quad or \quad R_c = \frac{2L_s}{C_i\,(2R_t+R_s)} \qquad (4.39)$$

If the noninverting integrator is used instead of the inverting one in Figure 4.31, its already existing zero (S_{zn} from 4.26) can be overlapped with S_{pc1} in the same manner as in (4.40):

$$S_{zn} = S_{pc1} \quad or \quad R_i = \frac{2L_s\,R_f}{R_fC_i\,(2R_t+R_s)-2L_s} \qquad (4.40)$$

This indicates that matching the integration gain/frequency of noninverting integrators is more difficult than matching the integration gain/frequency of inverting integrators despite the fact that the effects of a large R_f can be overlooked (which makes 4.39 and 4.40 similar in this regard). Similarly, the TF of the RC based on noninverting integrators from Figures 4.20 and 4.28 (which will have the same gain-Bode plot with Figure 4.31) can be defined as shown in (4.41):

$$\frac{V_{out}(s)}{I(s)} = \frac{-MR_tR_hC_h\left(R_i + R_f + R_fR_iC_is\right)S^2}{R_i(R_fC_is + 1)(L_sR_tC_s\,S^2 + (R_sR_tC_s + L_s)S + R_s + R_t)(R_hC_h.S + 1)} \quad (4.41)$$

A simple approximation of (4.38) and (4.41) can be used to determine the sensor's sensitivity at middle frequency (which is a combination of the coil and integrator gains) for both inverting and noninverting integrators as in 4.42:

$$Sens = \frac{MR_t}{R_iC_i(R_t + R_s/2)}\ (V/A) \qquad (4.42)$$

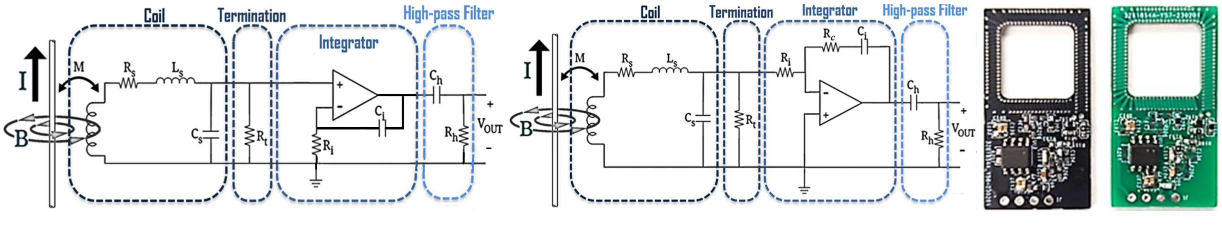

(a) (b) (c)

Figure 4.32: Sensors with: a) noninverting integrator, b) compensated inverting integrator, and their prototype (c) [202].

Table 4.5: Prototyped Rogowski coils properties.

Property	***N***	***M***	***L_s***	***C_s***	***R_s***	***R_t***	***Fpc1***	***Lower Band***	***Upper Band***	***Sens.***
Value	82	9 nH	360nH	30pF	0.62Ω	1Ω	0.6 MHz	220 Hz	100~500 MHz	26mV/A

In Figure 4.32(a-b), two types of RC circuits (where R_f is considered open) are shown, in which they both employ passive HPFs to remove offset and DC errors. According to the presented circuitry, switch-current sensors with the same coil (Table 4.5) have been constructed and tested. Experimental results are shown in Figure 4.33 for the prototyped sensors reading a DUT SiC module switching at 500 VDC, where a 50 MHz current probe (Tektronix TCP305A) is displayed in magenta and a prototyped RC switch-current sensor is displayed in blue along with a zoomed-in version. LM6172 is used as the integrator opamp, a voltage feedback opamp with a high slew rate (in agreement with guidelines for opamp selection in the previous section), along with R_i of 277 Ω, C_i of 1 nF, C_h of 1 μF, and R_h of 1 Ω. Having a clear output can serve as proof of the effectiveness of the ultra-wideband shield-less RC construction guidelines presented in the last three

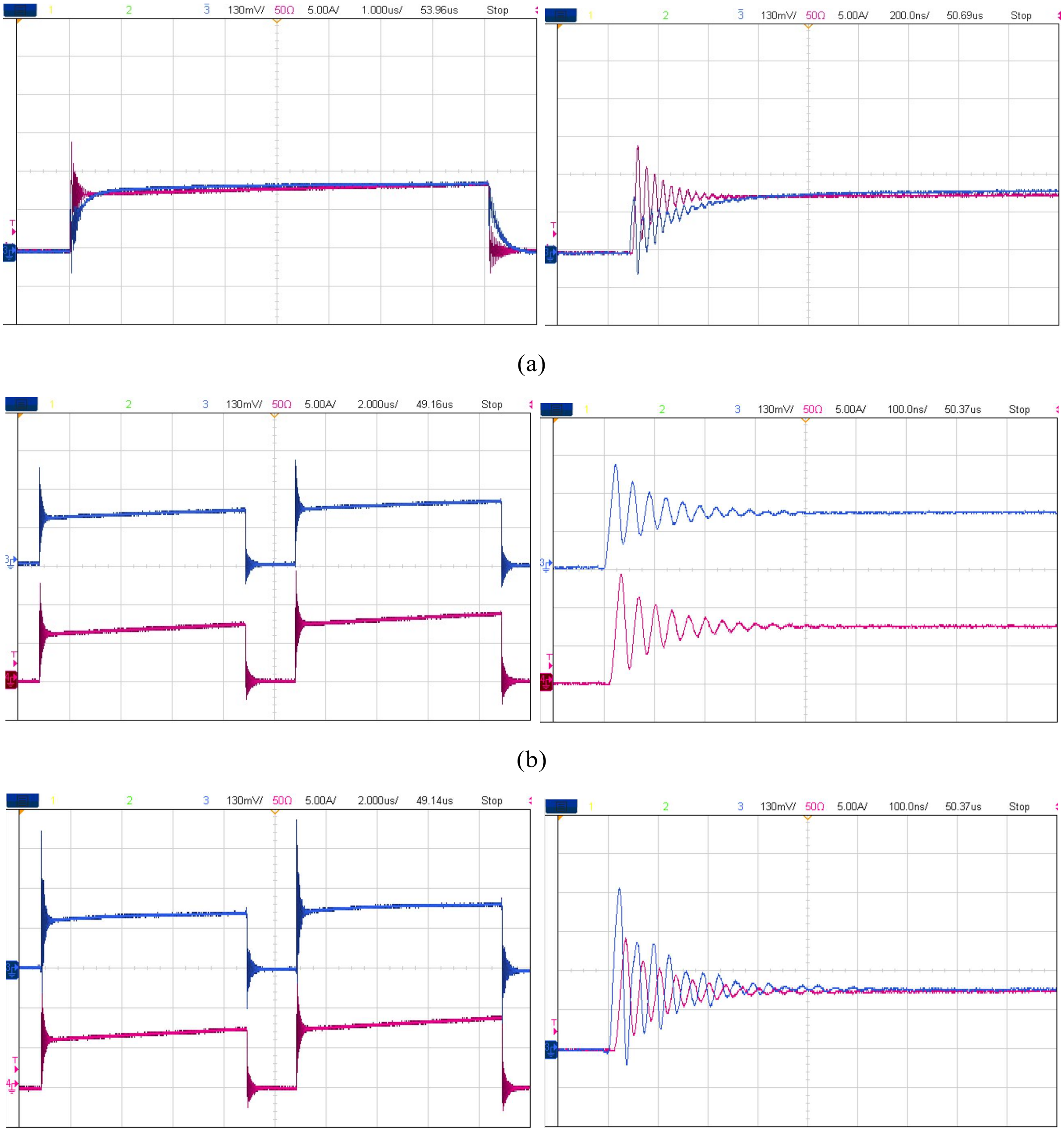

(a)

(b)

(c)

Figure 4.33: Switch-current waveform at 100kHz: a) inverting without R_c, b) inverting with R_c =270 Ω, c) noninverting [202].

sections. With all components chosen and assembled according to the guidelines, the resulting LM6172 integrator opamp delivered a clear output, validating the effectiveness of ultra-wideband shield-less RC construction. As shown in Figure 4.34, even the best RC current transducers cannot read the DC component of switch current, and as a result, the switch current waveform will appear to be an AC-coupled signal resulting from continuous pulse running (Figure 4.34(a)), also known as the "droop issue" in RC current sensors. The following section discusses potential solutions for fixing the droop issue when reading switch-currents.

4.4 Rogowski Coil Output Compensation as a Switch-Current Sensor

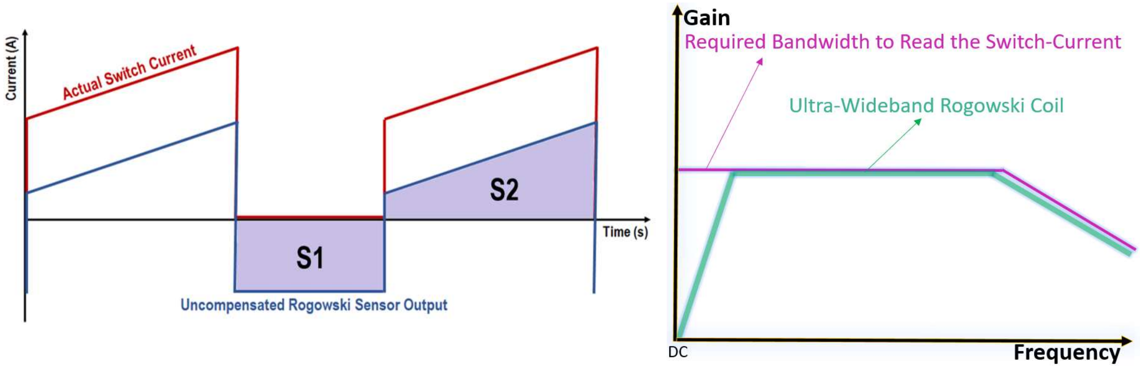

(a) (b)

Figure 4.34: Droop issue of Rogowski coil: a) Time domain switch-current [48] and b) Its frequency domain.

As shown in Figure 4.34, UWB RC current sensors cannot detect the DC component of switch current, referred to as "droop" issue. By their nature, RC current sensors only measure AC magnetic flux and require an external processing circuit to produce a proportional result. With classical RC, droop and drift are common issues, which implies that DC or extremely low-frequency components cannot be detected by the sensor itself (Figure 4.34(b)). The DC response of the coil is zero, so the integrator cannot replicate any DC components from the output voltage of the coil, so integration of a measured zero value is essentially an undetermined constant value, given an unknown initial value. The opamp-based integrator suffers from non-idealities, such as limited feedback resistance, which causes the integrator's starting frequency to be after a few Hz. However, different methods have been proposed to compensate for the lack of DC measurement in RC switch-current sensors. As a switch-current sensor, the RC can be configured in three different ways, resulting in minimal to no droop when reading switching currents with DC components: a) resetting the capacitor(s) during switch off-state, b) using precision rectifiers to mimic the DC component unidirectionally, and c) using a hybrid topology that incorporates a DC detector.

4.4.1 Resetting Rogowski Coil Switch-Current Sensor

As RC does not incorporate DC/LF sensing, a current waveform with DC components, such as the switch current, drifts periodically and eventually centers at zero (called droop issue). The lower sensing frequency band of RC determines the speed at which the droop process takes place, and it is important to note that the larger the lower frequency band, the faster the switching current will be centered around zero. As a result, RC should be designed with a minimum lower frequency band, which can reduce the droop issue and ensure better system performance. However, designing RC with a low enough lower frequency band may not be possible in all cases. Depending on the capacitance and resistance values chosen for a specific sensitivity, the lower frequency

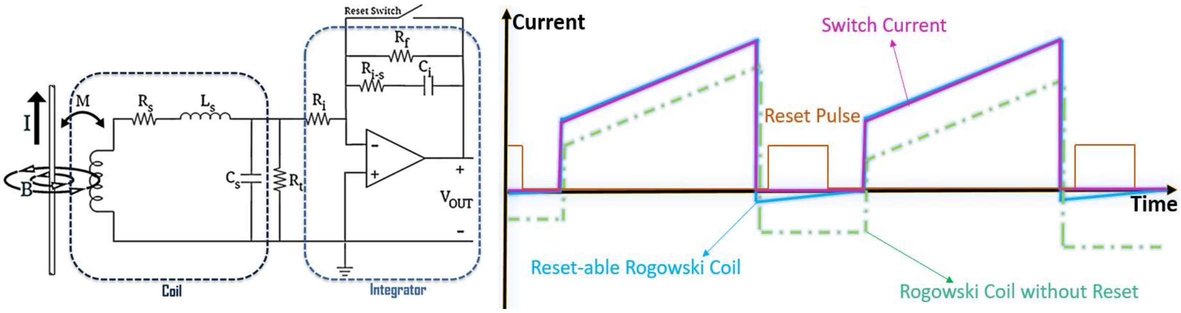

(a) (b)

Figure 4.35: Reset-able Rogowski coil: a) Circuitry and b) Its associated waveforms.

band may be limited by the RC time constant. Even the best-designed RCs will miss the DC component reading, which means that droop will eventually occur.

One method that has been used successfully for a long time is to periodically reset the RC capacitor(s) during the switch off-state in order to force the integration of the switch current to begin from zero during the on-state of the switch. It is possible to build up the switch current properly this way by resetting the sensor charges during the off-state (in which the switch current is assumed to be zero) of the switching period, and as long as the RC is sufficiently low-banded to experience a negligible droop during switch on-time. It is therefore necessary to provide a circuit for reset that can discharge the capacitor(s) of the integrator along with a periodic reset signal that is synchronized with the aimed switch off time (Figure 4.35). In Figure 4.36, some examples of previous reset implementations for RC switch-current sensors are illustrated.

Even though the reset circuitry has significant advantages, such as being small and lightweight, as well as having SS-topology for switch-current measurement and the ability to measure in both directions, it introduces some non-idealities. In some situations, the reset-able RC may be appropriate, particularly in switch-current sensing at lower switching frequencies. However, a major dispute in embedded WBG power electronics for higher switching frequency current detection utilizing RC is regarding how the reset is implemented and how long it needs to receive an active control signal. Overall, there are three major problems associated with implementing reset [24, 33, 144]:

1) Resetting needs additional circuitry, which adds to the system's complexity as well as introducing parasitics that diminish the sensor's desired BW. Figure 4.36(d) shows that the charge injected by the parasitics can be large enough to cause integration errors.

2) Active reset circuitry requires external control signals synchronized with switch cycles, which increases sensor complexity and may not be feasible in all applications.

3) Due to the very short time between the switch off-state and switching back on, it may be possible for the capacitor to not be fully discharged in high-frequency applications, which may result in an aggregated measurement error. It is important to investigate alternatives to reset-able RCs for measuring HF switch-currents, especially due to reasons number one and three.

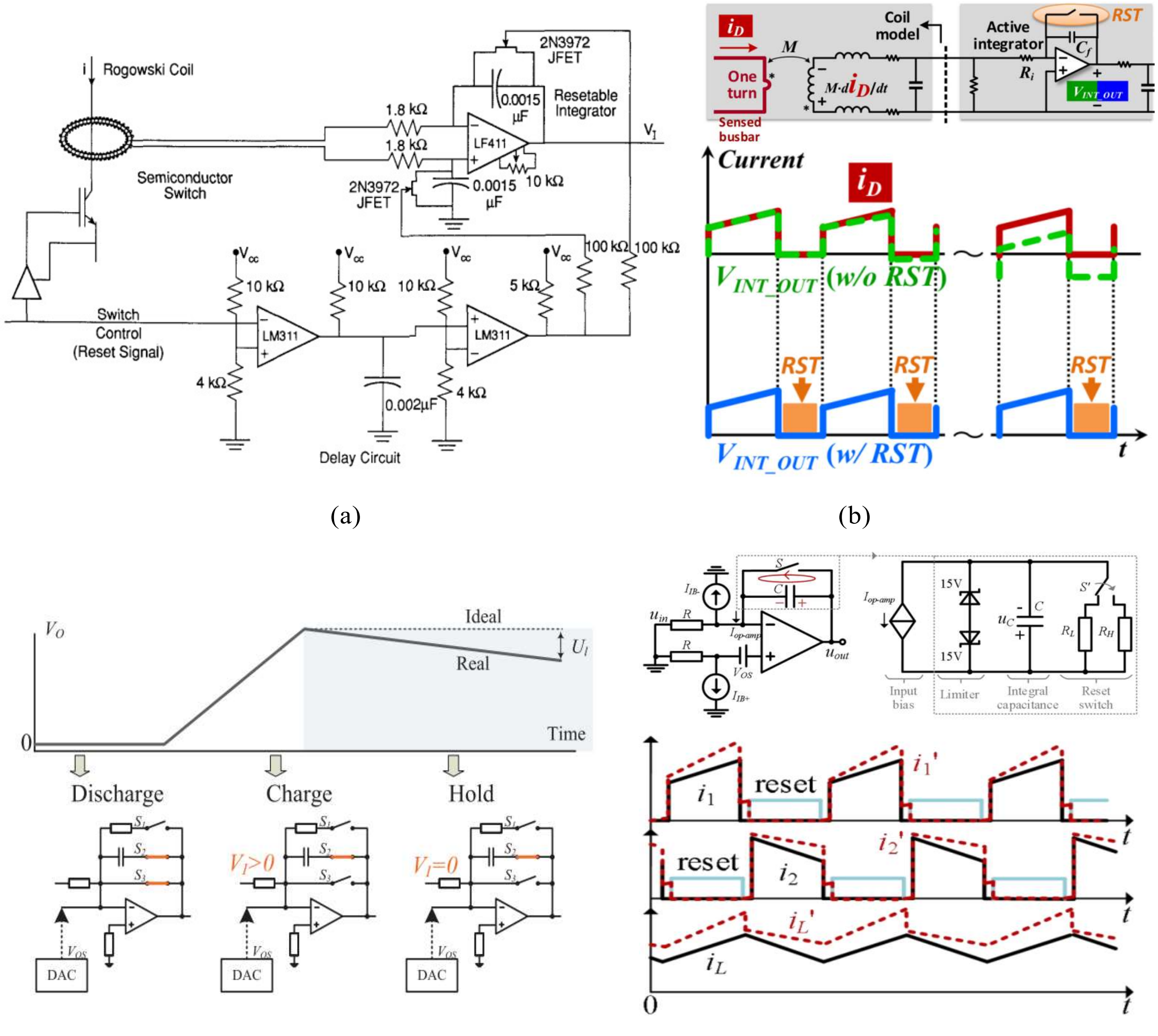

(a) (b)

(c) (d)

Figure 4.36: Resetting Rogowski coil: a) Resetting the capacitors of the hybrid integrator [180], b) Periodic reset effect [142], c) Conditional hybrid reset [172], and d) Reset non-idealities and its error coupling to the measurement [176].

4.4.2 Coupling Rogowski Coil with Precision Rectifiers

There has been evidence that resetting the RC may not be the best course of action for implementing it as a switch-current sensor in HF applications. One of the biggest issues with reset-able RC is the required time during off-state to discharge its integrator's capacitor, which is not a long enough time in HF switching frequencies with big switching duty ratios (typically 100 ns~1 us is usually the required time to discharge the capacitor, especially if the observed current is big). The reset signal must also be synchronized with the switching PWM signals, unless the complementary PWM signal for each switch-current sensor is used, which may also be too long-duration compared to what is required as a reset signal. This can in turn result in a misalignment of the reset signal and the switching PWM signals, leading to inaccurate measurements.

As indicated in Figure 4.37, AC square waveform rectification can be applied to the fully AC-coupled signal of RC reading switch currents (which can be achieved using a passive HPF with a cutoff frequency of approximately 100-400 Hz), which will result in a number close to the missing DC component value of the switch current. Traditionally, diode bridges and power rectifiers are not good choices for rectifiers, since the switches and diodes require either voltage drop or active signals in order to operate. Due to the absence of voltage drop or active signal, precision (full or half-wave) rectifiers based on opamps and diodes can be underutilized in such situations [165-167]. Figure 4.38 shows

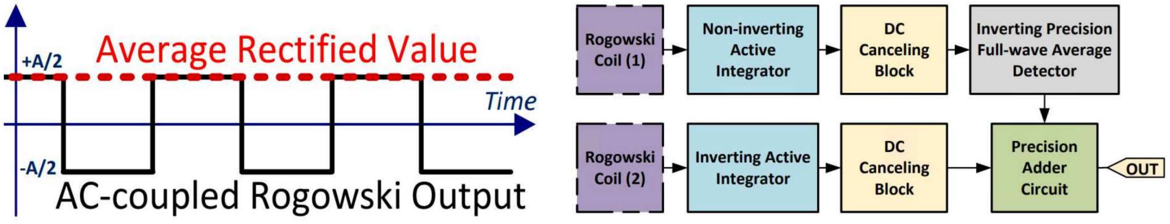

(a) (b)

Figure 4.37: Combinational Rogowski coil with rectifier: a) The idea behind it and b) Its block diagram [33].

three different models of precision rectifiers, of which Figure 4.38(a) shows a full-wave rectifier and Figures 4.38(b) and (c) are half-wave rectifiers.

In [33], the precision full-wave rectifier pictured in Figure 4.38(a) is incorporated into a structure shown in Figure 4.37(b), where a pair of RCs serve as a unidirectional switch. The precision full-wave rectifier enables the circuit to accurately rectify the input signal with low distortion. The RC pairs provide an additional level of filtering, allowing only the desired signal to pass through the circuit. The rectified signal will, assuming a unidirectional switching current, compensate for the missing DC value in the AC-coupled switch waveform. However, one could implement a single RC and terminate it with a precision half-wave rectifier from Figure 4.38(b) or (c), which is shown in Figure 4.39, in order to achieve the same function [48, 143, 144].

An inverting half-wave precision rectifier circuit is combined with the original AC-coupled RC (through an HPF) in Figure 4.39. When the switch is turned on, the inverting half-wave rectifier creates the inverse of the AC-coupled sensor's output during the off-cycle, and a zero value during the on-cycle [144]. This signal waveform is then fed forward (via R_{ff}) to the half-wave rectifier output, resulting in the full switch current waveform. Using this approach, the droop effect is eliminated immediately on every off-cycle, or in other words, it begins to cancel from the very first pulse, and the compensator ensures that the error does not increase over time [48].

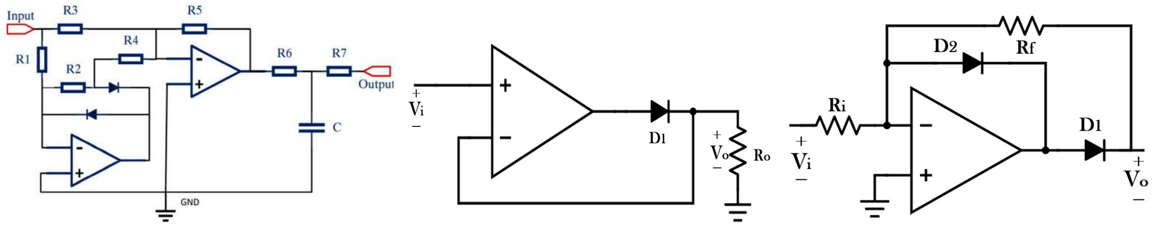

(a) (b) (c)

Figure 4.38: Precision rectifiers: a) Full-wave [33], b) half-wave (superdiode), and c) non-saturating half-wave [166].

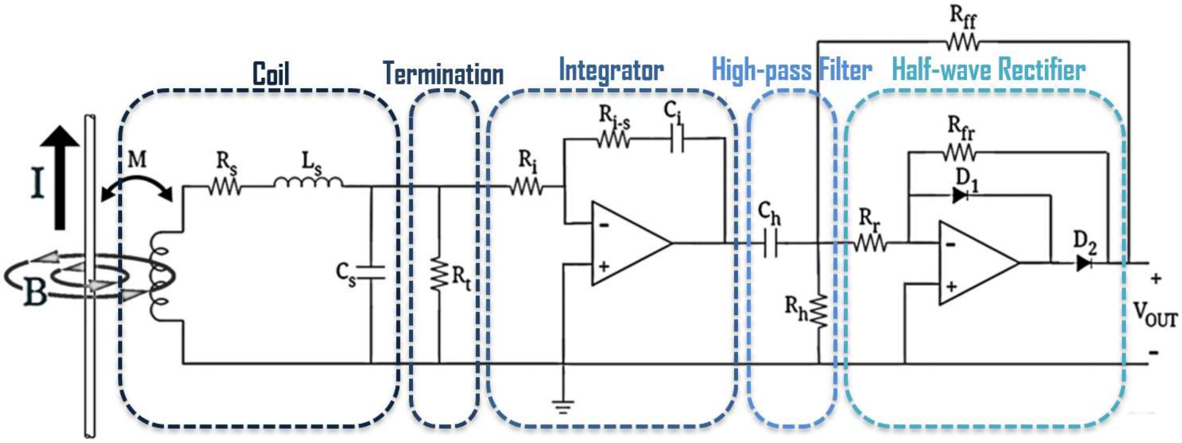

Figure 4.39: Unidirectional switch-current sensor proposed in [48, 144].

This type of switch-current sensor can be easily constructed and incorporated into double pulse testers (DPT) for characterization or monitoring. As shown in Figure 4.40, the prototype sensor based on Figure 4.39 circuitry is being used in a SiC-based DPT setup for characterization and shoot-through protection tests. Upon testing the sensor's accuracy, it was found to be within the desired range, demonstrating its value in a wide range of applications for measuring current in DPTs. In Figure 4.41, the switch-current waveform is displayed to verify the sensor's accuracy and high BW, while Figure 4.42 shows the results of the shoot-through protection test associated with the sensor. Based on the shoot-through test, a fault current of 240 A was extinguished in less than 500 nanoseconds using a

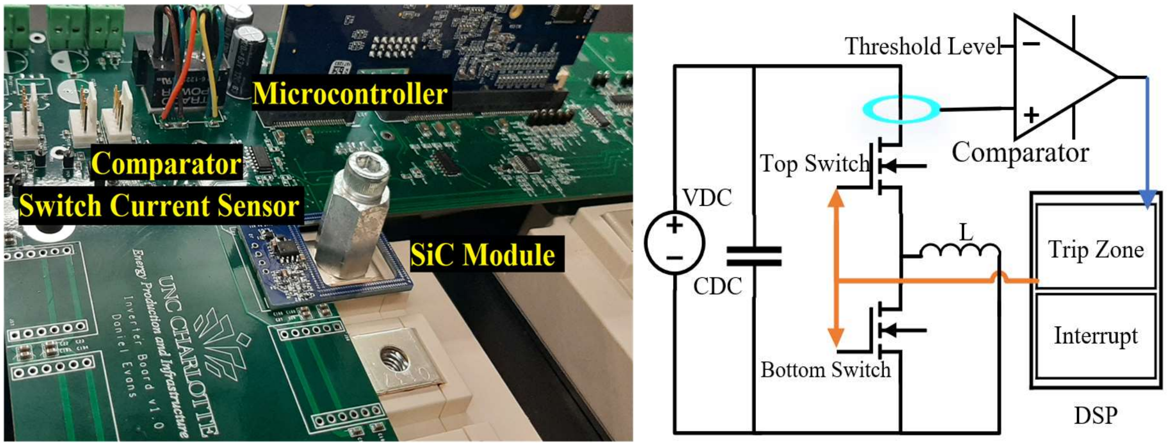

(a) (b)

Figure 4.40: Unidirectional switch-current sensor: a) Integration into DPT setup b) Protection scheme [48].

prototype switch-current sensor [48].

As compared to reset-able RC, this method has a number of advantages, including

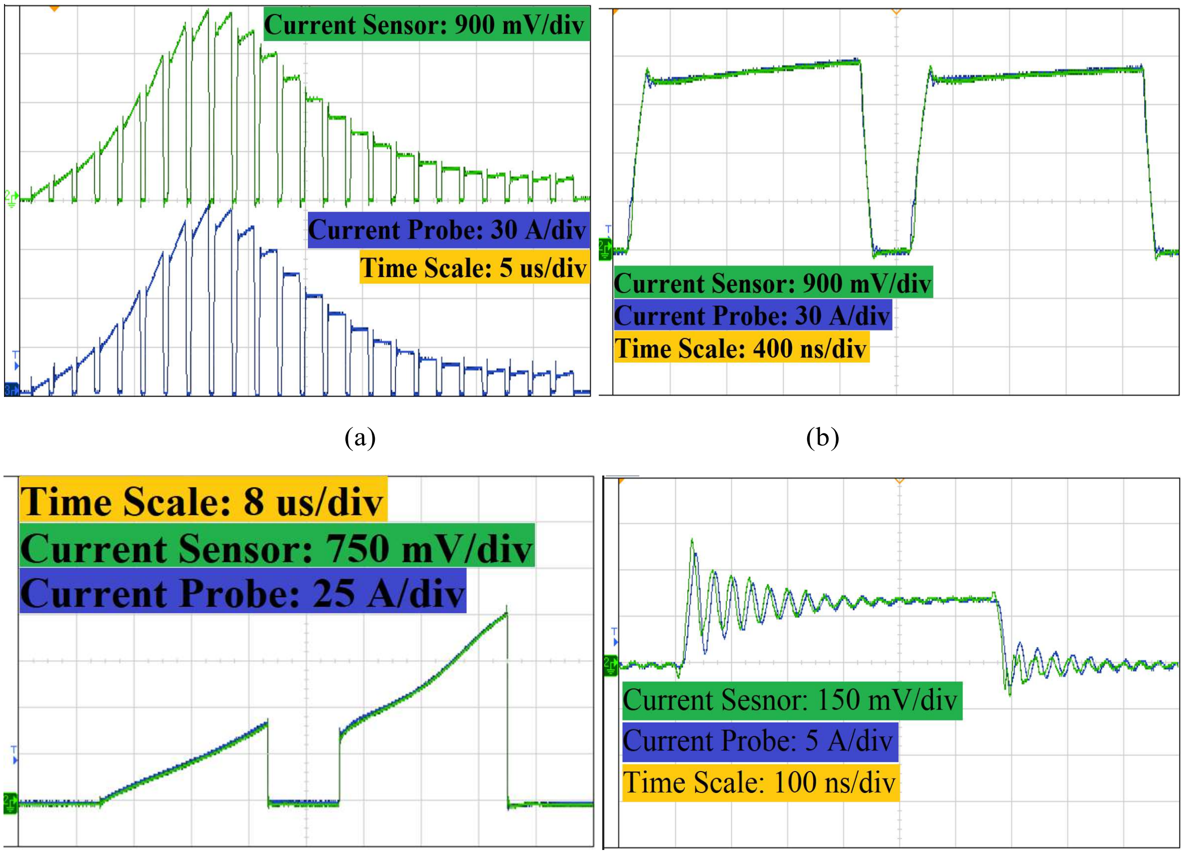

(a) (b)

(c) (d)

Figure 4.41: Unidirectional sensor’s switching current waveforms with different topologies and frequencies [48].

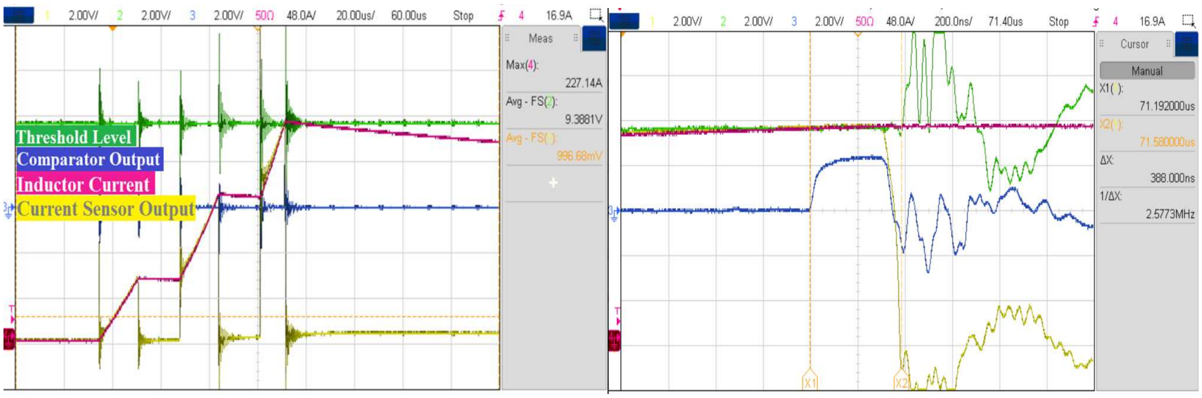

(a) (b)

Figure 4.42: Test results for the high-current shoot-through protection: a) Zoom-out on the three-pulse test, and b) Zoom-in on the fault clearing test [48].

the fact that there are no external reset circuits, no signal synchronization issues, and instant correction, which makes it an ideal solution for HF applications where the off-state time can be as short as 10 ns. It should be noted that the major limitation of this scheme is that it is only effective when switching currents are unidirectional. This means that it can only be applied to DPT or DC-DC power converters whose switch current is unidirectional.

4.4.3 Dual-Path Topology

It has previously been demonstrated that, although reset-able RC switch current sensors may provide sufficient performance for bidirectional applications at low switching frequencies, they are ineffective when switching frequencies exceed a few hundred kHz [33]. Conversely, precision-rectifier-based RC switch-current sensors can perform exceptionally well for applications operating at even MHz switching frequencies [144], however they are not suitable for applications with bidirectional switch-currents (such as in inverters or bidirectional DC-DC power converters) [48].

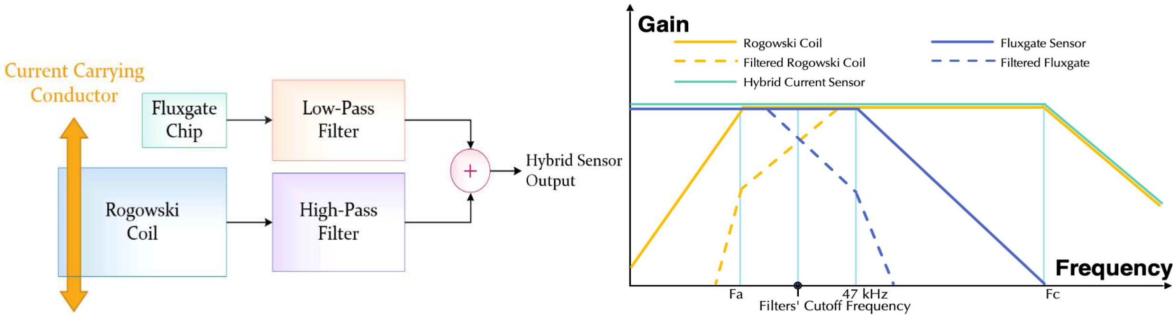

(a) (b)

Figure 4.43: The block diagram of the proposed hybrid current sensor (a), and its gain-frequency response (b) [203, 204].

It can be inferred from these two facts that a bidirectional switch-current sensor is required that performs well at switching frequencies over a few hundred kHz (or even a few MHz). In view of Chapter 3 information, UWB RC and an excellent quality contactless DC detector may constitute a viable MS topology. It has been demonstrated in Figures 3.30-32 that MS current sensors are already used for bidirectional switch-current sensing, but they all had issues related to size, invasiveness, or EMI immunity, which made them undesirable for HF switch-current measurements. UWB RC, however, provides a suitable solution to these issues. It is non-invasive, highly immune to EMI, and can be implemented in a relatively small size. Furthermore, it offers a high accuracy that is suitable for HF switch-current measurements.

Additionally, micro-FG ICs are widely recognized as the most accurate DC detectors among small contactless magnetometers [46]. Combined UWB RC and micro-FG may have good-enough qualities to serve as UWB contactless bidirectional switch-current sensors (Figure 4.43). By combining the design considerations discussed in Chapter 3 with the current chapter, the next chapter will provide guidelines for developing a contactless, light-size, bidirectional switch-current sensor that is noise-free and clean and has an accurate output using a micro-FG magnetometer and UWB RC.

4.5 Conclusion

As described in this chapter, switching current is the most challenging form of current to sense in power converters, and a variety of ideal switch-current sensor characteristics have been analyzed. As compared with other existing solutions, PCB-embedded RC sounded more practical to implement, for which all design parameters related to a UWB RC have been investigated, such as the coil and integrator design and their gain matching (Figure 4.44), and the layout of the sensor construction. Next, possible compensations have been analyzed to make the UWB RC a practical switch current sensor, including resetting and rectifying, as both have problems with either HF switching or bidirectional sensing. In conclusion, a bidirectional switch-current sensor based on UWB

RC that can operate at even HF switching frequencies has been proposed. A detailed analysis of the last solution will be presented in the following chapter.

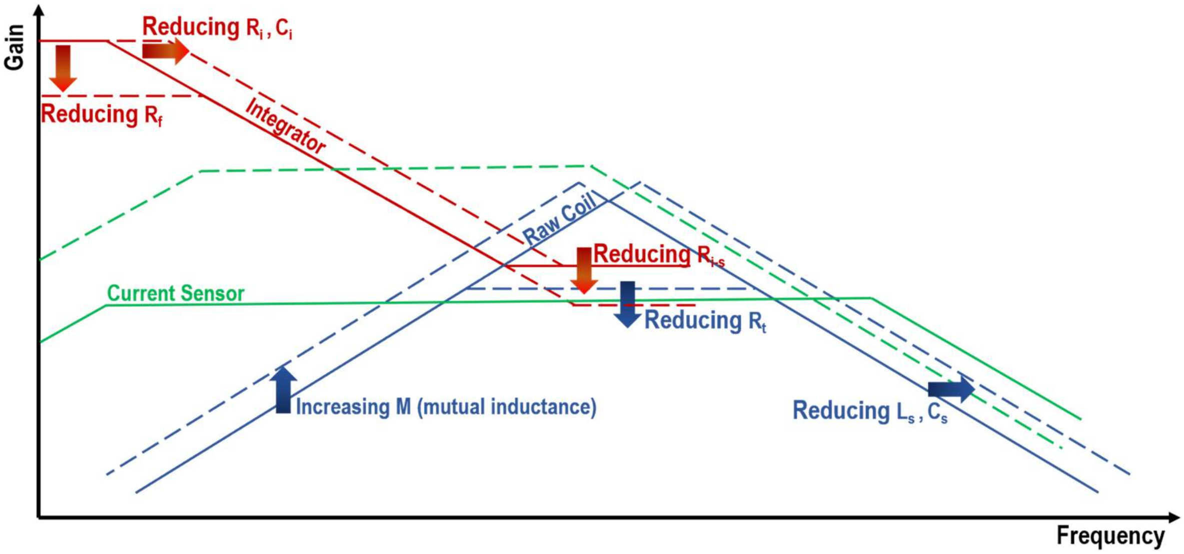

Figure 4.44: Gain matching in ultra-wideband Rogowski coil [48].

CHAPTER 5: ULTRA-WIDEBAND CONTACTLESS DC/AC CURRENT SENSORS

5.1 Introduction

In light of the three previous chapters, many of today's sensors are not suitable for HF WBG converters due to their size, EMI immunity, bandwidth, invasiveness, nonlinearity, cost, and accuracy [23-26]. This chapter addresses the issues mentioned in the previous chapter (including bidirectional measurement and lowering system complexity for HF switch-current sensing) by combining a contactless FG magnetic detector chip with a PCB-embedded UWB RC. This combination results in a compact, cost-effective, and accurate high-frequency sensing system, which is also immune to switching EMI noise and exhibits a wide measurement bandwidth. While the low-pass-filtered FG [61] or TMR [186] element accurately measures currents from DC to a few kHz, the RC is underutilized for detecting higher frequencies to cover frequencies upper than FG cutoff frequency up to dozens (or even hundreds) of MHz.

Combining scheme and guidelines from sections 2.2, 2.3, 3.3, 3.4, 4.3, and 4.4 can be viewed in Figure 5.1, which illustrates the placement of a micro-FG IC on the same PCB as the UWB RC to compensate for the lack of DC/LF sensing, in which most of the design considerations can be integrated into this easy-to-integrate scheme, such as lowpass

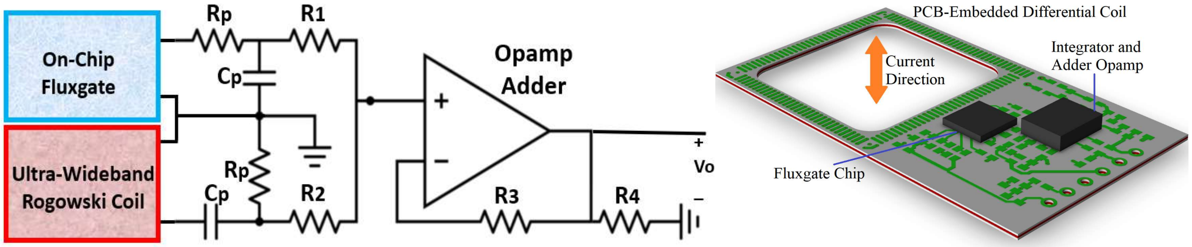

(a) (b)

Figure 5.1: The circuitry of the proposed dual-path current sensor (a), and one of its realizations (b) [203].

filtering the DC detector for greater noise immunity, highpass filtering the UWB RC for offset compensation (with the same cutoff frequency as the LPF of DC detector), gain and phase matching through an opamp adder system along with all other layout guidelines.

As a consequence of the RC element compensating for the frequency gap between the FG and the high-frequency elements (which a single coil can detect), both DC and HF currents are accurately measured by the same sensing system. Its ability to measure different types of currents against a DC-50 MHz current probe (Tektronix TCP305A [187]) verifies its superior performance in high-frequency power converters. From traction converters to telecommunications and digital power supplies, this sensing system can be proven successful in a wide range of applications as a future work task definition, in which its accuracy and reliability make it an ideal choice for measuring current in high-frequency power converters.

5.2 Bidirectional Sensing

During the last part of the previous chapter, it was stated that the use of precision rectifiers rather than resetting the RC can reduce or eliminate HF issues/burdens such as reset signal synchronization, the requirement for external reset circuitry (which introduces parasitic elements), or the too short time required for the capacitor(s) to be reset when the switch-current sensor is able to be reset. Yet, this does not apply to setups with both positive and negative DC switching currents, which means that they cannot correctly measure the bidirectional switch current. As can also be seen in Figure 4.34, RC switch-current sensors tend to droop due to the lack of DC/LF frequency components [188], which can be solved by using magnetic current sensors that measure bidirectional DC/LF components of the current accurately and noise-freely [189]. Based on these two facts, a suitable-size, noise-immune and DC-UHF MS sensing topology such as in Figure 4.43 can be built with the gain-Bode plot in Figure 4.34(b) to be employed as an HF bipolar switch-current sensor.

An effective bidirectional dual-path sensor (FG and RC), such as those shown in Figures 4.43 and 5.1, should have the same sensitivity and BW in both directions, making it possible for the sensor to accurately detect and measure signals coming from both directions. As a result, in addition to providing adequate noise immunity (so that measurements can be accurately and reliably made), both SS current sensors must offer the same response time, sensitivity, and range of bandwidth in both directions. A simple switch-current measurement can be used to test on-chip FGs by placing the sensor in two

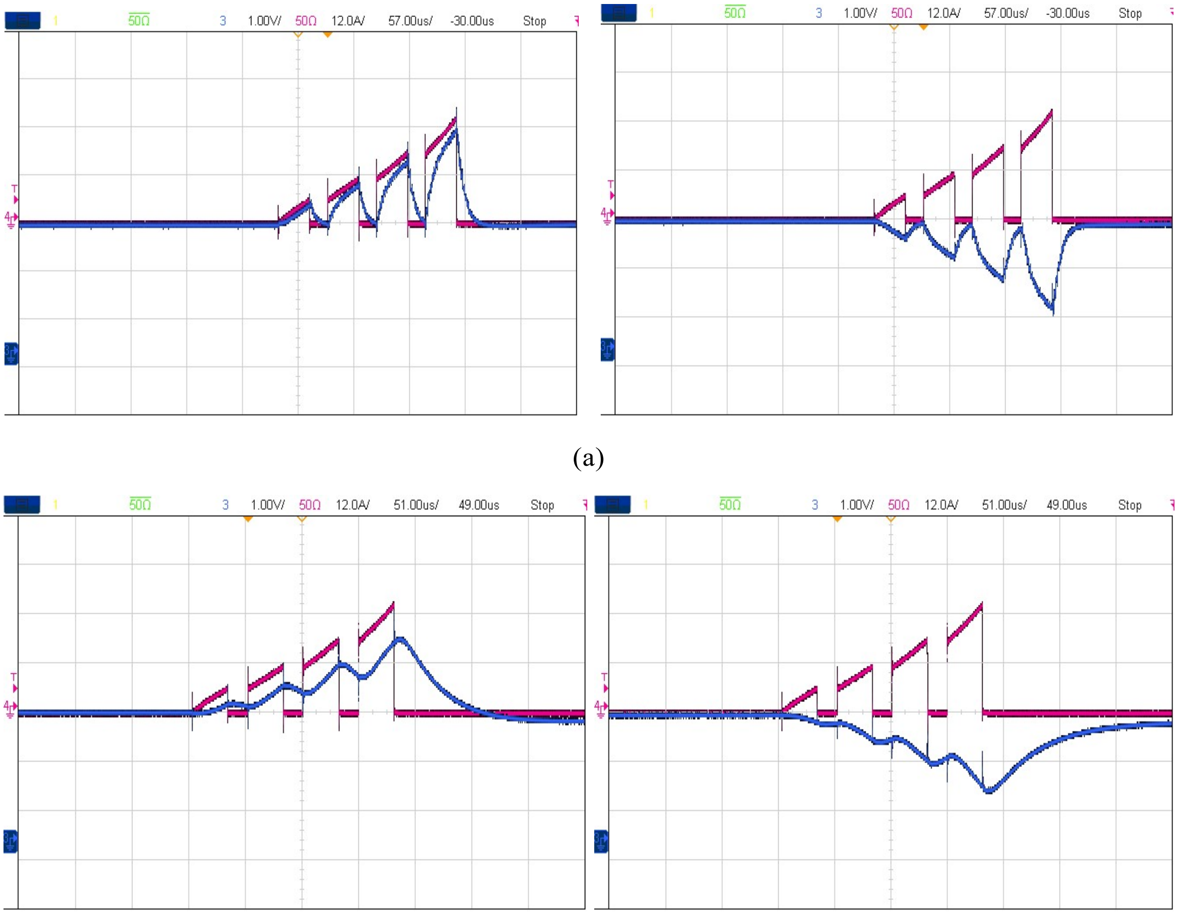

(a)

(b)

Figure 5.2: Micro-fluxgate bidirectional switching current waveforms: a) Raw output, and b) With an LPF.

identical conditions but with opposite directions in order to determine whether the output varies in either direction. A top-side switch-current was measured using a DPT setup in Figure 5.2, in which a micro-FG or DRV425 from TI [61] was placed at a predetermined distance and angle from the switch-current conductor, converting its magnetic flux density (B) to current by using (1.1), where the blue waveform represents DRV425 output compared to the magenta waveform representing Tektronix TCP305A DC-50 MHz current probe output. It is evident from Figure 5.2(a) that the DRV425 has a full bandwidth of 47 kHz for both directions, where the sensitivity can remain the same for both directions with the same LPF and cut-off frequency of 5 kHz in Figure 5.2(b). According to sections 2.2 and 2.3, FG has the best accuracy and noise-immunity among all DC magnetometers, as well as the least thermal and offset drift. This makes the DRV425 the ideal device to use for a broad range of applications, including automotive, consumer, and industrial. Overall, the DRV425 can provide the most accurate readings and the least drift with superior noise immunity. The next section will also investigate micro-FG's linearity and noise immunity to ensure that it is a suitable choice to be combined with UWB RC, using a 350 MHz oscilloscope [190].

Similarly, the UWB RC from Chapter 4 must be tested in the same manner as micro-FG to ensure that it can be used for bidirectional reading with the same accuracy. This can be accomplished through the construction of four differential PCB-embedded square-shaped helical coils with existing and proposed winding schemes (as shown in Figure 5.3), and the incorporation of an inverting integrator (for ease of frequency band control) to examine their BW and sensitivity in opposite switch-current directions. In Figure 5.3(b) and (c), the return path is incorporated in a more symmetrical manner than in Figure 5.3(a), while Figure 5.3(d) integrated the return path into the exiting winding (also referred to as double-winding). This double-winding configuration produces a more compact design and reduces the amount of copper required. Additionally, the double-winding configuration reduces the amount of capacitive coupling between the windings, leading to improved performance. In Figure 5.4, the switch-current readings for UWB RC current sensors (with the same circuitry) are shown (with the yellow waveform) in opposite directions in order to be compared (with the magenta waveform, which is the DC-50 MHz current probe) for more analytical purposes. Clearly, there will be differences in the bidirectional switch-current readings due to the return path, since many other circuit parameters and topologies in these four RCs are the same (integrator topology, HPF, coil

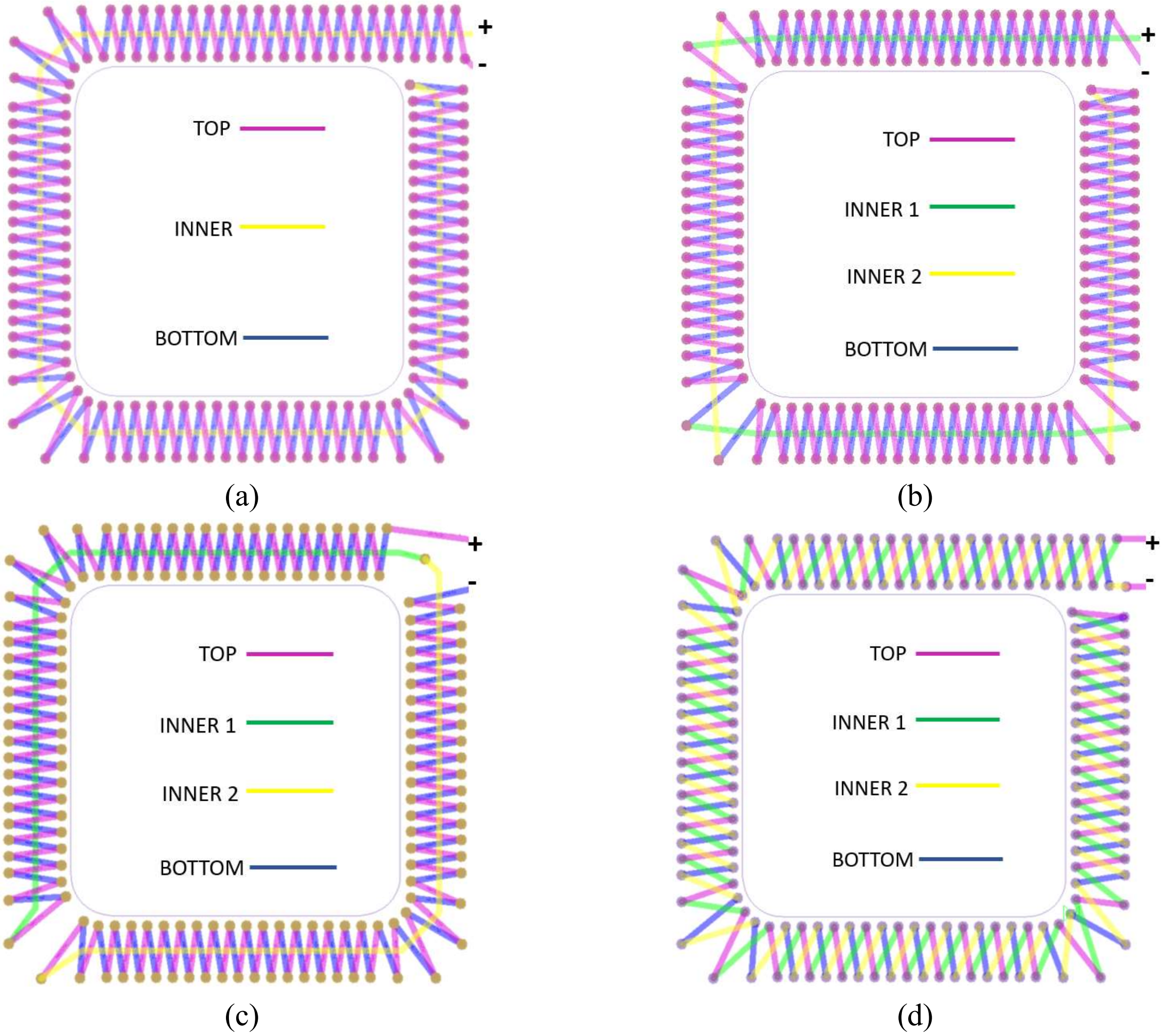

Figure 5.3: Various differential winding schemes for Rogowski coil's bidirectional switch-current test.

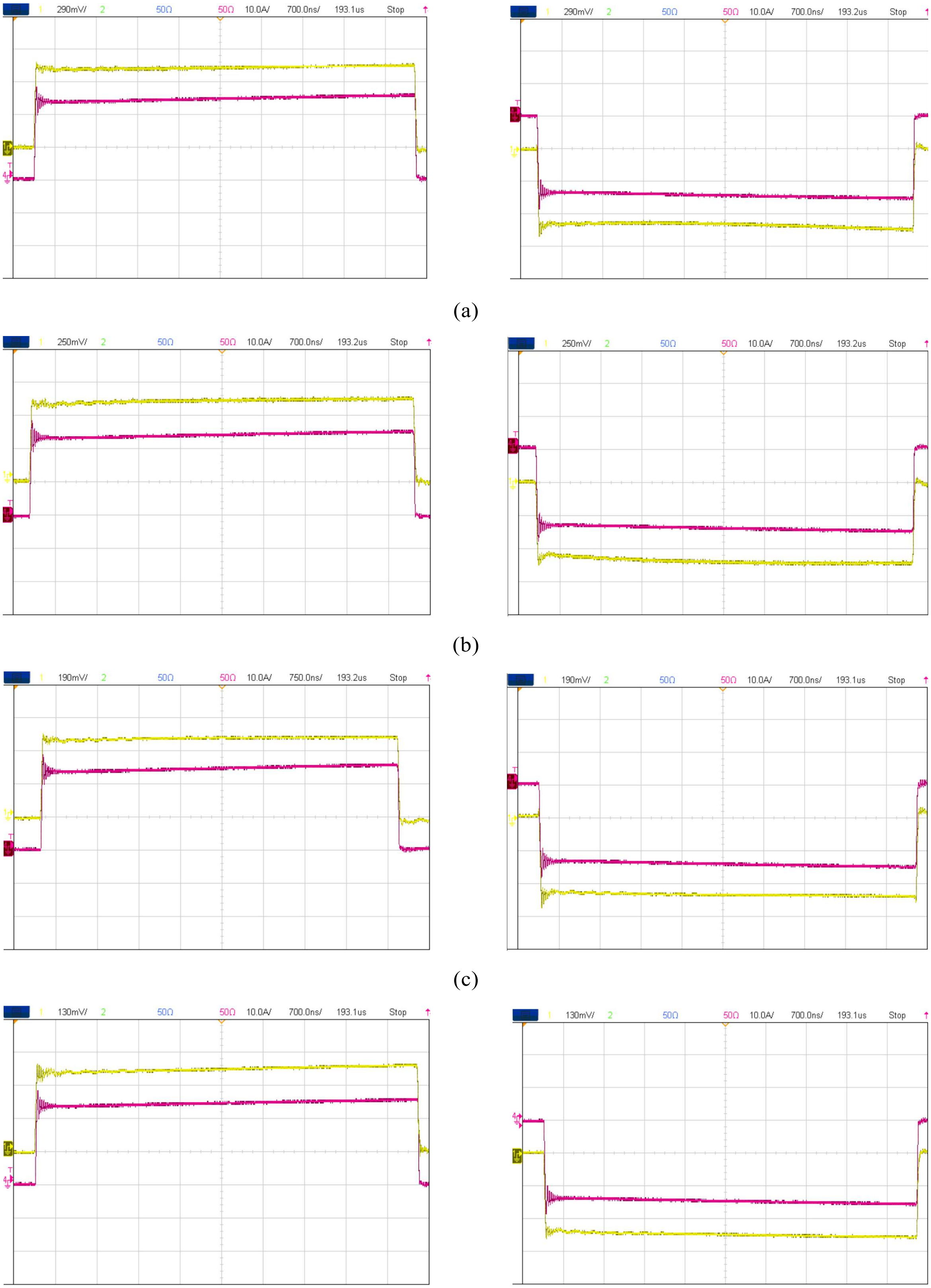

(a)

(b)

(c)

(d)

Figure 5.4: Bidirectional switch-currents with PCB-embedded Rogowski coil built with coils of figure 5.3.

termination, etc.). As illustrated in Figure 5.4(a), both sensitivity (the magnitude of the output of the current sensor at steady state) and BW (the rising and falling edges and the ringing frequency and amplitude) differ. As shown in Figure 5.4(b), the difference between sensitivity and BW in opposite directions is less than what is seen in Figure 5.4(a), however, the amount of error sensed in opposite directions is not negligible. It is evident from Figure 5.4(c) that the symmetrical results are substantially better than those in the previous two coils, where there is still a non-negligible difference between ringing in opposite directions. This could be due to the more symmetrical distribution in coil 5.3(d), which results in waveforms that are more similar in two opposite directions, thereby proving to be the best symmetrical results upstream from these four fabricated RCs. This finding indicates that the symmetrical distribution of the coils with regards to its return loop can be a major factor in generating the most symmetrical results. Table 5.1 provides the calculated electrical parameters of these four coils in order to explore the reasons behind double winding coil geometry in which symmetrical coil distributions should be preferred in order to obtain the best symmetrical results.

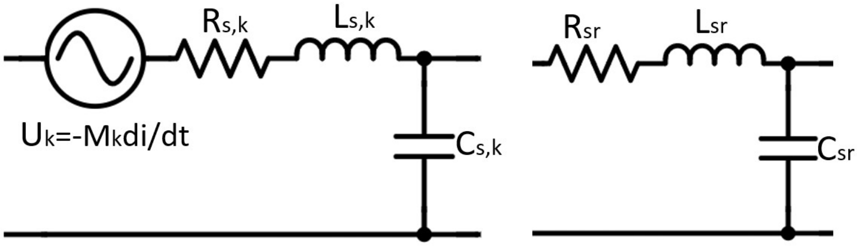

(a) (b)

Figure 5.5: The lumped parameter model of each coil winding (a), and the return path (b).

Table 5.1: Electrical properties of the coils in Figure 5.3.

Coil-Property	***M (nH)***	***L_s (nH)***	***C_s (pF)***	***R_s (mΩ)***
A	10	407	48	598
B	10	418	46	603
C	10	412	47	601
D	9	364	29	580

In the previous chapter, sufficient formulas have been presented for all of the coil's electrical parameters (each winding turn and their sum). Therefore, it may be possible to consider the distributed model of coil electrical parameters [191-200], which can also consider variations in the return path. This approach allows for a more accurate estimation of the total electrical parameters of the coils. Also, it can provide insight into the electrical properties of coils with different wiring/return path schemes. According to Figure 5.5, the associated parameter for each turn of the winding as well as the path of return can be seen.

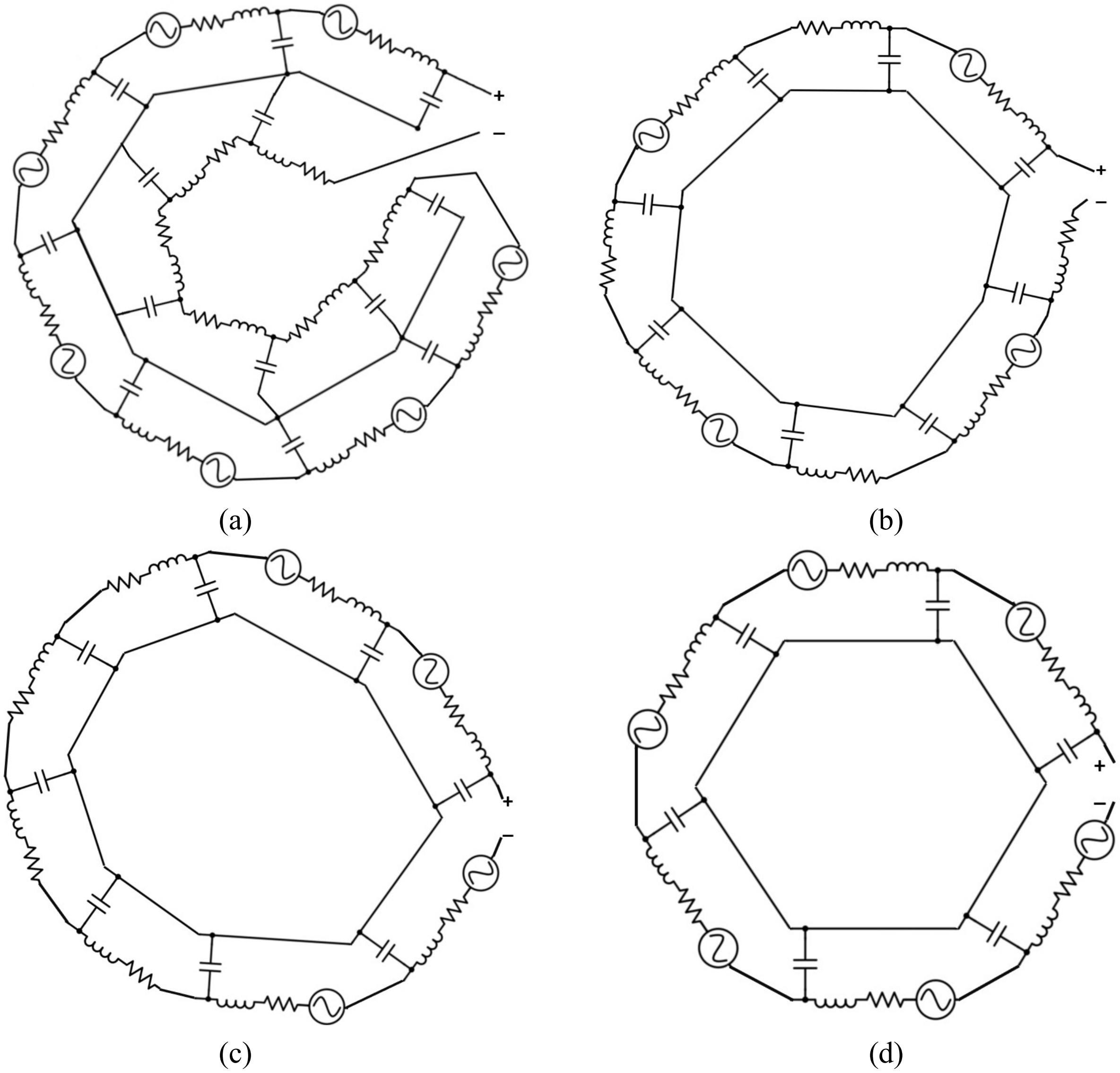

(a) (b)

(c) (d)

Figure 5.6: Various differential winding schemes (from Figure 5.3) distributed coil lumped model.

By extending the models in Figure 5.5 as in Figure 5.6, it is possible to obtain an even more accurate model of electrical parameters for each of the four winding schemes shown in Figure 5.3.

Figure 5.6 shows that double winding provides the best symmetrical distribution in comparison with the three other methods, and also has the least parasitic *RLC* embedded in windings. In addition, as one goes from (a) to (d), the symmetrical distribution of elements increases. A list of differences in the coil design can be used to determine why the coil (d) has the best bidirectional performance in comparison to others:

1) The mutual inductance of the coil (d) is less than three other winding methods, due to utilizing one of bottom/top layer along with an internal layer for each turn, which results in less effective coil cross-section area. Nevertheless, the lower M simply indicates a lower SNR for coil (d), which could have the least relation to the sensitivity difference in bidirectional sensing.

2) It is observed that the parasitic values of coil (d) are significantly less than those of three other models, in which C_s has the largest difference compared to R_s and L_s in the other coils (C_s of coil (d) is approximately 60% of the other coil's C_s, while R_s and L_s are approximately 85~90%).

3) Coil (d) has a greater number of distributed signals than the other three, allowing the coil termination to face the same impedance from each terminal independent from the signal polarity.

A lower parasitic capacitance and a symmetrical distribution seem more likely to improve bidirectional sensing performance among the above reasons. Compared to the other three coils, coil (d) has a higher resonance frequency (which is another indication that parasitic inductances and capacitances have been reduced), which implies that it may be used in a wider frequency range.

Further, the lower parasitic capacitance in general minimizes the noise and interference generated by the coil [200]. As HF sensing faces high *dV/dt*, parasitic capacitance appears to cause destructive currents at transient moments in the grounding of the sensor system, and their intensity depends on the polarity of the sensed signal and the grounding/terminating polarity. Accordingly, a large C_s will cause totally different HF components (ringing in the switch-current) for readings in opposite directions. During steady state, a large-enough parasitic capacitance can couple with a small periodic voltage at the coil termination. This voltage may cause differences in sensitivity in opposite directions when using opamp-integrators, along with other sensing errors associated with the termination of the opamp, which may also explain some of the reading differences in Figure 5.4. Increasing the distribution of parasitics within coil windings can significantly reduce unfavorable parasitic effects on signal polarity-based sensed differences. As such, carefully controlling the coil winding distribution is essential for achieving accurate signal polarity-based sensing. For this reason, it is important to optimize the design of the windings to ensure the desired distribution of parasitics, which will be essential for achieving the desired level of signal accuracy.

In order to verify the assumptions behind the bidirectional reading errors, another coil geometry can be constructed using the same integrator and circuitry system, with well-distributed differential windings and a small parasitic capacitance, for which the same test procedure can be used. The results of the tests can then be compared to the assumptions, and the validity of the assumptions can be determined. This process will provide valuable insight on how to improve the system and ensure the accuracy of the results. The pick-up coil shown in Figure 4.19 was selected for this purpose, and a prototype sensor and its bidirectional reading are shown in Figure 5.7. The Magenta waveform, which represents a DC-50MHz current probe used for measurement, indicates that there is an increased level of similarity in both transients and steady state (yellow indicates the sensor output relative to the Magenta reference waveform) than even the double winding coil (d) in Figure 5.4 (d), resulting from both a symmetrical distribution and a much lower stray capacitance (8 pF for the coil in Figure 5.7, against 29 pF in table 5.1).

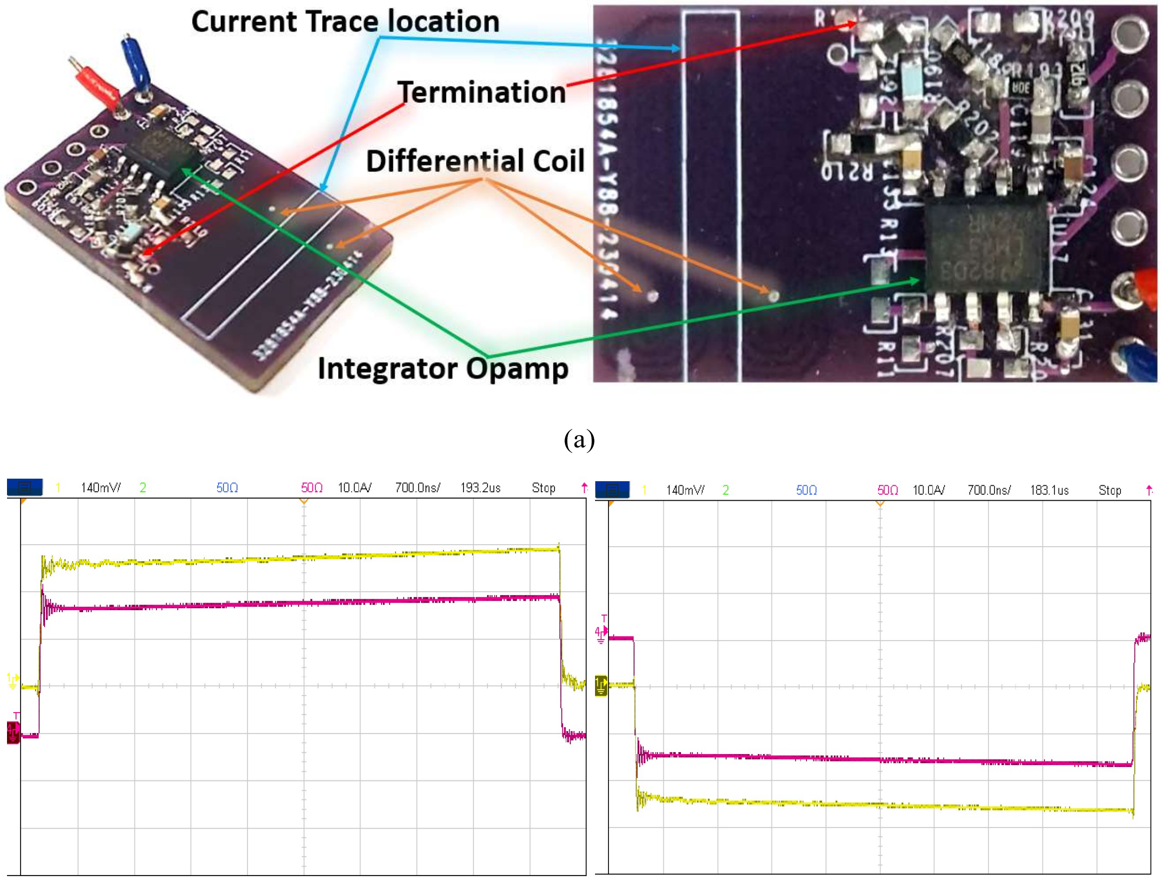

(a)

(b)

Figure 5.7: Bidirectional switch-current sensing (b) using RC with pick-up coil of figure 4.19 (a).

5.3 DC Magnetometer Performance at Switching Nodes

According to one of the previous statements, most magnetometers cannot reach a BW range of more than a few hundred kHz (except for some MRs that can go to a few

MHz), but that is not the only issue they face. As a result of their physical properties (metal plains, internal windings, or conductors) [201], most of them are susceptible to EMI emission/radiation/coupling near the switching node in power converters. There are several methods of reducing coupled noise currents, one of which is minimizing stray capacitance (by reducing conductor areas and increasing the distance between conductors from section 4.3.1), which is not always feasible in internal circuits of schemes that use metal plains, such as HE or large MRs. As well, in order to minimize the EMI noise voltage induced by the circuit, the parasitic inductance must be lowered, which is not fully feasible in schemes with a large number of internal windings or conductors, however the effect can be decreased by minimizing the parasitic inductance of the supply and conditioning circuits. Additionally, the use of differential or differential-like schemes with high-impedance voltage references can also help lower the EMI noise coupling. Shielding and filtering techniques can also be used to reduce EMI noise reaching sensitive circuits, depending on their applications.

Since discussed in section 3.3, FG and MR are candidates for DC sensing at the switching node. Hence, a micro-FG detector (DRV425) has been selected as the DC/LF detector in a dual-path MS topology, due to the fact that FG sensors/probes are widely recognized as the most accurate and noise-free DC magnetometers. In addition to verifying the bidirectional functionality of micro-FG and UWB RC, the output signal quality of UWB RC has been extensively presented in the previous chapter. This section compares the raw and low-pass-filtered switch-current output of the DRV425 to a well-known high-quality DC magnetometer such as a TMR that is used in our experiments (TMR2111S) [186]. As illustrated in Figure 5.8, oscilloscope captures were taken during the tests to clarify the results, in which the magenta waveform represents the DC-50MHz probe used as a reference and the yellow waveform represents the output of the magnetometer.

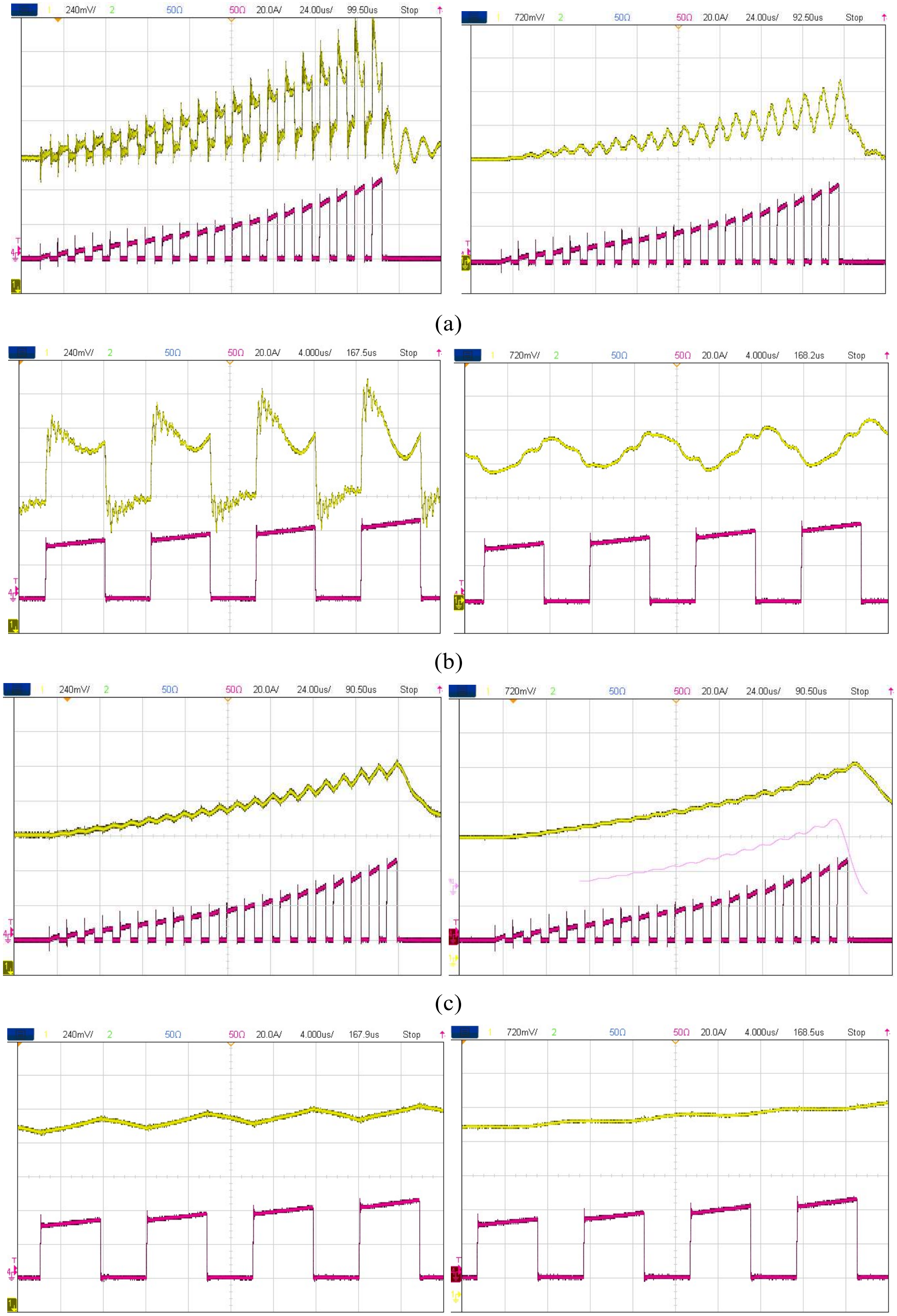

(a)

(b)

(c)

(d)

Figure 5.8: TMR2111S (Right) vs. DRV425(Left) switch current performance: a) Raw zoom-out of multiple 100kHz pulses, b) raw zoom-in capture, c) Zoom-out with a 15 kHz LPF, and d) Their zoom-in captures.

From 5.8 (a), it is apparent that TMR has a much wider BW (over 1 MHz) than micro-FG (47 kHz), which contributes to a much faster rising time for TMR. However, there is a substantial amount of induced/coupled EMI associated with the TMR output, which results in accumulating offset drift as well as a number of other linearity errors. Figure 5.8(b) shows the zoomed-in version of Figure 5.8(a), which highlights the measurement errors associated with non-filtered TMR. In order to eliminate/reduce the nonlinear measurement errors associated with these two magnetometers, a passive LPF with a 15 kHz cutoff frequency can be applied to their outputs, although this sacrifices the BW of the DC current sensor (it is already mentioned in chapter III that a lower cutoff frequency is more suitable for MS topology, and the HF detector will handle the remaining BW). This ensures that the overall noise level of the system is reduced, and the signal quality is preserved. An additional benefit is that the DC current sensor now has an increased resolution, allowing for more accurate measurements. Captures in Figure 5.8(c) are much cleaner than Figure 5.8(a), due to the effect of low-pass-filtering of most unwanted HF components. It is evident in this case that TMR output differs from FG output in that the TMR capture has sharp edges in contrast to FG capture. For rounded edges in FG capture, a LPF function of the oscilloscope is applied to the current reference in micro-FG scope capture (the pink waveform is a virtually low-pass filtered representation of the magenta waveform) in order to make it easier to comprehend. According to the pink waveform of the LFP function in oscilloscope, micro-FG output is similar to a 100 kHz switch-current when a LPF is applied.

TMR may experience sharp edges due to the induced/coupled EMI effect, which means that a lower cutoff frequency may be required to achieve error-free (or less error) operation. The experimental results show that the DRV425 is capable of providing accurate and reliable measurements in a variety of circumstances much better than the

TMR chip. Furthermore, the low-pass-filtered output of the DRV425 is found to be highly consistent in contrast with the output of the TMR2111S, which suggests that the DRV425 is a more suitable choice for our purposes. In this instance, TMR has only one advantage over FG ICs, namely its higher BW which is insignificant for our application. Despite this, the TMR can still be used to measure ultrahigh currents in applications such as power line protection and monitoring.

5.4 Ultra-Wideband Dual-Path Sensor Fabrication

In accordance with section 3.3 (compensated MS current sensor topology), micro-FG along with UWB RC have been selected for construction of a contactless DC-UHF current sensor as shown in Figure 4.43. In addition to the detailed BW (shown in Figure 4.43), Figure 5.1 illustrates a realization of the actual dimensions and geometry of the MS current sensor. This sensor is fabricated using DRV425 (the on-chip FG), with a measurement range of ±2 mT and a smaller footprint than the dual-opamp SOIC8, which is ideal for integration. With FG and RC performing accurately within their predetermined BW, the proposed sensor can measure a wide range of frequencies, and its high precision and accuracy would make it suitable for a variety of applications. As part of this study, micro-FG and UWB RC are analyzed to determine if the required signal quality and DC/LF performance can be achieved bidirectionally under high EMI emissions, for which both RC and FG elements appear to be suitable options. Thus, alternative implementations can be defined for applications such as GaN surface measurement and on-trace current sensing, in which the UWB RC shown in Figure 5.7 can also serve as the HF sensing part, as shown by Figure 5.9, where the FG IC can, for example, be mounted on the same PCB as the UWB RC. For better accuracy, one can combine an array of FG ICs stacked on the UWB RC as shown in Figure 5.9(b), which can even be extended for fully DC differential sensing by adding another FG PCB underneath the current carrying trace (or lateral GaN).

Due to the substantial differences in effective distance and angle as well as the magnitude of the trace current, the effect of external/random DC/LF magnetic fields on such on-trace sensing schemes is extremely negligible when compared with the field magnitude of the target current. This means one FG sensor as in Figure 5.9(a) can be enough for the sensed current quality, which significantly helps to reduce the size and number of the sensor's components. As a result, UWB RC can be used for surface sensing, where it provides a viable solution for measurement applications, with the potential to reduce the complexity of the sensing architecture.

The last statements can also be applied to dual-path current sensors implemented with the helical coils of Figure 5.3 (about simplifying the number of components required in the geometry of figure 5.1). Typically, these coils are used to measure the currents in power modules (such as SiC leg modules) and vertical power switches (such as single SiC Mosfets). Figure 5.10 illustrates some of the potential effects of interfering fields on SiC power semiconductors. With SiC modules (Figure 5.10(a)), there is a possibility that adjacent conductors or phases will induce a non-related voltage due to their interfering magnetic fields. In particular, the bottom switch source, which carries the current I_2, may create an interfering field (B_2) that makes it complicated to measure the exact magnetic field B_1 (which is used to extract the DC value of I_1), since the magnitude of B_2 divided by B_1 can be calculated using formula (2.1) as in (5.1):

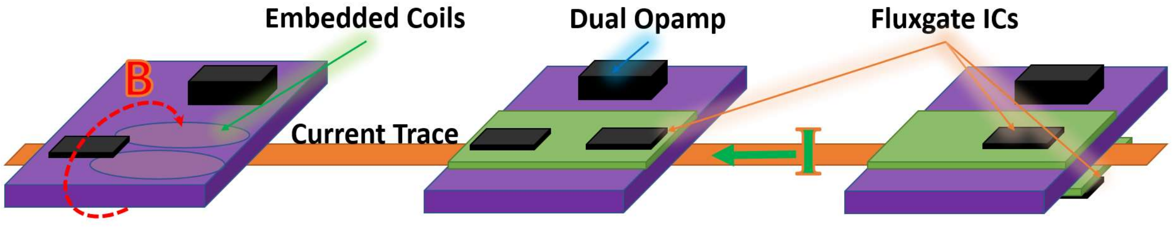

(a) (b) (c)

Figure 5.9: The on-trace realizations of the proposed dual-path current sensor: a) Both sensors on the same PCB, b) Stacked Sensors, and c) both-trace-sides stacked sensor PCBs for full-differential sensing [205].

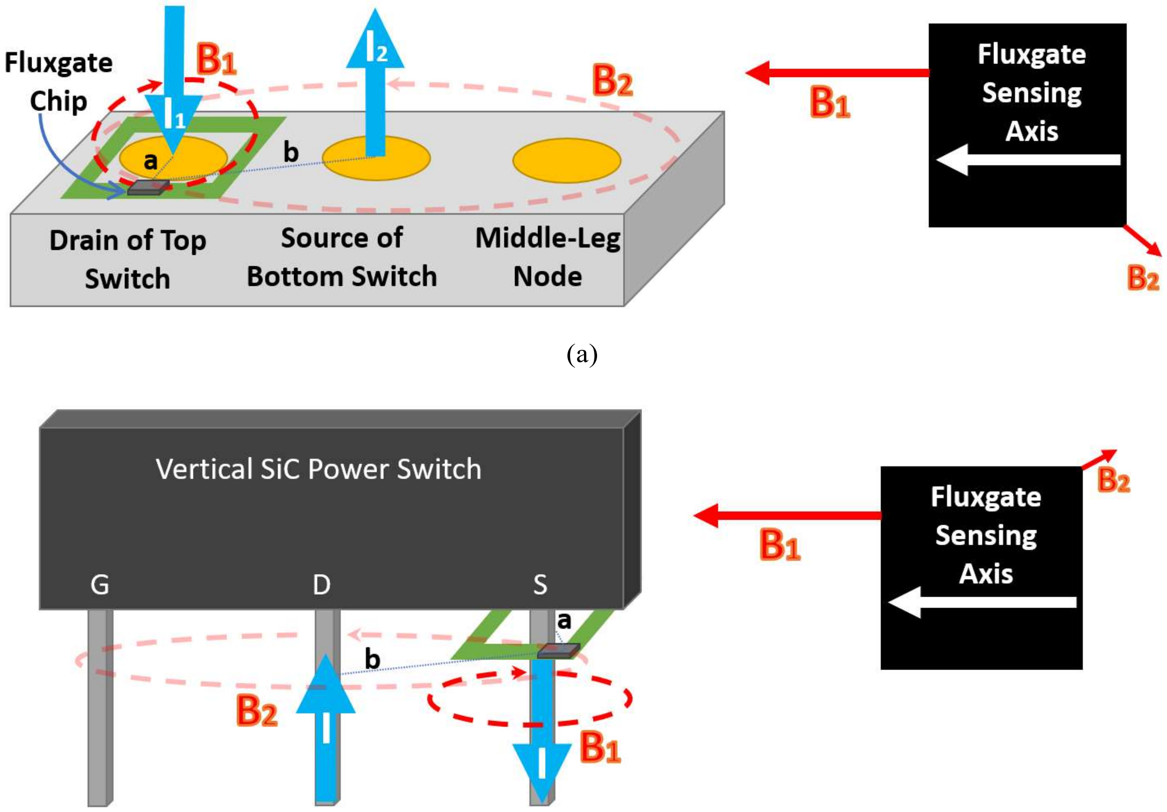

(a)

(b)

Figure 5.10: Possible disturbing fields impact in SiC power switches: a) The module, and b) The vertical switch [203].

$$\frac{B_2}{B_1} = \frac{I_2 . a^2}{I_1 b \sqrt{b^2 - a^2}} \tag{5.1}$$

where a corresponds to the distance between the micro-FG and the primary conductor, and b represents the distance between the micro-FG and the adjacent conductor. The following two considerations must be considered:

1) The closer the micro-FG is placed to its corresponding conductor, the smaller the error; for instance, if the micro-FG position determines an a 5 times smaller than b, B_2 will be less than 5% of B_1 (with considering equal I_1 and I_2), while with an a 10 times smaller than b, this error could be around 1%.

2) This is a half-bridge power module with a top and bottom switch inside. From power electronics knowledge, it is critical to note that top and bottom switches in a half-bridge leg never turn on at the same time, which will result in a short circuit at the DC input of the converter if they do so. Since the calculated error of the adjacent switch does not appear in the on-time magnitude, it will only have a minimal impact on the off-time switch current (which is supposed to be zero at steady-state).

Overall, the micro-FG should be placed in a position that maximizes the sensed current accuracy. All of these statements can be true in power converters composed of multiple vertical single switches on different legs and phases, in which the placement of the FG-sensor can be optimized to eliminate interference as much as possible. Even so, for each switch in Figure 5.10(b), the exact current entering its drain will return from its source, which simplifies the formula (5.1) to (5.2):

$$\frac{B_2}{B_1} = \frac{a^2}{b\sqrt{b^2 - a^2}} \tag{5.2}$$

The last formula does not depend on current, so it is possible to determine the exact switch current by placing FG at a fixed distance and considering the exact return field impact. Having established enough reasons to use the proposed MS current sensor topology with a minimum number of micro-FG sensors, it is worth mentioning that fewer components and simpler circuitry are more advantageous based on the following:

1) The size of a sensor is generally smaller when there are fewer components and processing circuits, which makes it easier to integrate it in limited spaces.

2) Simple circuits with fewer components are less likely to fail to deliver a sufficient-quality output signal in high-EMI environments.

3) Complex circuits need more connections and conductor traces, leading to higher parasitic element values. Apart from the negative effects of EMI coupling, the internal signals will be subjected to a lot of undesirable zeros, poles, and distortions.

Four different MS sensors are developed and manufactured according to the guidelines provided earlier in this chapter, as shown in figure 5.11 (one RC + FG for SiC power modules (figure 5.11(a) and one RC + TMR for SiC power modules (figure 5.11(b)), one small RC + FG for vertical SiC single Mosfets (figure 5.11(c)), and one with on-trace RC stacked with micro-FG PCB for surface current sensing (or lateral GaN) is shown in figure 5.11(d)). Furthermore, the sensors have been tested with a variety of power semiconductors in order to evaluate the performance of their sensing capabilities, which will be discussed in the following section.

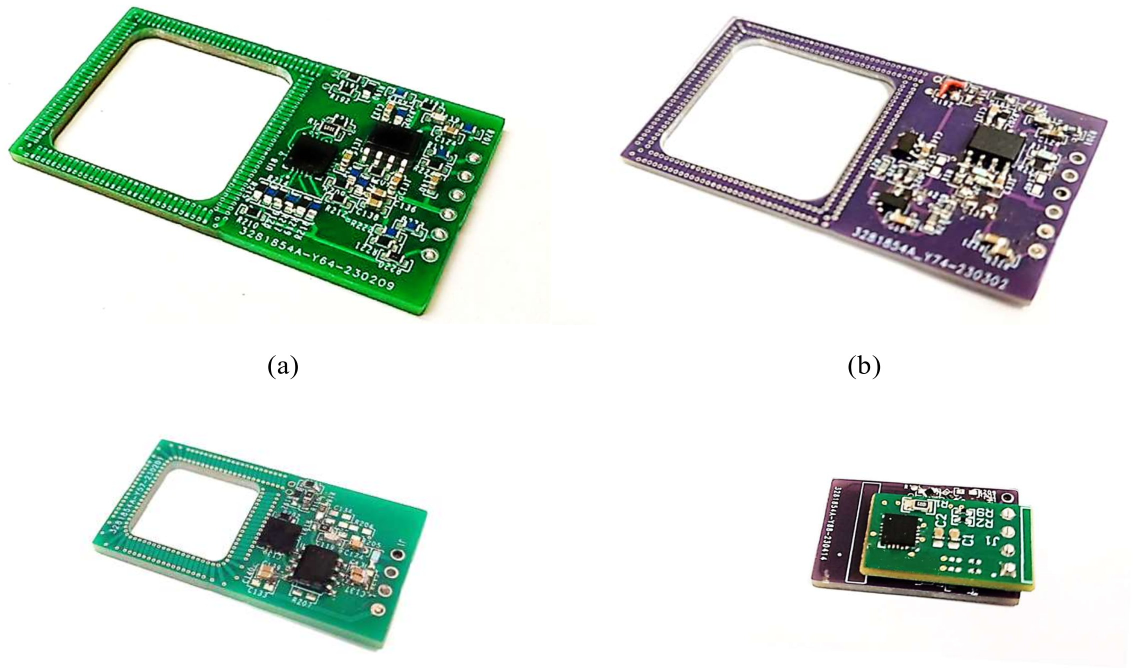

(a) (b)

(c) (d)

Figure 5.11: Different prototypes of dual-scheme current sensors.

5.5 Results and Analysis of Experimental Studies

During this section, further tests will be conducted on the fabricated dual-path sensors, including the frequency response test with a vector network analyzer as well as current measurements for semiconductor switches (or other current types within WBG power converters), which may provide significant insight into the optimal current sensor design for WBG power converters by enabling further evaluation of the dual-path sensors. For example, the frequency response test can help determine the accuracy of the dual-path sensors by comparing their response to a reference signal. This testing will be used to evaluate the accuracy and effectiveness of the dual-path sensors by comparing them against a high-quality DC-50 MHz current probe (Tektronix TCP305A), which will allow any adjustments to the sensors to be made based on the results. As the famous Italian

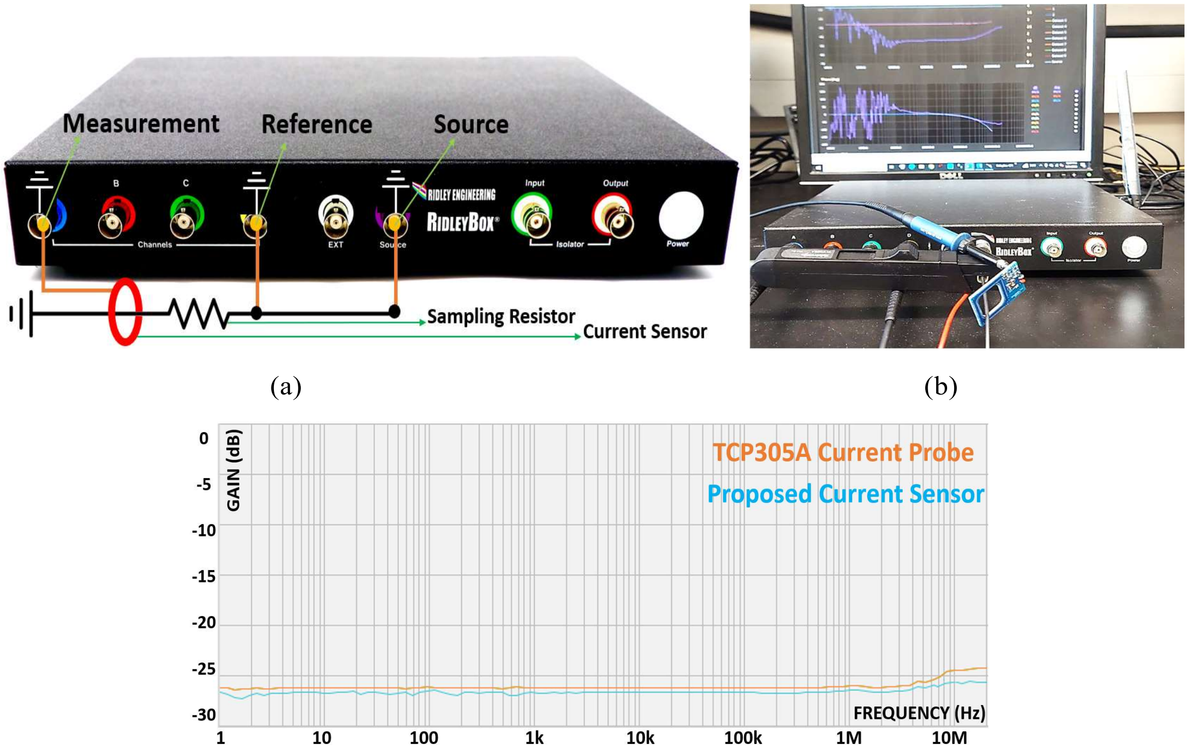

(a)

(b)

(c)

Figure 5.12: Vector network analyzer measurement: a) Ridley Box [206] setup for current sensor evaluation, b) Gain-Bode plot of the sensor in figure 5.11(c), and c) Our VNA setup [203, 204].

astronomer Galileo Galilei once said: “Measure what can be measured and make measurable what cannot be measured.”. Figure 12(a) illustrates how VNAs can calculate the physical BW of a current sensor, enabling a more precise evaluation of the sensor's performance over its defined frequency range. The gain Bode plot of the fabricated sensor (from Figure 5.11(c)) is shown in Figure 5.12(b) deploying a Ridley box VNA [206]. Figure 5.12(c) shows the same VNA setup used to verify the fabricated sensor's gain-frequency response quality. The Tektronix DC-50 MHz current probe (TCP305A) BW was also incorporated into the same Bode plot to verify the sensor's gain-frequency response quality. The results demonstrate that the fabricated sensor exhibits excellent gain-frequency response quality. According to the gain-frequency curve, the prototyped dual-path current sensor has a BW much higher than 20 MHz, which is easily confirmed by the almost linear response curve over a frequency range of 1 Hz to 20 MHz (the upper band of the VNA).

To evaluate the sensor's functionality in their actual application, a series of experiments can be conducted at the switch nodes of power converters (especially for switch-current measurement), which is very challenging for current sensors to maintain

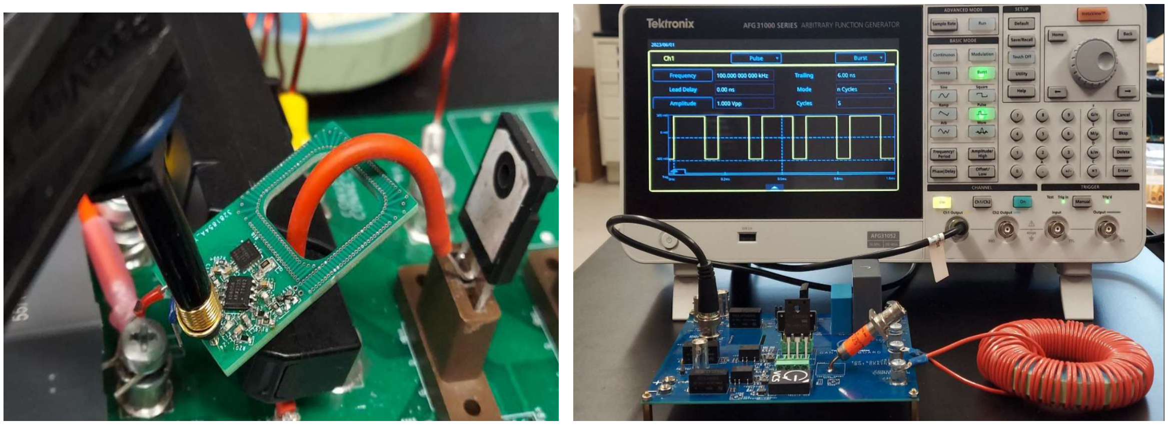

(a) (b)

Figure 5.13: The switch-current test setups: a) Under high EMI-emission, and b) Double pulse tester plus a 50MHz function generator [207].

their immunity and linearity under such conditions. Since the switching current has the highest number of frequency components, there could be a variety of frequencies responding simultaneously, as well as an increase in EMI emissions near the switching node, which could interfere with nearby circuits or devices as well as fake overshoots and undershoots of the sensed voltage. Additionally, power line noise and EMI from other sources can impact current measurement accuracy, both should be considered in the context of their real-world applications. Thus, it is paramount to ensure the immunity of the sensors to the surrounding environment.

In order to examine the current sensor functionality in harsh environments, one can use test setups such as in Figure 5.13, where a switch current node with a large loop in Figure 5.13(a) ensures excessive EMI emission when measuring the switching current, while Figure 5.13(b) provides a DPT setup that can be controlled using a function generator (such as Tektronix AFG31051 [207]) in order to simulate a wide range of switching frequencies and duty ratios. In order to measure the same switching current for the purpose of comparing the quality of the output signal, the use of a good-quality contactless current probe, such as a Tektronix over 30 MHz current gun is necessary. These two setups enable comprehensive testing of the sensor's functionality in a wide range of switching frequencies and EMI-coupled conditions, ensuring that the sensor is suitable in such environments. Combining the characteristics of the two switch-current sensing setups in Figure 5.13, the current sensors shown in Figure 5.11 have been tested for various switching current frequencies and their results are shown in Figures 5.14-25. The manufactured sensor output waveform (in blue) is compared to the output waveform of the Tektronix TPC305A (DC-50 MHz, 30 A-steady-state) current gun (in magenta) in all of these scope captures obtained with a 500 MHz passive probe and a Keysight 350

MHz 4-channel oscilloscope [190], where the sensors were measured for switching current using the Following method:

1) 50 kHz switching frequency and 48% duty ratio (4 pulses), with zoom-in captures of the pulse with the highest current magnitude, help determine whether the current sensor can maintain its DC/LF components.

2) 200 kHz switching frequency and 64% duty ratio, composed of 10 pulses, and a zoom-in image of the pulse with the largest magnitude, may indicate the sensor's ability to detect large currents with normal to high EMI levels.

3) 500 kHz switching frequency, 72% duty ratio, consisting of 12 pulses with zoom-in captures of the pulses with the largest current magnitude, which demonstrates sensor performance (if there is a significant offset drift) with a low off-time in HF switching conditions and excessive EMI levels.

Based on the comparison between the two helical MS current sensors presented in Figure 5.11(a and b), the one with the TMR required a lowpass filter to reduce unwanted noise, thus resulting in a slower rising time and BW. In Figure 5.11(c), the switch-current sensor has a good speed and BW, but its low distance to the conductor causes some coupled noises. On-trace sensors with stacked connections have parasitic inductances, which is why it did not perform as well as the first sensor, but still had a high BW.

5.6 Conclusion

Sensors manufactured today have been criticized for their size, EMI immunity, bandwidth, invasiveness, nonlinearity, cost, and accuracy as being insufficient for use with high-frequency converters. Through the use of a contactless magnetic detector chip, a UWB RC, and reduced system complexity, these issues are addressed in this chapter. These dual-path current sensors are compact, cost-effective, accurate, EMI-immune, and have extensive measurement bandwidth. The proposed sensor configuration also offers a high level of accuracy while maintaining a low profile and a low-cost solution for industrial applications. Moreover, it provides a reliable solution for high-frequency converters. Several guidelines regarding bidirectional sensing and noise immunity, along with the information from the previous two chapters, are underutilized in order to fabricate four DC-UHF current sensors that can be used even for applications as sensitive as monitoring switch current. The four sensors are designed to be stable and efficient and have been successfully tested with a large set of switching current profiles. They are highly suitable for a wide variety of industrial applications as they are capable of accurately measuring current with varying low and high values that require ultrafast detection speeds. The sensors also have a high tolerance for noise, meaning they can be used in environments with high levels of electrical disturbances. Furthermore, they are designed to be compact in size and geometry, making them ideal for integration into most existing systems.

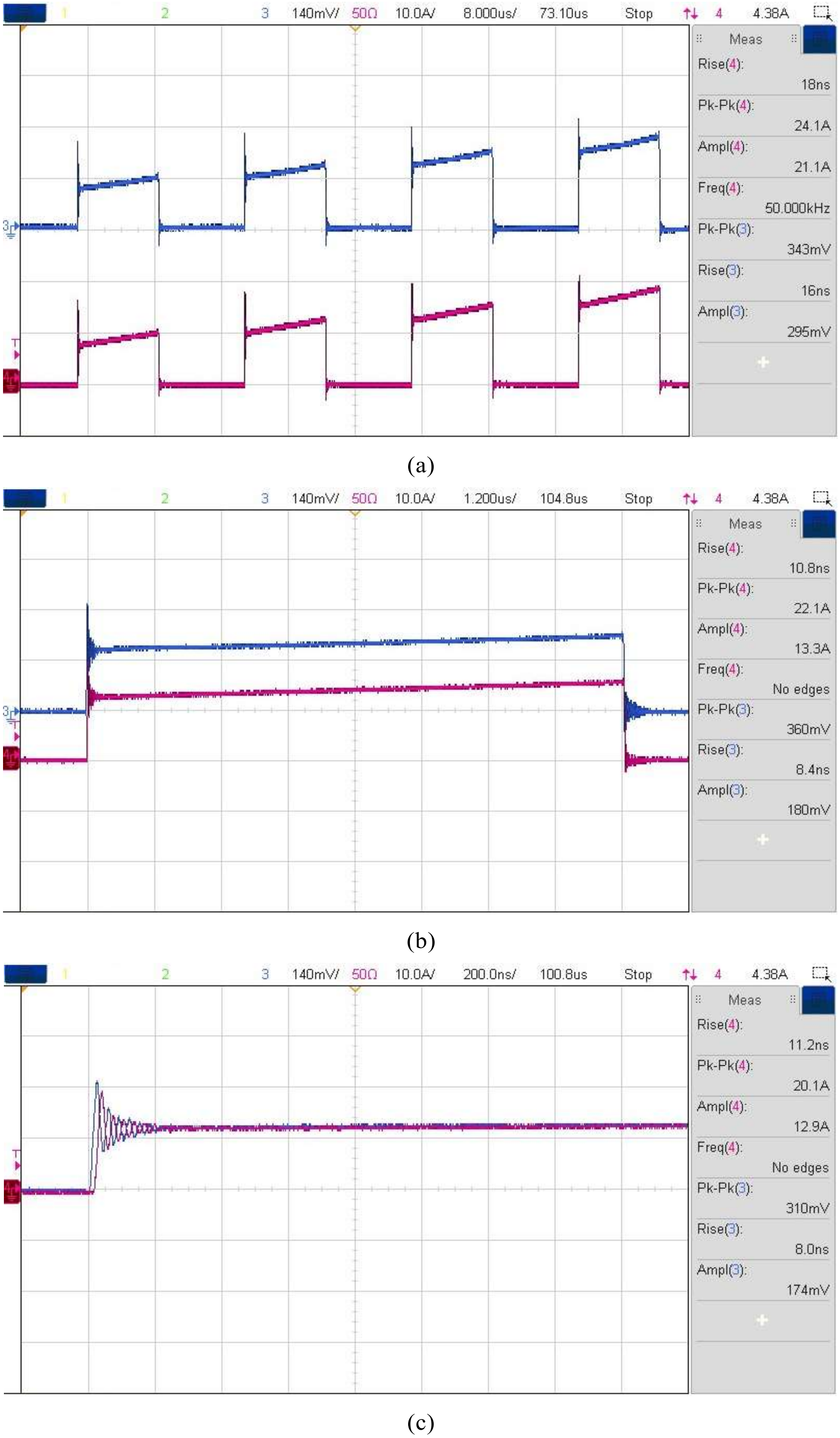
1 2 3 140mV/ 50Ω 10.0A/ 8.000us/ 73.10us Stop 4 4.38A

Meas

Rise(4): 18ns

Pk-Pk(4): 24.1A

Ampl(4): 21.1A

Freq(4): 50.000kHz

Pk-Pk(3): 343mV

Rise(3): 16ns

Ampl(3): 295mV

(a)

1 2 3 140mV/ 50Ω 10.0A/ 1.200us/ 104.8us Stop 4 4.38A

Meas

Rise(4): 10.8ns

Pk-Pk(4): 22.1A

Ampl(4): 13.3A

Freq(4): No edges

Pk-Pk(3): 360mV

Rise(3): 8.4ns

Ampl(3): 180mV

(b)

1 2 3 140mV/ 50Ω 10.0A/ 200.0ns/ 100.8us Stop 4 4.38A

Meas

Rise(4): 11.2ns

Pk-Pk(4): 20.1A

Ampl(4): 12.9A

Freq(4): No edges

Pk-Pk(3): 310mV

Rise(3): 8.0ns

Ampl(3): 174mV

(c)

Figure 5.14: Switching current results of the sensor in figure 5.11(a) at 50 kHz: a) 4 pulses, b) zoom-in of the largest pulse, and c) the last pulse rising time.

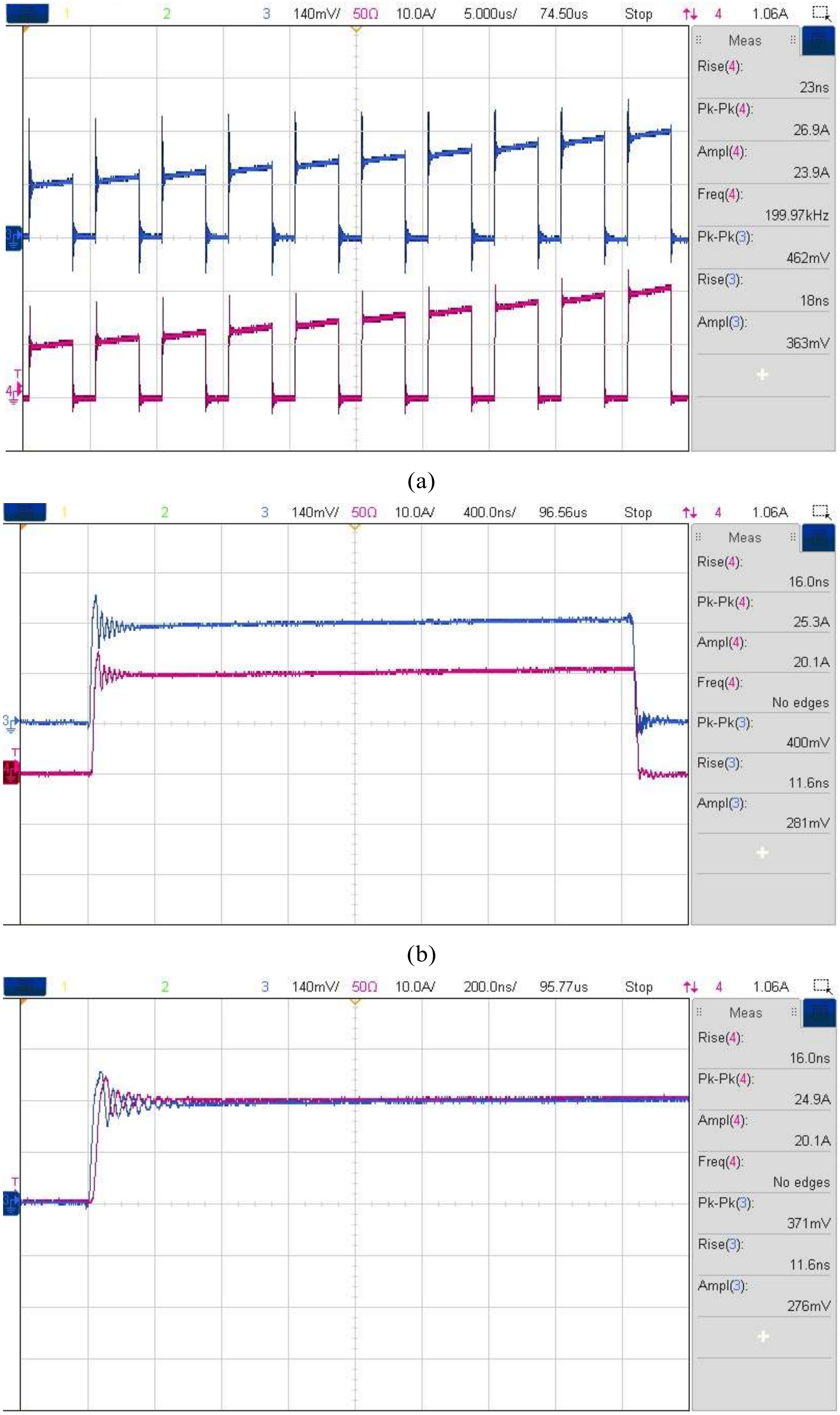

(a)

(b)

(c)

Figure 5.15: Switching current results of the sensor in figure 5.11(a) at 200 kHz: a) 10 pulses, b) zoom-in of the largest pulse, and c) the last pulse rising time.

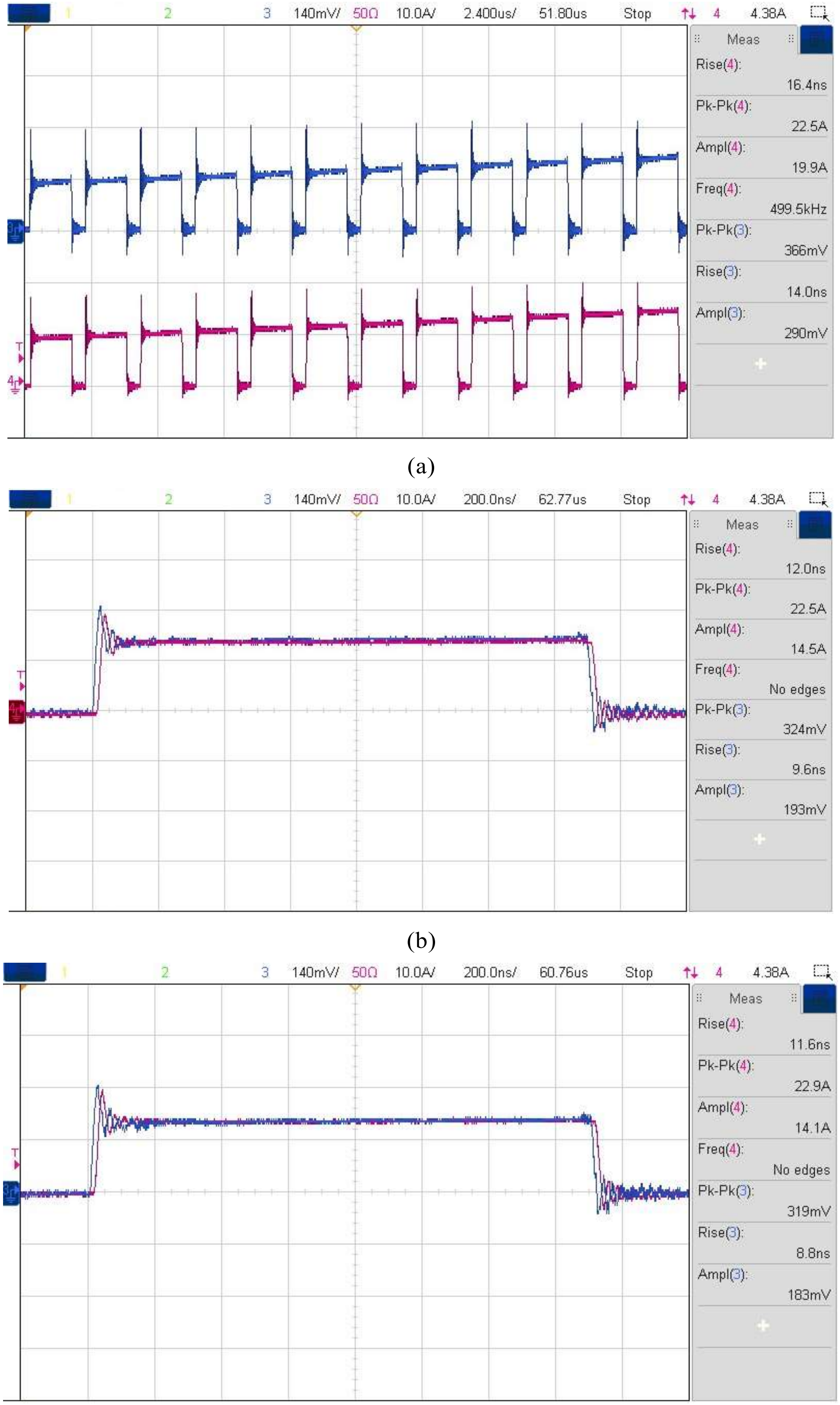

(a)

(b)

(c)

Figure 5.16: Switching current results of the sensor in figure 5.11(a) at 500 kHz: a) 12 pulses, b) zoom-in of the largest pulse, and c) the last pulse rising time.

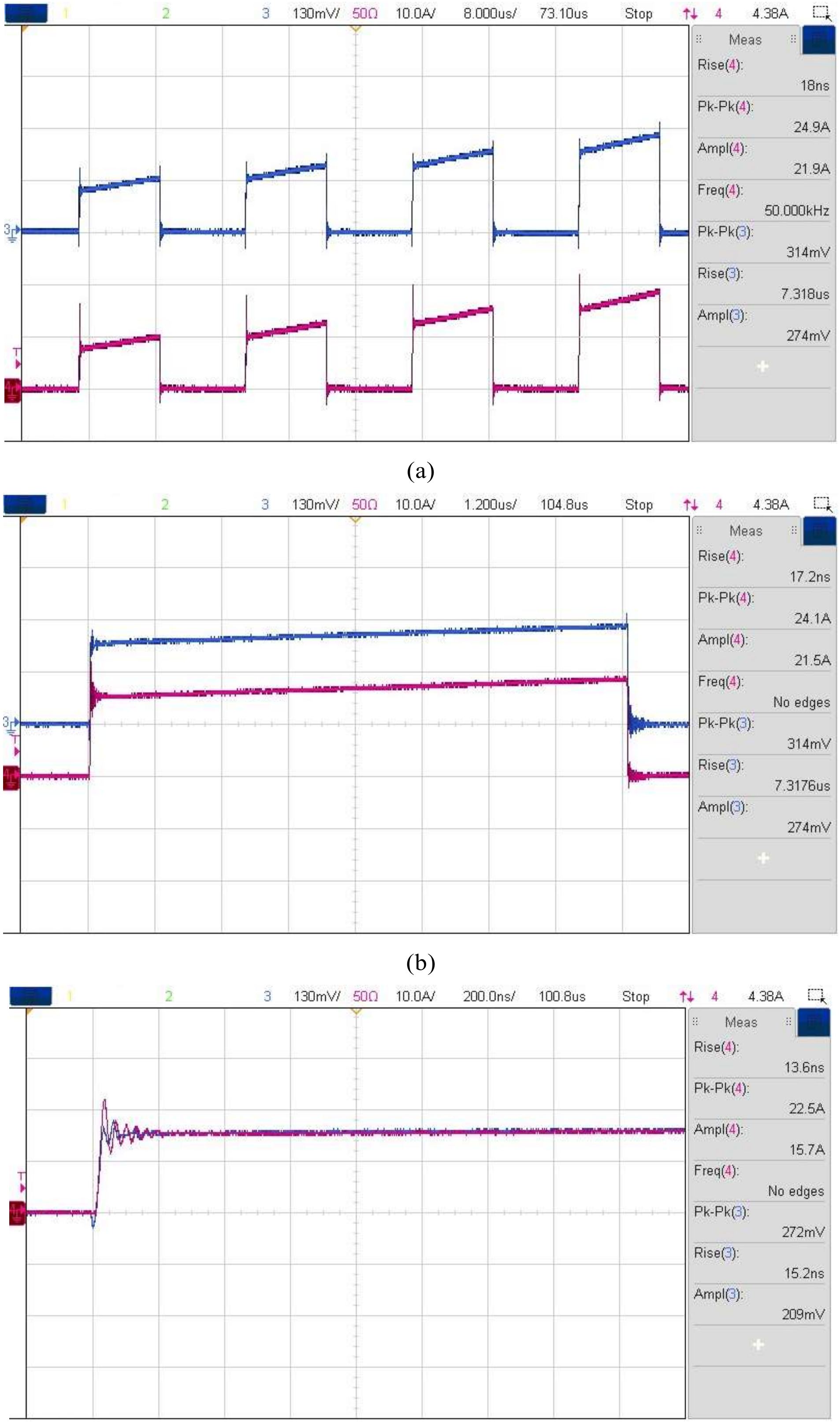

130mV/ 50Ω 10.0A/ 8.000us/ 73.10us Stop 4 4.38A

Rise(4): 18ns
Pk-Pk(4): 24.9A
Ampl(4): 21.9A
Freq(4): 50.000kHz
Pk-Pk(3): 314mV
Rise(3): 7.318us
Ampl(3): 274mV

(a)

130mV/ 50Ω 10.0A/ 1.200us/ 104.8us Stop 4 4.38A

Rise(4): 17.2ns
Pk-Pk(4): 24.1A
Ampl(4): 21.5A
Freq(4): No edges
Pk-Pk(3): 314mV
Rise(3): 7.3176us
Ampl(3): 274mV

(b)

130mV/ 50Ω 10.0A/ 200.0ns/ 100.8us Stop 4 4.38A

Rise(4): 13.6ns
Pk-Pk(4): 22.5A
Ampl(4): 15.7A
Freq(4): No edges
Pk-Pk(3): 272mV
Rise(3): 15.2ns
Ampl(3): 209mV

(c)

Figure 5.17: Switching current results of the sensor in figure 5.11(b) at 50 kHz: a) 4 pulses, b) zoom-in of the largest pulse, and c) the last pulse rising time.

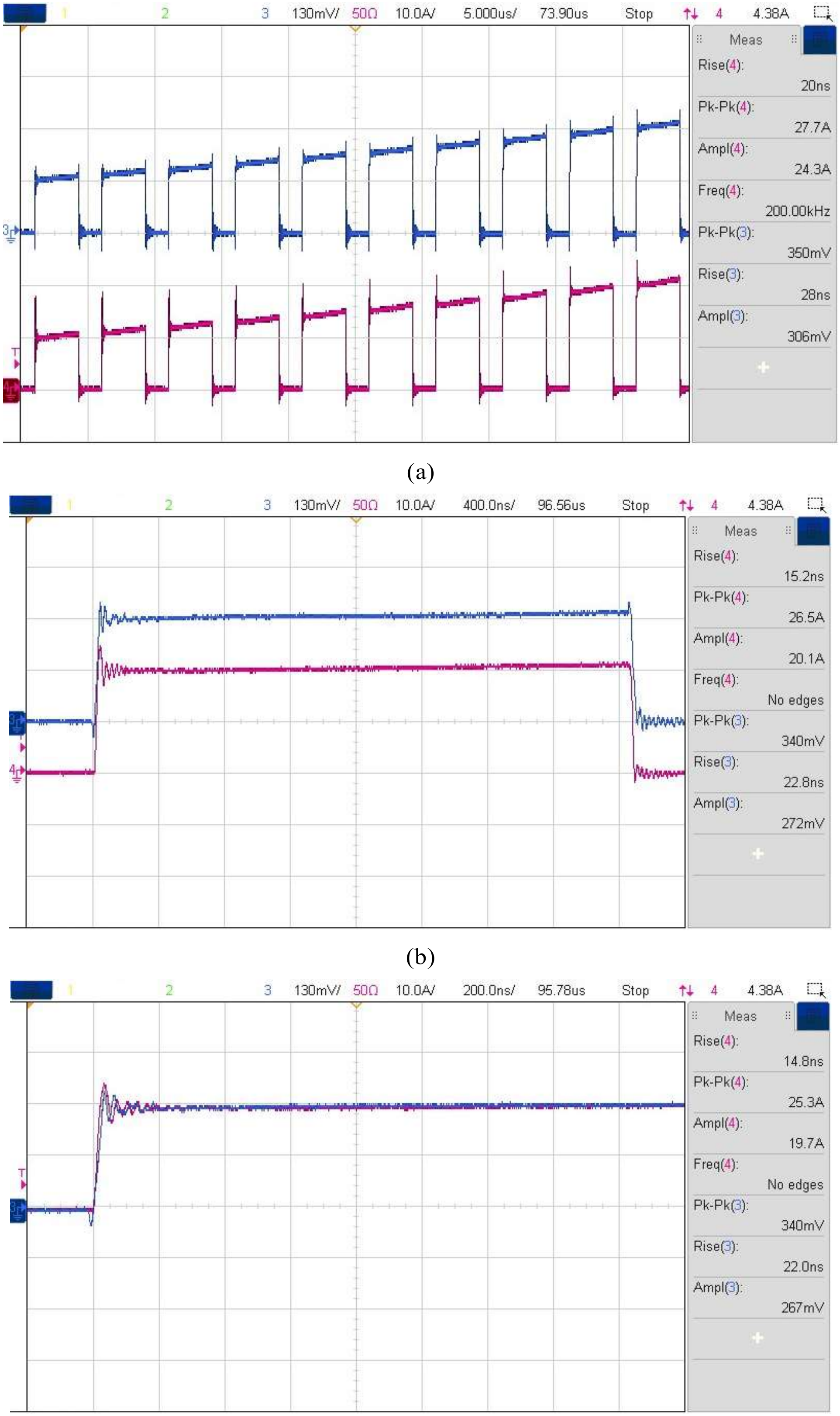

(a)

1 2 3 130mV/ 50Ω 10.0A/ 5.000us/ 73.90us Stop 4 4.38A

Meas
Rise(4): 20ns
Pk-Pk(4): 27.7A
Ampl(4): 24.3A
Freq(4): 200.00kHz
Pk-Pk(3): 350mV
Rise(3): 28ns
Ampl(3): 306mV

(b)

1 2 3 130mV/ 50Ω 10.0A/ 400.0ns/ 96.56us Stop 4 4.38A

Meas
Rise(4): 15.2ns
Pk-Pk(4): 26.5A
Ampl(4): 20.1A
Freq(4): No edges
Pk-Pk(3): 340mV
Rise(3): 22.8ns
Ampl(3): 272mV

(c)

1 2 3 130mV/ 50Ω 10.0A/ 200.0ns/ 95.78us Stop 4 4.38A

Meas
Rise(4): 14.8ns
Pk-Pk(4): 25.3A
Ampl(4): 19.7A
Freq(4): No edges
Pk-Pk(3): 340mV
Rise(3): 22.0ns
Ampl(3): 267mV

Figure 5.18: Switching current results of the sensor in figure 5.11(b) at 200 kHz: a) 10 pulses, b) zoom-in of the largest pulse, and c) the last pulse rising time.

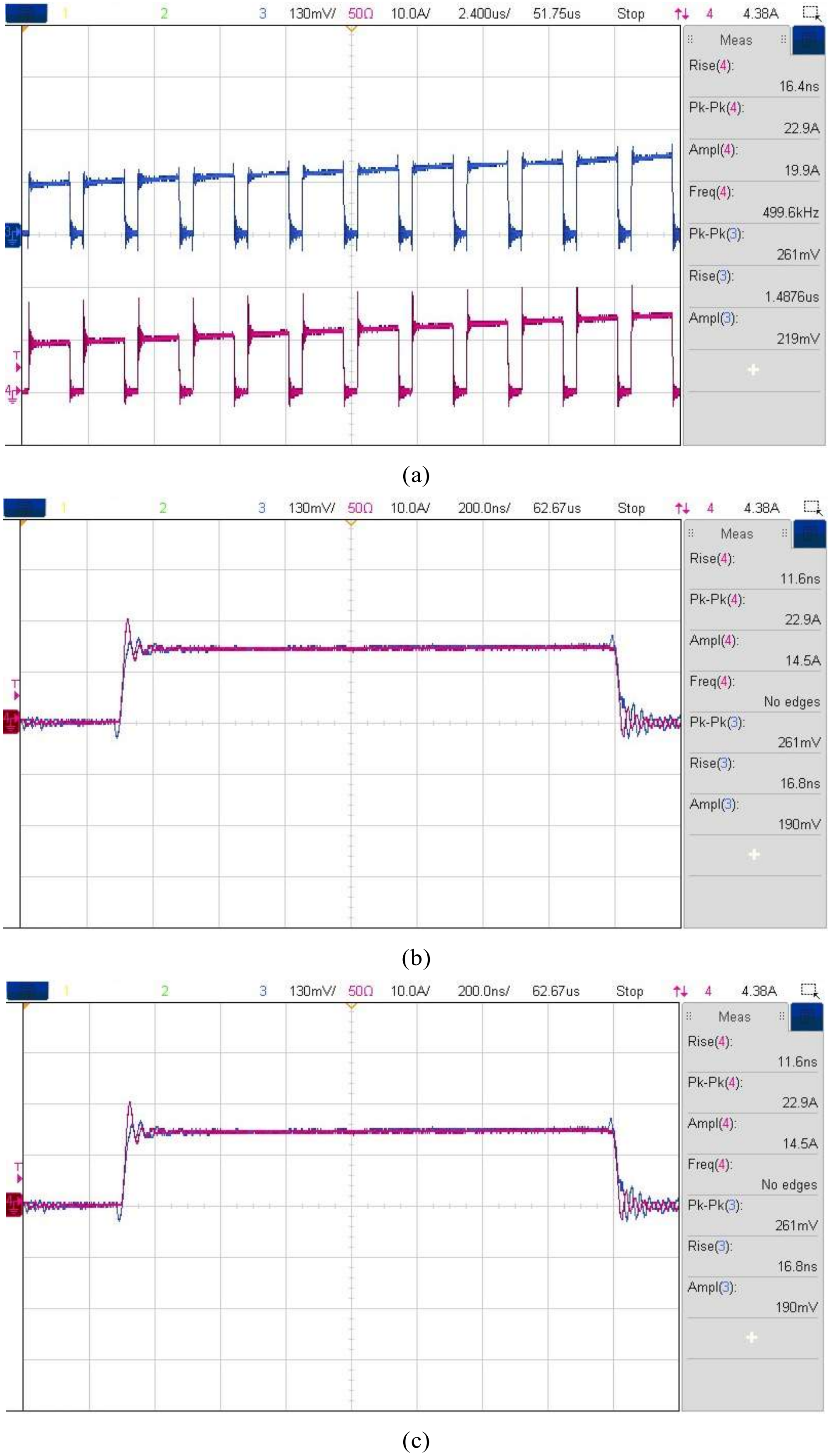

Figure 5.19: Switching current results of the sensor in figure 5.11(b) at 500 kHz: a) 12 pulses, b) zoom-in of the largest pulse, and c) the last pulse rising time.

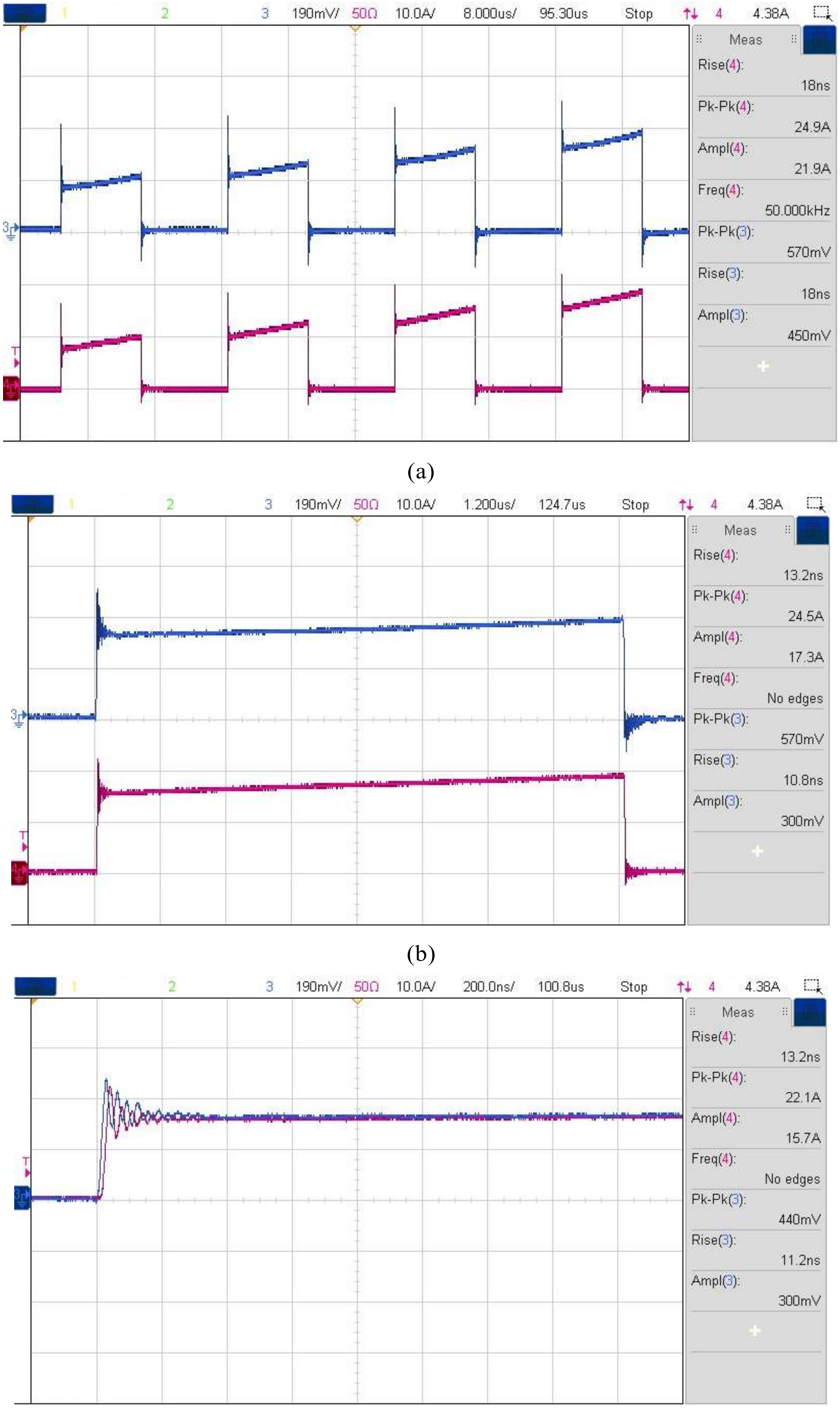

Rise(4): 18ns
Pk-Pk(4): 24.9A
Ampl(4): 21.9A
Freq(4): 50.000kHz
Pk-Pk(3): 570mV
Rise(3): 18ns
Ampl(3): 450mV

(a)

Rise(4): 13.2ns
Pk-Pk(4): 24.5A
Ampl(4): 17.3A
Freq(4): No edges
Pk-Pk(3): 570mV
Rise(3): 10.8ns
Ampl(3): 300mV

(b)

Rise(4): 13.2ns
Pk-Pk(4): 22.1A
Ampl(4): 15.7A
Freq(4): No edges
Pk-Pk(3): 440mV
Rise(3): 11.2ns
Ampl(3): 300mV

(c)

Figure 5.20: Switching current results of the sensor in figure 5.11(c) at 50 kHz: a) 4 pulses, b) zoom-in of the largest pulse, and c) the last pulse rising time.

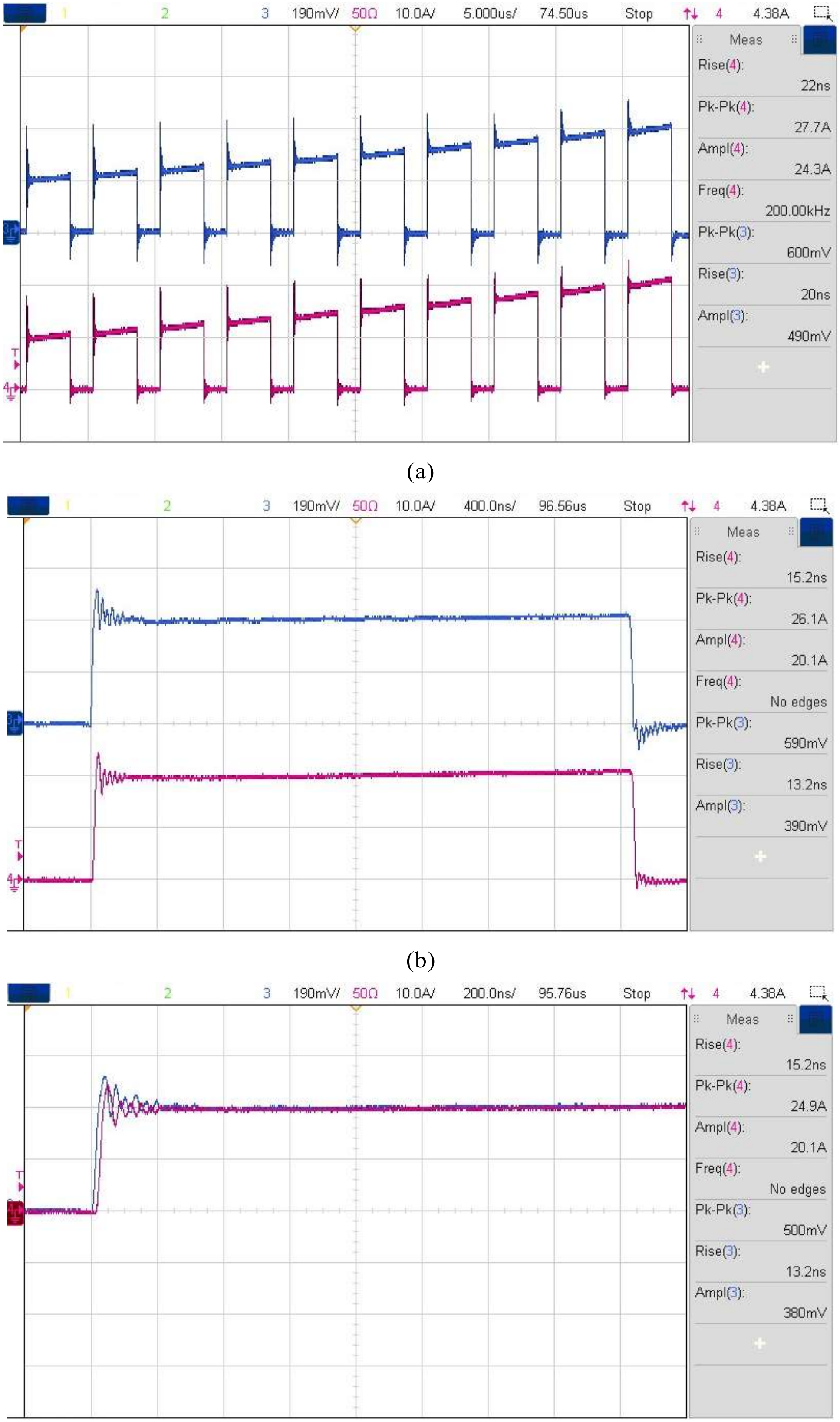

190mV/ 50Ω 10.0A/ 5.000us/ 74.50us Stop 4.38A

Rise(4): 22ns
Pk-Pk(4): 27.7A
Ampl(4): 24.3A
Freq(4): 200.00kHz
Pk-Pk(3): 600mV
Rise(3): 20ns
Ampl(3): 490mV

(a)

190mV/ 50Ω 10.0A/ 400.0ns/ 96.56us Stop 4.38A

Rise(4): 15.2ns
Pk-Pk(4): 26.1A
Ampl(4): 20.1A
Freq(4): No edges
Pk-Pk(3): 590mV
Rise(3): 13.2ns
Ampl(3): 390mV

(b)

190mV/ 50Ω 10.0A/ 200.0ns/ 95.76us Stop 4.38A

Rise(4): 15.2ns
Pk-Pk(4): 24.9A
Ampl(4): 20.1A
Freq(4): No edges
Pk-Pk(3): 500mV
Rise(3): 13.2ns
Ampl(3): 380mV

(c)

Figure 5.21: Switching current results of the sensor in figure 5.11(c) at 200 kHz: a) 10 pulses, b) zoom-in of the largest pulse, and c) the last pulse rising time.

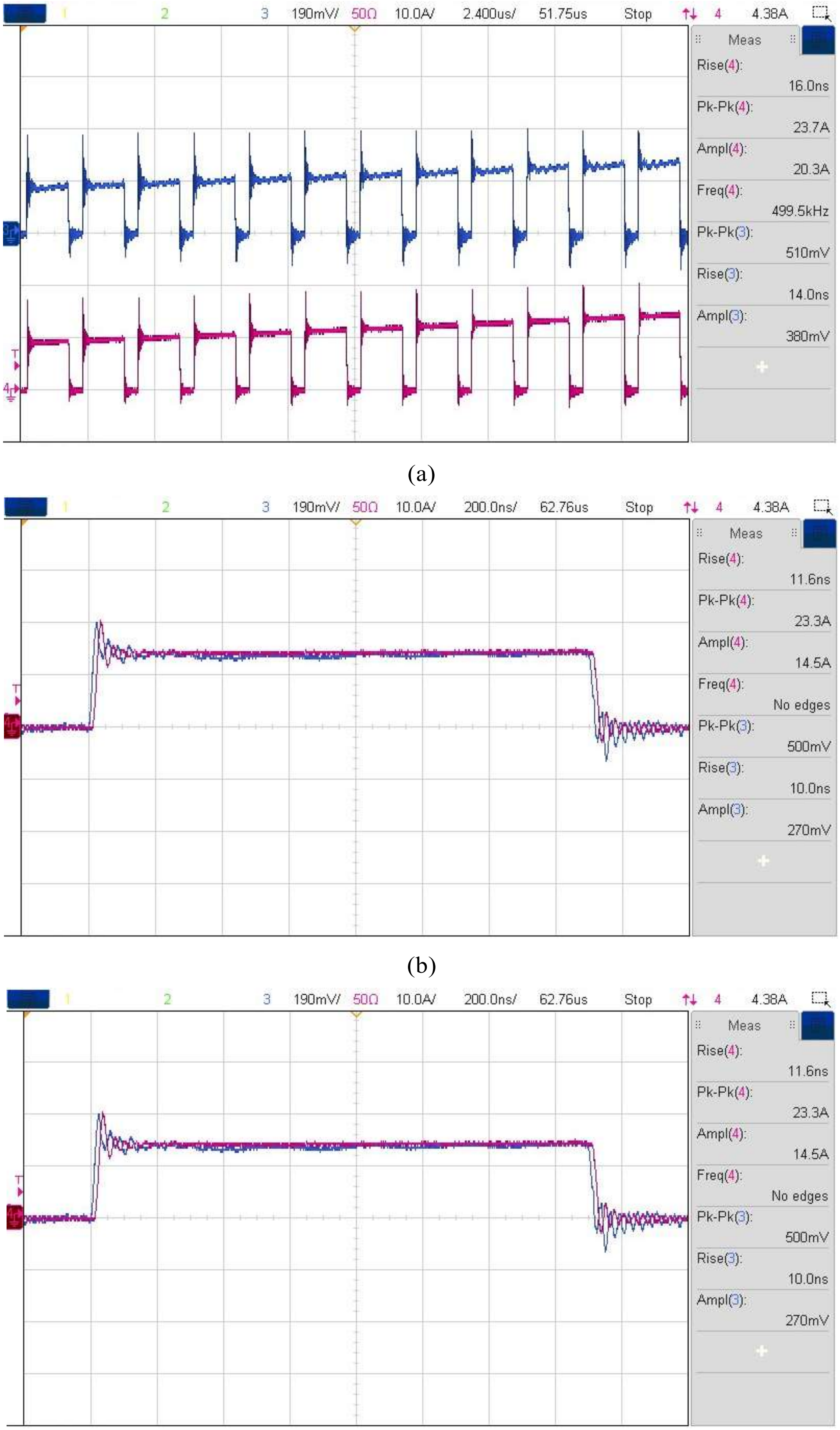

1 2 3 190mV/ 50Ω 10.0A/ 2.400us/ 51.75us Stop 4 4.38A

Meas
Rise(4): 16.0ns
Pk-Pk(4): 23.7A
Ampl(4): 20.3A
Freq(4): 499.5kHz
Pk-Pk(3): 510mV
Rise(3): 14.0ns
Ampl(3): 380mV

(a)

1 2 3 190mV/ 50Ω 10.0A/ 200.0ns/ 62.76us Stop 4 4.38A

Meas
Rise(4): 11.6ns
Pk-Pk(4): 23.3A
Ampl(4): 14.5A
Freq(4): No edges
Pk-Pk(3): 500mV
Rise(3): 10.0ns
Ampl(3): 270mV

(b)

1 2 3 190mV/ 50Ω 10.0A/ 200.0ns/ 62.76us Stop 4 4.38A

Meas
Rise(4): 11.6ns
Pk-Pk(4): 23.3A
Ampl(4): 14.5A
Freq(4): No edges
Pk-Pk(3): 500mV
Rise(3): 10.0ns
Ampl(3): 270mV

(c)

Figure 5.22: Switching current results of the sensor in figure 5.11(c) at 500 kHz: a) 12 pulses, b) zoom-in of the largest pulse, and c) the last pulse rising time.

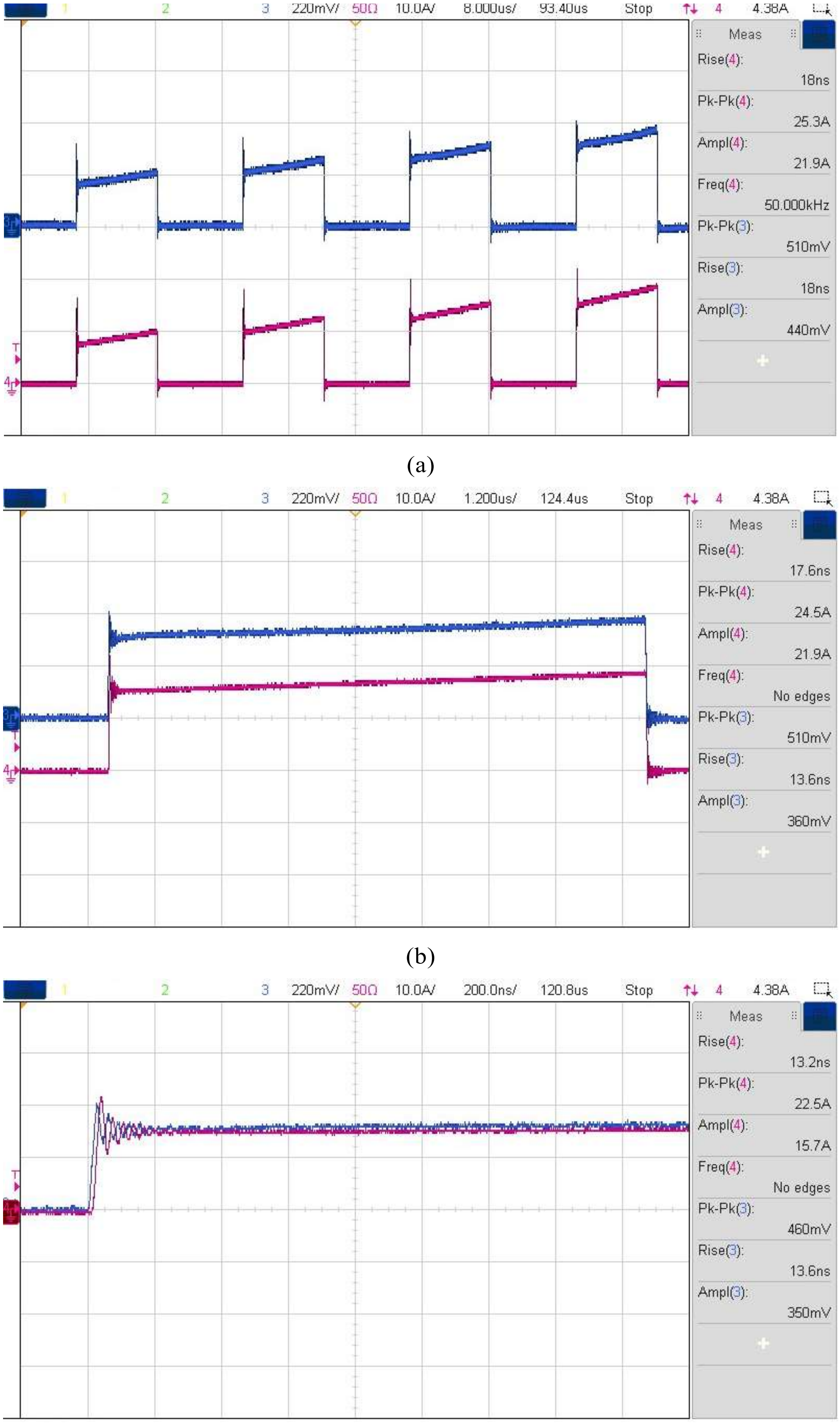

(a)

(b)

(c)

Figure 5.23: Switching current results of the sensor in figure 5.11(d) at 50 kHz: a) 4 pulses, b) zoom-in of the largest pulse, and c) the last pulse rising time.

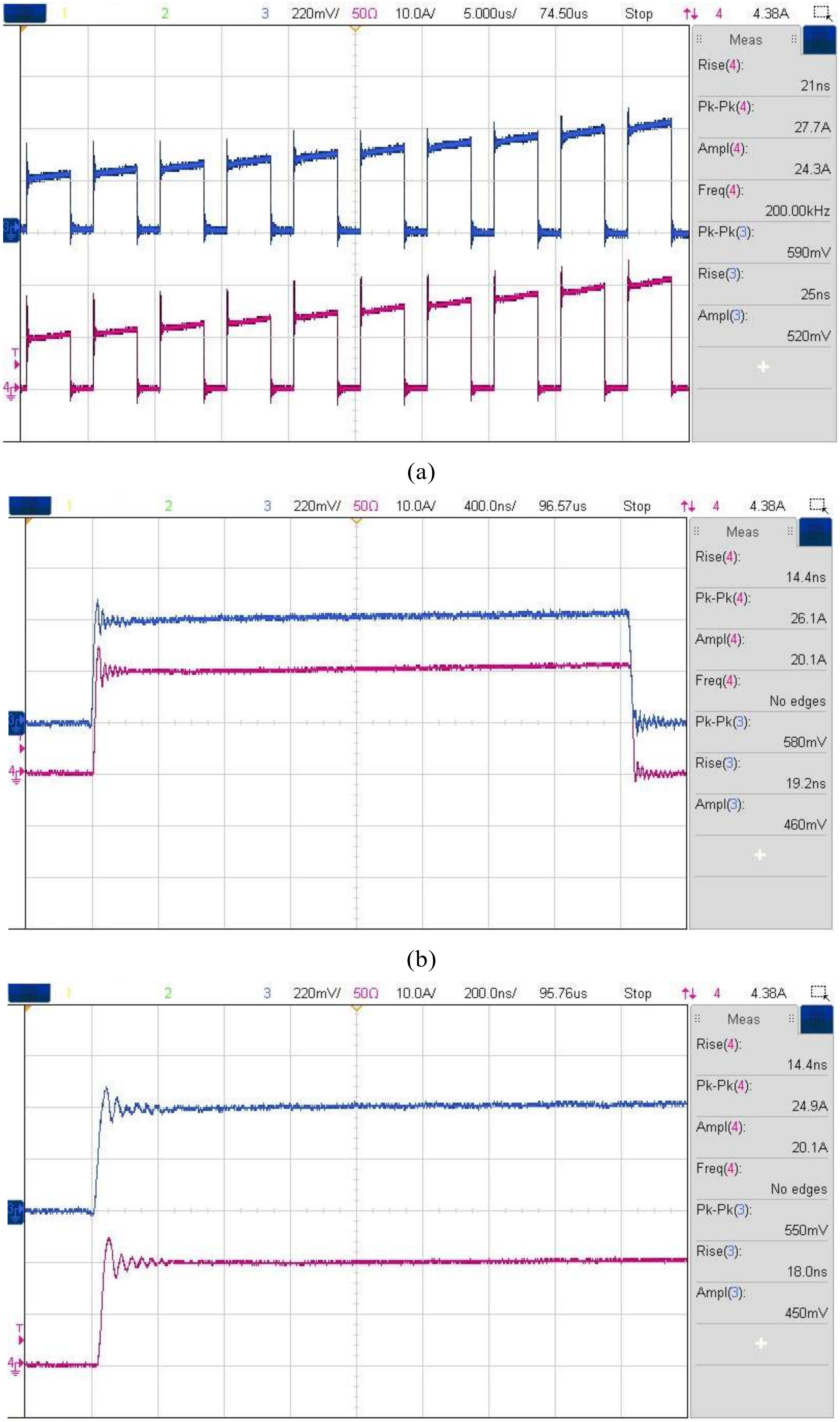

Rise(4): 21ns
Pk-Pk(4): 27.7A
Ampl(4): 24.3A
Freq(4): 200.00kHz
Pk-Pk(3): 590mV
Rise(3): 25ns
Ampl(3): 520mV

(a)

Rise(4): 14.4ns
Pk-Pk(4): 26.1A
Ampl(4): 20.1A
Freq(4): No edges
Pk-Pk(3): 580mV
Rise(3): 19.2ns
Ampl(3): 460mV

(b)

Rise(4): 14.4ns
Pk-Pk(4): 24.9A
Ampl(4): 20.1A
Freq(4): No edges
Pk-Pk(3): 550mV
Rise(3): 18.0ns
Ampl(3): 450mV

(c)

Figure 5.24: Switching current results of the sensor in figure 5.11(d) at 200 kHz: a) 10 pulses, b) zoom-in of the largest pulse, and c) the last pulse rising time.

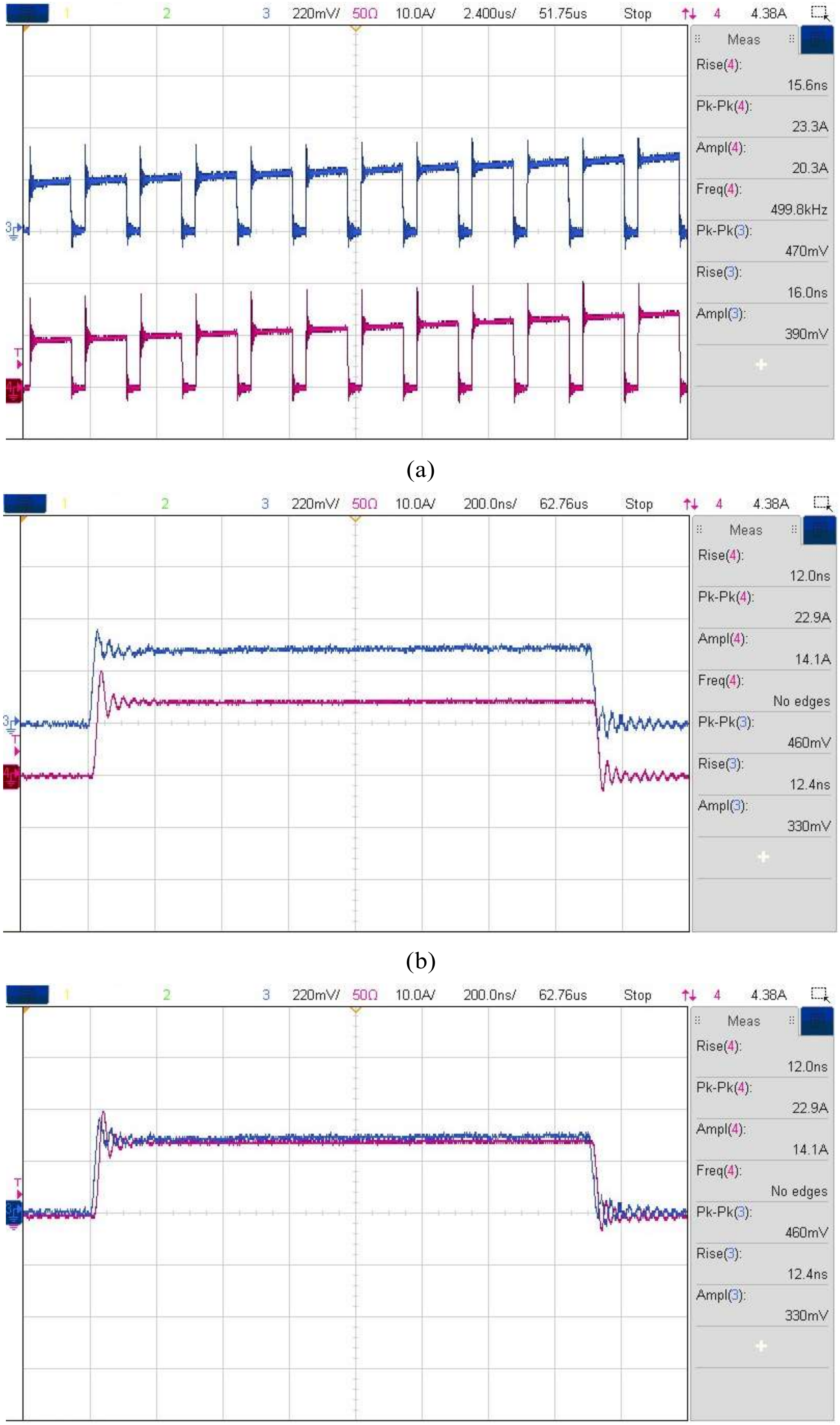

2.400us/ 51.75us

Rise(4): 15.6ns
Pk-Pk(4): 23.3A
Ampl(4): 20.3A
Freq(4): 499.8kHz
Pk-Pk(3): 470mV
Rise(3): 16.0ns
Ampl(3): 390mV

(a)

200.0ns/ 62.76us

Rise(4): 12.0ns
Pk-Pk(4): 22.9A
Ampl(4): 14.1A
Freq(4): No edges
Pk-Pk(3): 460mV
Rise(3): 12.4ns
Ampl(3): 330mV

(b)

200.0ns/ 62.76us

Rise(4): 12.0ns
Pk-Pk(4): 22.9A
Ampl(4): 14.1A
Freq(4): No edges
Pk-Pk(3): 460mV
Rise(3): 12.4ns
Ampl(3): 330mV

(c)

Figure 5.25: Switching current results of the sensor in figure 5.11(d) at 500 kHz: a) 12 pulses, b) zoom-in of the largest pulse, and c) the last pulse rising time.

CHAPTER 6: SUMMARY AND OUTLOOK

SS and MS current sensors have been comprehensively studied in this thesis, along with their integration into power electronics, particularly their application in emerging higher switching frequency WBG converters. According to the present study, there is almost no specific method of current sensing that can be identified as a general solution that simultaneously combines all the necessary sensing factors into a single solution. Based on the findings of this feasibility study, guidelines were developed for the development of high-quality current sensors, which could be readily applied to power converters of the future. The guidelines detailed the most appropriate current sensing techniques and the trade-offs between accuracy, dynamic range, BW and implementation complexity for each technique. The study concluded with recommendations for using the most appropriate sensors for different power converter designs, which require most of their sensing subcircuits to be modified, designed, and implemented according to physical and time/frequency domain requirements. Experimental results of fabricated sensors and sensor platforms have been presented in Chapters 3-5 under realistic conditions and setups to demonstrate their functionality. Conclusions and Future work of technology extensions in this thesis can be classified into three broad categories: 1) Power converter current sensing challenges, 2) Single-path current sensing corrections and applications, and 3) multi-path compensated current measurement.

6.1 Power Converter Current Sensing Challenges

It is also possible to consider physical and electrical properties when designing a power converter itself to determine a well-suited current sensor implementation and potential. Selecting a current sensor may be influenced by the operating temperature, the current range, and other operating parameters of a power converter, as well as its stability, noise immunity, and response time, depending on the application. In order to ensure proper operation of the power converter, it is important to select the current sensor with careful consideration based on the application. Moreover, the power converter layout needs to be analyzed in order to determine the best placement of current sensors, the measurement of EMI emissions, the mitigation of interference currents and fields, and the reduction of parasitics and couplings between power-switch traces. This can be done through careful design of the power-switch traces and via the addition of decoupling capacitors, ferrite beads, and shielding elements. Consequently, this ensures the smooth operation of the converter as well as the accuracy and reliability of the current sensing system, in which the power-switch traces are routed separately from the other sensing components to minimize interference risks and the introduction of parasitic elements. Additionally, the advantage of appropriate PCB design practices can help minimalize the impact of EMI and parasitics.

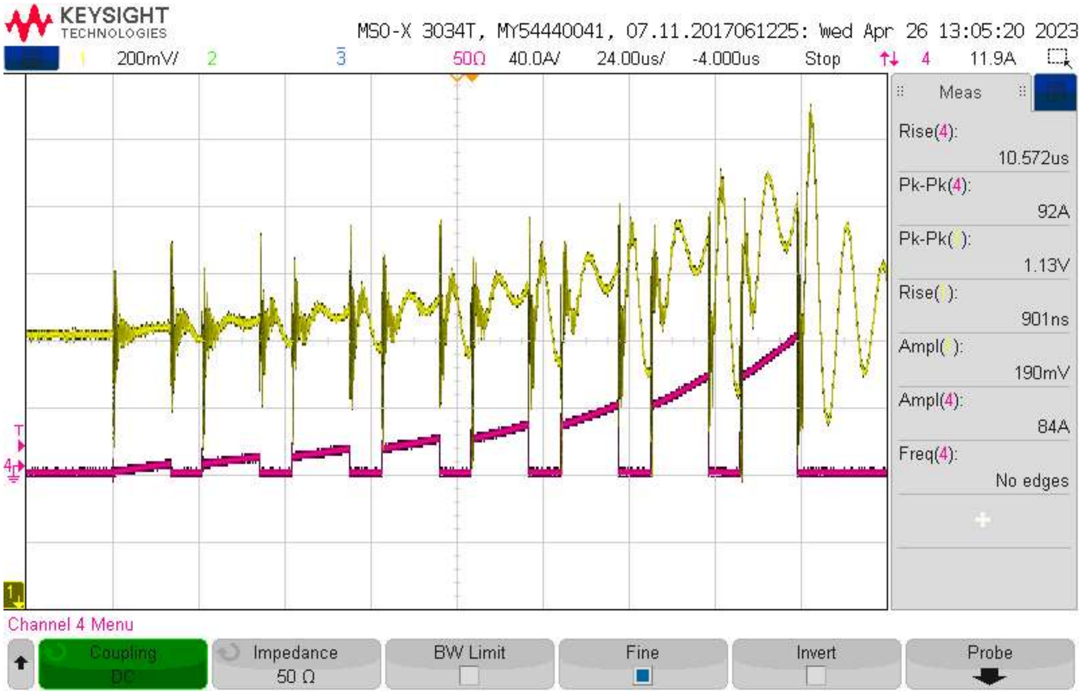

Rise(4): 10.572us
Pk-Pk(4): 92A
Pk-Pk(1): 1.13V
Rise(1): 901ns
Ampl(1): 190mV
Ampl(4): 84A
Freq(4): No edges

Figure 6.1: TMR’s output on a switching node with high EMI radiation [24].

For instance, when designing a DC-DC power converter, the board layout needs to consider the distances between the power switches and the ground plane to prevent excessive oscillations and EMI emissions. Figure 6.1 illustrates how a TMR chip can be adversely affected by high EMI radiation near a switching node.

6.2 Single-Path Current Sensing Corrections and Applications

In the case of WBG power converters, where physical constraints, the required BW, circuit invasiveness, and noise immunity make the measurement process difficult, there are no general solutions among SS current sensors that can be used as contactless measurement tools. Therefore, evaluating the current sensors extensively is crucial for meeting the needs of the power converter in a similar manner to studying the properties of the converter. A thorough assessment should include the analysis of the performance of all applicable current sensors under all operating conditions, which will allow the most suitable current sensor to be selected for the application to ensure accurate and reliable

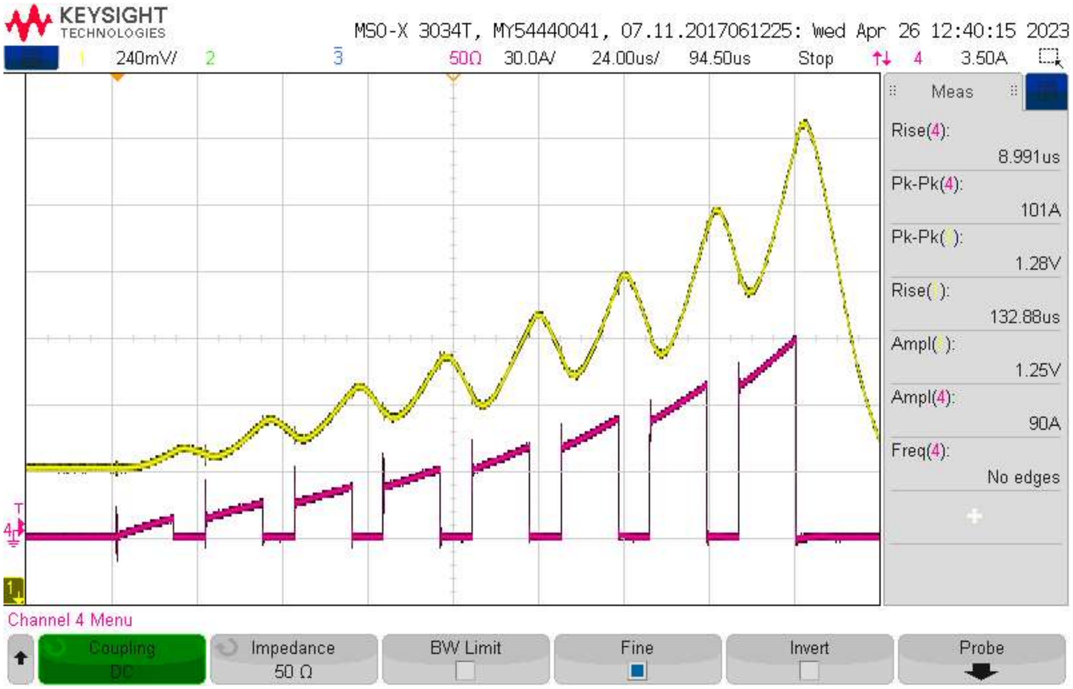

```
MSO-X 3034T, MY54440041, 07.11.2017061225: Wed Apr 26 12:40:15 2023
1  240mV/  2  3  50Ω  30.0A/  24.00us/  94.50us  Stop  4  3.50A
```

```
Rise(4):
8.991us
Pk-Pk(4):
101A
Pk-Pk(1):
1.28V
Rise(1):
132.88us
Ampl(1):
1.25V
Ampl(4):
90A
Freq(4):
No edges
```

Figure 6.2: Micro-fluxgate's on a switching node with an RC lowpass cutoff at 16 kHz [24].

measurements. Also, the cost and complexity of the current sensor should be carefully considered in order to achieve the highest level of performance and reliability. Choosing the right sensing solution for their intended application is essential, as each sensing technology has its own advantages and disadvantages, and for accurate results, it is imperative that the sensing circuit is designed and implemented carefully.

Despite the lack of a suitable commercial current sensor available for use in WBG converters to detect high BW currents non-invasively, existing SS current sensing technologies can be underutilized by implementing techniques such as EMI suppression

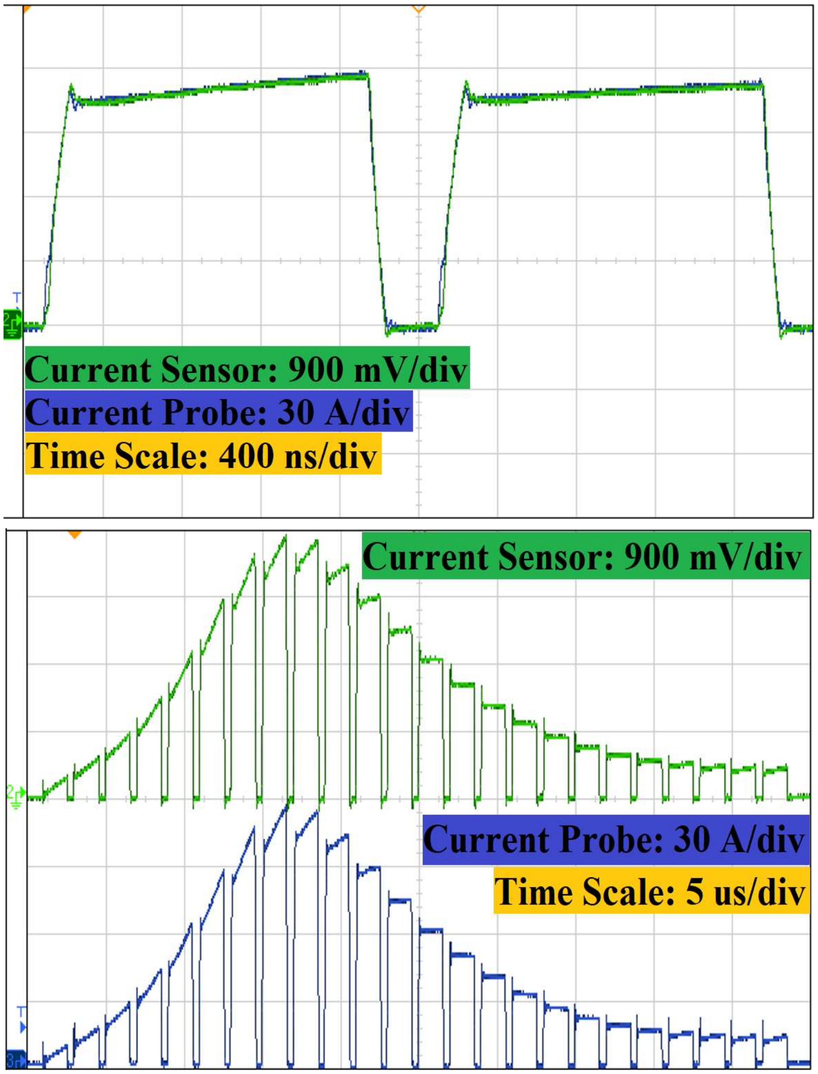

Figure 6.3: Ultra-wideband switch-current sensing with PCB-embedded Rogowski coil [48].

(Figure 6.2), BW extension, DC/HF coupling, etc., which can be reasonable for their intended applications in WBG power converters, where these techniques can be used to improve current sensing accuracy, allowing more precise control over the converter. Additionally, with the development of power electronics, reliable and accurate current sensing has become increasingly important, and further research is needed to develop compensated SS current sensing solutions for WBG converters, which can also be used to enhance the reliability and protection of these converters by increasing their current sensing accuracy. Additionally, such research could lead to the development of more efficient and cost-effective current sensing solutions, which could ultimately increase the reliability of WBG converters.

This work presented a series of passive and electronic filtering techniques as well as layout design considerations for low-frequency current sensors, and a set of carefully crafted guidelines has been developed for inductive-based SS current sensors that are suitable for use in applications involving high-frequency converters. For both LF and HF current transducers. With the help of the proposed new techniques, noise effects can be reduced, the accuracy and resolution of current sensing can be improved, and the dynamic range of the sensors can also be increased. Combining emerging techniques and facilities will allow for further improvements to be proposed and tested, as well as reducing the cost and size of the sensors while increasing their BW and accuracy.

6.3 Multi-Path Compensated Current Measurement

It is possible to combine various types of SS current sensors to achieve the desired performance, ranging from simple current sensing schemes to sophisticated multi-sensing schemes, depending on the application. Historically, power electronics applications have underutilized two SS sensing methods (widely known as hybrid current sensors/probes) to compensate for their limited BW, with MS configurations enhancing accuracy, speed, and robustness, making them advantageous in HF converters, in which SS sensing systems may not provide sufficient BW. As a result, hybrid current sensing provides a high-performance solution which combines the advantages of both DC and HF sensing technologies. Additionally, it can provide a small size and low cost (depending on the implementation of the subcircuits), making it an attractive option for a wide variety of

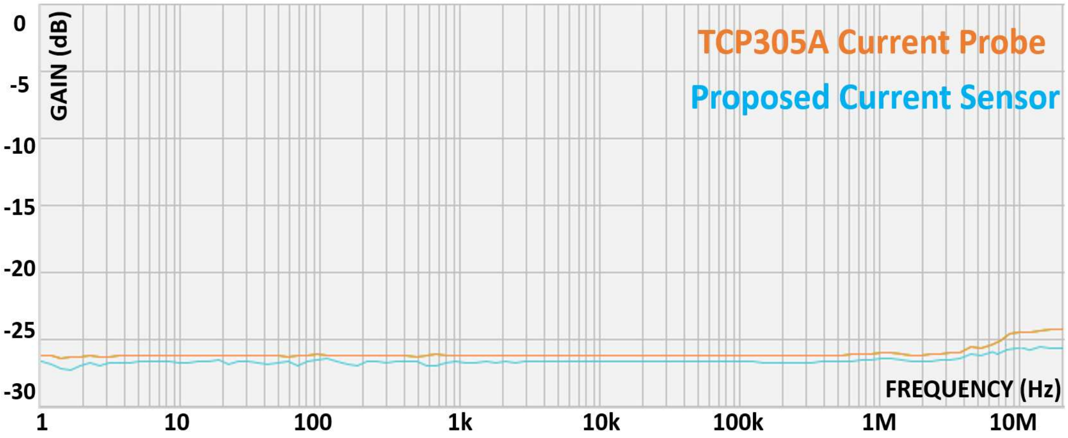

(a)

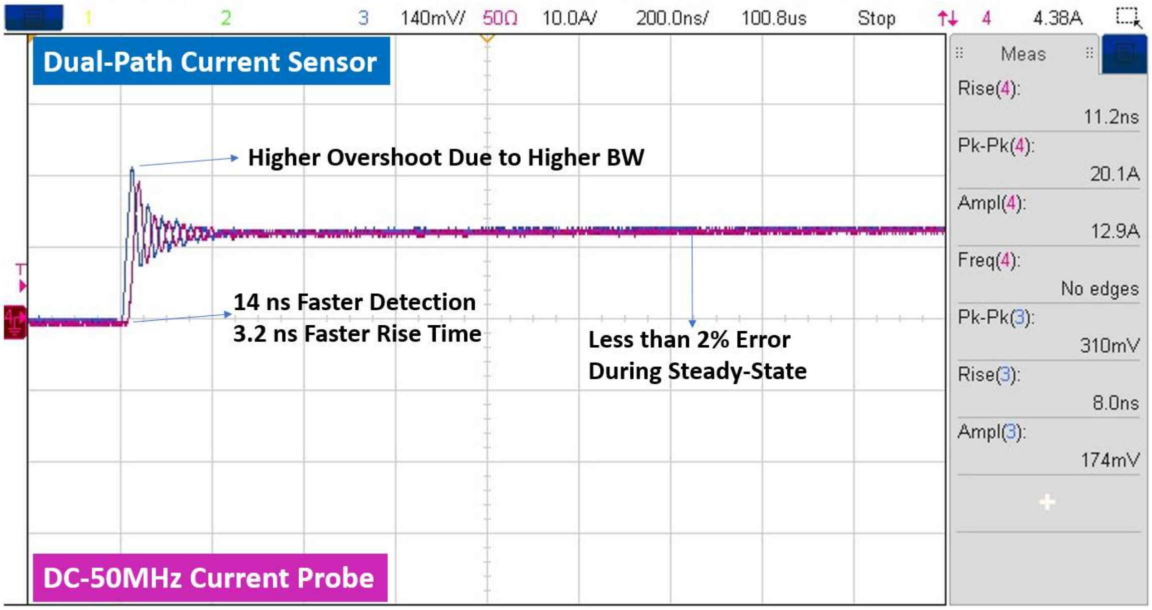

Rise(4): 11.2ns
Pk-Pk(4): 20.1A
Ampl(4): 12.9A
Freq(4): No edges
Pk-Pk(3): 310mV
Rise(3): 8.0ns
Ampl(3): 174mV

(b)

Figure 6.4: Comparison between the prototyped dual-path current sensor and DC-50 MHz current probe: a) frequency domain and b) time domain.

power electronics applications. While hybrid current sensing provides many benefits, but also some drawbacks. One potential drawback is that multi-path current sensing can be more complex to design and implement than SS sensing technologies, so that it may not be appropriate for all power electronics applications, depending on the specific requirements of each application.

During the course of this thesis, the associated challenges with MS current sensing have been explored as well as possible methods for overcoming them in some applications, which are used to propose compensated MS schemes based on SS sensing selection, design layout, cutoff frequency optimization, and possible physical realizations in accordance with the application requirements. As a consequence, these techniques may reduce the influence of external disturbances and enhance current sensing accuracy, which can also simplify the system structure and reduce hardware costs. More work can be further done to study better compound parasitic element mitigation in the MS sensor layout, investigation into employing more emerging technologies for the DC/LF sensing part, and more physical realization along with their conceivable application in control and diagnostics of WBG converters. as long as the existing dual-path system does not become too complex, MS topologies with more than two SS sensing elements can be further studied to develop robust and UWB (up to GHz) current sensors. With increased sensing elements, such topologies can provide improved performance, and the proposed DC-GHz current sensors are suitable for a variety of applications, such as low-power, high-accuracy sensors. To enhance the MS dual-path topology described in Chapter 5, it is possible, for example, to passively incorporate a PCB-embedded coil into the output of the existing current sensor, which can be modified to cover frequencies starting at the upper band of the dual-path sensor and reaching a GHz frequency range. This incorporation will enable the sensing of higher frequency signals, while also providing an effective noise reduction.

REFERENCES

[1] Ali, S., Zheng, Z., Aillerie, M., Sawicki, J.P., Pera, M.C. and Hissel, D., 2021. A review of DC Microgrid energy management systems dedicated to residential applications. Energies, 14(14), p.4308.

[2] S. Yang, D. Xiang, A. Bryant, P. Mawby, L. Ran and P. Tavner, "Condition Monitoring for Device Reliability in Power Electronic Converters: A Review," in IEEE Transactions on Power Electronics, vol. 25, no. 11, pp. 2734-2752, Nov. 2010, doi: 10.1109/TPEL.2010.2049377.

[3] S. J. Nibir, M. Biglarbegian and B. Parkhideh, "A Non-Invasive DC-10-MHz Wideband Current Sensor for Ultra-Fast Current Sensing in High-Frequency Power Electronic Converters," in IEEE Transactions on Power Electronics, vol. 34, no. 9, pp. 9095-9104, Sept. 2019, doi: 10.1109/TPEL.2018.2883639.

[4] H. H. Zeineldin, H. M. Sharaf, D. K. Ibrahim and E. E. -D. A. El-Zahab, "Optimal Protection Coordination for Meshed Distribution Systems with DG Using Dual Setting Directional Over-Current Relays," in IEEE Transactions on Smart Grid, vol. 6, no. 1, pp. 115-123, Jan. 2015, doi: 10.1109/TSG.2014.2357813.

[5] R. Rodrigues, Y. Du, A. Antoniazzi and P. Cairoli, "A Review of Solid-State Circuit Breakers," in IEEE Transactions on Power Electronics, vol. 36, no. 1, pp. 364-377, Jan. 2021, doi: 10.1109/TPEL.2020.3003358.

[6] M. Andresen, K. Ma, G. Buticchi, J. Falck, F. Blaabjerg and M. Liserre, "Junction Temperature Control for More Reliable Power Electronics," in IEEE Transactions on Power Electronics, vol. 33, no. 1, pp. 765-776, Jan. 2018, doi: 10.1109/TPEL.2017.2665697.

[7] Rezaei, O., Mirzapour, O., Panahazari, M. and Gholami, H., 2022. Hybrid AC/DC Provisional Microgrid Planning Model Considering Converter Aging. Electricity, 3(2), pp.236-250.

[8] Bajpai, P. and Dash, V., 2012. Hybrid renewable energy systems for power generation in stand-alone applications: A review. Renewable and Sustainable Energy Reviews, 16(5), pp.2926-2939.

[9] J. M. Carrasco et al., "Power-Electronic Systems for the Grid Integration of Renewable Energy Sources: A Survey," in IEEE Transactions on Industrial Electronics, vol. 53, no. 4, pp. 1002-1016, June 2006, doi: 10.1109/TIE.2006.878356.

[10] Castellazzi, A., Gurpinar, E., Wang, Z., Suliman Hussein, A. and Garcia Fernandez, P., 2019. Impact of wide-bandgap technology on renewable energy and smart-grid power conversion applications including storage. Energies, 12(23), p.4462.

[11] A. S. Abdelrahman, Z. Erdem, Y. Attia and M. Z. Youssef, "Wide Bandgap Devices in Electric Vehicle Converters: A Performance Survey," in Canadian Journal of Electrical and Computer Engineering, vol. 41, no. 1, pp. 45-54, winter 2018, doi: 10.1109/CJECE.2018.2807780.

[12] M. Salehi, M. Khodabandeh and M. Amirabadi, "Zeta-Based AC-Link Universal Converter," 2022 IEEE Energy Conversion Congress and Exposition (ECCE), Detroit, MI, USA, 2022, pp. 1-7, doi: 10.1109/ECCE50734.2022.9947744.

[13] Y. Bérubé, A. Ghazanfari, H. F. Blanchette, C. Perreault and K. Zaghib, "Recent Advances in Wide Bandgap Devices for Automotive Industry," IECON 2020 The 46th Annual Conference of the IEEE Industrial Electronics Society, Singapore, 2020, pp. 2557-2564, doi: 10.1109/IECON43393.2020.9254478.

[14] S. M. S. H. Rafin, M. A. Haque, R. Islam and O. A. Mohammed, "A Review of Power Electronic Converters for Electric Aircrafts," 2023 Fourth International Symposium on 3D Power Electronics Integration and Manufacturing (3D-PEIM), Miami, FL, USA, 2023, pp. 1-8, doi: 10.1109/3D-PEIM55914.2023.10052535.

[15] Ravinchandra, K., Freddy, T.K.S., Lee, J.S., Lee, K.B., Mantooth, H.A., Thiruchelvam, V. and Xian, J.I.Y.Y., 2022. Review of wide band-gap technology: power device, gate driver, and converter design. Journal of Power Electronics, 22(8), pp.1398-1413.

[16] H. Dai, R. A. Torres, T. M. Jahns and B. Sarlioglu, "Analysis and Suppression of Conducted Common-Mode EMI in WBG-Based Current-Source Converter Systems," in IEEE Transactions on Transportation Electrification, vol. 8, no. 2, pp. 2133-2148, June 2022, doi: 10.1109/TTE.2022.3144426.

[17] Kumar, A., Moradpour, M., Losito, M., Franke, W.T., Ramasamy, S., Baccoli, R. and Gatto, G., 2022. Wide Band Gap Devices and Their Application in Power Electronics. Energies, 15(23), p.9172.

[18] Q. Yang, A. Nabih, R. Zhang, Q. Li and Y. Zhang, "A Converter Based Switching Loss Measurement Method for WBG Device," 2023 IEEE Applied Power Electronics Conference and Exposition (APEC), Orlando, FL, USA, 2023, pp. 8-13, doi: 10.1109/APEC43580.2023.10131509.

[19] Robles, E., Matallana, A., Aretxabaleta, I., Andreu, J., Fernandez, M. and Martín, J.L., 2022. The role of power device technology in the electric vehicle powertrain. International Journal of Energy Research, 46(15), pp.22222-22265.

[20] L. Makki et al., "Equivalent Circuit Model of a Pulse Planar Transformer and Endurance to Abrupt dv/dt," in IEEE Transactions on Power Electronics, vol. 37, no. 9, pp. 10585-10593, Sept. 2022, doi: 10.1109/TPEL.2022.3160278.

[21] Pirino, P., 2022. OPTIMIZATION OF THE GATE DRIVER PARAMETERS IN A WIDE BAND GAP MATERIAL BASED DC-DC CONVERTERS FOR HIGH POWER APPLICATIONS.

[22] Choi, Y.H., Choe, H.J. and Yun, J.J., 2023. Study on 2 MHz GaN-Based Light-Emitting Diode Driver for Automotive Headlamps. Journal of Electrical Engineering & Technology, 18(1), pp.249-260.

[23] Z. Xin, H. Li, Q. Liu and P. C. Loh, "A Review of Megahertz Current Sensors for Megahertz Power Converters," in IEEE Transactions on Power Electronics, vol. 37, no. 6, pp. 6720-6738, June 2022, doi: 10.1109/TPEL.2021.3136871.

[24] Parsa Sirat, A.; Parkhideh, B. Current Sensor Integration Issues with Wide-Bandgap Power Converters. Sensors 2023, 23, 6481. https://doi.org/10.3390/s23146481.

[25] S. Ziegler, R. C. Woodward, H. H. -C. Iu and L. J. Borle, "Current Sensing Techniques: A Review," in IEEE Sensors Journal, vol. 9, no. 4, pp. 354-376, April 2009, doi: 10.1109/JSEN.2009.2013914.

[26] Ripka, P., 2010. Electric current sensors: a review. Measurement Science and Technology, 21(11), p.112001.

[27] Chucheng Xiao, Lingyin Zhao, T. Asada, W. G. Odendaal and J. D. van Wyk, "An overview of integratable current sensor technologies," 38th IAS Annual Meeting on Conference Record of the Industry Applications Conference, 2003., Salt Lake City, UT, USA, 2003, pp. 1251-1258 vol.2, doi: 10.1109/IAS.2003.1257710.

[28] Wang, J., 2018. Switching-cycle control and sensing techniques for high-density SiC-based modular converters (Doctoral dissertation, Virginia Tech).

[29] X. Yuan, I. Laird and S. Walder, "Opportunities, Challenges, and Potential Solutions in the Application of Fast-Switching SiC Power Devices and Converters," in IEEE Transactions on Power Electronics, vol. 36, no. 4, pp. 3925-3945, April 2021, doi: 10.1109/TPEL.2020.3024862.

[30] Nowicki, M., Kachniarz, M. and Szewczyk, R., 2017. Temperature error of Hall-effect and magnetoresistive commercial magnetometers. Archives of electrical engineering, 66(3), pp.625-630.

[31] L. Dalessandro, N. Karrer and J. W. Kolar, "High-Performance Planar Isolated Current Sensor for Power Electronics Applications," in IEEE Transactions on Power Electronics, vol. 22, no. 5, pp. 1682-1692, Sept. 2007, doi: 10.1109/TPEL.2007.904198.

[32] A. Parsa Sirat, H. Niakan, M. Campo, J. De La Rosa Garcia and B. Parkhideh, "An All-Passive Compound Current Sensor for Fast Switching Current Monitoring," 2022 IEEE Energy Conversion Congress and Exposition (ECCE), Detroit, MI, USA, 2022, pp. 01-07, doi: 10.1109/ECCE50734.2022.9947615.

[33] A. Parsa Sirat, H. Niakan, C. Roy and B. Parkhideh, "Rogowski-Pair Sensor for High-Speed Switch Current Measurements without Reset Requirement," 2022 IEEE Energy Conversion Congress and Exposition (ECCE), Detroit, MI, USA, 2022, pp. 1-8, doi: 10.1109/ECCE50734.2022.9948065.

[34] M. F. Snoeij, V. Schaffer, S. Udayashankar and M. V. Ivanov, "Integrated Fluxgate Magnetometer for Use in Isolated Current Sensing," in IEEE Journal of Solid-State Circuits.

[35] S. Shao, N. Yu, X. Xu, J. Bai, X. Wu and J. Zhang, "Tunnel Magnetoresistance-Based Short-Circuit and Over-Current Protection for IGBT Module," in IEEE Transactions on Power Electronics, vol. 35, no. 10, pp. 10930-10944, Oct. 2020, doi: 10.1109/TPEL.2020.2980680.

[36] A. Patel and M. Ferdowsi, "Current Sensing for Automotive Electronics—A Survey," in IEEE Transactions on Vehicular Technology, vol. 58, no. 8, pp. 4108-4119, Oct. 2009, doi: 10.1109/TVT.2009.2022081.

[37] Z. QiS et al., "A High-Bandwidth and Easy-to-Integrate Parasitics-Based Switching Current Measurement Method for Fast GaN Devices," in IEEE Transactions on Power Electronics, vol. 38, no. 1, pp. 447-459, Jan. 2023, doi: 10.1109/TPEL.2022.3200407.

[38] L. Shillaber, Y. Jiang, L. Ran and T. Long, "Ultrafast Current Shunt (UFCS): A Gigahertz Bandwidth Ultra-Low-Inductance Current Sensor," in IEEE Transactions on Power Electronics, vol. 37, no. 12, pp. 15493-15504, Dec. 2022, doi: 10.1109/TPEL.2022.3184638.

[39] T. Wickramasinghe et al., "A Study on Shunt Resistor-based Current Measurements for Fast Switching GaN Devices," IECON 2019 - 45th Annual Conference of the IEEE Industrial Electronics Society, Lisbon, Portugal, 2019, pp. 1573-1578, doi: 10.1109/IECON.2019.8927490.

[40] Caruso, M.J., Bratland, T., Smith, C.H. and Schneider, R., 1998. A new perspective on magnetic field sensing. SENSORS-PETERBOROUGH-, 15, pp.34-47.

[41] Díaz-Michelena, M., 2009. Small magnetic sensors for space applications. Sensors, 9(4), pp.2271-2288.

[42] J. Lenz and S. Edelstein, "Magnetic sensors and their applications," in IEEE Sensors Journal, vol. 6, no. 3, pp. 631-649, June 2006, doi: 10.1109/JSEN.2006.874493.

[43] Popovic, R.S., 2003. Hall effect devices. CRC Press.

[44] Paun, M.A., Sallese, J.M. and Kayal, M., 2010. Geometry influence on Hall effect devices performance. UPB Sci. Bull. Ser. A, 72(Suppl. 4), pp.257-271.

[45] Tamanaha, C.R., Mulvaney, S.P., Rife, J.C. and Whitman, L.J., 2008. Magnetic labeling, detection, and system integration. Biosensors and Bioelectronics, 24(1), pp.1-13.

[46] N. Hadjigeorgiou, K. Asimakopoulos, K. Papafotis and P. P. Sotiriadis, "Vector Magnetic Field Sensors: Operating Principles, Calibration, and Applications," in IEEE Sensors Journal, vol. 21, no. 11, pp. 12531-12544, 1 June1, 2021, doi: 10.1109/JSEN.2020.3045660.

[47] R. P. Singh and A. M. Khambadkone, "Giant Magneto Resistive (GMR) Effect Based Current Sensing Technique for Low Voltage/High Current Voltage Regulator Modules," in IEEE Transactions on Power Electronics, vol. 23, no. 2, pp. 915-925, March 2008, doi: 10.1109/TPEL.2007.915771.

[48] A. Parsa Sirat, H. Niakan, D. Evans, J. Gafford and B. Parkhideh, "Ultra-Wideband Unidirectional Reset-Less Rogowski Coil Switch Current Sensor Topology for High-Frequency DC-DC Power Converters," 2023 IEEE Applied Power Electronics Conference and Exposition (APEC), Orlando, FL, USA, 2023, pp. 1662-1669, doi: 10.1109/APEC43580.2023.10131463.

[49] Swieboda, C., Walak, J., Soinski, M., Rygal, J., Leszczynski, J. and Grybos, D., 2019. Nanocrystalline oval cut cores for current instrument transformer prototypes. Measurement, 136, pp.50-58.

[50] Bai, J.G., Lu, G.Q. and Lin, T., 2003. Magneto-optical current sensing for applications in integrated power electronics modules. Sensors and Actuators A: physical, 109(1-2), pp.9-16.

[51] S. Saadatmand, P. Shamsi and M. Ferdowsi, "Power and Frequency Regulation of Synchronverters Using a Model Free Neural Network-Based Predictive Controller," in IEEE Transactions on Industrial Electronics, vol. 68, no. 5, pp. 3662-3671, May 2021, doi: 10.1109/TIE.2020.2984419.

[52] M. Biglarbegian, N. Kim, T. Zhao and B. Parkhideh, "Development of Isolated SenseGaN current monitoring for boundary conduction mode control of power converters," 2018 IEEE Applied Power Electronics Conference and

Exposition (APEC), San Antonio, TX, USA, 2018, pp. 2725-2729, doi: 10.1109/APEC.2018.8341402.

[53] Fluri, R., Schmid, J. and Braun, P., 2011, June. Applications of low power current and voltage sensors. In Proceedings of the 21st International Conference on Electricity Distribution, Frankfurt, Germany (pp. 6-9).

[54] C. New, A. N. Lemmon and A. Shahabi, "Comparison of methods for current measurement in WBG systems," 2017 IEEE 5th Workshop on Wide Bandgap Power Devices and Applications (WiPDA), Albuquerque, NM, USA, 2017, pp. 87-92, doi: 10.1109/WiPDA.2017.8170527.

[55] P. Garcha et al., "A Duty-Cycled Integrated-Fluxgate Magnetometer for Current Sensing," in IEEE Journal of Solid-State Circuits, vol. 57, no. 9, pp. 2741-2751, Sept. 2022, doi: 10.1109/JSSC.2022.3156572.

[56] Chojowski, M., Dziadecki, A., Baszyński, M., Dudek, R., Stobiecki, A. and Skotniczny, J., 2021. Wide Bandwidth and Inexpensive Current Sensor for Power Electronics—An Augmented LEM Current Sensor. Energies, 14(14), p.4194.

[57] D. Han, S. Li, Y. Wu, W. Choi and B. Sarlioglu, "Comparative Analysis on Conducted CM EMI Emission of Motor Drives: WBG Versus Si Devices," in IEEE Transactions on Industrial Electronics, vol. 64, no. 10, pp. 8353-8363, Oct. 2017, doi: 10.1109/TIE.2017.2681968.

[58] B. Liu, R. Ren, Z. Zhang, B. Guo, F. Wang and D. Costinett, "Impacts of high frequency, high di/dt, dv/dt environment on sensing quality of GaN based converters and their mitigation," in CPSS Transactions on Power Electronics and Applications, vol. 3, no. 4, pp. 301-312, Dec. 2018, doi: 10.24295/CPSSTPEA.2018.00030.

[59] B. Zhang and S. Wang, "A Survey of EMI Research in Power Electronics Systems with Wide-Bandgap Semiconductor Devices," in IEEE Journal of Emerging and Selected Topics in Power Electronics, vol. 8, no. 1, pp. 626-643, March 2020, doi: 10.1109/JESTPE.2019.2953730.

[60] Multi Dimension, TMR2111 Linear TMR Sensor.

[61] Texas Instruments, DRV425 Fluxgate Magnetic-Field Sensor, https://www.ti.com/lit/gpn/drv425.

[62] D. Ying and D. A. Hall, "Current Sensing Front-Ends: A Review and Design Guidance," in IEEE Sensors Journal, vol. 21, no. 20, pp. 22329-22346, 15 Oct.15, 2021, doi: 10.1109/JSEN.2021.3094830.

[63] https://www.digikey.com/

[64] R. Rodrigues, Y. Du, A. Antoniazzi and P. Cairoli, "A Review of Solid-State Circuit Breakers," in IEEE Transactions on Power Electronics, vol. 36, no. 1, pp. 364-377, Jan. 2021, doi: 10.1109/TPEL.2020.3003358.

[65] S. Mocevic et al., "Comparison and Discussion on Shortcircuit Protections for Silicon-Carbide MOSFET Modules: Desaturation Versus Rogowski Switch-Current Sensor," in IEEE Transactions on Industry Applications, vol. 56, no. 3, pp. 2880-2893, May-June 2020, doi: 10.1109/TIA.2020.2972816.

[66] Baeckeland, N., Herteleer, B. and Kleemann, M., 2020. Modelling fault behaviour of power electronic converters. International Journal of Electrical Power & Energy Systems, 123, p.106230.

[67] F. Z. Peng, Y. W. Li and L. M. Tolbert, "Control and protection of power electronics interfaced distributed generation systems in a customer-driven microgrid," 2009 IEEE Power & Energy Society General Meeting, Calgary, AB, Canada, 2009, pp. 1-8, doi: 10.1109/PES.2009.5275191.

[68] J. Wang, S. Mocevic, R. Burgos and D. Boroyevich, "High-Scalability Enhanced Gate Drivers for SiC MOSFET Modules With Transient Immunity Beyond 100 V/ns," in IEEE Transactions on Power Electronics, vol. 35, no. 10, pp. 10180-10199, Oct. 2020, doi: 10.1109/TPEL.2020.2980564.

[69] A. Parsa Sirat, C. Roy, D. Evans, J. Gafford and B. Parkhideh, "In-Situ Ultrafast Sensing Techniques for Prognostics and Protection of SiC Devices," 2022 IEEE 9th Workshop on Wide Bandgap Power Devices & Applications (WiPDA), Redondo Beach, CA, USA, 2022, pp. 142-147, doi: 10.1109/WiPDA56483.2022.9955254.

[70] S. Scherner and R. Slatter, "New applications in power electronics for highly integrated high-speed magnetoresistive current sensors," CIPS 2014; 8th International Conference on Integrated Power Electronics Systems, Nuremberg, Germany, 2014, pp. 1-7.

[71] Y. Feng, S. Shao, J. Du, Q. Chen, J. Zhang and X. Wu, "Short-Circuit and Over-Current Fault Detection for SiC MOSFET Modules Based on Tunnel Magnetoresistance With Predictive Capabilities," in IEEE Transactions on Power Electronics, vol. 37, no. 4, pp. 3719-3723, April 2022, doi: 10.1109/TPEL.2021.3121572.

[72] J. Samanes et al., "Control Design and Stability Analysis of Power Converters: The MIMO Generalized Bode Criterion," in IEEE Journal of Emerging and Selected Topics in Power Electronics, vol. 8, no. 2, pp. 1880-1893, June 2020, doi: 10.1109/JESTPE.2019.2941829.

[73] D. Y. Qiu, S. C. Yip, H. S. . -H. Chung and S. Y. R. Hui, "On the use of current sensors for the control of power converters," in IEEE Transactions on Power Electronics, vol. 18, no. 4, pp. 1047-1055, July 2003, doi: 10.1109/TPEL.2003.813767.

[74] Latham, A. and Milano, S., 2013. Current sensing for renewable energy. Electron. Products, Hearst Bus. Commun., Uniondale, NY, USA, pp.40-43.

[75] F. Xiong, J. Wu, Z. Liu and L. Hao, "Current Sensorless Control for Dual Active Bridge DC–DC Converter with Estimated Load-Current Feedforward," in IEEE Transactions on Power Electronics, vol. 33, no. 4, pp. 3552-3566, April 2018, doi: 10.1109/TPEL.2017.2705344.

[76] Suzdalenko, A., Zakis, J., Suskis, P. and Ribickis, L., 2020. Bidirectional single-loop current sensorless control applied to NPC multi-level converter considering conduction losses. International Journal of Power Electronics and Drive Systems, 11(4), p.1945.

[77] M. Ghadrdan, B. Abdi, S. Peyghami, H. Mokhtari and F. Blaabjerg, "On-Line Condition Monitoring System for DC-Link Capacitor of Back-to-Back Converters Using Large-Signal Transients," in IEEE Journal of Emerging and Selected Topics in Power Electronics, vol. 11, no. 1, pp. 1132-1142, Feb. 2023, doi: 10.1109/JESTPE.2022.3163012.

[78] S. Pu, E. Ugur, F. Yang and B. Akin, "In situ Degradation Monitoring of SiC MOSFET Based on Switching Transient Measurement," in IEEE Transactions on

Industrial Electronics, vol. 67, no. 6, pp. 5092-5100, June 2020, doi: 10.1109/TIE.2019.2924600.

[79] J. P. Kozak, R. Zhang, J. Liu, K. D. T. Ngo and Y. Zhang, "Degradation of SiC MOSFETs Under High-Bias Switching Events," in IEEE Journal of Emerging and Selected Topics in Power Electronics, vol. 10, no. 5, pp. 5027-5038, Oct. 2022, doi: 10.1109/JESTPE.2021.3064288.

[80] S. Pu, F. Yang, B. T. Vankayalapati, E. Ugur, C. Xu and B. Akin, "A Practical On-Board SiC MOSFET Condition Monitoring Technique for Aging Detection," in IEEE Transactions on Industry Applications, vol. 56, no. 3, pp. 2828-2839, May-June 2020, doi: 10.1109/TIA.2020.2980220.

[81] G. Zu et al., "Review of Pulse Test Setup for the Switching Characterization of GaN Power Devices," in IEEE Transactions on Electron Devices, vol. 69, no. 6, pp. 3003-3013, June 2022, doi: 10.1109/TED.2022.3168238.

[82] https://www.lem.com/en/product-list/la-100p

[83] Ghislanzoni, L., 1989, August. Magnetic coupled current sensing techniques for spacecraft power systems. In European Space Power Conference (Vol. 294, p. 323).

[84] Ghislanzoni, L., Agence Spatiale Europeenne, 1990. Magnetically-coupled apparatus for measuring electrical current. U.S. Patent 4,961,049.

[85] J. A. Carrasco, E. Sanchis-Kilders, D. Ramirez and E. J. Dede, "Improved magnetic coupled current sensing techniques [space power applications]," PESC Record. 27th Annual IEEE Power Electronics Specialists Conference, Baveno, Italy, 1996, pp. 829-834 vol.1, doi: 10.1109/PESC.1996.548677.

[86] Ulrich, B., 2019. Open-source wideband (DC to MHz range) isolated current sensor. HardwareX, 5, p.e00057.

[87] G. Laimer and J. W. Kolar, "Wide bandwidth low complexity isolated current sensor to be employed in a 10 kW/500 kHz three-phase unity power factor PWM rectifier system," 2002 IEEE 33rd Annual IEEE Power Electronics Specialists Conference. Proceedings (Cat. No.02CH37289), Cairns, QLD, Australia, 2002, pp. 1065-1070 vol.3, doi: 10.1109/PSEC.2002.1022316.

[88] P. S. Niklaus, D. Bortis and J. W. Kolar, "High-Bandwidth High-CMRR Current Measurement for a 4.8 MHz Multi-Level GaN Inverter AC Power Source," 2021 IEEE Applied Power Electronics Conference and Exposition (APEC), Phoenix, AZ, USA, 2021, pp. 200-207, doi: 10.1109/APEC42165.2021.9487044.

[89] P. Poulichet, F. Costa and E. Laboure, "A new high-current large-bandwidth DC active current probe for power electronics measurements," in IEEE Transactions on Industrial Electronics, vol. 52, no. 1, pp. 243-254, Feb. 2005, doi: 10.1109/TIE.2004.841066.

[90] Karrer, N., Hofer-Noser, P. and Henrard, D., 1999, September. A new current probe with a wide bandwidth. In 8 European Conference on Power Electronics and Applications.

[91] N. Karrer, P. Hofer-Noser and D. Henrard, "HOKA: a new isolated current measuring principle and its features," Conference Record of the 1999 IEEE Industry Applications Conference. Thirty-Forth IAS Annual Meeting (Cat. No.99CH36370), Phoenix, AZ, USA, 1999, pp. 2121-2128 vol.3, doi: 10.1109/IAS.1999.806028.

[92] Hudoffsky, B., Roth-Stielow, J. and Karrer, N., 2010. Realization of a (400 A/DC-10 MHz) clamping HOKA current probe. In Proceedings: PCIM Europe 2010: International Exhibition & Conference for Power Electronics Intelligent Motion Power Quality, 4-6 May 2010, Exhibition Centre Nuremberg (pp. 556-561). VDE-Verl..

[93] B. Hudoffsky and J. Roth-Stielow, "New evaluation of low frequency capture for a wide bandwidth clamping current probe for ±800 A using GMR sensors," Proceedings of the 2011 14th European Conference on Power Electronics and Applications, Birmingham, UK, 2011, pp. 1-7.

[94] N. Tröster, J. Wölfle, J. Ruthardt and J. Roth-Stielow, "High bandwidth current sensor with a low insertion inductance based on the HOKA principle," 2017 19th European Conference on Power Electronics and Applications (EPE'17 ECCE Europe), Warsaw, Poland, 2017, pp. P.1-P.9, doi: 10.23919/EPE17ECCEEurope.2017.8099003.

[95] N. Tröster, T. Eisenhardt, M. Zehelein, J. Wölfle, J. Ruthardt and J. Roth-Stielow, "Improvements of a Coaxial Current Sensor with a Wide Bandwidth Based on the HOKA Principle," 2018 20th European Conference on Power Electronics and Applications (EPE'18 ECCE Europe), Riga, Latvia, 2018, pp. P.1-P.9.

[96] P. Ziegler, N. Tröster, D. Schmidt, J. Ruthardt, M. Fischer and J. Roth-Stielow, "Wide Bandwidth Current Sensor for Commutation Current Measurement in Fast Switching Power Electronics," 2020 22nd European Conference on Power Electronics and Applications (EPE'20 ECCE Europe), Lyon, France, 2020, pp. P.1-P.9, doi: 10.23919/EPE20ECCEEurope43536.2020.9215686.

[97] P. Ziegler, F. Stjepandic, J. Ruthardt, P. Marx, M. Fischer and J. Roth-Stielow, "Wide Bandwidth Current Sensor for Characterization of High Current Power Semiconductor Modules," 2021 23rd European Conference on Power Electronics and Applications (EPE'21 ECCE Europe), Ghent, Belgium, 2021, pp. 1-9, doi: 10.23919/EPE21ECCEEurope50061.2021.9570438.

[98] A. Jouyaeian, Q. Fan, M. Motz, U. Ausserlechner and K. A. A. Makinwa, "5.6 A 25A Hybrid Magnetic Current Sensor with 64mA Resolution, 1.8MHz Bandwidth, and a Gain Drift Compensation Scheme," 2021 IEEE International Solid- State Circuits Conference (ISSCC), San Francisco, CA, USA, 2021, pp. 82-84, doi: 10.1109/ISSCC42613.2021.9365767.

[99] J. Jiang and K. Makinwa, "11.3 A hybrid multipath CMOS magnetic sensor with 210µTrms resolution and 3MHz bandwidth for contactless current sensing," 2016 IEEE International Solid-State Circuits Conference (ISSCC), San Francisco, CA, USA, 2016, pp. 204-205, doi: 10.1109/ISSCC.2016.7417978.

[100] A. Jouyaeian, Q. Fan, M. Motz, U. Ausserlechner and K. A. A. Makinwa, "23.3 A 51A Hybrid Magnetic Current Sensor with a Dual Differential DC Servo Loop and 43mArms Resolution in a 5MHz Bandwidth," 2023 IEEE International Solid- State Circuits Conference (ISSCC), San Francisco, CA, USA, 2023, pp. 22-24, doi: 10.1109/ISSCC42615.2023.10067677.

[101] T. Funk, J. Groeger and B. Wicht, "An Integrated and Galvanically Isolated DC-to-15.3 MHz Hybrid Current Sensor," 2019 IEEE Applied Power Electronics

Conference and Exposition (APEC), Anaheim, CA, USA, 2019, pp. 1010-1013, doi: 10.1109/APEC.2019.8722098.

[102] T. Funk and B. Wicht, "A fully integrated DC to 75 MHz current sensing circuit with on-chip Rogowski coil," 2018 IEEE Custom Integrated Circuits Conference (CICC), San Diego, CA, USA, 2018, pp. 1-4, doi: 10.1109/CICC.2018.8357028.

[103] P. S. Niklaus, D. Bortis and J. W. Kolar, "Beyond 50 MHz Bandwidth Extension of Commercial DC-Current Measurement Sensors with Ultra-Compact PCB-Integrated Pickup Coils," in IEEE Transactions on Industry Applications, vol. 58, no. 4, pp. 5026-5041, July-Aug. 2022, doi: 10.1109/TIA.2022.3164865.

[104] A. M. Luciano and M. Savastano, "Wide band transformer based on a split-conductor current sensor and a Rogowski coil for high current measurement," Proceedings of 1995 IEEE Instrumentation and Measurement Technology Conference - IMTC '95, Waltham, MA, USA, 1995, pp. 454-, doi: 10.1109/IMTC.1995.515360.

[105] L. Ghislanzoni and J. A. Carrasco, "A DC current transformer for large bandwidth and high common-mode rejection," in IEEE Transactions on Industrial Electronics, vol. 46, no. 3, pp. 631-636, June 1999, doi: 10.1109/41.767072.

[106] Wenbin Yu, Guoqing Zhang and Zhizhong Guo, "A hybrid optical current sensor for power system metering and protection," IECON'03. 29th Annual Conference of the IEEE Industrial Electronics Society (IEEE Cat. No.03CH37468), Roanoke, VA, USA, 2003, pp. 2517-2521 Vol.3, doi: 10.1109/IECON.2003.1280641.

[107] L. Dziuda, P. Niewczas and J. R. McDonald, "Hybrid fiber-optic current sensor for remote monitoring of electrical submersible plant," SENSORS, 2005 IEEE, Irvine, CA, USA, 2005, pp. 4 pp.-, doi: 10.1109/ICSENS.2005.1597896.

[108] P. Niewczas, G. Fusiek and J. R. McDonald, "Dynamic Capabilities of the Hybrid Fiber-Optic Voltage and Current Sensors," SENSORS, 2006 IEEE, Daegu, Korea (South), 2006, pp. 295-298, doi: 10.1109/ICSENS.2007.355464.

[109] Dziuda, L., Fusiek, G., Niewczas, P., Burt, G.M. and McDonald, J.R., 2007. Laboratory evaluation of the hybrid fiber-optic current sensor. Sensors and Actuators A: Physical, 136(1), pp.184-190.

[110] C. -C. Lu, Y. -C. Lin, Y. -Z. Tian and J. -T. Jeng, "Hybrid Microfluxgate and Current Transformer Sensor," in IEEE Transactions on Magnetics, vol. 58, no. 8, pp. 1-5, Aug. 2022, Art no. 8002105, doi: 10.1109/TMAG.2022.3157052.

[111] J. D. Bull, N. A. F. Jaeger and F. Rahmatian, "A new hybrid current sensor for high-voltage applications," in IEEE Transactions on Power Delivery, vol. 20, no. 1, pp. 32-38, Jan. 2005, doi: 10.1109/TPWRD.2004.833889.

[112] P. Orr et al., "An Optically-Interrogated Rogowski Coil for Passive, Multiplexable Current Measurement," in IEEE Sensors Journal, vol. 13, no. 6, pp. 2053-2054, June 2013, doi: 10.1109/JSEN.2013.2252614.

[113] F. Han, S. Harada and I. Sasada, "Fluxgate and Search Coil Hybrid: A Low-Noise Wide-Band Magnetometer," in IEEE Transactions on Magnetics, vol. 48, no. 11, pp. 3700-3703, Nov. 2012, doi: 10.1109/TMAG.2012.2196762.

[114] S. B. Sohid, H. H. Cui, W. Zhang, F. Wang and B. Holzinger, "Combinational Rogowski Coil with Enhanced DC Measurement Capability for Double Pulse Test Applications," 2022 IEEE Energy Conversion Congress and Exposition (ECCE), Detroit, MI, USA, 2022, pp. 1-7, doi: 10.1109/ECCE50734.2022.9947541.

[115] W. Guo, G. Xiao, K. Gao and L. Wang, "A Compact Hybrid Sensor for Chip-level Online Current Sensing in Press-pack Power Module," 2023 IEEE Applied Power Electronics Conference and Exposition (APEC), Orlando, FL, USA, 2023, pp. 2545-2549, doi: 10.1109/APEC43580.2023.10131588.

[116] A. Mahar et al., "An On-chip DC to 42.8 MHz Bandwidth Readout Interface for Hybrid Current Sensor," 2023 IEEE Applied Power Electronics Conference and Exposition (APEC), Orlando, FL, USA, 2023, pp. 769-774, doi: 10.1109/APEC43580.2023.10131281.

[117] S. J. Nibir, S. Hauer, M. Biglarbegian and B. Parkhideh, "Wideband contactless current sensing using hybrid magnetoresistor-Rogowski sensor in high frequency power electronic converters," 2018 IEEE Applied Power Electronics

Conference and Exposition (APEC), San Antonio, TX, USA, 2018, pp. 904-908, doi: 10.1109/APEC.2018.8341121.

[118] P. Ziegler, M. Bura, J. Haarer, P. Marx, D. Hirning and J. Roth-Stielow, "Optimization Approaches for the Signal Processing of Hybrid Current Sensors," 2022 International Power Electronics Conference (IPEC-Himeji 2022- ECCE Asia), Himeji, Japan, 2022, pp. 506-513, doi: 10.23919/IPEC-Himeji2022-ECCE53331.2022.9807001.

[119] A. Mahar, A. Hassan, R. Murphree, J. De La Rosa Garcia, B. Parkhideh and H. A. Mantooth, "A DC to 42.8 MHz Bandwidth Current Sensor Readout Interface using Amplifiers with Feedforward Compensation for Power Electronics Applications," 2022 23rd International Middle East Power Systems Conference (MEPCON), Cairo, Egypt, 2022, pp. 1-5, doi: 10.1109/MEPCON55441.2022.10021690.

[120] S. M. Ahsanuzzaman and A. Prodić, "An on-chip integrated auto-tuned hybrid current-sensor for high-frequency low-power dc-dc converters," 2015 IEEE Applied Power Electronics Conference and Exposition (APEC), Charlotte, NC, USA, 2015, pp. 445-450, doi: 10.1109/APEC.2015.7104388.

[121] W. Li, G. Zhang, H. Zhong and Y. Geng, "A Wideband Current Transducer Based on an Array of Magnetic Field Sensors for Rectangular Busbar Current Measurement," in IEEE Transactions on Instrumentation and Measurement, vol. 70, pp. 1-11, 2021, Art no. 9004511, doi: 10.1109/TIM.2021.3105239.

[122] R. Weiss, A. Itzke, J. Reitenspieß, I. Hoffmann and R. Weigel, "A Novel Closed Loop Current Sensor Based on a Circular Array of Magnetic Field Sensors," in IEEE Sensors Journal, vol. 19, no. 7, pp. 2517-2524, 1 April1, 2019, doi: 10.1109/JSEN.2018.2887302.

[123] S. Qian et al., "Design of a Nonintrusive Current Sensor with Large Dynamic Range Based on Tunneling Magnetoresistive Devices," 2022 IEEE 5th International Electrical and Energy Conference (CIEEC), Nangjing, China, 2022, pp. 3405-3409, doi: 10.1109/CIEEC54735.2022.9846524.

[124] Mușuroi, C., Oproiu, M., Volmer, M., Neamtu, J., Avram, M. and Helerea, E., 2021. Low field optimization of a non-contacting high-sensitivity GMR-based DC/AC current sensor. Sensors, 21(7), p.2564.

[125] C. Roy, N. Kim, H. Niakan, A. Parsa Sirat and B. Parkhideh, "An Ultra-Fast and Non-Invasive Short Circuit Protection Strategy for a WBG Power Electronics Converter with Multiple Half-Bridge Legs," 2020 IEEE Energy Conversion Congress and Exposition (ECCE), Detroit, MI, USA, 2020, pp. 2505-2510, doi: 10.1109/ECCE44975.2020.9235341.

[126] Infineon, Half-bridge 1200 V CoolSiC™ MOSFET Module, www.infineon.com/cms/en/product/power/mosfet/silicon-carbide/modules/ff3mr12km1/.

[127] Y. Xue, J. Lu, Z. Wang, L. M. Tolbert, B. J. Blalock and F. Wang, "A compact planar Rogowski coil current sensor for active current balancing of parallel-connected Silicon Carbide MOSFETs," 2014 IEEE Energy Conversion Congress and Exposition (ECCE), Pittsburgh, PA, USA, 2014, pp. 4685-4690, doi: 10.1109/ECCE.2014.6954042.

[128] S. Fu et al., "Current Measurement Method of Multiple Chips Using Rectangular PCB Rogowski Coils Integrated in Press Pack IGBT Device," in IEEE Transactions on Power Electronics, vol. 38, no. 1, pp. 96-100, Jan. 2023, doi: 10.1109/TPEL.2022.3205353.

[129] J. Walter, J. Acuna and I. Kallfass, "Design and Implementation of an Integrated Current Sensor for a Gallium Nitride Half-Bridge," PCIM Europe 2018; International Exhibition and Conference for Power Electronics, Intelligent Motion, Renewable Energy and Energy Management, Nuremberg, Germany, 2018, pp. 1-8.

[130] P. E. Schneider and R. D. Lorenz, "Evaluation of point field sensing in IGBT modules for high bandwidth current measurement," 2011 IEEE Energy Conversion Congress and Exposition, Phoenix, AZ, USA, 2011, pp. 1950-1957, doi: 10.1109/ECCE.2011.6064025.

[131] L. Ravi, J. Liu, S. Schmalz, A. Schroedermeier, R. Burgos and D. Dong, "A Compact Anisotropic Magnetoresistance Based Contactless Current Sensor for

Medium Voltage Power Electronics Applications," 2023 IEEE Applied Power Electronics Conference and Exposition (APEC), Orlando, FL, USA, 2023, pp. 1670-1675, doi: 10.1109/APEC43580.2023.10131423.

[132] Niklaus, P.S., 2022. 4.8 MHz GaN Class-D Power Amplifier and Measurement Systems for Next Generation Power Electronics (Doctoral dissertation, ETH Zurich).

[133] Kim, U.J. and Kim, R.Y., 2020. Analysis of various pickup coil designs in nonmodule-type GaN power semiconductors. Sensors, 20(21), p.6066.

[134] N. Oswald, P. Anthony, N. McNeill and B. H. Stark, "An Experimental Investigation of the Tradeoff between Switching Losses and EMI Generation with Hard-Switched All-Si, Si-SiC, and All-SiC Device Combinations," in IEEE Transactions on Power Electronics, vol. 29, no. 5, pp. 2393-2407, May 2014, doi: 10.1109/TPEL.2013.2278919.

[135] J. Lautner and B. Piepenbreier, "Impact of current measurement on switching characterization of GaN transistors," 2014 IEEE Workshop on Wide Bandgap Power Devices and Applications, Knoxville, TN, USA, 2014, pp. 98-102, doi: 10.1109/WiPDA.2014.6964632.

[136] Y. Wang, Z. Zeng, T. Long, P. Sun, L. Wang and M. Zou, "Impedance-Matching Shunt: Current Sensor With Ultrahigh Bandwidth and Extremely Low Parasitics for Wide-Bandgap Device," in IEEE Transactions on Power Electronics, vol. 37, no. 10, pp. 11528-11533, Oct. 2022, doi: 10.1109/TPEL.2022.3175973.

[137] M. Sheng, M. H. Alvi and R. D. Lorenz, "Die Level Sensor Integration in SiC Power Modules," 2018 IEEE Transportation Electrification Conference and Expo (ITEC), Long Beach, CA, USA, 2018, pp. 353-358, doi: 10.1109/ITEC.2018.8450247.

[138] J. Du, Y. Feng, Q. Chen and S. Shao, "Tunnel Magnetoresistance-Based Short-circuit Protection for SiC MOSFET in HybridPACK™ Drive Package," IECON 2022 – 48th Annual Conference of the IEEE Industrial Electronics Society, Brussels, Belgium, 2022, pp. 1-5, doi: 10.1109/IECON49645.2022.9968334.

[139] Cha, H.R., Kim, K.M., Song, M.S. and Kim, R.Y., 2020. PCB-embedded spiral pattern pick-up coil current sensor for WBG devices. Energies, 13(21), p.5747.

[140] Mocevic, S., 2018. PCB-embedded phase current sensor and short-circuit detector for high power SiC-based converters (Doctoral dissertation, Virginia Tech).

[141] D. Koch, H. Bantle, J. Acuna, P. Ziegler and I. Kallfass, "Design Methodology for Ultra-Compact Rogowski Coils for Current Sensing in Low-Voltage High-Current GaN Based DC/DC-Converters," 2021 23rd European Conference on Power Electronics and Applications (EPE'21 ECCE Europe), Ghent, Belgium, 2021, pp. P.1-P.9, doi: 10.23919/EPE21ECCEEurope50061.2021.9570596.

[142] J. Wang, S. Mocevic, Y. Xu, C. DiMarino, R. Burgos and D. Boroyevich, "A High-Speed Gate Driver with PCB-Embedded Rogowski Switch-Current Sensor for a 10 kV, 240 A, SiC MOSFET Module," 2018 IEEE Energy Conversion Congress and Exposition (ECCE), Portland, OR, USA, 2018, pp. 5489-5494, doi: 10.1109/ECCE.2018.8557631.

[143] Niakan, H., 2023. Current Sensing Solutions for Modern Power Electronic (Master Thesis, The University of North Carolina at Charlotte).

[144] H. Niakan, A. Parsa Sirat and B. Parkhideh, "A Novel Reset-Less Rogowski Switch-Current Sensor," in IEEE Transactions on Power Electronics, vol. 38, no. 4, pp. 4203-4206, April 2023, doi: 10.1109/TPEL.2022.3227536.

[145] Z. Yan and L. Hongbin, “ The reliable design of PCB Rogowski coil current transformer,” in Proc. IEEE Int. Conf. Power Syst. Technol., Oct. 2006, pp. 1–4.

[146] Y. Shi, Z. Xin, P. C. Loh and F. Blaabjerg, "A Review of Traditional Helical to Recent Miniaturized Printed Circuit Board Rogowski Coils for Power-Electronic Applications," in IEEE Transactions on Power Electronics, vol. 35, no. 11, pp. 12207-12222, Nov. 2020, doi: 10.1109/TPEL.2020.2984055.

[147] Yue, X., Zhu, G., Wang, J.V., Deng, X. and Wang, Q., 2023. PCB Rogowski Coils for Capacitors Current Measurement in System Stability Enhancement. Electronics, 12(5), p.1099.

[148] M. Koga, M. Tsukuda, K. Nakashima and I. Omura, "Application-specific micro Rogowski coil for power modules - Design tool, novel coil pattern and demonstration," CIPS 2016; 9th International Conference on Integrated Power Electronics Systems, Nuremberg, Germany, 2016, pp. 1-5.

[149] K. Wang, X. Yang, H. Li, L. Wang and P. Jain, "A High-Bandwidth Integrated Current Measurement for Detecting Switching Current of Fast GaN Devices," in IEEE Transactions on Power Electronics, vol. 33, no. 7, pp. 6199-6210, July 2018, doi: 10.1109/TPEL.2017.2749249.

[150] Y. Kuwabara, K. Wada, J. -M. Guichon, J. -L. Schanen and J. Roudet, "Design of an Integrated Air Coil for Current Sensing," in IEEE Journal of Emerging and Selected Topics in Power Electronics, vol. 8, no. 4, pp. 4122-4129, Dec. 2020, doi: 10.1109/JESTPE.2020.2977102.

[151] Kim, U.J., Song, M.S. and Kim, R.Y., 2020. PCB-based current sensor design for sensing switch current of a nonmodular GaN power semiconductor. Energies, 13(19), p.5161.

[152] Q. Xu et al., "Design of PCB Rogowski Coil Current Sensor with Low Droop Distortion," in IEEE Transactions on Power Electronics, vol. 38, no. 4, pp. 5513-5523, April 2023, doi: 10.1109/TPEL.2022.3233075.

[153] S. Mocevic et al., "Phase Current Reconstruction based on Rogowski Coils Integrated on Gate Driver of SiC MOSFET Half-Bridge Module for Continuous and Discontinuous PWM Inverter Applications," 2019 IEEE Applied Power Electronics Conference and Exposition (APEC), Anaheim, CA, USA, 2019, pp. 1029-1036, doi: 10.1109/APEC.2019.8722167.

[154] Rothwell, E.J. and Cloud, M.J., 2018. Electromagnetics. CRC press.

[155] Bansal, R. ed., 2004. Handbook of engineering electromagnetics. CRC Press.

[156] Cheng, D.K., 1993. Fundamentals of engineering electromagnetics.

[157] Ulaby, F.T. and Ravaioli, U., 2015. Fundamentals of applied electromagnetics (Vol. 7). Upper Saddle River, NJ: Pearson.

[158] Fritz, J.N., Neeb, C. and De Doncker, R.W., 2015. A PCB integrated differential Rogowski coil for non-intrusive current measurement featuring high bandwidth and dv/dt immunity.

[159] P. Ziegler, T. Festerling, J. Haarer, P. Marx, D. Hirning and J. Roth-Stielow, "Influences of Parasitic Capacitances in Wide Bandwidth Rogowski Coils for Commutation Current Measurement," 2022 24th European Conference on Power Electronics and Applications (EPE'22 ECCE Europe), Hanover, Germany, 2022, pp. 1-10.

[160] W. F. Ray and C. R. Hewson, "High performance Rogowski current transducers," Conference Record of the 2000 IEEE Industry Applications Conference. Thirty-Fifth IAS Annual Meeting and World Conference on Industrial Applications of Electrical Energy (Cat. No.00CH37129), Rome, Italy, 2000, pp. 3083-3090 vol.5, doi: 10.1109/IAS.2000.882606.

[161] L. Ming, Z. Xin, C. Yin, M. Chen and P. C. Loh, "Integrator Design of the Rogowski Current Sensor for Detecting Fast Switch Current of SiC Devices," 2019 IEEE Energy Conversion Congress and Exposition (ECCE), Baltimore, MD, USA, 2019, pp. 4551-4557, doi: 10.1109/ECCE.2019.8911874.

[162] L. Ming, Z. Xin, C. Yin, P. C. Loh and Y. Liu, "Screen-Returned PCB Rogowski Coil for the Switch Current Measurement of SiC Devices," 2019 IEEE Applied Power Electronics Conference and Exposition (APEC), Anaheim, CA, USA, 2019, pp. 958-964, doi: 10.1109/APEC.2019.8721915.

[163] Thomas, R.E., Rosa, A.J. and Toussaint, G.J., 2016. The analysis and design of linear circuits. John Wiley & Sons.

[164] Razavi, B., 2021. Fundamentals of microelectronics. John Wiley & Sons.

[165] Gupta, J.B., 2009. Electronic Devices and circuits. Seagull Books Pvt Ltd.

[166] Jaeger, R.C., Blalock, T.N. and Blalock, B.J., 1997. Microelectronic circuit design (pp. 1033-1036). New York: McGraw-Hill.

[167] Bell, D.A., 1997. Operational amplifiers and linear ICs. DA Bell.

[168] Pettinga, J. J. and John N Siersema. “A polyphase 500 kA current measuring system with Rogowski coils.” (1983).

[169] Pokryvailo, A. and Kushnerov, A., 2006. Design of Rogowski coil with integrator.

[170] C. Qing, L. Hong-bin, H. Ben-xiong and D. Qiao-qi, "Rogowski Sensor for Plasma Current Measurement in J-TEXT," in IEEE Sensors Journal, vol. 9, no. 3, pp. 293-296, March 2009, doi: 10.1109/JSEN.2009.2013497.

[171] Vos, M.J., 3M Innovative Properties Co, 2017. Electronic integrator for Rogowski coil sensors. U.S. Patent 9,588,147.

[172] Xia, Y.J., Zhang, Z.D., Xia, Z.X., Zhu, S.L. and Zhang, R., 2015. A precision analogue integrator system for heavy current measurement in MFDC resistance spot welding. Measurement Science and Technology, 27(2), p.025104.

[173] H. Watanabe, K. Yamamoto, I. Nomura, S. Sumi and T. Wada, "Small-Diameter Rogowski Coil and Integrator for Wide-Band Current Sensor," 2019 11th Asia-Pacific International Conference on Lightning (APL), Hong Kong, China, 2019, pp. 1-6, doi: 10.1109/APL.2019.8816010.

[174] H. Li, Z. Xin, X. Li, J. Chen, P. C. Loh and F. Blaabjerg, "Extended Wide-Bandwidth Rogowski Current Sensor With PCB Coil and Electronic Characteristic Shaper," in IEEE Transactions on Power Electronics, vol. 36, no. 1, pp. 29-33, Jan. 2021, doi: 10.1109/TPEL.2020.3001058.

[175] J. Wang, Z. Shen, C. DiMarino, R. Burgos and D. Boroyevich, "Gate driver design for 1.7kV SiC MOSFET module with Rogowski current sensor for shortcircuit protection," 2016 IEEE Applied Power Electronics Conference and Exposition (APEC), Long Beach, CA, USA, 2016, pp. 516-523, doi: 10.1109/APEC.2016.7467921.

[176] Z. Zhou, Z. Xin, Q. Liu and C. Li, "A Differential Compensated Air Coil Current Sensor for Switching Current Measurement of Power Devices," in IEEE Transactions on Industrial Electronics, vol. 70, no. 5, pp. 5356-5364, May 2023, doi: 10.1109/TIE.2022.3181368.

[177] S. Mocevic, J. Wang, R. Burgos and D. Boroyevich, "Rogowski Switch-Current Sensor Self-Calibration on Enhanced Gate Driver for 10 kV SiC MOSFETs," 2021 IEEE 12th Energy Conversion Congress & Exposition - Asia

(ECCE-Asia), Singapore, Singapore, 2021, pp. 1420-1425, https://doi.org/10.1109/ECCE-Asia49820.2021.9478973.

[178] Hagh, A.K.A., Ashtiani, S.J. and Akmal, A.A.S., 2017. A wideband, sensitive current sensor employing transimpedance amplifier as interface to Rogowski coil. Sensors and Actuators A: Physical, 256, pp.43-50.

[179] S. M. Kim, R. Burgos and T. Kwon, "Design of Rogowski Switch-Current Sensor with Offset Compensation for Three-Phase SiC Inverter," in IEEE Transactions on Power Electronics, vol. 37, no. 10, pp. 11636-11649, Oct. 2022, https://doi.org/10.1109/TPEL.2022.3170545.

[180] A. Radun, "An alternative low-cost current-sensing scheme for high-current power electronics circuits," in IEEE Transactions on Industrial Electronics, vol. 42, no. 1, pp. 78-84, Feb. 1995, https://doi.org/10.1109/41.345849.

[181] Texas Instruments, LM6172 Dual High Speed, Low Power, Low Distortion, Voltage Feedback Amplifiers, 2013, https://www.ti.com/lit/gpn/lm6172.

[182] Texas Instruments, LM7372 Dual High Speed, High Output Current, Voltage Feedback Amplifiers, 2014, https://www.ti.com/product/LM7372.

[183] Ming, L., Xin, Z., Liu, W. and Chiang Loh, P. (2020), Structure and modelling of four-layer screen-returned PCB Rogowski coil with very few turns for high-bandwidth SiC current measurement. IET Power Electronics, 13: 765-775. https://doi.org/10.1049/iet-pel.2019.0694.

[184] X. Zhao et al., "Design of Ultra-Compact Gate Driver Integrated with Current Sensor and Commutation Path for a 211-kW Three-Level SiC Aircraft Propulsion Inverter," in IEEE Journal of Emerging and Selected Topics in Power Electronics, doi: 10.1109/JESTPE.2023.3247378.

[185] S. Panigrahi and S. K. Pramanick, "A Comparison Between Screen-Return and Trace-Return PCB Rogowski Coils for SiC Power Modules," 2022 IEEE Global Conference on Computing, Power and Communication Technologies (GlobConPT), New Delhi, India, 2022, pp. 1-6, doi: 10.1109/GlobConPT57482.2022.9938167.

[186] Multi Dimension, TMR2111 Linear TMR Sensor.

[187] Tektronix Current Probe, DC - 50 MHz, 50 A DC (TCP305A), https://www.tek.com/en/datasheet/ac-dc-current-measurement-systems.

[188] Du, X., Du, L., Chen, Y., Wei, Y., Stratta, A. and Mantooth, H.A., 2023. A Nonlinear-Model-Based High-Bandwidth Current Sensor Design for Switching Current Measurement of Wide Bandgap Devices. Sensors, 23(10), p.4626.

[189] Nibir, S.J., 2017. INVESTIGATION ON MAGNETORESISTORS AS CONTACTLESS CURRENT SENSORS FOR HIGH FREQUENCY POWER ELECTRONIC CONVERTERS (Doctoral dissertation, The University of North Carolina at Charlotte).

[190] Keysight DSOX3034A Oscilloscope: 350 MHz, 4 Channels, https://www.keysight.com/us/en/product/DSOX3034A/oscilloscope-350-mhz-4-channels.html.

[191] M. Xiang, H. Gao, B. Zhao, C. Wang and C. Tian, "Analysis on transfer characteristics of Rogowski coil transducer to travelling wave," 2011 International Conference on Advanced Power System Automation and Protection, Beijing, China, 2011, pp. 1056-1059, doi: 10.1109/APAP.2011.6180705.

[192] Qu, Z., Zhu, Z., Liu, Y., Yu, M. and Ye, T.T., 2023. Parasitic capacitance modeling and measurements of conductive yarns for e-textile devices. Nature Communications, 14(1), p.2785.

[193] R. Qin, J. Li, J. Sun and D. Costinett, "Shielding Design for High-Frequency Wireless Power Transfer System for EV Charging with Self-Resonant Coils," in IEEE Transactions on Power Electronics, vol. 38, no. 6, pp. 7900-7909, June 2023, doi: 10.1109/TPEL.2023.3251990.

[194] Y. Xie, J. Zhang, F. Leonardi, A. R. Munoz, M. W. Degner and F. Liang, "Modeling and Verification of Electrical Stress in Inverter-Driven Electric Machine Windings," in IEEE Transactions on Industry Applications, vol. 55, no. 6, pp. 5818-5829, Nov.-Dec. 2019, doi: 10.1109/TIA.2019.2937068.

[195] X. Liu, H. Huang and Y. Dai, "Effect of Frequency on the Linearity of Double-Layer and Single-Layer Rogowski Coils," in IEEE Sensors Journal, vol. 20, no. 17, pp. 9910-9918, 1 Sept.1, 2020, doi: 10.1109/JSEN.2020.2988073.

[196] J. Mai, X. Zeng, Y. Yao, Y. Wang and D. Xu, "Improved Winding and Compensation Methods for the Multilayer Coil in IPT System," in IEEE Transactions on Industrial Electronics, vol. 69, no. 5, pp. 5375-5380, May 2022, doi: 10.1109/TIE.2021.3082061.

[197] K. Chen and Z. Zhao, "Analysis of the Double-Layer Printed Spiral Coil for Wireless Power Transfer," in IEEE Journal of Emerging and Selected Topics in Power Electronics, vol. 1, no. 2, pp. 114-121, June 2013, doi: 10.1109/JESTPE.2013.2272696.

[198] B. Razavi, "The Bridged T-Coil [A Circuit for All Seasons]," in IEEE Solid-State Circuits Magazine, vol. 7, no. 4, pp. 9-13, Fall 2015, doi: 10.1109/MSSC.2015.2474258.

[199] Y. Mei, J. Wu and X. He, "Common Mode Noise Analysis for Inductive Power Transfer System Based on Distributed Stray Capacitance Model," in IEEE Transactions on Power Electronics, vol. 37, no. 1, pp. 1132-1145, Jan. 2022, doi: 10.1109/TPEL.2021.3098848.

[200] C. Wu, H. Kim, S. Penugonda and J. Fan, "Analysis and Modeling of the Common-Mode Conducted EMI From a Wireless Power Transfer System for Mobile Applications," in IEEE Transactions on Electromagnetic Compatibility, vol. 63, no. 6, pp. 2143-2150, Dec. 2021, doi: 10.1109/TEMC.2021.3087700.

[201] N. G. Hadjigeorgiou and P. P. Sotiriadis, "Parasitic Capacitances, Inductive Coupling, and High-Frequency Behavior of AMR Sensors," in IEEE Sensors Journal, vol. 20, no. 5, pp. 2339-2347, 1 March1, 2020, doi: 10.1109/JSEN.2019.2953351.

[202] A. Parsa Sirat, H. Niakan, J. Gafford, and B. Parkhideh, " Design Guidelines for Shield-Less PCB-Based Rogowski Coil Sensors With Passive Offset Compensation for Switching Current Measurement," 2023 IEEE Energy Conversion Congress and Exposition (ECCE), Nashville, TN, USA.

[203] A. Parsa Sirat, H. Niakan, and B. Parkhideh, " Utilizing a Micro-Fluxgate Magnetometer in Dual-Path Configuration for Fast Switch-Current Sensing," 2023 IEEE Energy Conversion Congress and Exposition (ECCE), Nashville, TN, USA.

[204] A. Parsa Sirat, Z. Matheson, and B. Parkhideh, " Developing Compact High-Bandwidth Transducer for Contactless Switch-Current Sensing in Emerging Grid-Tied Wide-Bandgap High-Power Converters," 2023 IEEE North American Power Symposium (NAPS), Asheville, NC, USA.

[205] A. Parsa Sirat, H. Niakan, and B. Parkhideh, " Ultra-Wideband Surface Current Sensor Topology for WBG Power Electronics Applications," 2023 IEEE 10th Workshop on Wide Bandgap Power Devices & Applications (WiPDA), Charlotte, NC, USA.

[206] Ridely Box, 1Hz-20MHz 4-Channel Frequency Response Analyzer, https://www.ridleyengineering.com/hardware/ridleybox.html.

[207] Tektronix AFG31051 Arbitrary Function Generator, 50 MHz, Single Channel, AFG31000 Series, https://www.tek.com/en/products/signal-generators/arbitrary-function-generator/afg31000.